The Pennsylvania State University

The Graduate School

ASSESSING THE IMPACT OF MODEL STRUCTURAL COMPLEXITY OF

THE METHANE CYCLE ON THE EARTH SYSTEM RESPONSE

A Dissertation in

Meteorology and Atmospheric Science

by

Kristina Alixis Rolph

Submitted in Partial Fulfillment

of the Requirements

for the Degree of

Doctor of Philosophy

December 2020

The dissertation of Kristina Alixis Rolph was reviewed and approved by the following:

Chris E. Forest
Professor of Climate Dynamics
Dissertation Advisor
Chair of Committee

Kenneth J. Davis
Professor of Atmospheric and Climate Science

Melissa M. Gervais
Assistant Professor of Meteorology and Atmospheric Science

Tom L. Richard
Professor of Agricultural and Biological Engineering

David J. Stensrud
Professor of Meteorology
Head of the Department of Meteorology and Atmospheric Science

Abstract

Atmospheric methane concentrations are at an unprecedented level and are on a trajectory to continue climbing as the demand for food and energy increase anthropogenic emissions. As a potent greenhouse gas, rising methane concentrations pose a serious threat to global temperatures. Any small change in global temperature can amplify the effects of climate forcing agents, resulting in impacts to human and environmental systems. In the interest of strategically reducing methane emissions, it is imperative we evaluate methane's growing role in the changing climate. In this dissertation, we begin by demonstrating that plausible methane reductions in the global agricultural sector help mitigate projected global warming. Guided by measurements of low-emission practices on U.S. dairy farms, life cycle assessments, and detailed emission inventories, we can design science-informed emission reduction scenarios. To simulate the climatic response to lower emissions, we use an intermediate-complexity Earth system model, the Massachusetts Institute of Technology Earth System Model (MESM). Having modeled the critical role of future methane reductions, we then characterize the specific impact atmospheric methane has on future climate change. Through impulse response tests, we assess feedbacks associated with the methane and carbon cycles that would otherwise be obscured in standard emission scenarios. Our results demonstrate that the MESM impulse response is non-linear due to feedbacks that arise from interactive atmospheric chemistry and biogeochemistry. Unlike the MESM and other comprehensive models, several reduced-form climate models and integrated assessment models do not account for these methane feedbacks. Lacking feedbacks is a flaw that leads to poor projections. To correct this limitation, we modify the methane components of the FaIR and FUND models to emulate the evolution of atmospheric methane in the MESM. Incorporating representations of a self-abundance feedback on methane's lifetime and a temperature-feedback on natural wetland methane emissions greatly improves the model's ability to project changes in atmospheric methane. As an integrated assessment model, FUND links socioeconomic factors to changes in emissions and the climate. We use the updated FUND model to estimate the impact of the newly introduced methane feedbacks on the calculation of the social cost of methane. Our study shows that the higher methane abundance, largely

due to the feedback mechanisms, increases the monetary damages of future climate change to an incremental emission pulse. Consequently, the social cost of methane rises. Overall, this dissertation contributes to the understanding of how methane emissions and emergent methane cycle feedbacks impact the Earth system behavior within a range of model complexities.

Table of Contents

Chapter 3

Earth system response to impulse changes in methane   38

Chapter 4

Introducing a concentration dependency on methane lifetime and natural

  emissions model into the FaIR climate model   60

List of Figures

List of Tables

List of Abbreviations

ACCMIP	The Atmospheric Chemistry and Climate Model Intercomparison Project
AR(1)	Autoregressive model with lag-1
AR5	The Fifth Assessment Report of the Intergovernmental Panel on Climate Change
BMP	Best management practice
CEDS	Community Emissions Data System
CMIP	Coupled Model Intercomparison Project
Dairy-CAP	Sustainable Dairy Coordinated Agricultural Project
ECS	Equilibrium Climate Sensitivity
EMIC	Earth System Model of Intermediate Complexity
EPA	U.S. Environmental Protection Agency
EPPA	Economic Projection and Policy Analysis model
ESM	Earth System Model
FaIR	Finite Amplitude Impulse Response model
FAOSTAT	Food and Agriculture Organization Corporate Statistical Database
FUND	Climate Framework for Uncertainty, Negotiation, and Distribution
GCM	General circulation model
GDP	Gross domestic product
GMSAT	Global mean surface air temperature
GWP	Global warming potential
HFC	Hydrofluorocarbon

IAM	Integrated assessment model
IFSM	Integrated Farm System Model
IPCC	Intergovernmental Panel on Climate Change
IRF	Impulse Response Function
IWG	Interagency Working Group
LHS	Latin Hypercube Sampling
LCA	Life cycle assessment
MAGGIC	Model for the Assessment of Greenhouse Gas Induced Climate Change
MCMC	Markov Chain Monte Carlo
MESM	MIT Earth System Model
MIT	Massachusetts Institute of Technology
NEM	Natural Ecosystem Model
NMVOC	Non-methane volatile organic compound
NFD	Neutral detergent fiber
NSF	National Science Foundation
PETM	Paleocene–Eocene Thermal Maximum
RAM	Robust Adaptive Metropolis
RCP	Representative Concentration Pathway
SCC	Social Cost of Carbon
SC-CH$_4$	Social cost of methane
SCRiM	Network for Sustainable Climate Risk Management
SSP	Shared Socioeconomic Pathways
TCR	Transient climate response
USDA	United States Department of Agriculture

Acknowledgments

Chapter 1

Introduction

Evidence of rapid climate change is compelling and unequivocal. Extreme changes seen in the last thirty years from multiple records are largely unprecedented for over decades to millennia. As the primary indicator of climate change, Earth's average surface temperature has risen 0.85 °C between 1880 and 2012, a change predominately driven by emissions of heat-trapping gases and aerosols from human activities (IPCC, 2013). Powerful evidence comes from atmospheric and oceanic measurements, as well as, reconstructions of paleoclimate data (Delmas et al., 1980; Keeling et al., 1976). From these measurements, discoveries of past glacial cycles, periods of extreme drought, human developments, and much more are unveiled. Essentially, each specific measurement takes a snapshot of the whole system but it does not reveal the whole picture.

To better perceive the complex interactions that shape the climate, scientists develop comprehensive models that portray the intertwined processes of the land, atmosphere, ocean, and cryosphere (McGuffie and Henderson-Sellers, 2014). Climate models, also known as Earth System Models, reveal the short and long response-timescales of how the world naturally functions. They also uncover the influence humans make on climate and the ramifications of rapid climate change to society. Without quick adaptation to meet the projected changes, societal consequences of climate change can seriously affect human welfare, health, food security, water resources, and biodiversity (Xu et al., 2009; Gregory et al., 2005; Adams et al., 1995). This dissertation aims to improve climate predictions by evaluating the impact of a potent greenhouse gas, methane, on the Earth's response, particularly, the atmospheric chemistry and biogeochemistry. Implications of our results could help decision-makers prioritize environmental issues based on climate projections and scientific evidence.

1.1 Why Methane Matters

Global dependence on fossil fuel use continues to remain high and the pathway to low-emission or net-zero emission technologies is a gradual transition that has yet to strongly compete in international markets. The urgency of the climate crises and the setback of carbon dioxide reductions implies that additional reductions in other greenhouse gases must be included in a set of solutions. With established mitigation opportunities, combating methane emissions is a much needed low-hanging fruit that we can use to limit rising global temperatures. Methane (CH_4) is a more potent greenhouse gas than carbon dioxide (CO_2) because it significantly traps more heat in the atmosphere. As a result, reductions in methane emissions could undoubtedly help reach well-established temperature targets. In the following sections, we introduce the many concerns of rising atmospheric methane and potential trajectory of future methane emissions.

1.1.1 Evolution of Global Methane

Long-term records of polar ice cores provide direct evidence of past atmospheric concentrations up to 800,000 years ago (Loulergue et al., 2008), with discontinuous samples as far back as 2.7 million years ago (Yan et al., 2019). Multi-millennial timescales reveal that maximum methane concentrations of 800 parts per billion (ppb) were observed during interglacial periods and minimum concentrations of 350 ppb during glacial periods (Loulergue et al., 2008). The most rapid variations (greater than 50 ppb) occurred within the last glacial period and are likely due to strong Northern Hemispheric temperature fluctuations. Scientists have also speculated that a large and rapid release of carbon stocks initiated the Paleocene–Eocene Thermal Maximum (PETM), the warmest 170-thousand year period since the extinction of the dinosaurs (Bowen et al., 2004). Methane emissions from terrestrial permafrost could have acted as positive feedbacks to prolong the warming (DeConto et al., 2012). Other proposed carbon sources that led to the PETM warming include methane hydrates, hydrothermal vents, and volcanic intrusions (Turner et al., 2019; Frieling et al., 2016; Zeebe, 2013).

Nowhere in the climate record have global atmospheric methane concentrations been as high as the present-day (Figure 1.1). Atmospheric methane levels reached 1850 ppb in 2017, more than 2.6 times greater than its estimated preindustrial equilibrium value (Saunois et al., 2020). There is no debate that the increase is human caused. The late 1970s marked the beginning

of global monitoring of methane emissions (Blake et al., 1982) and soon scientists took notice of the strong anthropogenic increase coming from the Soviet gas industry through the 1980s (Dlugokencky et al., 1998). While the general trend indicated anthropogenic sources dominated, there were periods of volcanic eruptions (e.g. Mt. Pinatubo in 1992) and the major El Niño events (1997–1998) that led to higher methane growth rates (Nisbet et al., 2016). Positive-phase El Niño events create warmer and drier conditions in the tropics, generating widespread fire and biomass burning that release anomalously emissions (Rowlinson et al., 2019).

In the early 2000s, global atmospheric levels stabilized at 1750 ppb (Dlugokencky, 2019). But in 2007, atmospheric levels began increasing again (Rigby et al., 2008), with contradictory speculations on the particular cause (Nisbet et al., 2016; Kirschke et al., 2013). It is difficult to attribute the trend as there is a multitude of uncertain natural and anthropogenic emission processes that are arduous to monitor. Suggested culprits include changes to methane sources; wetlands, livestock, fossil fuels, biomass burning, and to the atmospheric chemical sink (Rigby et al., 2017; Hausmann et al., 2016; Schaefer et al., 2016). While uncertainties in the methane budget exist, it is becoming more evident that anomalous stabilization periods fall within a long-term, increasing trend due to human activities (Figure 1.1).

1.1.2   An Imbalance of Sources and Sinks

Attributing changes to different sources is important for generating better projections and determining effective mitigation strategies to lower methane emissions (Karakurt et al., 2012). Since the stagnation period of the early 2000's, the globally averaged atmospheric growth rate has varied between 5–10 ppb per year (Kirschke et al., 2013), reflecting fluctuations in methane sources and sinks. The methane budget refers to the atmospheric concentration variation that results from an imbalance of the cumulative emission sources and atmospheric chemical sink. A schematic representation of the 2008–2017 methane budget is shown in Figure 1.2. The methane budget is updated regularly to reflect new data from observations and global models (Saunois et al., 2020, 2016). However, large uncertainties in emissions from anthropogenic sources (up to 20–35% uncertainty) and natural sources (50–100% uncertainty) affect the budget. Uncertainties in emission inventories reflect the difficulty in differentiating geographically-overlapping methane sources, as well as, monitoring emissions at regional scale and aggregating to the global scale (Saunois et al., 2020).

1.1.2.1 Primary Sources

In total, 572 Teragrams of methane per year (Tg-CH$_4$ yr^{-1}) were emitted from all methane sources for the 2008-2017 decade (Saunois et al., 2020). The greatest source of uncertainty is attributed to natural emissions coming from wetlands and other inland waters (lakes, ponds, rivers). High water content areas limit oxygen availability, creating an environment that promotes decomposition of organic matter by methane-producing bacteria or methanogens (Fiedler and Sommer, 2000; Ferry, 1999). In these environments, methane formation accompanies methane consumption or oxidation by methanotroph bacteria. What determines the magnitude of the flux from wetlands is environmental factors like water saturation, temperature, and availability of organic matter (Kip et al., 2010; Frenzel and Karofeld, 2000). Analyses indicate a rise in soil temperature up to 30 °C could generate a 57-fold increase in methane emissions (Yvon-Durocher et al., 2014). Additional uncertainties arise from modeling wetland extent and seasonal variations, as regional differences are difficult to capture (Poulter et al., 2017; Wania et al., 2013). Globally, it is estimated wetlands emit 148 $\pm$ 25 Tg-CH$_4$ yr^{-1}, making up 30% of all total methane
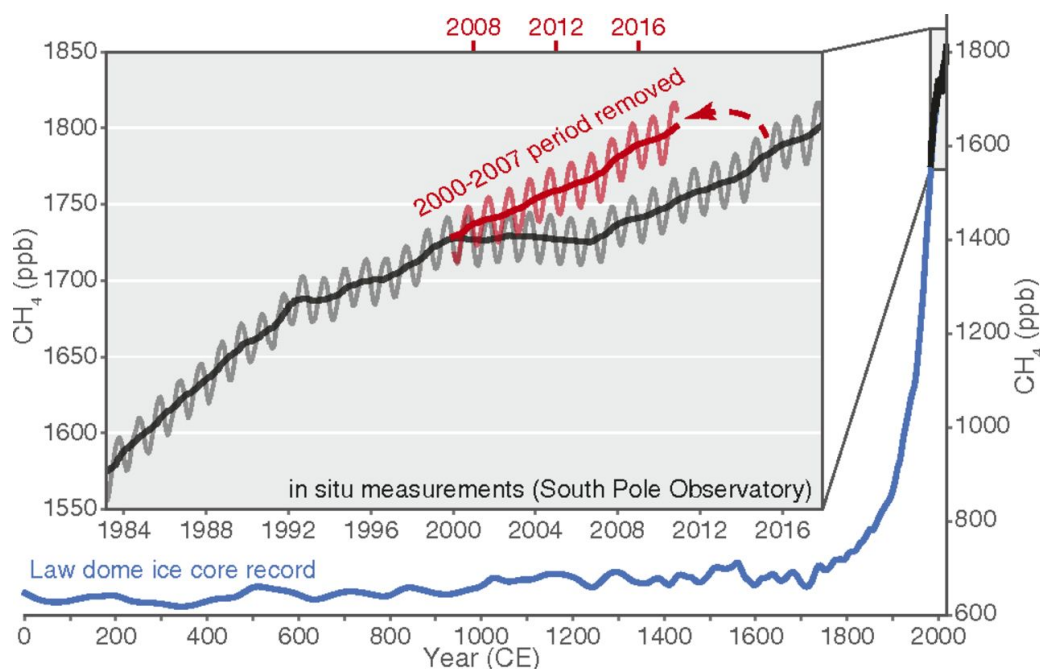
Figure 1.1. Atmospheric methane over the past 2000 years from the Law Dome ice core record (blue) and seasonal record of the South Pole (gray). Also shown is the hypothetical continuation of the trend if the 2000–2007 stagnation period did not occur (red). Figure taken from Turner et al. (2019).

emissions (Saunois et al., 2020). And, other inland water bodies emit an additional 117 Tg-CH$_4$ yr^{-1} (Stanley et al., 2016; Deemer et al., 2016; Bastviken et al., 2011).

Although not as significant as wetlands, additional natural methane emissions come from geothermal systems, oceans, and permafrost (Saunois et al., 2020). Geologic sources including emissions from volcanoes, seepage from gas-oil fields, and microbial sedimentary basins make up 37 Tg-CH$_4$ yr^{-1} (Etiope et al., 2019). Possible oceanic emissions result from biogenic origins (6 Tg-CH$_4$ yr^{-1}) and seabed plumes (65 Tg-CH$_4$ yr^{-1}) (Saunois et al., 2020). Marine hydrates, ice formations which trap methane, are largely uncertain in extent but are considered to be negligible as water column absorption prevents a measurable flux to the atmosphere (Wallmann et al., 2012; Milkov, 2005). A growing concern is emissions from permafrost, which consist of frozen organic carbon in soils and sediments. While nearly negligible in present-day, a warming climate could thaw extensive areas permafrost in the Northern Hemisphere (Schuur et al., 2015) making 5–15% of the carbon pool vulnerable to a 130–160 Gigaton (GtC) release over the next century (Koven et al., 2015).
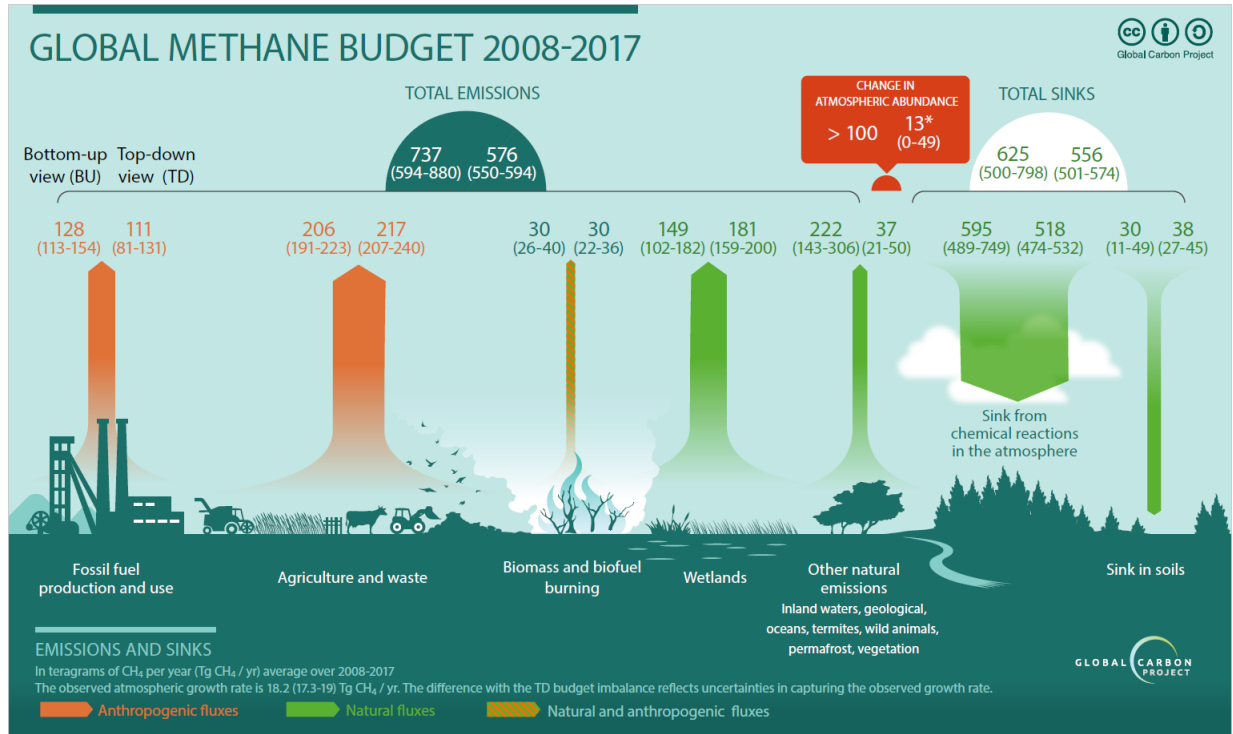
Figure 1.2. The global methane budget (2008–2017) including estimated emissions and sinks from bottom-up and top-down approaches. Figure taken from Saunois et al. (2020).

While natural biogeochemical and geologic sources make up a considerable fraction of the methane budget, methane emissions are predominately anthropogenic, accounting for 50–65% of total emissions (IPCC, 2013). Livestock production is by far the largest source of anthropogenic methane emissions (Tubiello et al., 2013). Methanogens living within the digestive tracks of ruminant animals emit methane as a by-product of consuming plant matter (Johnson and Johnson, 1995). Manure decomposition within anaerobic conditions also creates conditions favorable for microorganisms to produce methane. Considering both emission sources, global livestock emissions are estimated to be 111 Tg-CH_4 yr^{-1}, about a third of total anthropogenic emissions (Saunois et al., 2020).

Additional methane emissions result from human operations and exploitation of natural resources. Human initiated forest fires and burned agricultural residues emit methane when low-oxygen availability prohibits full combustion (van der Werf et al., 2017). Along the same lines, burning of biofuel for energy production and domestic cooking also produce substantial methane. Biomass and biofuel burning make up about 11% of anthropogenic methane emissions. A larger fraction (35%) of anthropogenic methane emissions come from fossil fuel production and use of coal, oil, and natural gas (Saunois et al., 2020).

Finally, we touch on methane emissions from waste management and agricultural cultivation of rice. Shallow-flooded paddy fields deplete oxygen in the soils to form anaerobic conditions for microbial methane production. It is estimated rice paddies, largely in China and India, make up 8% of anthropogenic emissions of methane (Saunois et al., 2020; Carlson et al., 2017; Hayashida et al., 2013). And, degradable organic material in wastewater and landfills is treated anaerobically, leading to increased emissions (Börjesson and Svensson, 1997). Wastes make up 12% of global anthropogenic emissions (Saunois et al., 2020), but in the U.S. waste is the largest single contributor to anthropogenic methane, almost 26% of all anthropogenic methane in 2014 (EPA, 2016).

1.1.2.2 Atmospheric Sink

After methane reaches the troposphere, about 90% of the removal is through chemical oxidation by hydroxyl radical (OH) (Ehhalt, 1974). Additional small losses occur by stratospheric reactions (Brasseur et al., 2006), soil uptake (Curry, 2007), and reactions with chloride in the marine boundary layer (Allan et al., 2007). But, our focus will be on the predominant loss mechanism

due to oxidation by OH. When methane oxidizes, the net reaction removes tropospheric OH, the main driver for methane's atmospheric sink, and produces greenhouse gases, CO_2 and H_2O. OH does not only react with methane, it oxidizes atmospheric pollutants such as nitrogen oxides (NOx), carbon monoxide (CO), non-methane volatile organic compounds (NMVOCs), and hydrofluorocarbons (HFCs) (DeMore, 1996). Globally, methane directly removes 15% of tropospheric OH. Accounting for the indirect effect methane has on other species, the amount of OH removed from the troposphere increases to approximately 40% (Holmes, 2018). Since OH is very reactive in the atmosphere, its lifetime is only a few seconds (Lelieveld et al., 2004). However, such a short lifespan makes measurements very difficult on the regional to global scales, creating substantial uncertainty in the methane chemical loss (Prather et al., 2012). Variations in anthropogenic emissions, natural tropical ecosystem emissions, and El Niño–Southern Oscillation can lead to changes in OH, with interannual variability ranging 0.4–1.8% (Zhao et al., 2019).

1.1.3 Methane Lifetime

Methane lifetime refers to the ratio of global atmospheric burden to the total loss from all sinks in a steady state condition (Ehhalt et al., 2001). In several simplifications, methane lifetime refers only to the loss by OH oxidation, neglecting the small losses to the stratosphere, soils, and marine boundary layer. Multi-modeled estimates of the steady state tropospheric lifetime range 7.2–10.1 years (Morgenstern et al., 2018). Since methane is not presently in steady state, the lifetime is always changing in response to small perturbations in concentration and atmospheric chemistry. In particular, changes to the OH sink inversely affect the methane lifetime.

The amount of methane in the atmosphere is the most significant variable to affect the OH sink, and subsequently methane lifetime. Just a 1% increase in methane decreases mean tropospheric OH by 0.31% (Holmes et al., 2013). Any subtle changes in tropospheric OH will have a direct impact on methane levels. For example, Rigby et al. (2017) found that a declining trend in OH abundance during the post-stagnation period (2007–2014) is statistically attributable (64–70% probability) to the rise in methane concentration. The oxidation rate decreases with increasing methane concentration, affecting the amount of time methane spends in the atmosphere. This results in a self-abundance positive feedback known as the methane lifetime feedback effect (Prather, 1994). Holmes (2018) has shown that the lifetime feedback strength varies geographically and seasonally with OH concentration, where the feedback is strongest over tropical oceans in the summer and generally weaker over the continents and poles.

1.1.4 Methane Climate Forcing and Indirect Effects

Radiative forcing is the net change in the radiative flux (shortwave plus longwave) at the top of the atmosphere to an imposed perturbation (Myhre et al., 2013). Methane creates a powerful radiative forcing effect due to its absorption of infrared radiation at wavelengths of 3.3 and 7.7 μm (Reay et al., 2018). Since 1750, atmospheric methane has contributed 23% (0.62 $W\,m^{-2}$) to the additional radiative forcing (Etminan et al., 2016). Including the indirect effects on its lifetime and other chemical compounds, methane's total radiative forcing is 0.97 $W\,m^{-2}$, making it the second largest contributor (behind CO_2, 1.68 $W\,m^{-2}$) to the increase in radiative forcing (Myhre et al., 2013).

1.1.5 The Future of Atmospheric Methane

The twenty-first century is likely to see a continual rise in methane as underlying emission drivers, like demand for energy and food, increase with population. Climate researchers are continuously adopting and updating plausible emission trajectories. The current general body of literature has adopted the Representative Concentration Pathways (RCPs) from the Fifth Assessment Report (AR5) of Intergovernmental Panel on Climate Change (IPCC) (IPCC, 2013). Each RCP scenario is identified by their approximate total radiative forcing in year 2100 relative to 1750 (Moss et al., 2010; Meinshausen et al., 2011b; van Vuuren et al., 2011b). At our current rate of global anthropogenic emissions, our trajectory most closely resembles RCP8.5, the highest concentration scenario (Schwalm et al., 2020).

Standardized setups of inter-comparison model studies use prescribed RCP concentrations to drive complex climate models and produce projections of the Earth system response. Results from simulations performed for the Atmospheric Chemistry and Climate Modeling Intercomparison Project (ACCMIP) indicate end of century methane concentration could increase 117% relative to year 2000 for RCP8.5 (Voulgarakis et al., 2013). In addition, the inter-comparison project showed methane lifetime is projected to increase 8.5±10.4% for RCP8.5, but could decrease 4.5±9.1% for RCP2.6.

1.1.6 Methane Mitigation Opportunities

Methane mitigation refers to capturing methane at the source or preventing its formation. Across the globe, cost-effective mitigation technologies and practices are already widely available and in-use. Shindell et al. (2017) projects another 110 Tg-CH$_4$ yr^{-1} of abatement is possible by scaling up existing technologies. Naturally, the mitigation potential and particular practices that could be put into place will vary by country and available resources. Besides mitigating climate change, solutions have shown to provide additional societal benefits to local environments and human health that outweigh implementation costs (Nisbet et al., 2020). We provide a brief synopsis of current technologies for the energy and agricultural sectors.

The energy sector provides a substantial opportunity for methane mitigation. As one practice, coal miners can drill holes before excavation and capture methane for energy use (Dontala et al., 2015). This ventilation provides the extra benefits of improved air quality and safety within the mines (Karacan et al., 2011). In a promising review by the EPA, better mining practices could eliminate 64% of mining methane emissions in 2030 (EPA, 2019). Other energy sector mitigation opportunities eliminate fugitive emissions by upgrading equipment to detect gas leaks (Lamb et al., 2015).

This dissertation focuses more deeply on mitigation opportunities within the agricultural sector, particularly mitigation of dairy farms. Agricultural emissions tend to be geographically disseminated and hard to pin-point for abatement purposes (Reisinger and Clark, 2018), but implementation of several better farming practices can make substantial cuts in methane emissions (Veltman et al., 2018; Smith et al., 2008). Mitigation measures aim to cut emissions from livestock manure and enteric fermentation. For one, separating the solid and liquid components of manure can reduce 81% of manure methane emissions (VanderZaag et al., 2018). Another option for industrial-scale dairy farms is sealing manure in anaerobic digester tanks to produce nutrient-rich fertilizer and biogas (Pratt and Tate, 2018). As an extra benefit, burning the biogas by-product can be used for heating or equipment fuel. Changes in livestock diets have also proved to decrease enteric methane emissions from the cattle digestive tracks. Feed additives and supplements combined with typical cattle feed inhibit enteric methane production and subsequently reduce emissions (Knapp et al., 2014).

1.2 A Hierarchy of Earth System Models

Models exhibit a wide range of physics, parametric simplifications, and spacial scales. The most fundamental of climate models aim to understand the Earth's energy balance and thermodynamics of the system (North et al., 1981). As more components are represented, a model hierarchy tends to develop (Figure 1.3) (McGuffie and Henderson-Sellers, 2005). Depending on the nature of the scientific question posed, the most relevant model will be chosen based on complexity level and the pertinent timescales.

Performing at the highest feasible spatiotemporal resolution are fully coupled Earth System Models (ESMs). Their model components account for the best current representations of the full climate system, including the atmosphere, ocean, land surface, carbon cycle, and ice sheet dynamics (Arora et al., 2013). Considered the most comprehensive instruments available,
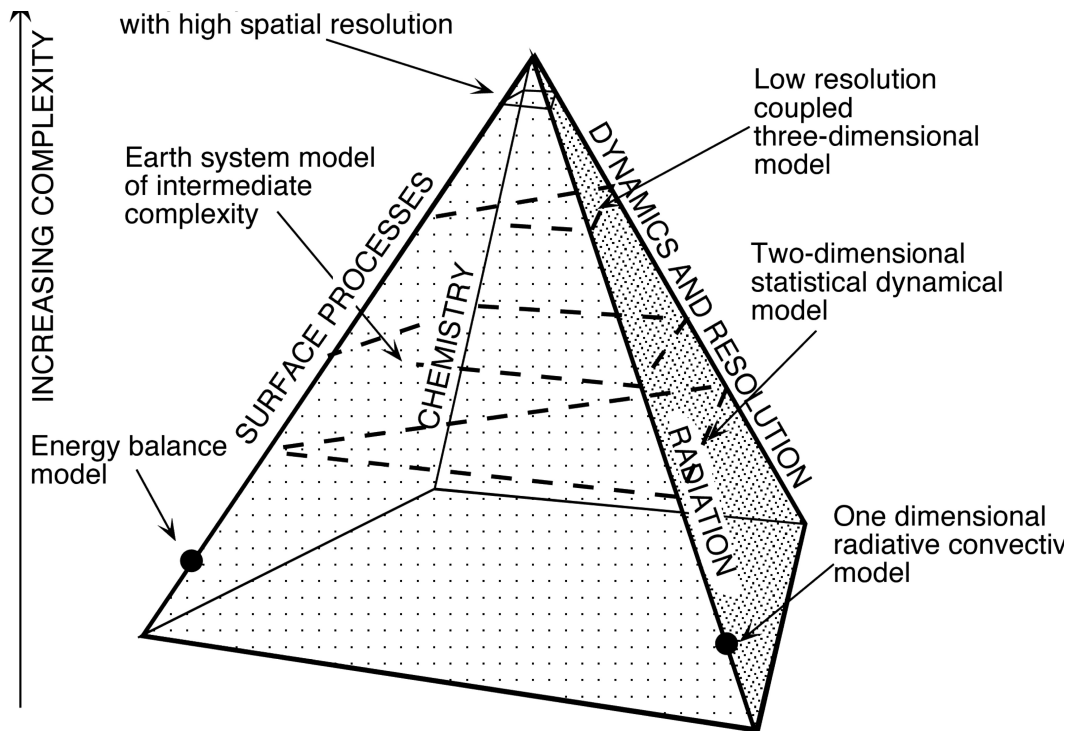
Figure 1.3. The climate modeling pyramid. Progression up the pyramid indicates greater complexity for four primary pillars; dynamics, radiation, surface processes, and chemistry. Figure taken from McGuffie and Henderson-Sellers (2005).

ESMs contain high spatial resolutions, detailed surface processes, biogeochemistry, and intricate radiation schemes (McGuffie and Henderson-Sellers, 2014). Given the number of processes included and the need for high resolution, ESMs require significant computational resources, limiting the number of experiments or ensemble simulations that can be run.

As computing power can be a significant barrier to conducting multiple simulations, Earth system models of intermediate complexity (EMICs) have been developed to operate at lower temporal and spatial resolutions (Weber, 2010). Albeit in a more reduced and parameterized form, EMICs include most of the processes described in state-of-the-art models (Claussen et al., 2002). Because they are calibrated to replicate results of complex models, they are very useful in representing the climate system with fewer computational resources. This makes EMICs ideal for long simulations to understand decade to century timescale processes. They are also ideal for uncertainty studies requiring multiple model runs with slightly altered inputs (Zickfeld et al., 2013; Claussen et al., 2002).

Having the lowest resolution of the modeling hierarchy, reduced-complexity models can take anywhere from a few seconds to minutes on a personal computer to simulate century-long experiments. This is because they parameterize complex processes seen in higher complexity models (McGuffie and Henderson-Sellers, 2014). They have been instrumental for investigating the sensitivity of the climate system to external forcing agents and interpreting results of more complex ESMs (Knutti and Sedláček, 2013b). As one type of reduced-complexity model, box models resemble reservoirs of the climate system, where fluxes into and out of the box represent the exchange between system components. Other examples of reduced-complexity models include energy balance models and one-dimensional radiative convective models (McGuffie and Henderson-Sellers, 2014). As the name suggests, energy balance models illustrate the amount of energy coming in and out of the Earth system, which is assumed to be in an equilibrium state. With more detail in the vertical direction, one-dimensional radiative convective models simulate how energy is absorbed, emitted, and scattered (Harvey et al., 1997).

While climate models are often used as stand-alone models, they can also be linked to socioeconomic models to form integrated assessment models (IAMs) (Tol and Fankhauser, 1998). IAMs usually follow a cause-and-effect chain, where emissions and land-use modifications from human activities drive changes in the climate system. An economic component will then translate the physical climate changes into impacts on human health, agriculture, and economic activity (Schneider, 1997).

1.3 Impulse Response Behavior

A way to explore a model's behavior is to insert a large instantaneous perturbation and conduct idealized impulse response tests. By doing so, we can uncover climate behavior that is not discernible in observations or standard emission-driven model simulations (Schwarber et al., 2019). A way to approximate the complex model results in a simplified mathematical manner is fitting it to an impulse response function (IRF). The IRF of some perturbed subsystem (x) likens as a superposition of decaying exponential functions of different amplitudes (A_i) and perturbation times (τ_i):

$$IRF_x(t) = \sum_{i=0}^{n-1} A_i * exp\frac{-t}{\tau_i} \tag{1.1}$$

Many studies have developed IRFs for the global carbon cycle by fitting a function to the atmospheric response to a CO_2 perturbation of a more complex model or a multi-model mean (van Vuuren et al., 2011a; Hooss et al., 2001; Maier-Reimer and Hasselmann, 1987). The parameters of the IRF are then adjusted to match the full representation of the carbon cycle of the more complex model (Maier-Reimer and Hasselmann, 1987). Standing alone, the IRF can reproduce the time evolution of how carbon is transferred from the atmosphere to the terrestrial and oceanic carbon pools. Because IRFs are designed to replicate the behavior of complex models, they are often used within the structure of conventional IAMs (eg. FUND (Tol, 2006) and MERGE (Manne and Richels, 2005)).

1.3.1 Nonlinearities and Feedback Limitations

IRFs are able to accurately mimic a fully linear system. By definition they assume the climate responds slowly and predictably as atmospheric concentrations increase (Olivié and Peters, 2013). Yet, the climate is subject to rapid nonlinear changes and feedbacks. For example, an increase in greenhouse gases accelerates warming and in turn that warming affects the atmospheric concentration and carbon cycle. Complex model simulations that include an interactive carbon cycle indicate that the climate-carbon cycle feedback decreases the net absorption into the land and ocean carbon pools, resulting in an extension of the CO_2 lifetime in the atmosphere (Archer et al., 2009). The IPCC AR5 impulse response model, designed to quantify the carbon

cycle response to a 100 Gigaton carbon (GtC) pulse (Joos et al., 2013), does not include the temperature feedback on the carbon sinks. As a result it greatly overestimates the global mean temperature response to an instantaneous quadrupling of CO_2 (Schwarber et al., 2019).

For small perturbations, IRFs can approximate some nonlinearities exhibited in complex climate models (Hooss et al., 2001). As an example, the Finite-amplitude Impulse Response model (FaIR) (Smith et al., 2018; Millar et al., 2017) can simulate the decreasing efficiency of the carbon sinks with increasing global temperature, thus replicating the behaviors and feedbacks seen in more complex ESMs (Fung et al., 2005).

However, IRFs are limited in their ability to only describe one state of the climate system that they were built to emulate. Depending on the state of the system, background concentrations, and size of a perturbation, nonlinearities that arise could generate very different climate response outcomes (Joos et al., 2013; Zickfeld and Herrington, 2015; Gregory et al., 2005). For example, when the FaIR model tests an impulse emission under changing background conditions, it loses
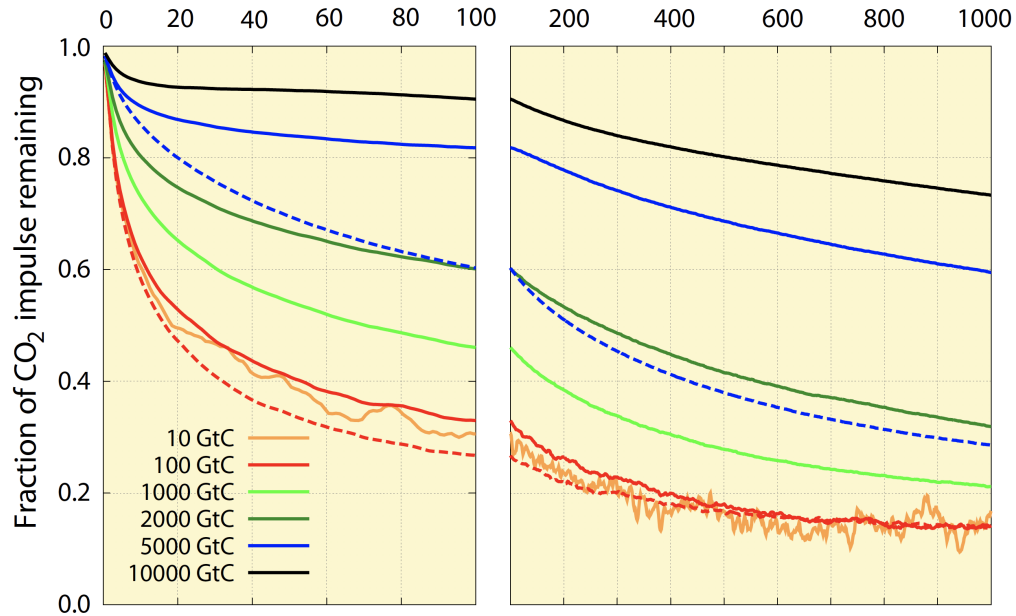
Figure 1.4. Fraction of the CO_2 impulse perturbation remaining in the atmosphere for 1000 model years. Impulse response functions shown for pulse emissions 10 to 10,000 GtC simulated in the comprehensive Bern3D-LPJ model. Dashed lines represent a constant climate without carbon cycle feedbacks. Figure taken from Joos et al. (2013).

its strength in predictability. The results show an underestimate of the airborne CO_2 fraction following a standard emission impulse (Schwarber et al., 2019).

Also, the size of the perturbation matters when calibrating the IRF (Maier-Reimer and Hasselmann, 1987). Figure 1.4 shows the time-integrated IRF for several pulse sizes between 10 and 10,000 GtC for one of the coupled EMICs, the Bern3D-LPJ, in Joos et al. (2013). The larger pulse sizes show a slower response to remove carbon from the atmosphere as the carbon pools become overwhelmed by the influx of carbon. The investigation also demonstrates how carbon cycle-climate feedbacks influence IRF evolution. When feedbacks are omitted (dashed lines in Figure 1.4) the model underestimates the fraction of CO_2 remaining in the atmosphere.

1.4 Integrated Assessment Models and their Implications

While climate models are often used as stand-alone models, they can also be linked to socioeconomic models to form integrated assessment models (IAMs) (Tol and Fankhauser, 1998). Encompassing several disciplines, IAMs risk becoming too complex. For this reason, many existing IAMs operate on uncomplicated equations (Goodess et al., 2003). Developers of IAMs simplify more complex models by using box models that represent the bulk properties of the reservoirs. Within an atmospheric box model, an IRF will simulate the evolution of an greenhouse gas (Joos and Bruno, 1996). As simplifications are often flawed, they can end up generating a great deal of imprecision and impact the result quality (Füssel, 2007; Smith and Edmonds, 2006). To improve IAMs, a number of studies have focused on the technical deficiencies of the economic components, suggesting that the approaches to future discounting rates and damage functions are inadequate (Tol and Fankhauser, 1998; de Bruin et al., 2009). As research progresses on the economic components, more progress is needed to better represent the climate system in IAMs.

Recent attention has shifted to updating IAMs to reflect modeling progress in carbon cycle dynamics and non-CO_2 impacts (Hof et al., 2012). A few IAMs are aggregating all feedbacks into a single equation that relates natural emissions to linear temperature changes (Bouwman et al., 2006). Despite the effort, calculated temperature feedbacks in IAMs appear to fall short of complex model results under high emission scenarios (van Vuuren et al., 2011a). In addition, many widely-used IAMs (e.g. FUND, PAGE, DICE) do not include feedbacks related to changes in non-CO_2 greenhouse gases that are seen in complex model results. For example, they lack

14

the methane lifetime feedback, which extends the methane atmospheric residence time with increasing abundance (Voulgarakis et al., 2013). This dissertation aims to rectify this limitation by parameterizing the methane lifetime feedback in the FUND integrated assessment model.

Further, commonly used IAMs tend to show lower radiative forcing projections when compared to expert models of the ACCMIP model range in Figure 1.5. Especially for a high emission scenario like the RCP8.5, non-CO_2 forcing agents fall short of the more complex models, largely due to the exclusion methane's indirect effect on other atmospheric species like ozone (Harmsen et al., 2015).

In summary, IAMs are in need of upgrades to their climate model components. Many lack the necessary representations of carbon cycle processes and timescales, as well as, interactive atmospheric chemistry. Our research aims to address the flaws in integrated assessment modeling by bridging the gap between reduced-complexity climate models and fully coupled models.
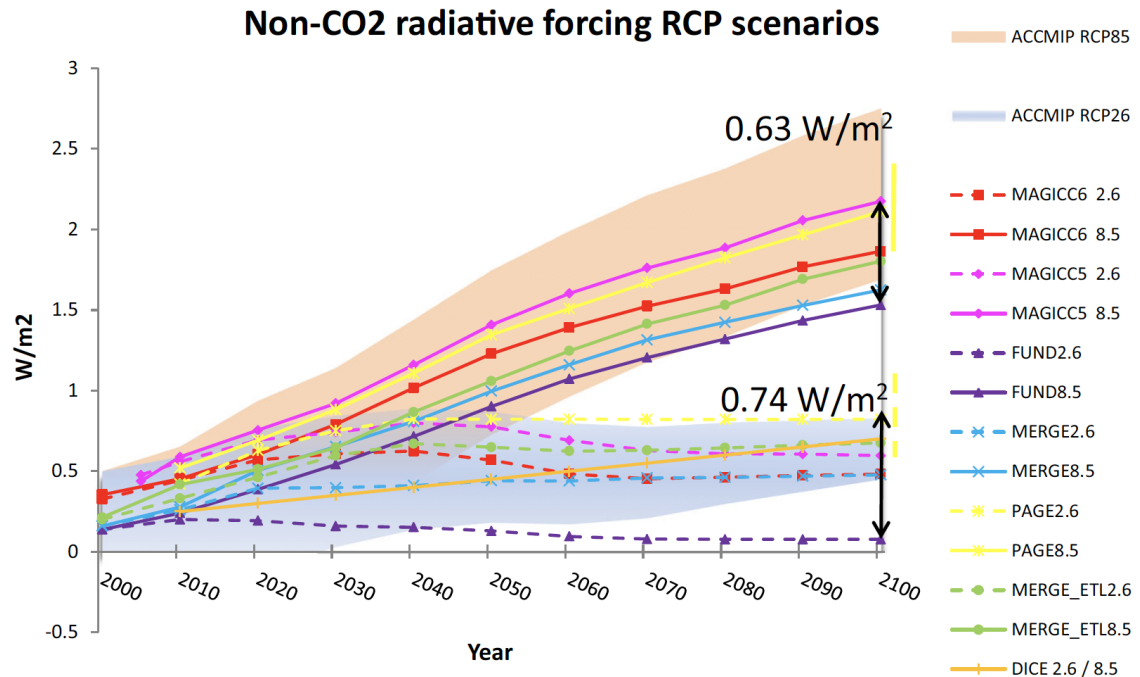
Figure 1.5. Total non-CO_2 forcing for projected RCP2.6 and RCP8.5 scenarios for individual IAMs and expert model ranges from the Atmospheric Chemistry and Climate Model Intercomparison Project (ACCMIP). Figure taken from Harmsen et al. (2015).

1.4.1 Social Cost of Carbon

One use of integrated assessment models is for the calculation of the Social Cost of Carbon (SCC), which refers to the marginalized monetary cost of climate damages resulting from an incremental emission of a greenhouse gas (National Academies, 2017). Typically this is calculated by comparing trajectory of climate damages from a baseline emission scenario to a pulsed emission trajectory, where an additional unit ton emission of a greenhouse gas is released in a single year onto the baseline scenario. The climate model component of the IAM will estimate the changes in climate properties; temperature, precipitation, and sea level (Thompson, 2018; Nordhaus, 2017). The farther the climate properties are from idealized threshold values, the greater the IAM estimates damages to human health, natural ecosystems, productivity, and property. The difference in monetary damages from the baseline and pulsed trajectory is the marginal damage per unit emission, otherwise known as the SCC.

Because several IAMs contain a model structure that prevents the exogenous modeling of non-CO_2 greenhouse gases, very few estimates of the social cost of methane (SC-CH_4) exist. The current SC-CH_4 estimates used by the U.S. Government for emission regulations were determined by Marten et al. (2015). However, their methane calculation underestimates the fraction of methane in the atmosphere following the impulse emission. Our improvement of this work represents methane's self-abundance feedback on its lifetime.

1.5 Driving Research Questions

In this dissertation, we aim to assess the impact of the methane cycle on the Earth system response within reduced- and intermediate-complexity models. As discussed, we rely on the best available models to draw conclusions about past and future climate. Intermediate-complexity models allow for multiple simulations to explore uncertainties in model assumptions and their potential to influence future projections. Using approximations (e.g. zonal-mean atmosphere), EMICs can run more quickly while still replicating processes described in state-of-the-art Earth System Models (ESMs). Although EMICs are very useful for many modeling applications, they might not always be the best tool. In this case, reduced-form models and integrated assessment models may be more appropriate.

Climate system representations within integrated assessment models (IAMs) account for complexity by aggregating and reducing comprehensive model results into a manageable set of equations, often in the form of an impulse response function (IRF). They serve the purpose of computational efficiency and transparency where large sample simulations cannot be made with highly complex and slow-to-run ESMs. Integrated assessment models also simulate the socioeconomic consequences to changes to the climate, as they connect an economic component to the climate component. Albeit, to some extent, all reduced-complexity models are flawed and could lead to poor projections. The one flaw we focus on and try to remedy is the lack of methane feedbacks within IAMs and the calculation of the social cost of methane. Our research exemplifies how an intermediate-complexity model can be used to improve reduced-form climate models to better reproduce the response of the Earth system and methane cycle.

One application of climate modeling is to help inform policy by providing the science. Keeping this in mind, we are providing model simulations which will help address policy-relevant questions, rather than directly making policy decisions from the model results. We begin this dissertation by addressing a scientific question stemmed from policy; **To what extent can plausible reductions in agricultural greenhouse gas emissions, specifically methane, help mitigate projected impacts of global warming?** As the agricultural sector is a major emitter of methane, we aim to understand the importance of non-CO_2 mitigation. In this research, we advocate for the application of an EMIC as a proper tool for emission reduction simulations. We use an EMIC that includes the representation of atmospheric chemistry, as well as, nonlinearities associated with the carbon cycle.

EMICs and complex ESMs demonstrate that interactions across model components result in nonlinearities in the response of the system. Of particular interest are the feedbacks that arise from perturbations of atmospheric methane. As a reactive greenhouse gas, methane can indirectly affect other atmospheric gases by its reaction with hydroxyl radical. This in turn affects methane's own lifetime. Knowing this we then ask a follow up question: **How do feedbacks in an Earth system model of intermediate complexity influence the response to an idealized methane perturbation?** Depending on the state of the system and size of a perturbation, nonlinearities that arise within the system could generate very different climate response outcomes. By conducting this research we better understand how model interactions between the atmosphere, ocean, and biosphere define the system response and produce emergent feedbacks.

Current IAMs used for policy analysis and social cost estimates are lacking crucial representations of atmospheric chemistry, carbon cycle processes, and nonlinear dynamics. As a result, several important methane feedbacks are not represented. When compared to more complex models, the reduced-complexity models within IAMs are falling short in their response to high emission scenarios, thus underestimating the damages resulting from additional emissions. We ask a two-part question: **Does incorporating methane feedbacks in a reduced-complexity climate model improve its ability to reproduce the results of higher complexity models?** We introduce formulations to mirror feedbacks to methane's lifetime and natural emission sources. The model is tuned to emulate the Earth system response of the EMIC. Having improved the methane component of a model conventionally used to calculate the Social Cost of Carbon, we ask a final question: **How much does the social cost of methane change with additional feedbacks included in an integrated assessment model?** In this final project, we update the social cost of methane to more accurately reflect the emergent feedbacks on the methane and carbon cycles.

In summary, we aim to address the overarching question: How does the methane cycle impact the Earth system response within reduced- and intermediate-complexity models? Given this broad topic, it is only feasible to address parts of it and so we focus on the following questions:

1) To what extent can plausible reductions in agricultural greenhouse gas emissions, specifically methane, help mitigate projected impacts of global warming?

2) How do feedbacks in an Earth system model of intermediate complexity influence the response to an idealized methane perturbation?

3) Does incorporating methane feedbacks in a reduced-complexity climate model improve its ability to reproduce the results of higher complexity models?

4) How much does the social cost of methane change with additional feedbacks included in an integrated assessment model?

Chapter 2

Non-CO$_2$ Mitigation Options Within the Dairy Industry for Pursuing Climate Change Targets

2.1 Abstract

Mitigation of non-CO$_2$ climate forcing agents must complement the mitigation of CO$_2$ to achieve long-term temperature and climate policy goals. A large share of global non-CO$_2$ greenhouse gas emissions is attributed to agriculture, with a significant contribution related to dairy production. As demonstrated by the results of a recent USDA coordinated project, Dairy-CAP, dairy farmers can significantly reduce their greenhouse gas emissions by implementing beneficial management practices. This study assesses the potential mitigation of projected climate change if greenhouse gases associated with the dairy subsector were reduced. To compare the performance of several mitigation measures under future climate change, we employ a fully coupled Earth system model of intermediate complexity, the MIT Earth System Model (MESM). With an interactive

carbon-cycle, the model is capable of addressing important feedbacks between the climate and terrestrial biosphere impacting greenhouse gas concentrations. We illustrate the importance of ongoing mitigation efforts in the agricultural sector to reduce non-CO_2 greenhouse gas emissions towards established climate goals. If beneficial management practices are implemented globally within the next three decades, projected warming by the end of the century can be reduced by 0.21 °C on average or 6% of total warming, with dairy farm mitigation contributing to 0.03 °C of the temperature reduction.

2.2 Introduction

Substantial reductions in anthropogenic greenhouse gas emissions are needed to limit the rise in global temperatures to 2 °C above the preindustrial level (Sanderson et al., 2016; Rogelj et al., 2015; Meinshausen et al., 2009; Matthews and Caldeira, 2008). While anthropogenic emissions of carbon dioxide (CO_2) are the largest contributors, non-CO_2 emissions collectively contribute to a quarter of the total current greenhouse gas emissions based on equivalent emissions using the 100-year global warming potential (GWP) (van Vuuren et al., 2006). To meet climate stabilization goals, efforts to reduce CO_2 would benefit from complementary efforts in reducing non-CO_2 emissions (Gambhir et al., 2017; Hansen et al., 2000). Mitigation of short-lived climate pollutants such as methane (CH_4) can lead to a rapid decline in radiative forcing, and will significantly impact the magnitude of the peak temperature response and CO_2 budget set for a policy-relevant temperature limit (Montzka et al., 2011). Following strict CH_4 mitigation, a CO_2 emissions budget could extend to 25% higher than a budget that does not limit CH_4 (Rogelj et al., 2015). Long-lived non-CO_2 emission reductions can also provide additional benefits. Mitigation of nitrous oxide (N_2O) will offer the combined benefit of limiting dangerous climate change and sustaining stratospheric ozone. With soils producing the most N_2O emissions, the greatest mitigation potential lies in the agricultural sector (Reay et al., 2012).

The agricultural sector is the principal contributor to anthropogenic non-CO_2 greenhouse gas emissions, accounting for 45% of global CH_4 emissions and 82% of global N_2O emissions in 2005 (EPA, 2012). Between 1961-2010, on average, agricultural emissions increased at 1.6% per year with the greatest growth in Africa, Asia, and the Americas (Tubiello et al., 2014). During this same period, some emission growth was offset by sustainable farming practices in Europe and Oceania. As the demand for food increases with population growth, agricultural emissions

are projected to further increase by 20% before 2030 (EPA, 2012). As a whole, the sector must reduce emissions and increase resilience to changes in future climate, while simultaneously increasing productivity and achieving sustainable food security (Wollenberg et al., 2016).

To address food security challenges and support agricultural development, the U.S. Department of Agriculture launched the Sustainable Dairy Coordinated Agricultural Project (hereafter, Dairy-CAP). Dairy-CAP brought together multi-disciplinary teams of researchers to understand how U.S. dairy agroecosystems are connected to the global environment and how improved farm management practices can reduce greenhouse gas emissions. The coordinated Dairy-CAP project developed multiple agricultural beneficial management practices (BMPs) to reduce greenhouse gas emissions, while ensuring continued productivity and economic profitability of the U.S. dairy industry (Veltman et al., 2018). BMPs identified by the collaboration included changes to animal feed, manure management systems, and field systems (Hristov et al., 2013; Montes et al., 2013). The Dairy-CAP project differs from other agricultural investigations by considering combinations of practices on the whole-farm rather than assessing implementation of a single BMP at a time (Dolfing, 2017; Wollenberg et al., 2016). Whole-farm solutions are necessary because introducing a BMP for one farm component can impact total farm emissions by counteracting emission reductions in another farm component (Dijkstra et al., 2011). If considered as whole-farm strategies, BMPs in dairy production systems have the potential to reduce 41% of carbon and reactive nitrogen footprints, while increasing net monetary return and milk production (Veltman et al., 2018).

As a component of the Dairy-CAP project, we evaluate the global impact and effectiveness of the management practices that were developed for U.S. dairy farms. We seek to understand how implementation of whole-farm BMPs can contribute to the reduction in atmospheric non-CO_2 greenhouse gases in an effort to reach policy-relevant temperature targets in a warming world.

To our knowledge, no studies exist that estimate the dairy contribution to warming or calculate how mitigation efforts in the dairy subsector can limit future warming. However, several modeling studies look at net livestock emissions, in which emissions from beef production and dairy production are aggregated together (Beach et al., 2015; Persson et al., 2015). Using a carbon-climate model, a recent study determined that global livestock emissions caused about 23% of the total warming in 2010 and could potentially lead to an additional 0.23 °C of warming by 2100 (Reisinger and Clark, 2018).

Our work extends beyond previous livestock studies by using whole-farm BMP strategies to inform plausible emission reductions within an Earth system model of intermediate complexity. The model we employ contains a more sophisticated representation of the carbon-cycle with interactive atmospheric chemistry to capture the time-evolving chemical feedbacks that extend the lifetime of atmospheric species like CH_4 and ozone.

Dairy-CAP research results guide the development of future emission scenarios for this Earth system modeling study. We design two plausible emission scenarios based on the whole-farm BMP strategies for two farm sizes; a representative 150-cow and 1500-cow U.S. dairy farm as defined in Veltman et al. (2018). The scenarios assume whole-farm BMPs begin to be globally implemented in 2020 and are fully employed within 30 years. Because it is unlikely all farms would abruptly implement BMPs, we use a linear trend in emissions reductions to broadly represent a wide range of pathways for economies to adjust to new farming technologies and practices. With this study, we demonstrate the global impact agricultural mitigation options can have on the global mean temperature. By demonstrating how non-CO_2 reductions from globally implemented BMPs will limit future warming, our study could help motivate the dairy and agricultural policy makers to begin transitioning to better farm practices.

2.3 Methods

2.3.1 Whole-farm Beneficial Management Practices

Here, we briefly summarize the Dairy-CAP work of Veltman et al. (2018) which developed whole-farm beneficial management practices (BMPs) for two distinct but representative U.S. dairy farms. Simulated farms portray present-day dairy farming practices of a small 150 herd-size Wisconsin farm and a 1500 herd-size New York farm. As a comparison, a control farm with no BMPs was simulated for each farm size. BMPs were applied to three farm components; animal feed, manure management, and field cultivation. The individual BMPs for each component were combined to provide whole-farm mitigation strategies. Implementation of the combined strategies was simulated on a whole-farm process-based model, Integrated Farm System Model (IFSM4.3) (Alan Rotz et al., 2015). In the simulations, cultivated area and herd size were fixed, milk production was allowed to increase, and purchases of crops and proteins were minimized.

Table 2.1. Emission scenarios including whole-farm BMP scenario descriptions, prescribed emission reductions, and global mean temperature change relative to preindustrial levels using a 20-year running mean centered on 2090. BMP descriptions and raw data provided by Veltman et al. (2018).

Scenario	Description	Global Emission Reduction			GMSAT (relative to 1861-1880)
		CH_4	N_2O	CO_2	Δ T (°C)
No Mitigation	Business as usual projection. No climate policies after 2015. No BMPs included.	0%	0%	0%	3.14
Dairy - Low Mitigation	Resembles a 1500-cow farm. Non-CO_2 emission reductions applied to the global dairy subsector. Feed BMPs: 50% forage rations, high NDF, high feed efficiency, decreased diet protein. Manure BMPs: anaerobic digester, manure solids separated. Field BMPs: cover crop, no-till system, subsurface injection of manure, summer application of manure.	43%	4%	10%	3.12
Dairy - High Mitigation	Resembles a 150-cow farm. Non-CO_2 emission reductions applied to the global dairy subsector., Feed BMPs: 50% forage rations, high NDF, high feed efficiency, decreased diet protein. Manure BMPs: sealed flare storage, free-stall barn for heifers. Field BMPs: no-till system, subsurface injection of manure, summer application of manure.	53%	56%	20%	3.10
Agr - Low Mitigation	Same percent emission reductions as the Dairy - Low Mitigation scenario but emission reductions applied to the whole agricultural sector.	43%	4%	10%	2.95
Agr - High Mitigation	Same percent emission reductions as the Dairy - High mitigation scenario but emission reductions applied to the whole agricultural sector.	53%	56%	20%	2.92

Three types of BMPs were considered; cow feed, manure processing, and field cultivation. A description for each BMP is in Table 2.1. Both the 150-cow and 1500-cow mitigation strategies assumed the same feed BMPs. This included providing lactating cows feed with low forage rations at 50% dry matter intake, increased (2%) neutral detergent fiber, decreased diet protein (14%), and increased cow feed efficiency (1.65 kg milk per kg feed of dry matter intake). The mitigation strategies varied in their prescribed manure management and field cultivation practices. The 150-cow farm applied a flare to burn trapped biogas in a sealed manure storage system and shelters the heifers in a separate free-stall barn. In comparison, the larger 1500-cow farm used a separator to remove the manure-solids and ran an anaerobic digester on the liquid manure. The two farm strategies were similar in the way fields were managed. Both used a no-till crop establishment with subsurface injection of manure and summer manure application on the fields. The larger farm also applied an additional grass cover-crop following corn harvest. Further details about each BMP studied by the Dairy-CAP project can be found in Veltman et al. (2018).

For both the large and small herd-size farms, there is an overall potential to reduce greenhouse gas emissions by implementing whole-farm BMP strategies (Table 2.1). Smaller farms have greater mitigation potential than large farms due to the scale of the infrastructure, applied practices, and herd size. For this reason, we describe the 150-cow farm as the Dairy-High Mitigation scenario and the 1500-cow farm the Dairy-Low Mitigation scenario. Compared to a controlled no-BMP farm scenario, a small 150-cow farm can reduce CH_4 emissions by 53% per hectare, and reduce N_2O and CO_2 emissions by 56% and 20%, respectively per hectare. A large 1500-cow farm can reduce CH_4 emissions by 43% per hectare, N_2O emissions by 4%, and CO_2 emissions by 10% per hectare.

2.3.2 Estimation of Regional and Global Dairy Emissions

Because emission projections that drive Earth system models rarely separate agricultural emissions into subsectors, it is necessary to estimate dairy emissions from an external data set. We infer percentage contributions of non-CO_2 emissions attributable to the global dairy subsector using the FAOSTAT database (FAO, 2018). The FAOSTAT classifies agricultural emissions into commodity and activity categories for nearly 200 countries without relying on any equivalence metric like the GWP (Tubiello et al., 2013). Direct and indirect emissions of CH_4 and N_2O are documented for dairy activities related to manure management, manure

24

Fraction of Dairy to Total Agricultural Emissions
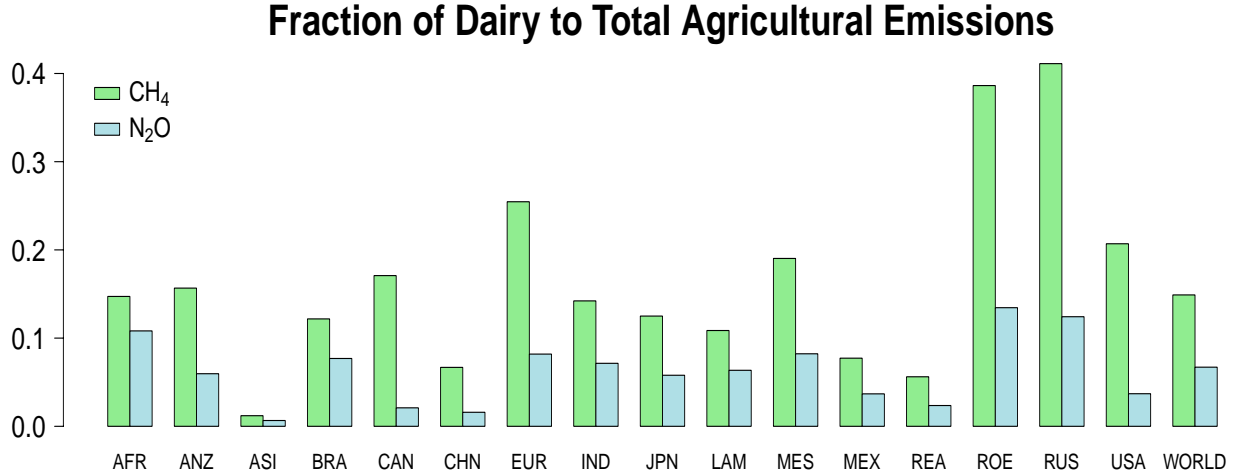
Figure 2.1. Fraction of CH_4 and N_2O agricultural emissions that come from dairy practices of manure management, manure application to soils and pasture, and enteric fermentation for the world and 16 economic regions, averaged over 2007–2016. Africa [AFR], Australia and New Zealand [ANZ], High Income East Asia [ASI], Brazil [BRA], Canada [CAN], China [CHN], European Union [EUR], India [IND], Japan [JPN], Central and South America [LAM], Middle East [MES], Mexico [MEX], Rest of East Asia [REA], Rest of Europe and Central Asia [ROE], Russia [RUS], United States of America [USA]. Data provided by the FAOSTAT (FAO, 2018).

application to soils and pasture, and enteric fermentation. However, the FAOSTAT omits CO_2 emissions from dairy and treats them as carbon neutral. We take a 10-year average for the non-CO_2 emissions over the 2007–2016 period to reflect recent emission trends in dairy activities. To account for localized differences in dairy production and practices, we partition country-level dairy emissions into 16 economic regions.

Non-CO_2 dairy emissions are then compared to emissions from the whole agricultural sector to calculate fractional contributions for each region (Figure 2.1). In every region, CH_4 emissions, originating primarily from enteric fermentation, predominate all dairy emissions. Methane emissions also vary significantly across regions, from 1% in high income countries of East Asia to 41% in Russia, reflecting the diversity in farm practices and production sizes. Unlike the variability in dairy CH_4 emissions, N_2O emissions remain fairly homogeneous across nations. Nitrous oxide emissions coming from manure management and field application tend to stay less than 13% of total N_2O agricultural emissions.

We assert that our approach is likely to underestimate dairy emissions and thus potential warming mitigation attributed to milk production because the FAOSTAT data does not constitute a full life-cycle assessment (LCA). Methodologies for LCA are designed to assess the environmental impact at all stages of dairy production from the development of feed to the processing of milk. Only a select number of studies have conducted LCA approaches for dairy systems on a country-by-country basis (Mc Geough et al., 2012; Yan et al., 2013; Weiler et al., 2014). But, LCA quantification of global dairy emissions remains a challenge as measurements, particularly those in developing nations, are limited and often highly uncertain. In addition, the data products from LCA use aggregated CO_2-equivalencies to compare emissions of greenhouse gases, making it difficult to extract separate emissions. Using different life cycle assessment models, two studies have estimated global dairy emissions make up around 2.7% of total anthropogenic emissions (Gerber et al., 2010; Hagemann et al., 2012). This figure agrees with our estimate of 1.2% based on CH_4 and N_2O dairy activities within the FAOSTAT.

2.3.3 Emission Scenarios

We develop five emission scenarios (Table 2.1) to demonstrate the influence agricultural mitigation strategies have on future global climate change. We include a business as usual scenario to represent the future in anthropogenic emissions without any climate policies. And, we develop emission reduction strategies designed to reflect the mitigation potential of the two U.S. dairy farms considered by the Dairy-CAP project (Veltman et al., 2018).

To design our emission scenarios, we use emissions output of the Economic Projection and Policy Analysis model Version 5.0 (EPPA), a computable general equilibrium model of the world economy and human system (Paltsev et al., 2005; Chen et al., 2017). EPPA projects global economic development at multi-regional and multi-sectoral levels by solving for the prices of consumer goods, as well as, domestic and international trade of energy and non-energy markets. It allows for simulation of changes in land-use, technological advancements, and greenhouse gas emissions. Using population mapping, the scenarios spatially distribute anthropogenic emissions as either agricultural or non-agricultural and interpolate to yield yearly latitudinal emissions. More importantly, emissions from agricultural subsectors are aggregated within EPPA. Modeling detailed changes in individual farm practices, food demand, and production by country is not structurally possible in EPPA's current configuration.

For our No Mitigation scenario, we use a projection that assumes no climate policies restrict greenhouse gas emissions or pollutants after 2015 (Chen et al., 2015). Starting from about 330 million tons (Mt) in 2005, CH_4 emissions grow to nearly 700 Mt in 2100 (Figure 2.2), primarily driven by agricultural growth in East Asia and Africa. In the No Mitigation scenario, N_2O emissions initially increase from 10 Mt in 2005 to 17.8 Mt in 2060, but are then followed by a slight decrease in emissions to 17 Mt in 2100. Increases in CO_2 emissions are largely attributed to the fossil fuel industry during the twenty-first century, with some land-use changes offsetting the increase. Agricultural emissions of CO_2 are minuscule compared to the energy and industrial sectors. By 2100, total CO_2 emissions are about 60 Gigatons (Gt) per year, nearly doubling from 2005.

The No Mitigation scenario is comparable to the range in emission trajectories of the IPCC Shared Socioeconomic Pathways (SSPs) (Calvin et al., 2017; Fricko et al., 2017; Fujimori et al., 2017; Kriegler et al., 2017; van Vuuren et al., 2017). For emissions through the twenty-first century, the No Mitigation scenario considers CH_4 and N_2O emissions on the higher end of the SSP range, while CO_2 emissions fall between the mid-to-low end of the SSP range (Figure 2.2). The differences lie within the assumptions of technological growth and regional economic development.

We evaluate four plausible emission reduction scenarios to assess the potential mitigation of future climate change with the implementation of best management practices on dairy farms. The mitigation scenarios are developed as an extension of the results from the Dairy-CAP project (Veltman et al., 2018). The Dairy-CAP project analyzed emissions from two farm sizes, a 150-cow farm and 1500-cow farm, and concluded that they are able to reduce emissions of CH_4, N_2O, and CO_2 by implementing whole-farm BMP strategies.

Because the EPPA model output aggregates agricultural emissions, we estimate dairy emissions for CH_4 and N_2O by applying fractional contributions of dairy to total agricultural emissions for each region in EPPA (see Figure 2.1). Without specific details of future dairy systems (e.g., regional effects or improved mitigation strategies), this makes the assumption that the fraction of dairy emissions for all agricultural emissions remains constant over time. However, the method does allow for fluctuations in future dairy emissions as the projection in total agricultural emissions fluctuates.
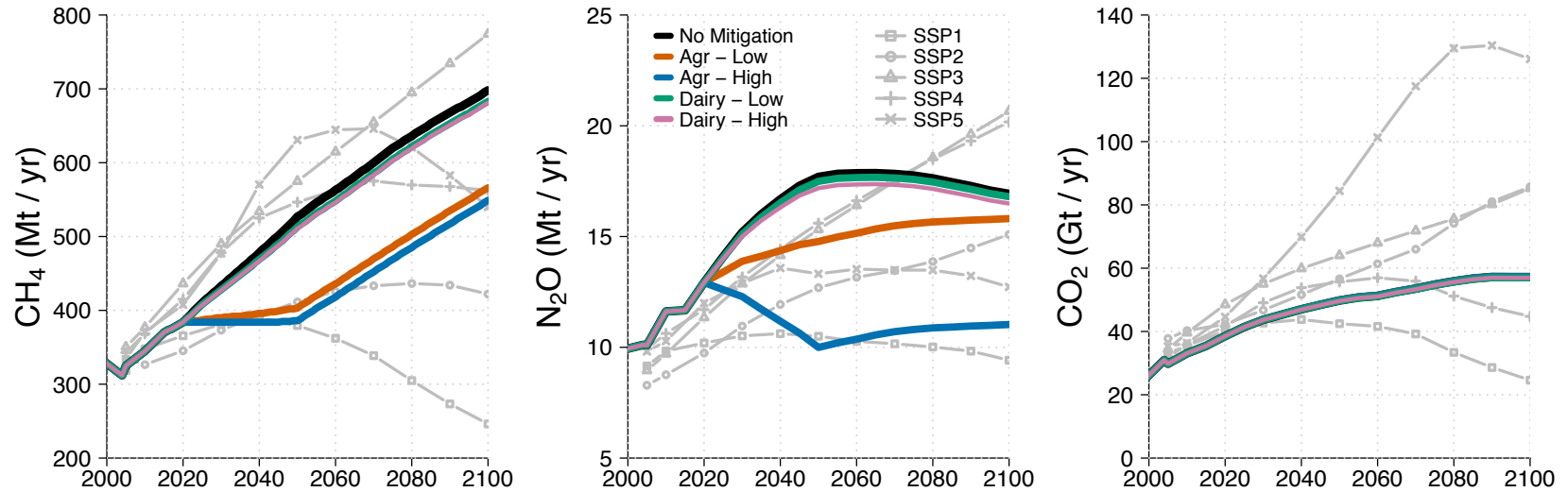
Figure 2.2. Net global emissions of CH$_4$, N$_2$O, CO$_2$ for the No Mitigation scenario (black), low agricultural mitigation (red-orange), high agricultural mitigation (blue), small (pink) and large (green) dairy farm mitigation. The shaded light gray lines indicate the range in the IPCC Shared Socioeconomic Pathways (SSP) for the five marker scenarios.

Using the No Mitigation scenario, we apply percent reductions of CH_4, N_2O, and CO_2 (Table 2.1) to the estimated dairy emissions from 2020 to 2050, with linear interpolation. Whole-farm BMPs are assumed to be fully implemented on a global scale by 2050 and continue to be implemented at their full reduction potential through 2100. For CO_2, emission reductions are applied to the whole agricultural sector. All other non-dairy agricultural and non-agricultural emissions of greenhouse gases and pollutants follow the No Mitigation scenario emissions. We call the two dairy farm mitigation scenarios Dairy-Low Mitigation (DairyLow) and Dairy-High Mitigation (DairyHigh) for the large and small farm strategies, respectively. Designing the two farm emission scenarios recognizes the existing heterogeneity in dairy farms across the globe, where it is presumed the average farm would most likely fall somewhere between the two scenarios.

Because we are interested in the potential impact of emission reductions within the whole agricultural sector, we design an additional two scenarios based on the same percent emission reduction estimates as the farm strategies. The Agri-Low Mitigation (AgLow) scenario applies percent emission reductions to the whole agricultural sector as described by the DairyLow scenario, while the Agri-High Mitigation (AgHigh) applies DairyHigh reductions to the whole agricultural sector. Emission pathways and non-agricultural emissions remain the same as the farm mitigation scenarios. With these assumptions, it is important to note that agricultural and dairy emissions constitute a decreasing share of total anthropogenic emissions as CO_2 emissions from fossil fuels increase unabated in the emission scenarios.

2.3.4 Earth System Modeling

We use the MIT Earth System Model (MESM) to simulate future climate from the emissions projections. The MESM couples submodels of the atmosphere, ocean, thermodynamic sea-ice, and terrestrial biosphere, and thus simulates critical feedbacks within the Earth system (Sokolov et al., 2018). The model is advantageous in its ability to simulate the Earth system response to imposed climate policy and emission abatement measures, as well as, providing a tool to analyze uncertainties intrinsic to the climate system and emission scenarios (Reilly et al., 2012; Gurgel et al., 2011).

The MESM includes a two-dimensional zonally-averaged atmospheric dynamics and chemistry submodel with a statistical dynamical description of the atmosphere (Sokolov et al., 2005).

The detail in carbon cycle dynamics and atmospheric chemistry makes the model ideal for the application of testing reductions in anthropogenic emissions. Atmospheric composition is determined by solving the continuity equations in mass conservative flux form for 33 chemical species, along with 41 gas-phase and 12 heterogeneous reactions (Wang et al., 1998; Sokolov and Stone, 1998). For long-lived species, concentrations are affected by transport, surface deposition, and production and loss by chemical reactions. As a result, the MESM accounts for time-evolving and temperature dependent chemical feedbacks that extend the lifetime and loss rate of atmospheric species. One example is the inclusion of the impacts of CH_4 and N_2O on both the production of tropospheric water vapor and the depletion of tropospheric ozone. However, atmospheric chemistry is turned off in the stratosphere and stratospheric ozone is prescribed beyond the 150 mb level.

The terrestrial submodel consists of a full representation of the carbon cycle, with the inclusion of natural CH_4 and N_2O fluxes (Sokolov et al., 2008). A mixed layer anomaly diffusing ocean model completes the carbon cycle through explicit parameterization of mixed layer biogeochemistry and simulation of carbon and heat uptake.

Climate model parameters that set the equilibrium climate sensitivity (3.30 °C), square root of the average diffusion coefficient of heat anomalies into the ocean below the mixed-layer (4.41 $cm^2 s^{-1}$), and net anthropogenic aerosol forcing (-0.25 W m^{-2}) account for the uncertainty in future climate system behavior. We select values for the three model parameters based on the greatest likelihood probabilistic estimation that yields model output that best match with observational records of surface warming and ocean heat content (Libardoni et al., 2018b). The combination of equilibrium climate sensitivity and rate of ocean heat uptake sets the transient climate sensitivity of the model run (1.75 °C).

Each MESM simulation has two distinct stages. In the first stage, the model is driven with historical concentrations of relevant greenhouse gases and aerosols from 1861 to 2005. The climate model parameters remain the same when the model transitions from being concentration-driven to emission-driven (Sokolov et al., 2018). The second stage uses derived latitudinally distributed emissions from EPPA to convert greenhouse gases and pollutants into atmospheric concentrations.

2.4 Results

Following global implementation in 2020, atmospheric concentrations of mitigated greenhouse gases decline when compared to the No Mitigation scenario (Figure 2.3). The AgHigh demonstrates the greatest mitigation potential, having an atmospheric CH_4 reduction of over 27% compared to the No Mitigation scenario in 2100. The AgLow strategy shows a similar decline in CH_4 concentration, declining by 24%. However, the two simulations vary greatly in their N_2O response. N_2O shows a drop in concentration by 34% for a AgHigh strategy when compared with No Mitigation in 2100. In comparison, the AgLow strategy provides about a 3% decline in mean N_2O concentration. Although not as extensive, dairy emission reductions provide a notable impact on non-CO_2 concentrations. Both the DairyLow and DairyHigh simulations reduce CH_4 concentrations by more than 100 ppb in 2100. And, the dairy simulations reduce N_2O concentrations by 1.3 to 3.3 ppb.

However, there are no substantial decreases in CO_2 concentration for the mitigation scenarios despite a 10–20% reduction in agricultural emissions. This is because agricultural CO_2 emissions are minuscule, less than 1%, compared to net anthropogenic CO_2 emissions by the end of the century. As a result, the temperature impact is primarily influenced by non-CO_2 emission reductions.

The reduction in greenhouse gas concentrations generates a change in the projected response for the global mean temperature relative to the 1861–1880 average for the five emission scenarios (Figure 2.4). The chaotic nature of the global temperature curves reflects the uncertainty in internal processes of the climate system and decadal to multi-decadal regional weather fluctuations. By 2100, the No Mitigation scenario increases to 3.5 °C, well above the 2 °C temperature target of the Paris Agreement (Meinshausen et al., 2009).

The mitigation scenarios begin to show a deviation in global mean temperature from the No Mitigation scenario immediately following BMP implementation (Figure 2.4). If the global agricultural industry could reduce emissions to the level seen by the simulated small and large farms, global temperature may be reduced by 0.21 °C on average by the end of the century. Although global emission cuts would be small, dairy farms have the potential to make an impact on mitigating future warming. We determine that the average 0.03 °C decrease in global mean temperature results from a 43–53% reduction in CH_4 emissions, 4–54% reduction in N_2O

emissions, and 10–20% reduction in CO_2 emissions of the global dairy subsector, in which reductions are guided by findings from BMP implementation in U.S. dairy farms.

To understand the mitigation potential of each greenhouse gas reduced, we simulate the AgHigh strategy with individual reductions of CH_4, CO_2, and N_2O, and reduction combinations of the three gases (Figure 2.5). In this case study, only agricultural emissions are reduced. Non-agricultural emissions follow the No Mitigation scenario. Reducing all three greenhouse gases has the potential to limit warming by $0.25\,°C$ in the year 2100. However, no significant change in the global temperature occurs when only CO_2 emissions are reduced. As fossil fuel emissions increase unabated, the proportion of CO_2 agricultural emissions to total anthropogenic CO_2 emissions becomes minuscule, making the impact of a 20% reduction less apparent. This suggests that the emission reductions of non-CO_2 gases in the agricultural sector have a significant impact in mitigating projected temperature change.

Simulations of N_2O and CH_4 agricultural emission reductions show greater promise in limiting future warming (Figure 2.5). Reductions in N_2O and more notably reductions in CH_4 decrease the projected temperature rise by $0.07\,°C$ and $0.22\,°C$, respectively, in 2100. The substantial difference results from the larger mitigation in CH_4, where early reductions in CH_4 result in a larger decrease in radiative forcing and leads to decreased warming rates. The combined agricultural reductions in N_2O and CH_4 are able to reduce the 2100 temperature projection by $0.23\,°C$, because they contribute 6% of the instantaneous radiative forcing in 2100. We note that the temperature projections are influenced by internal variability and therefore are not additive for each combination of greenhouse gas mitigation.

Projected Atmospheric Concentrations
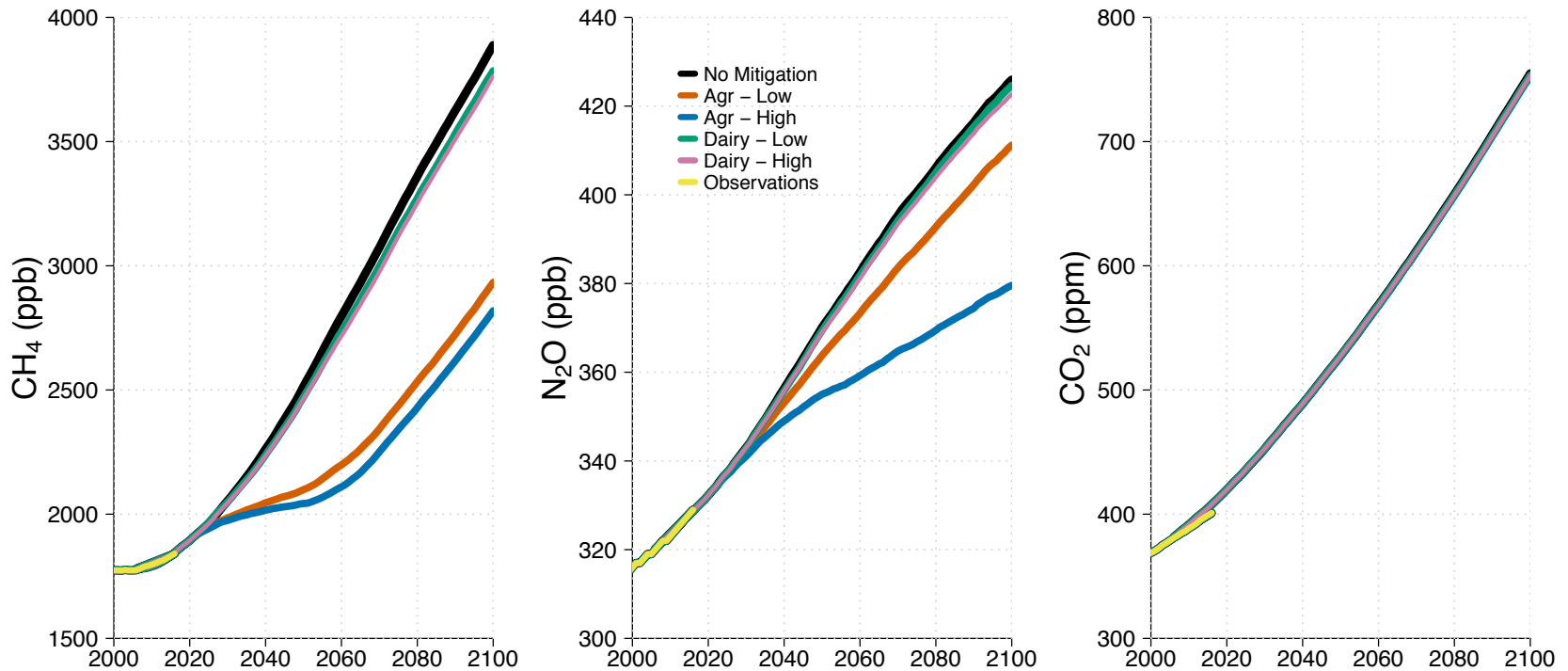
Figure 2.3. Global mean atmospheric concentrations of CH_4, N_2O, and CO_2 for the No Mitigation scenario (black), low (red-orange) and high (blue) agricultural mitigation scenarios, and low (green) and high (pink) dairy farm mitigation scenarios. Overlaid in each panel is the observed concentration (yellow).
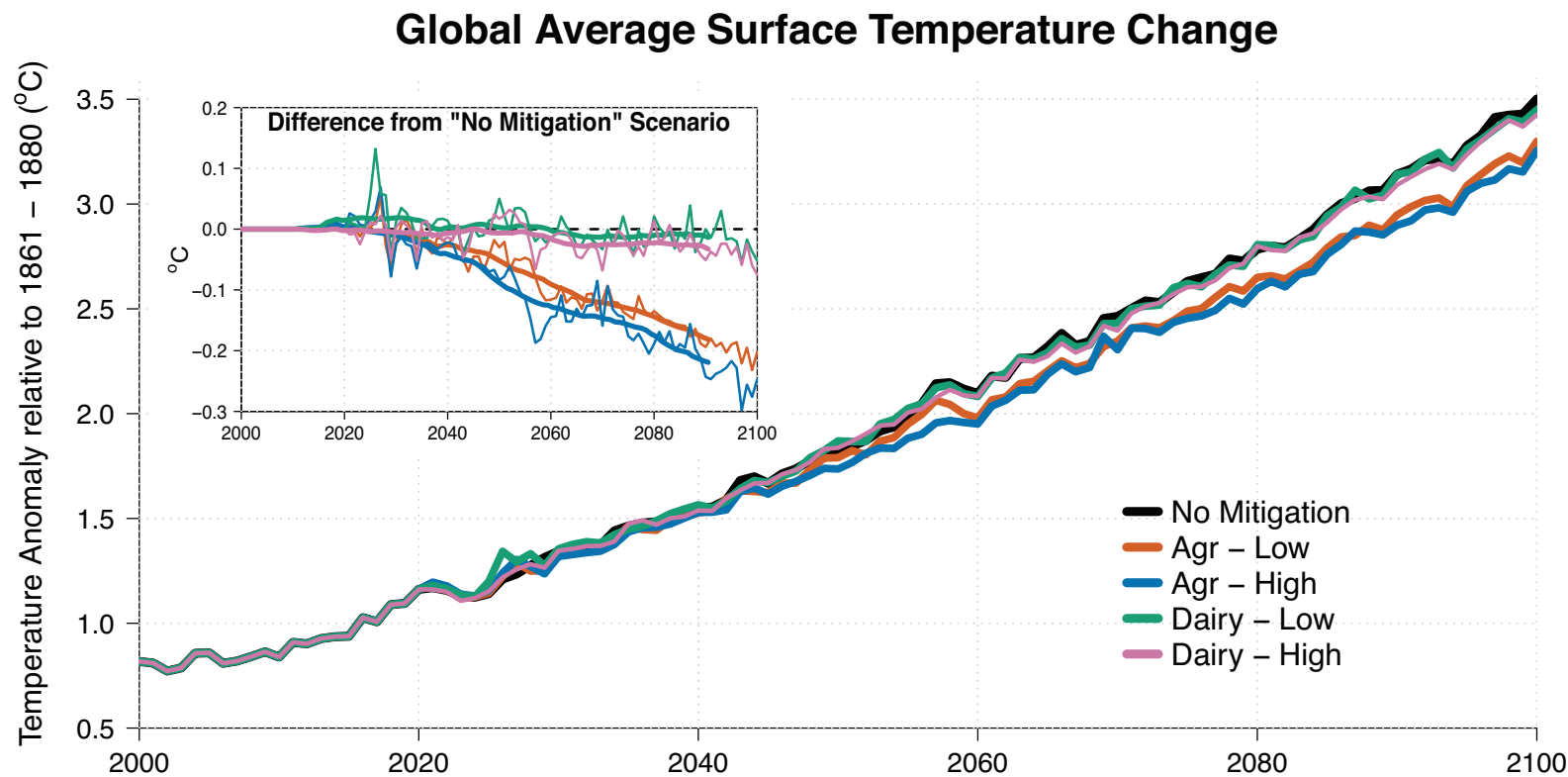
Figure 2.4. Projected global mean surface temperature anomaly relative to the 1861–1880 average for the No Mitigation scenario (black), low (red-orange) and high (blue) agricultural mitigation scenarios, and low (green) and high (pink) dairy farm mitigation scenarios. Inset Figure - the effective temperature change for the mitigation scenarios as a difference from the No Mitigation scenario with 20-year running means (bold-lines).
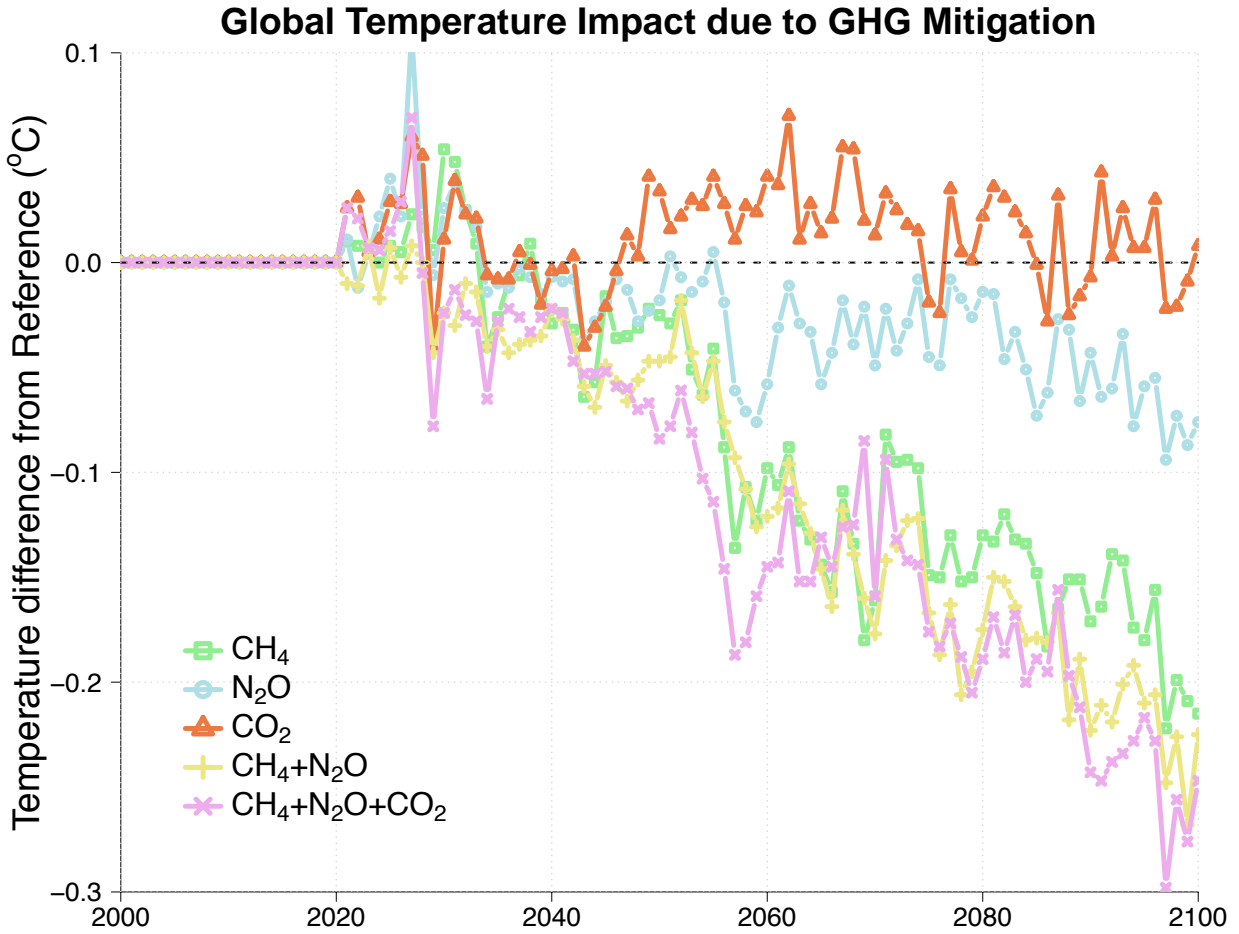
Figure 2.5. Combinations of CH_4, N_2O, and CO_2 mitigation are simulated for a high agricultural mitigation scenario (AgHigh). Shown is the annual global mean surface temperature relative to the temperature response from the No Mitigation scenario for each greenhouse gas mitigation combination.

2.5 Discussion and Conclusion

In this study, we focus on how global implementation of BMPs in the agricultural sector can further reduce non-CO_2 greenhouse gas emissions and assist in reaching temperature goals set by international policy. We have two main advances in this work. First, we use a coupled Earth system model containing full chemistry and interactive carbon cycle components to project changes in future greenhouse gas concentrations. Second, the idealized emission reductions are guided by the results of the coordinated Dairy-CAP project, in which whole-farm emission reductions were estimated for representative 150-cow and 1500-cow U.S. dairy farms (Veltman et al., 2018). Using Dairy-CAP results, we apply emission reductions of CH_4, N_2O, and CO_2 across the global dairy subsector.

Based on our simulations, we find that if BMP implementation for the dairy industry is fully realized by 2050 and sustained, warming in the late century can be reduced on average by $0.03\,^\circ$C or 1% of total warming when compared to a business as usual emission scenario. We emphasize that our result could be an underestimate since dairy emissions from the FAOSTAT lack full life cycle assessment, and only account for a selection of CH_4 and N_2O dairy practices. While this may be the case, our results agree with a recent analysis looking at the contribution of livestock (combined beef, dairy, poultry, etc) to past and future warming (Reisinger and Clark, 2018). Under a low emissions scenario (RCP2.6) with an additional 50% reduction in CH_4 and N_2O from livestock, $0.08\,^\circ$C is reduced by 2100. However, if emissions continue unabated under a high emissions scenario (RCP8.5), the study found direct livestock non-CO_2 emissions alone could lead to $0.23\,^\circ$C or 5% of total warming in 2100.

Our results also suggest that immediate action taken across the whole agricultural sector could potentially reduce future warming $0.21\,^\circ$C on average or 6% of projected total warming by the end of the century. We find that reductions in agricultural non-CO_2 gases provide the greatest mitigation impact because their high emission rates and their stronger radiative effect per molecule is diminished. However, abatement of non-CO_2 agricultural greenhouse gases alone could not reach a $2\,^\circ$C target. To reach such a temperature target would require supplemental reductions in CO_2 from the fossil fuel sector. Any delay in the onset of implementation or falling short of full emission reductions would result in higher non-CO_2 atmospheric concentrations and limit the temperature mitigation potential (Luderer et al., 2013). Our study therefore demonstrates the importance for immediate action across the globe to begin curtailing agricultural

emissions with new management practices.

Through changes in farm techniques, infrastructure, scale, and efficiency, there are countless possible ways in which agricultural emissions can be reduced across the globe. We apply distinct linear emission reductions to the global dairy subsector and aggregated agricultural sector to address the uncertainty in the future emission pathway. By doing so, this method accounts for possible technological advances and newly developed BMPs that have yet to be implemented on the farm scale. It also accounts for potential trade-offs across the globe, where some industrialized nations may reduce emissions while others increase their emissions.

We acknowledge and account for the fact that not all farms resemble the representative highly-efficient U.S. dairy farms used to calculate the BMP emission reductions. Using both a small farm and large farm scenario allows for the true distribution of all farm sizes to fall somewhere in between the two scenarios. It is well known that the mitigation potential varies around the globe depending on production volume and emission intensities (Zhang et al., 2017). High production areas, usually in industrialized countries, have a high mitigation potential and can begin to reduce emissions from the largest sources of emissions; feed production, manure, and enteric fermentation (Gerber et al., 2013). Low production regions, such as Sub-Saharan Africa, are generally characterized by high emission intensities and low mitigation potential. Albeit, areas such as these are often remote and have financial difficulties adopting new practices. But if adopted, sustainable agricultural practices could yield substantial improvements in emission intensities and food security (Lipper et al., 2014).

Chapter 3

Earth system response to impulse changes in methane

3.1 Abstract

Idealized simulations of pulse-like perturbations are used to understand the Earth system response and quantify climate feedbacks resulting from additional emissions. With much attention spent on impulse behavior of carbon dioxide (CO_2), a gap exists in the research community on impulse response behavior of the methane cycle. Our primary focus is to model the Earth system response to impulse changes in methane emissions under present day concentrations. Depending on the state of the system and size of the perturbation, nonlinearities that arise within the system generate perturbations in atmospheric concentration and global mean temperature. In our simulations, we apply methane pulse emissions of various magnitudes to explore how the depletion of hydroxyl radical during oxidation leads to an extension of methane's atmospheric residence time. We determine that methane's atmospheric residence time is dependent on the remaining airborne fraction and the level of atmospheric warming that results following the pulse emission. An emergent temperature-dependence of atmospheric chemistry and carbon pools provides insight into future changes in the methane cycle as the global climate is projected to warm. Our analysis provides a basis for understanding how uncertainties in future methane and CO_2 emissions could influence the Earth system and lead to potential feedbacks that may further alter the climate.

3.2 Introduction

Understanding how anthropogenic perturbations of heat-trapping gases are affecting the Earth's climate is of utmost importance for the prediction of future climate change. The Earth system response to perturbations can be explored through idealized impulse response tests of comprehensive climate models. A typical model scenario is to inject a sizable emission or atmospheric concentration perturbation and simulate the decay of the perturbation back to a steady-state (Joos and Bruno, 1996). Impulse simulations are able to uncover chemical and physical feedbacks that would otherwise be obscured in standard emission scenarios. These experiments have been particularly useful in modeling the change in atmospheric concentration of a species and to understand the complex subsystems like the carbon cycle (Gasser et al., 2017; Zickfeld et al., 2011; Gregory et al., 2009; Hooss et al., 2001). Impulses of carbon dioxide (CO_2) have been extensively studied for Earth System Models (ESMs) and models of intermediate complexity (EMICs) (Joos et al., 2013). Their results showed complex models are sensitive to perturbation size, climatic background conditions, and carbon cycle-climate feedbacks. Building upon their findings, we further explore feedbacks related to methane that arise from impulse changes to atmospheric chemistry and biogeochemistry in an intermediate-complexity model.

As motivation for our work, few studies examine the model behavior to impulse responses to non-CO_2 gases. Those studies that do provide non-CO_2 impulse responses use reduced-form models that do not simulate feedback processes that can further alter the climate system. Those studies also are primarily aimed at the calculation of climate metrics that compare radiative impacts of atmospheric species (Kumari et al., 2019; Persson et al., 2015; Collins et al., 2013; Prather, 1996), and tend to include limited discussions on the physical foundations and science behind the metrics. As a result, a gap in the literature exists for assessing non-CO_2 impulse responses, particularly from methane, in comprehensive climate models (Schwarber et al., 2019). As a reactive short-lived gas, methane emission perturbations influence chemical interactions and abundances of other atmospheric species. This results in relative climate impact that changes over time (Myhre et al., 2013).

Because it is computationally expensive to run multiple impulse simulations for long timescale processes within ESMs, cost-efficient reduced-form models called impulse response functions (IRFs) emulate the behavior of the comprehensive models. Built as Green's functions, or sums of exponential decay functions of differing timescales, an IRF can serve as a substitute for

subsystem of a fully complex model (Leach et al., 2020; Strassmann and Joos, 2018; Millar et al., 2017). By definition, impulse response functions are simple formulations that describe the linear nature of a dynamical subsystem of the Earth to a perturbation (Joos and Bruno, 1996). Taking this into consideration, IRFs are limited in their ability to only describe one state of the climate system. Depending on the state of the system emerging nonlinearities could generate very different climate response outcomes (Gregory et al., 2009; Zickfeld and Herrington, 2015). For example, the IPCC AR5 impulse response model, developed to replicate a multi-model response to a 100 Gigaton carbon (GtC) pulse from Joos et al. (2013), greatly overestimates the global mean temperature response to an even greater instantaneous quadrupling of CO_2 (Schwarber et al., 2019). The poor IRF representation of the complex model behavior is primarily due to the fact that the IRF is insensitive to the pulse size and background concentration.

For small perturbations, IRFs can approximate some nonlinearities exhibited in complex climate models, but only in an implicit manner (Hooss et al., 2001). The performance of reduced-complexity IRF models tend to improve when the carbon cycle-climate feedback is included. But, there is room for improvement as a pulsed emission can still result in an underestimate of fractional airborne CO_2 even with simplified feedbacks (Schwarber et al., 2019). Therefore, it is imperative to explore how multiple climate states, indirect effects, and size of the idealized perturbation lead to nonlinearities that could affect impulse responses.

In this study, we diagnose the Earth system response of an intermediate complexity model to stylized emission perturbations, thus justifying the need for reduced-form models to incorporate feedbacks into IRFs. This is highly motivated by the need to understand the uncertainties in projected model responses due to chemical and physical feedbacks associated with the carbon cycle. While there are several greenhouse gases and pollutants worth modeling, we focus on how to characterize the response to pulse emissions of methane. Through impulse tests, we gain insight into the time-dependence and temperature-dependence of the atmospheric chemistry that induce some of the emerging nonlinearities of the climate system. Our results analyze the perturbation's decay as it depends on the magnitude of the pulse size, saturation of the sinks, and the increasing longevity of carbon in the atmosphere. We put the impulse response into perspective by simulating an identical pulse of CO_2. By comparing the results from both gases, we highlight the different radiative efficiencies and timescales that result from the atmospheric balance of the emission sources and carbon sinks.

3.3 Methods

3.3.1 MIT Earth System Model Framework

For this research, we use the Massachusetts Institute of Technology (MIT) Earth System Model (MESM) (Sokolov et al., 2018, 2005) because the model is capable of flexibility in parameter space and computational speed at handling uncertainty analysis, and can diagnose the model response to alternative emission scenarios. The MESM links models of zonally-averaged atmospheric dynamics, ocean, terrestrial biosphere, and thermodynamic sea-ice to understand their evolution and interactions under different forcing scenarios (Figure 3.1). Being fully coupled, the model includes simulations of critical feedbacks among its components comparable to those of more complex models (Brasseur et al., 2016).

The MESM contains carbon cycle dynamics, biogeochemistry, and interactive atmospheric chemistry; critical components of an ESM that provide an appropriate modeling system to
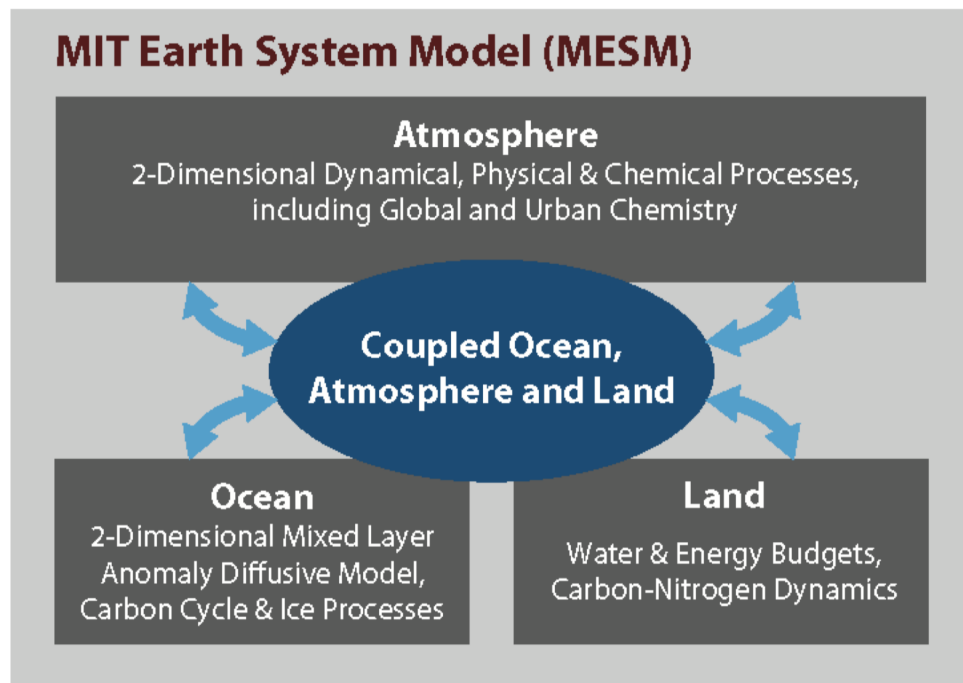
Figure 3.1. Schematic of the MIT Earth System Model (MESM) of Intermediate Complexity. Figure taken from Sokolov et al. (2018).

assess the IRF emulation of the climate system. Primarily, we focus on the components of the biogeochemistry that control the magnitude and decay rate of the CO_2 and CH_4 pulses and how these are closely connected to the climate response. Terrestrial carbon and nitrogen dynamics determine the carbon storage pool and natural fluxes of CO_2, CH_4, and N_2O (Sokolov et al., 2008; Schlosser et al., 2007). By including processes such as soil hydraulics, nutrient cycling, and carbon sequestration, the model includes an ecosystem component that is required to study the terrestrial carbon cycle. The other distinguishing component of the MESM model is its interactive atmospheric chemistry. Calculated on a daily timestamp, the atmospheric composition of climate-relevant gases and aerosols simulate the impact other trace atmospheric species have on methane's primary sink, OH (Wang et al., 1998; Sokolov and Stone, 1998).

Both natural and anthropogenic climate forcing agents drive the coupled system. In historical simulations, the model is first spun up by prescribed changes in greenhouse gases, aerosols, and solar irradiance from 1861 to 2005. Once the historical simulation is completed, the fully coupled-carbon chemistry model is initiated at year 2006 and driven by emission projections.

3.3.2 Uncertain Parameter Selection

The MESM was designed to be flexible through its ability to change key climate system properties: equilibrium climate sensitivity, the rate of ocean heat uptake, and adjustments to forcing efficacy. Given the model's computational efficiency, testing multiple combinations of the climate system parameters and estimating their probability distributions makes the MESM a powerful tool for uncertainty analysis (Forest, 2002; Forest et al., 2006, 2008; Libardoni and Forest, 2011; Libardoni et al., 2018a,b, 2019). The selection in parameter values must be chosen so that the model reproduces observational records, but also allows for spanning parametric uncertainty.

In our work, to obtain a range of climate system responses to the impulse forcings, we systematically vary the three parameters by drawing from the joint probability distribution of Libardoni et al. (2019). We sample from the joint distributions using Latin Hypercube Sampling (LHS) technique. LHS is a convenient sampling method because it samples evenly across all parametric values and samples more frequently in areas of high probability density. We produce 50 drawings of parameter sets to run a 50 member ensemble of the MESM. Due to one set of parameters causing a numerical error in the terrestrial ecosystem model of the MESM, our ensemble is cut down to 49 members for our analysis. Parameter sets are shown in Appendix A.

3.3.3 Emission Scenario Descriptions

We run two simulations with the same parameter settings. In the first, we run a baseline scenario. In the second, we add a pulse of emissions for CO_2 or CH_4. This approach allows us to estimate the impact of the pulse while the climate is changing similar to the current trajectory. We conduct impulse tests against a time-changing concentration background since it is a more realistic scenario that can reveal outcomes that are not evident under steady state conditions used in prior studies (Joos et al., 2013).

The baseline emission scenario produced by the MIT Economic Projection Policy Analysis (EPPA) model (Paltsev et al., 2005), which represents climate policies and economic projections proposed during the 2015 Paris Climate Conference, up until 2100 (Chen et al., 2016). Beyond 2100, annual emissions are held constant at the 2100 rate. To capture some of the long timescale processes of the carbon cycle, we run the model for several centuries. As stated earlier, 49 ensemble members are run for the baseline scenario and each pulse scenario.
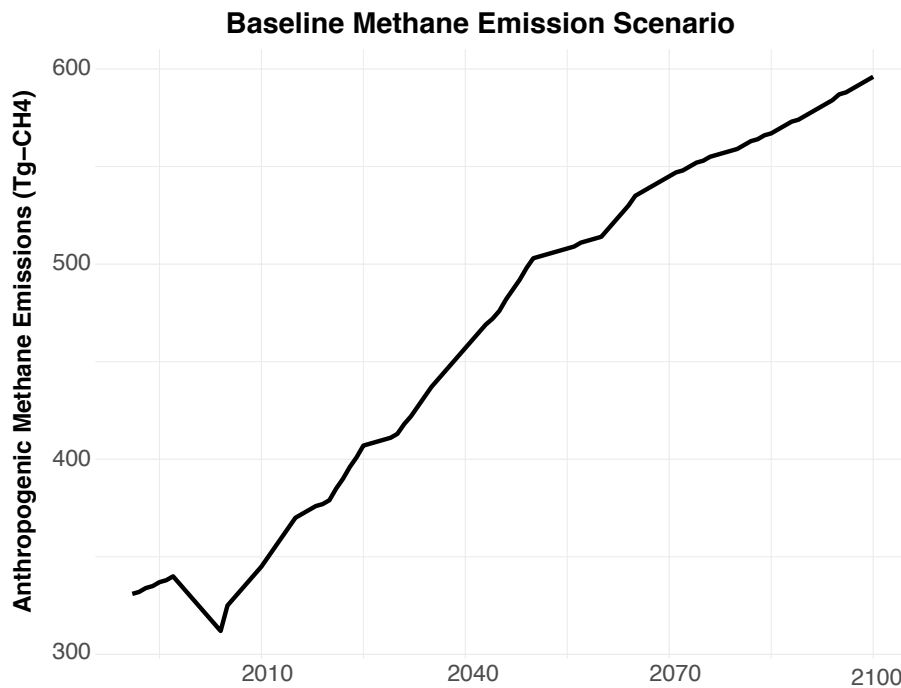
Figure 3.2. Global annual anthropogenic methane emissions for the baseline emission scenario for 2006-2100.

Emission pulses occur over the first year of the MESM coupled carbon-chemistry run (i.e. year 2006), added to the baseline scenario. To better understand the time-evolution of the pulse response as a function of magnitude, we conduct impulse scenarios for sizes of 0.1, 0.5, 1.0, 5.0, 10.0, and 50.0 Gigatons of carbon (GtC). We use units of GtC to directly compare emissions of methane and carbon dioxide, where a Gigaton of carbon is equivalent to 1336 Teragrams of methane (Tg-CH_4) and 3.67 Gigatons of CO_2 (Gt-CO_2). We follow the procedure of Joos et al. (2013), where the standard size of a CO_2 pulse that produces a good signal-to-noise ratio is 100 GtC. The response from the CO_2 pulse is compared with a methane pulse of the same magnitude. To show impulse behavior, our results take the difference between pulse perturbation scenario and the baseline scenario.

3.3.3.1 Pulse Size Analogues

To put the pulse sizes into perspective with typical annual anthropogenic emissions of methane, it is estimated 0.28 GtC yr^{-1} (378 Tg-CH_4 yr^{-1}) was released in 2017 (Saunois et al., 2020). Including natural emissions, total global methane emissions are estimated at 0.55 GtC yr^{-1} (745 Tg-CH_4 yr^{-1}). This indicates pulse sizes between 0.1 and 0.5 GtC are representative of annual methane emissions.

A large potential source of carbon emissions could come from a rapid thawing of permafrost. Surface warming melts ground ice, making the soil more vulnerable to decomposition by microbes and out-gassing of CO_2 and CH_4 (Holm et al., 2020; Schuur et al., 2015). Current estimates of permafrost methane emissions make up a modest portion of the methane budget, estimated at 0.01–0.03 GtC yr^{-1} (15–40 Tg-CH_4 yr^{-1}) (Kirschke et al., 2013). With the largest terrestrial organic carbon pool of 1330–1580 GtC (Hugelius et al., 2014), northern permafrost soils are predicted to release a cumulative 28–113 GtC by 2100 under a high emission scenario, Representative Concentration Pathway (RCP) 8.5 scenario (Koven et al., 2015). Of the increased carbon emissions, annual permafrost methane emissions could increase by 35% by the end of the century, but still equate to far less than wetland and anthropogenic emissions (< 0.04 GtC yr^{-1}). Given this, our large pulse sizes (10–100 GtC) are analogous to all of the estimated permafrost emissions released in a single year - a very unlikely scenario. Nevertheless, the large methane pulses push the MESM to explore nonlinearities and temperature thresholds of the climate system, as well as, allowing for comparison with 100 GtC carbon dioxide pulses found in previous studies (Joos et al., 2013).

3.4 Results

3.4.1 Influence of Methane Pulse Size on Earth System Response

Immediately following the pulse emission year, the level of atmospheric methane concentration peaks (Figure 3.3). The evolution of the methane pulse response shows a rapid decrease in concentration over the first several years and thereafter continues with a slow decline to zero. The pulse size greatly determines the magnitude of the peak concentration and the decay rate; where larger pulses take longer to decay to zero. A 0.1 GtC methane pulse leads to 46 ppb rise in atmospheric concentration, whereas a pulse size 1000 times greater rises to 49,921 ppb. We note that the responses are not directly proportional (i.e. 49,921 is not 1000x46) because the pulse emissions are spread out over one year, giving the model time to start to decay the perturbation before the year's end.
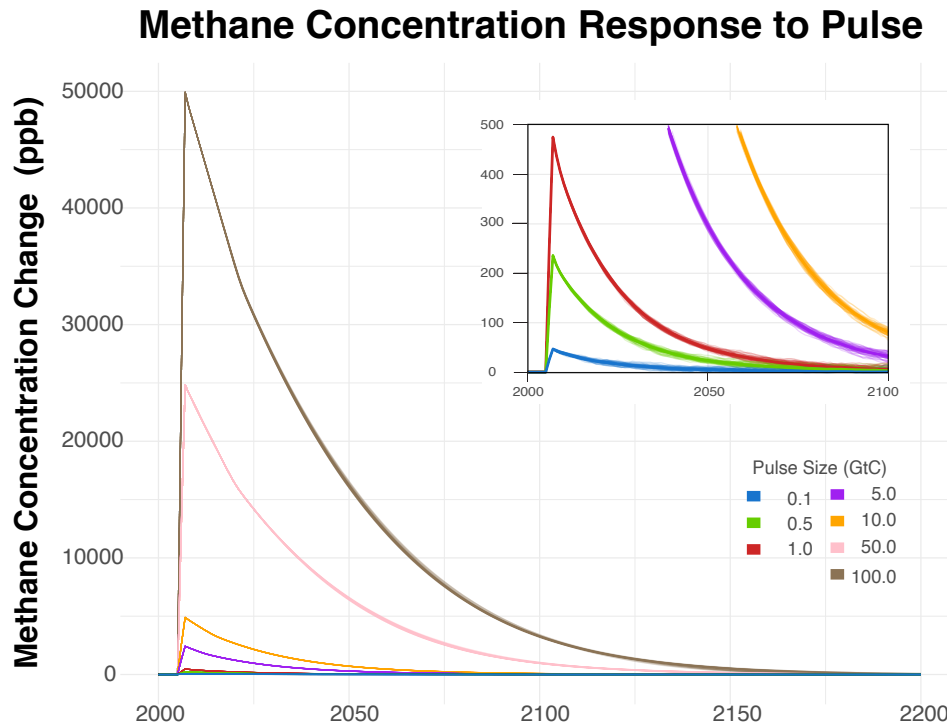
Figure 3.3. The change in atmospheric methane concentration following a methane pulse of various sizes. There is a 49 member ensemble for each size pulse. Inset: Magnification of smaller pulses.
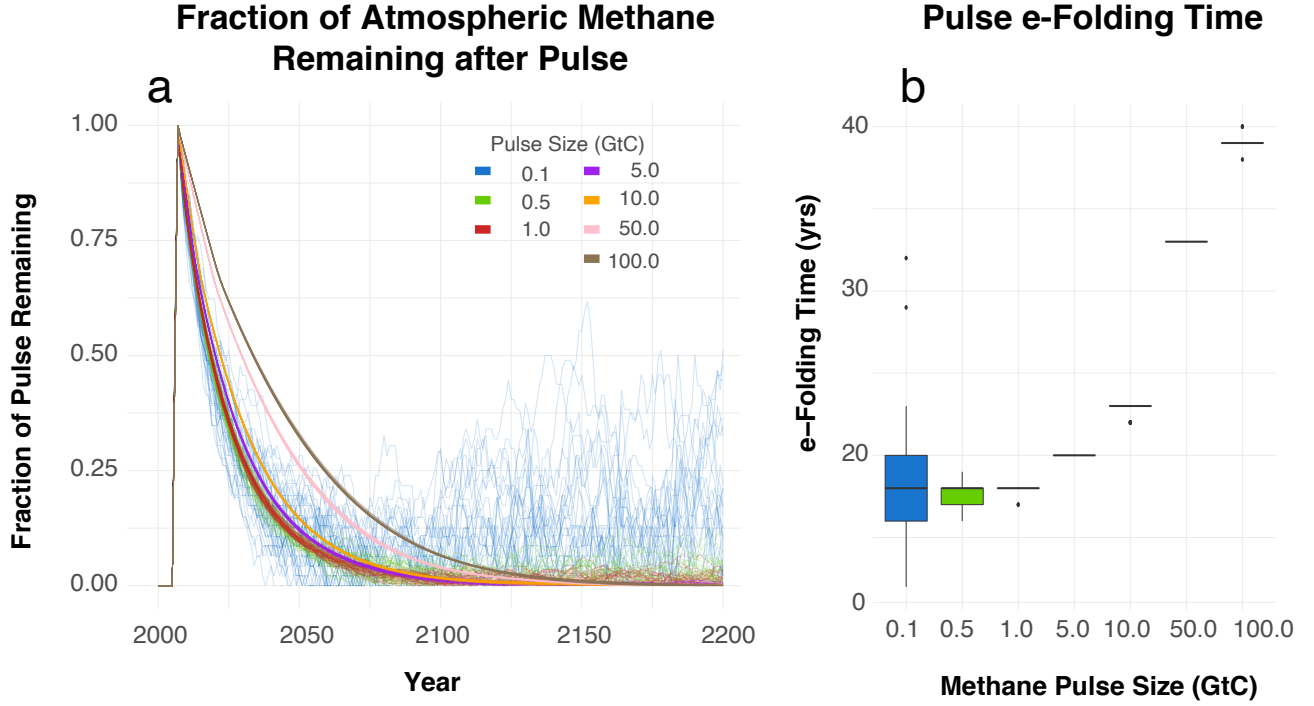
Figure 3.4. Methane concentration response to various sizes of pulse emissions. a) Ensemble of fraction of atmospheric methane perturbation remaining following the pulse. b) Box-plots of the perturbation e-folding time, the time it takes the perturbation to decrease by a factor of $1/e$ of its peak value.

To better compare the pulse sizes, we show the fraction of atmospheric methane remaining after the pulse emission (Figure 3.4a). We caution that the 0.1 GtC methane pulse shows significant noise, as the year to year variability in atmospheric concentration hides the signal of the pulse. For our analysis, we will focus on the mean response. The ensemble averages of the 0.1, 0.5 and 1.0 GtC methane pulses, show nearly identical evolutionary behavior. Within 18 years of the initial peak perturbation for the ensemble average to remove 63% (i.e. the e-folding time; amount of time it takes to reach a fraction of 0.36). The average e-folding time increases for pulse sizes over 1 GtC (Figure 3.4b). A 5 GtC methane pulse takes 20 years and a 50 GtC pulse takes 33 years to remove 63%, exemplifying the nonlinear response of the methane cycle. To completely remove the perturbations from the atmosphere, it takes 60–166 years. In other words, the 0.1–0.5 GtC annual anthropogenic methane emissions we emit this year could linger in the atmosphere for over 60 years.

The nonlinear responses to the increasing pulse sizes are directly related to the feedbacks of the Earth System that affect the oxidation and removal of methane. The chemical oxidation of CH_4 leads to the production of CO_2 and ozone (O_3) through the reaction with hydroxyl radical (OH) (Ehhalt, 1974; Ehhalt and Schmidt, 1978). Any variations in tropospheric OH will have a direct impact on methane levels and methane atmospheric residence time (Prather, 1994). The net reaction eliminates tropospheric OH, the main driver for methane's atmospheric sink (Figure 3.5). Because hydroxyl radicals are highly reactive and short lived species, their abundance promptly falls following the pulse. As their concentrations recover, OH shows an evolution that mirrors the evolution of the methane perturbation. From this, we see the magnitude of the OH depletion also shows a nonlinearity, where the peak depletion of the 50 GtC pulse and double its size (i.e. the 100 GtC pulse) only differ by 11%. Potentially, this could be related to a threshold limit within the reaction rate calculations of atmospheric chemistry.
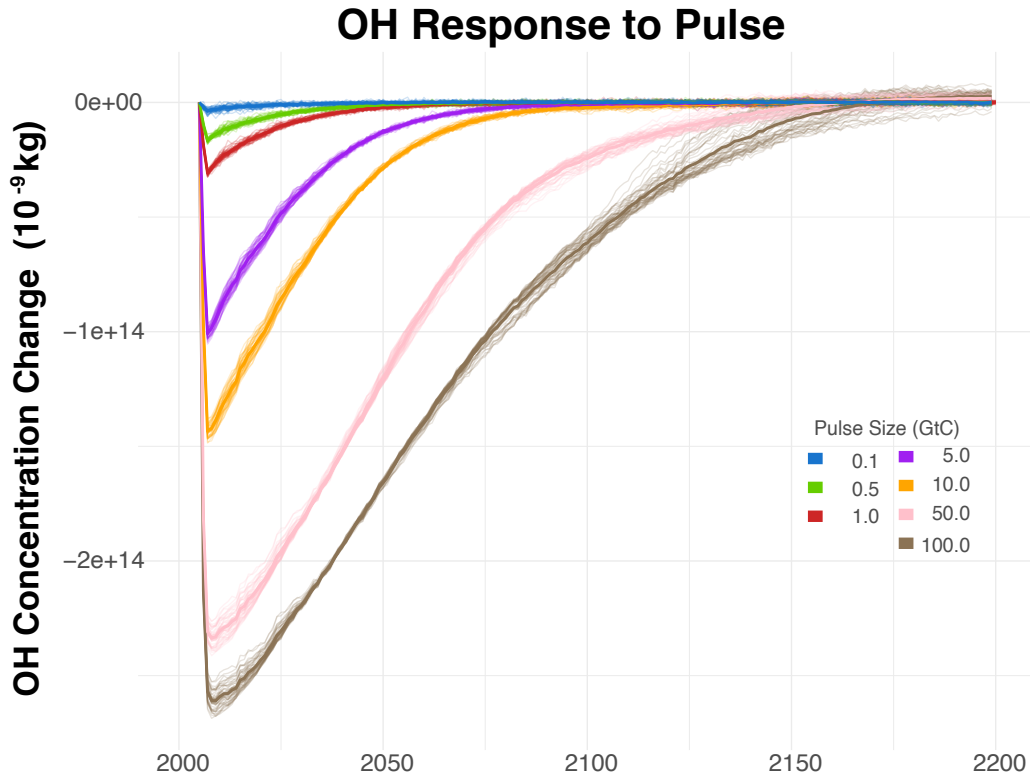
Figure 3.5. Change in tropospheric hydroxyl radicals for several methane pulse sizes. Solid dark lines are the ensemble means.
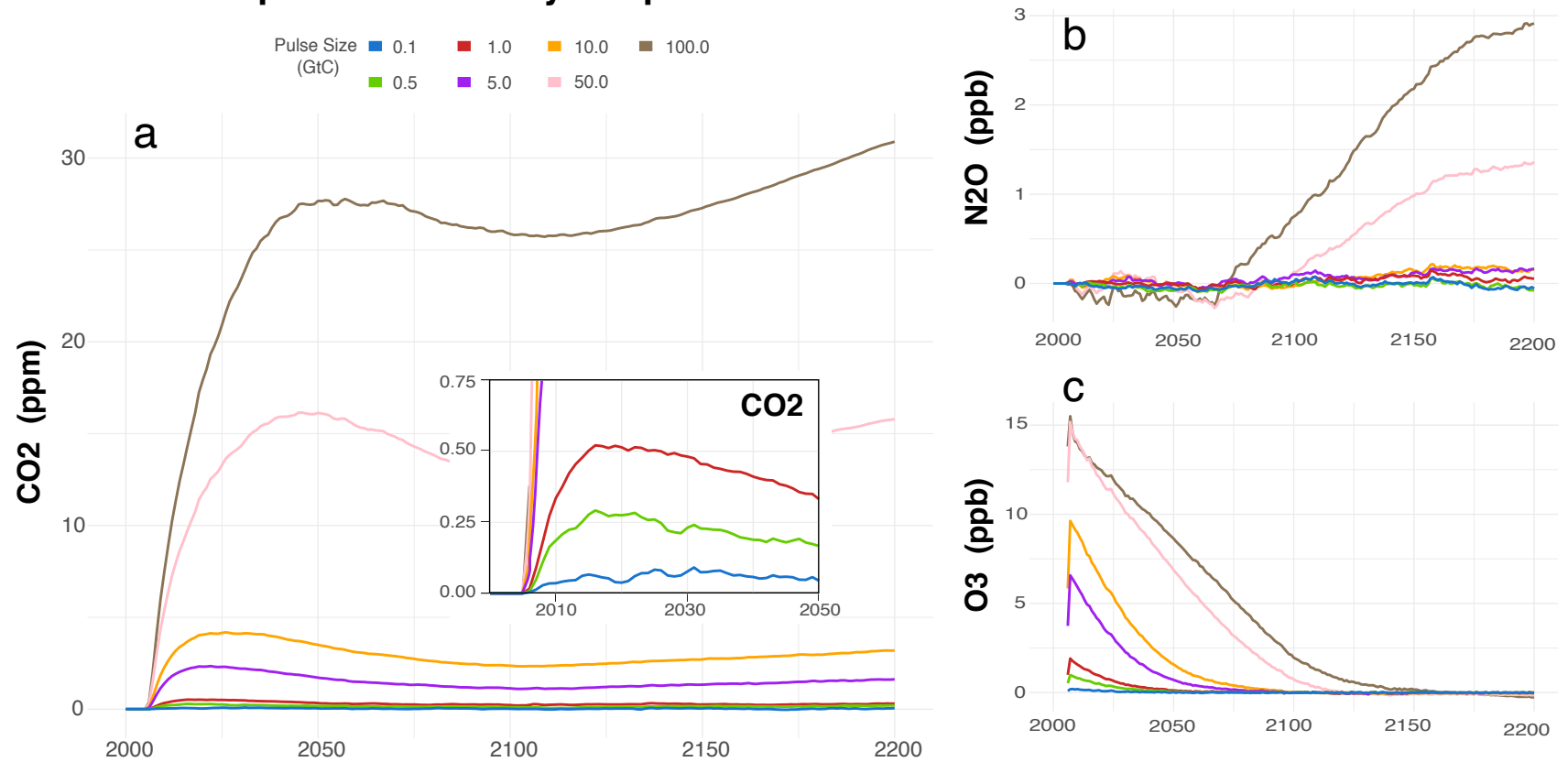
Figure 3.6. Atmospheric chemical response to methane pulse perturbations. Shown are the ensemble means. a) The change in carbon dioxide concentration and inset figure magnifying smaller pulses. b) Nitrous oxide and c) ozone concentration changes.

Because OH reacts with several pollutants in the atmosphere, the depletion of OH abundance leads to a chain reaction in several atmospheric constituents (See Appendix B, Figure B.2). For one, OH is the primary driver of removing ozone (O_3) from the atmosphere. Global ozone levels increase as the OH abundance decreases (Figure 3.6c). The response time is immediate. Even for the smallest pulse size, atmospheric ozone increases by 0.2 ppb following a 0.1 GtC methane pulse. Perturbed ozone levels return to the baseline soon after the methane perturbation is completely removed.

Through a series of chemical reactions, the carbon molecule from CH_4 ends in the production of a CO_2 molecule (Figure 3.6a). Because the chemical production is not immediate, the rise in atmospheric CO_2 occurs more slowly than the response in CH_4 or OH. After 13 years following the methane emission, a 1 GtC methane emission will lead to a peak increase in CO_2 concentration by 0.52 ppm. The peak concentration is reached at a later time for larger pulses, as it takes longer for a larger methane pool to be oxidized into CO_2. For roughly 100 years, CO_2 concentrations drop as terrestrial and ocean carbon sinks uptake and store carbon (Figure 3.8). The CO_2 response increases again as high global temperatures weaken carbon sinks and additional background CO_2 emissions continue to rise. Effectively, the methane pulse will lead to an enduring impact on the carbon cycle.

All of the perturbations will lead to a cumulative effect on the global mean surface temperature (Figure 3.7). Nonetheless, the degree of warming is dependent on the size of the perturbation. A 0.5 GtC pulse size leads to an average peak warming of 0.03 °C about 7 years following the methane emission, as it takes time for an initial increase in radiative forcing to heat the surface layers of the land and ocean (Joos et al., 2013). After another 40 years, global temperatures return to the baseline. The time it takes to reach the peak temperature increases for larger pulse sizes. Compared to the 0.5 GtC pulse, the time to reach the peak temperature increases by 42% for a 5 GtC pulse and by 242% for a 50 GtC methane pulse.

The MESM simulates the feedbacks to the terrestrial and ocean carbon sinks following an emission perturbation (Figure 3.8). For all pulse sizes, the carbon uptake of the terrestrial biosphere and ocean surface weaken. For instance, in the three years following a 0.5 GtC methane pulse, an additional 0.28 GtC of carbon remains in the atmosphere that would otherwise be absorbed by the land and ocean carbon pools in the baseline scenario. The weakened carbon pools can be traced back to biogeochemical responses following a release of methane. For one, O_3 that enters the stomata of a plant can damage plant cells and ultimately reduce the species
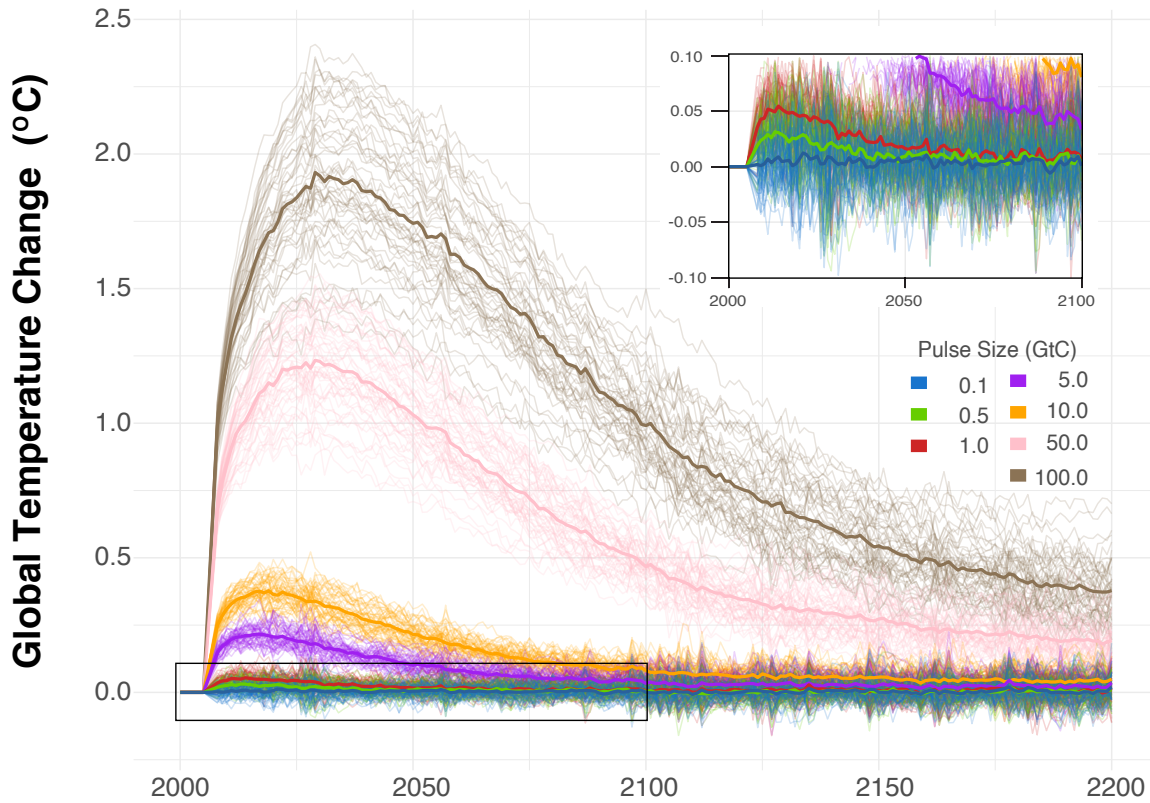
Figure 3.7. Global mean surface air temperature change following several pulse perturbations. Shown are the 49 individual ensemble members and the ensemble mean. Inset: Magnification of smaller pulses.

ability to photosynthesize (Felzer et al., 2005; Norby et al., 2005). In our simulations, the increase in global tropospheric ozone (Figure 3.6) creates a detrimental effect on photosynthesis (i.e. carbon fixation) and carbon sequestration. As a result, vegetation absorbs less CO_2 than the baseline scenario. Interestingly, for pulse cases above 0.5 GtC, the terrestrial carbon sink reverses course and becomes a source of CO_2 emissions as the combination of ozone damage and high temperatures increase plant and soil respiration (See Appendix B, Figure B.3) (Zhuang et al., 2004).

The oceans remain a sink through the pulse simulations. However, the transient response shows a weakening of the ocean carbon sink within the first decade following the perturbation (Figure 3.8b). What drives carbon uptake by the ocean is the partial pressure differences in CO_2 between the atmosphere and the dissolved inorganic carbon just below the ocean surface

Carbon Uptake of Terrestrial and Ocean Sinks
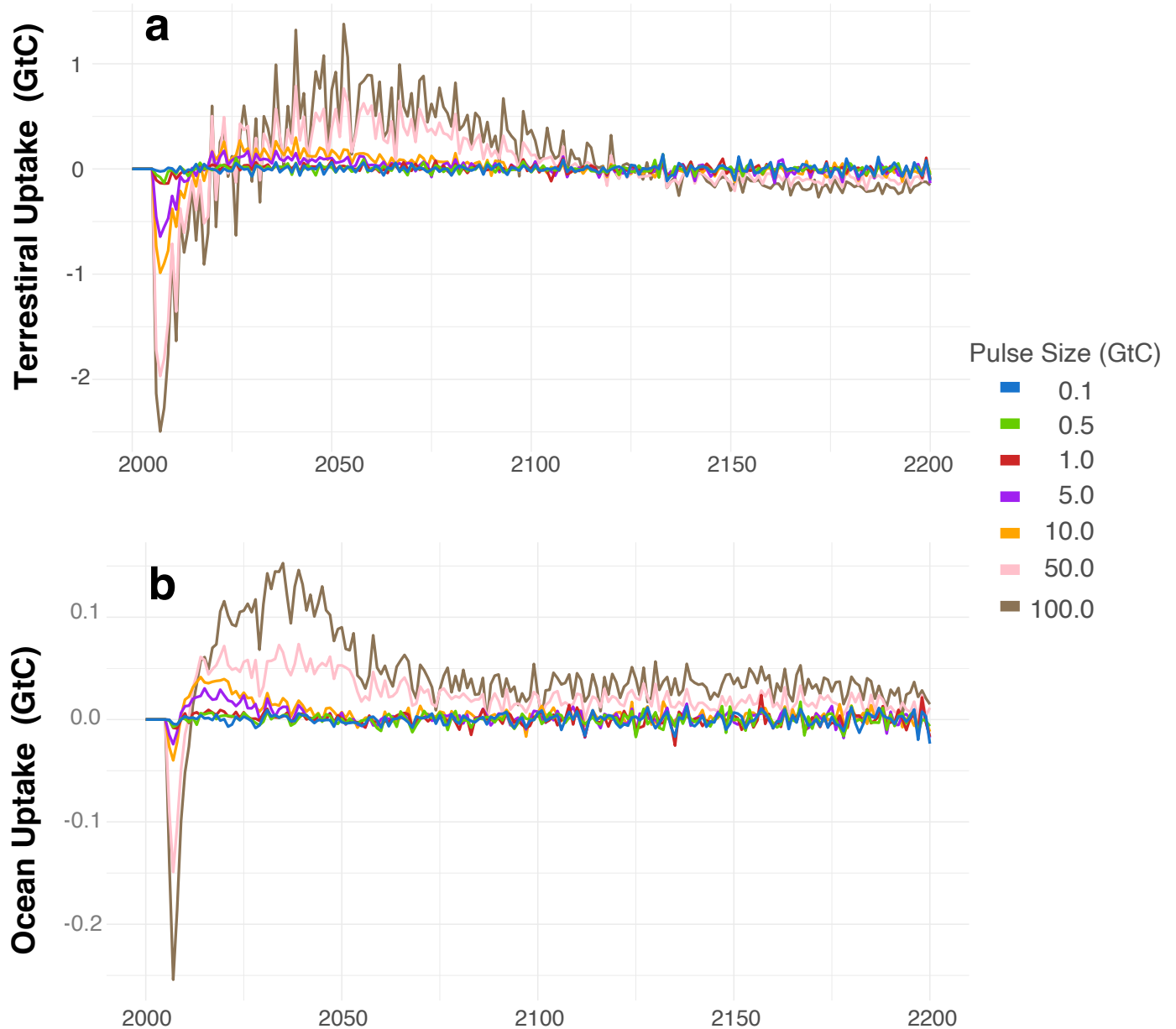
Figure 3.8. The change in carbon uptake from the a) terrain and b) ocean sinks. Shown are the ensemble means for each pulse size.

Natural Ecosystem Response to Pulse
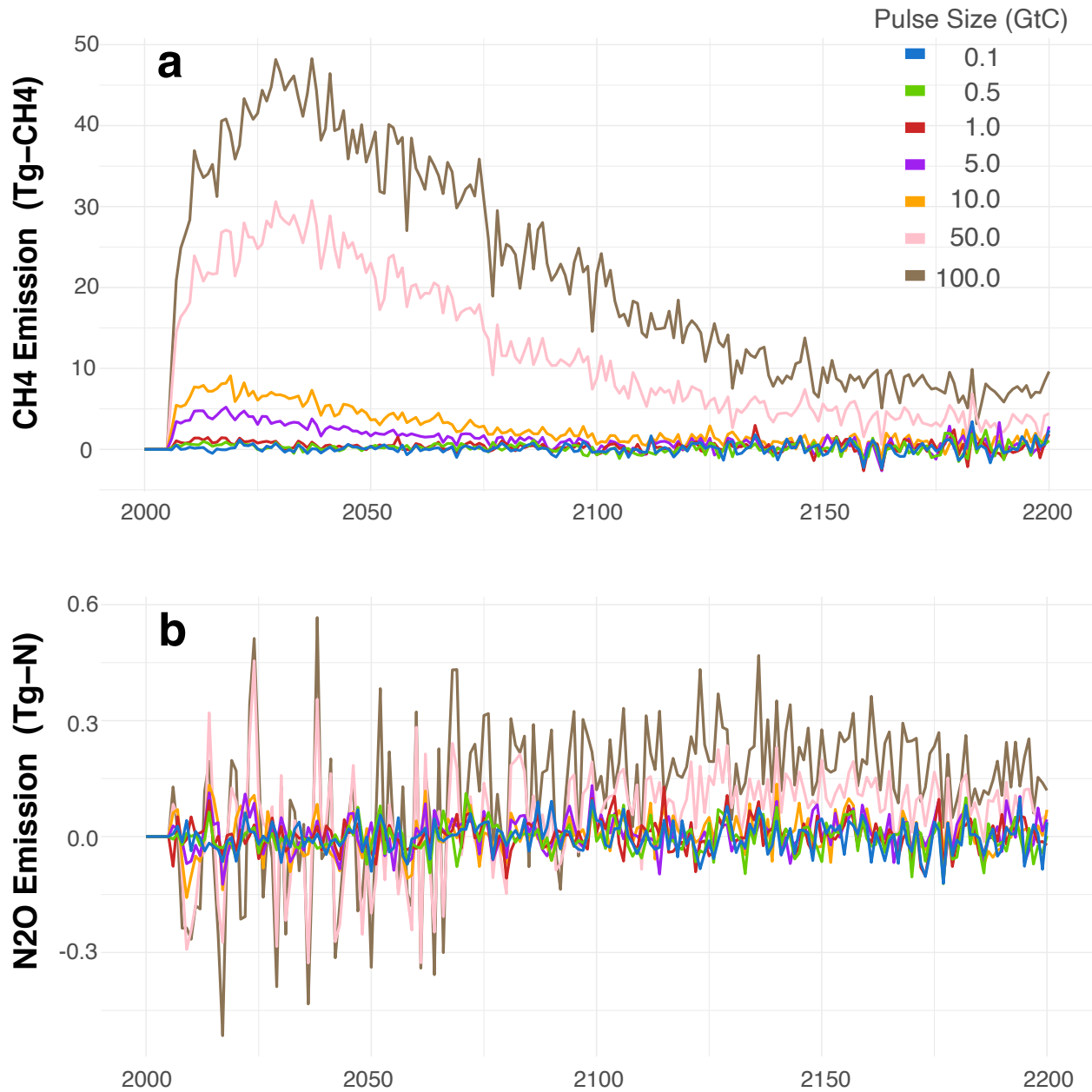
Figure 3.9. The natural ecosystem response to methane pulse perturbations. Shown are the ensemble means for a change in a) wetland methane emissions and b) soil nitrous oxide emissions.

(Friedlingstein et al., 2006). The ratio that measures the ocean's resistance to CO_2 absorption is the Revelle factor (Revelle and Suess, 1957). The strength of Revelle factor depends on the ocean's biogeochemical and thermodynamic responses (Sarmiento et al., 1998). Ocean carbon uptake is most sensitive to increased sea surface temperature (Joos et al., 1999), as CO_2 solubility has a strong inverse relationship with temperature (Murray and Riley, 1971). In the methane pulse simulations, an increased sea surface temperature effectively decreases CO_2 solubility, thus showing a weakened uptake when compared to the baseline scenario. Presumably the weakened uptake is not attributed to changes in atmospheric CO_2, as atmospheric CO_2 does not greatly differ from the baseline scenario in the first few years following the pulse (Figure 3.6a).

The MESM also simulates flux changes of natural ecosystems (Figure 3.9). For instance, wetland microbes react to the increase in temperature by emitting additional methane emissions. Over 10 years following a 0.5 GtC pulse, an additional 6.3 Tg-CH_4 (0.004 GtC) are released from global wetlands. As for natural N_2O emissions, the biogeochemical feedback to the nitrogen cycle is less evident. Only in large pulse sizes, and consequently high temperature simulations, increased bacterial denitrification leads to a minuscule increase in nitrogen emissions and N_2O concentration (Figure 3.6b). While this may be the case for the idealized 50 and 100 GtC pulses, realistic methane emission pulses do not indicate any significant change to the nitrogen cycle.

3.4.2   Methane and Carbon Dioxide Pulse Comparison

Identical 100 GtC emission pulses are separately simulated for CH_4 and CO_2 (Figure 3.10). By comparing the two species, we are able to identify the different timescales of the atmospheric response as they are redistributed by the biogeochemical cycles among the atmosphere, land, and ocean components. In addition, model results demonstrate how much the gases differ in their ability to absorb energy, or radiative efficiency. The contribution of the gas to the radiative forcing depends on the combination of the molecular properties of the gas, the magnitude of the atmospheric concentration increase, and the species' residence time. It is important to note that a 100 GtC emission pulse of CO_2 is approximately 10x the global annual fossil emissions (Friedlingstein et al., 2019), whereas the 100 GtC methane pulse is more than 350x greater than annual anthropogenic methane emissions (Saunois et al., 2020). As such, the magnitude of the atmospheric concentration increase is greater for the methane pulse than the CO_2 pulse. We justify the use of 100 GtC pulses in order to demonstrate reliable signal-to-noise from CO_2 pulse and directly compare the same carbon mass flux of the two species.

CH$_4$ and CO$_2$ Pulse Comparison

100 GtC Pulse: ▬ CH$_4$ ▬ CO$_2$
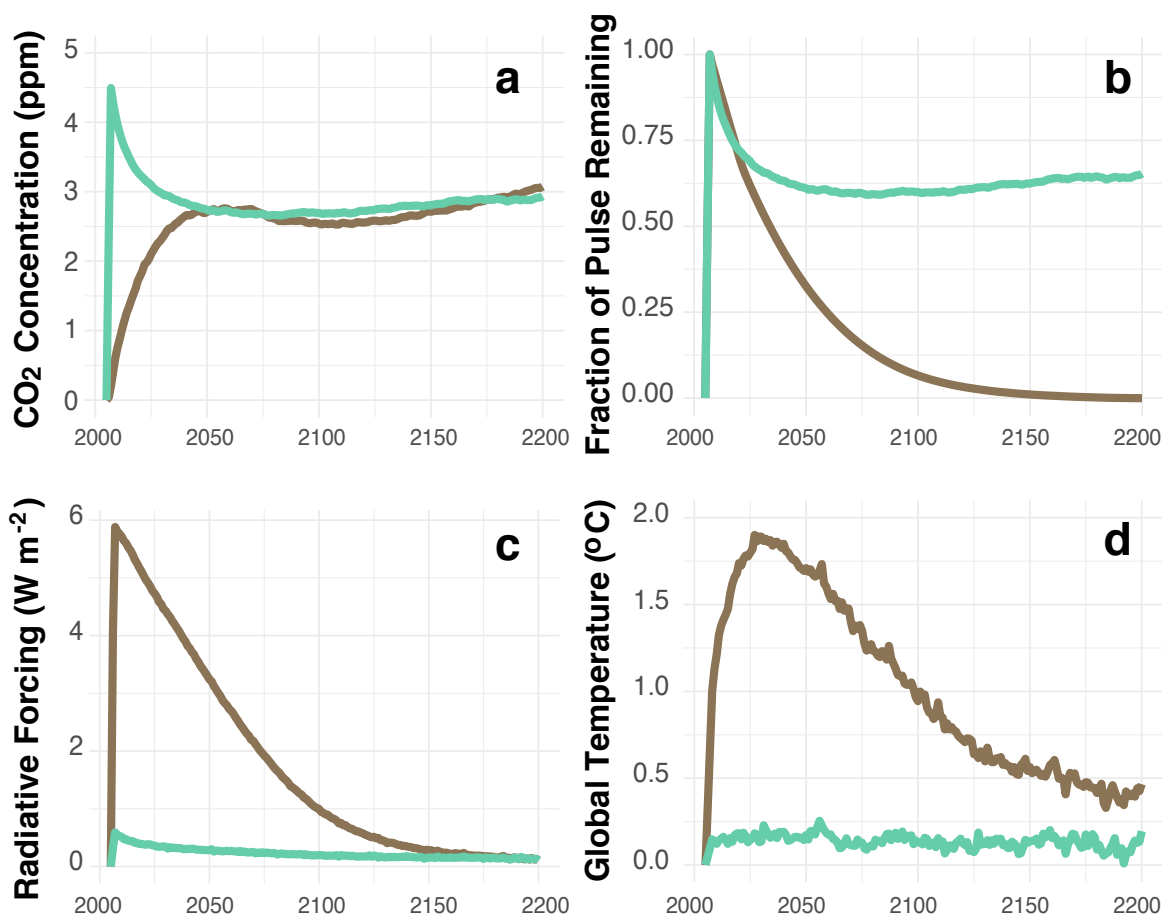
Figure 3.10. A comparison of the Earth system response to a 100 GtC pulse of methane and carbon dioxide. a) Change in the CO$_2$ atmospheric concentration. b) The fraction of the pulse perturbation remaining in the atmosphere, c) the total radiative forcing, and d) the global temperature response.

Following the pulse perturbation, the atmospheric concentration of both species increases to a peak perturbation anomaly. The CO$_2$ concentration anomaly after a 100 GtC pulse reaches a peak 44.9 ppm in the first year (Figure 3.10a), in agreement with the ensemble mean of several EMICs and ESMs simulated in Joos et al. (2013). Soon after the peak perturbations are reached, the evolution and decay of the perturbations begin to greatly differ (Figure 3.10b). Initially, the CO$_2$ perturbation decays at a faster rate than the methane perturbation, where in the first ten years following the pulse, 25% of the CO$_2$ and 23% of the methane perturbation is removed. This

may seem counter-intuitive as methane has a shorter residence time than CO_2. As demonstrated from prior results (Figures 3.3 and 3.5), the decay of the methane perturbation depends on the abundance of tropospheric OH, where higher emission pulses lead to an overabundance of methane and depletion of OH. The overall effect extends the methane residence time (refer to Figure 3.4).

Carbon Uptake of Terrestrial and Ocean Sinks
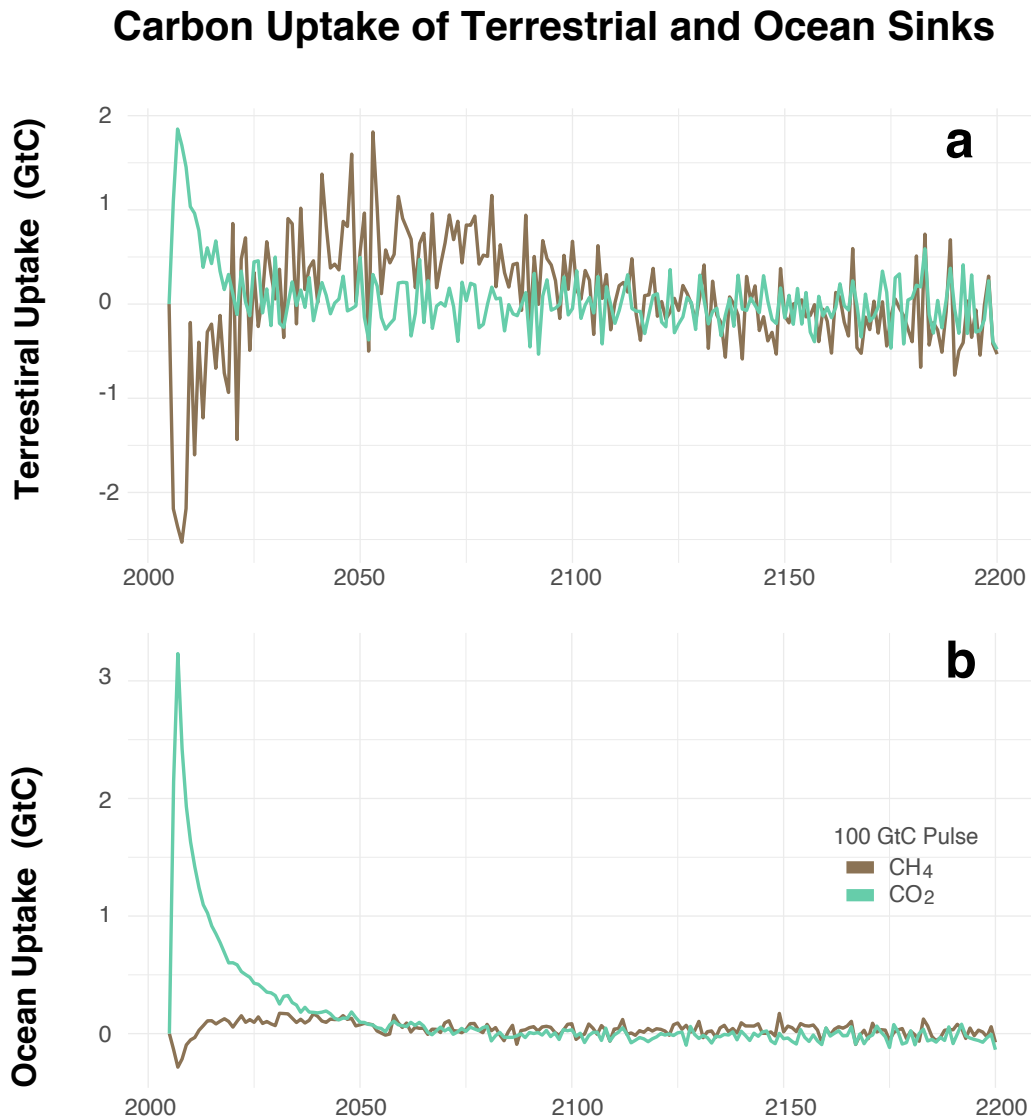
Figure 3.11. The change in carbon uptake from the a) terrain and b) ocean sinks for a 100 GtC pulse of CH_4 and CO_2.

The faster decay of the CO_2 is directly related to the ability of the ocean and land sinks to absorb and store carbon from the atmosphere (Figure 3.11). Most of the initial uptake occurs through rapid dissolution of the ocean surface (3.2 GtC) and CO_2 fertilization of the land biosphere (1.9 GtC). The rate at which the ocean will uptake carbon depends on the CO_2 partial pressures between the ocean surface and atmospheric layer above (Friedlingstein et al., 2006). On land, the rate of the land uptake is driven by elevated photosynthesis in a higher CO_2 environment (Norby et al., 2005). Increased global temperatures over fifty years (Figure 3.10d) lead to a saturation of the carbon sinks and decline in the uptake efficiency of the land and ocean, a behavior seen in other EMICs and ESMs (Joos et al., 2013; Zickfeld et al., 2011)). A sizable fraction (60–65%) of CO_2 remains in the atmosphere through the remainder of the simulation, which is also consistent with earlier model studies (Joos et al., 2013; Eby et al., 2009; Sarmiento et al., 1992; Maier-Reimer and Hasselmann, 1987). The decay stages are a product of the many different processes and timescales that remove CO_2 from the atmosphere. The long perturbation tail is an indicator of the slow processes of weathering and deposition, which can persist longer than 10,000 years (Archer et al., 2009; Eby et al., 2009).

While the methane pulse continues to decay to zero, the fraction of CO_2 begins to slowly increase again at an approximately linear rate after year 2075. By 2200, the CO_2 concentration reaches up to 65% of the perturbed peak. With the already weakened carbon sinks and the rise in global temperature, background CO_2 concentrations from the described emission scenarios add an additional stress to the carbon sinks. Effectively, the response is unique to the changing background concentration (Gillett and Matthews, 2010). This behavior is not captured by impulse-response functions that are used to calculate the the GWP and social cost of carbon (SCC) since a constant background concentration is often assumed (Aamaas et al., 2013; Joos et al., 2013).

An instantaneous increase in greenhouse gas concentrations disrupts the Earth's radiative energy balance. For a 100 GtC pulse of CO_2, there is a 0.6 $W\,m^{-2}$ increase in total radiative forcing (Figure 3.10c). In comparison, the total radiative impact (5.9 $W\,m^{-2}$) from a methane pulse perturbs the radiative efficiency of other trace constituents. Of the total radiative forcing following the pulse, methane contributes to 68% and another 8% is due to an increase in O_3 (See Appendix B, Figure B.1). As the concentration of CH_4 quickly dissipates, the net radiative forcing anomaly decreases exponentially due to an increase in outward longwave radiation. By 2200, the net radiative forcing anomaly resulting from a methane pulse is 0.1 $W\,m^{-2}$ (Figure 3.10c) driven primarily by the residual CO_2 in the atmosphere following methane oxidation.

Equal pulse emissions of CO_2 and methane have significantly different impacts on the global mean surface air temperature (GMSAT) because of their differing radiative properties and atmospheric residence times. A methane pulse size of 100 GtC is shown to reach a peak temperature anomaly of 1.9 °C after 20 years. The temperature anomaly from the methane pulse declines from its peak to a near steady state of about 0.42 °C, after all of the methane is oxidized to CO_2. As for the CO_2 simulated pulse, the CO_2 temperature anomaly peaks at approximately 0.2 °C, nearly 10% of the peak anomaly seen by the methane pulse. Through the remainder of the CO_2 pulse simulation, the radiative forcing and temperature anomalies show a long decaying tail, indicating an irreversible temperature impact that lasts for centuries.

3.5 Discussion and Conclusion

Pulse methane emissions of various magnitudes are applied to a business as usual baseline emission scenario. Increasing the abundance of methane greatly influences atmospheric chemistry and the concentration of other non-CO_2 gases and related aerosols. It is well known that the chemical oxidation of methane leads to the production of CO_2 through a chain reaction with OH. Still, the net reaction depletes OH. For pulse sizes above 1 GtC, the result has a direct effect on the residence time of methane and ozone. Even for the smallest pulse sizes, O_3 levels increase as the OH is depleted. The competition for a reaction with OH, extends the perturbation time of methane so that it takes more than 60 years to be completely removed for an emission pulse (0.1 GtC) equivalent to half of the annual anthropgogenic CH_4 emissions.

There is a delay in atmospheric CO_2 levels, as the chain reaction following methane oxidation takes time. A peak CO_2 concentration is reached when all of the methane is oxidized. Ocean and land sinks operate to remove the perturbed carbon from the atmosphere. While the atmospheric CO_2 abundance begins to drop soon after reaching a peak, it reverses course and rises again to the point that it surpasses the initial peak response. In this case, the changing background concentration from the high emission scenario decreases the efficiency of the sinks to uptake carbon. This is due to the climate-carbon feedback effect where warming climate lowers the ability of the sinks to hold carbon. By the end of the simulation, more CO_2 exists in the atmosphere than originally was perturbed by the methane pulse, suggesting our annual methane emissions will have a lasting effect on the carbon cycle so long as we keep emitting more CO_2.

Our study goes further into the impulse response investigation by analyzing the temperature-induced feedbacks of the biosphere, an area not yet studied in methane impulse response tests. While no major changes occur in the nitrogen cycle, the methane cycle shows a clear impact on natural wetland emissions. For every pulse-size case, there was a rise in the wetland methane emissions as the initial temperature perturbation drives an increase in modeled methanogenesis. While the emission increase from wetlands is minuscule (6.3 Tg over 10 years) compared to annual anthropogenic methane emissions (378 Tg yr^{-1}), it does add to the abundance of methane in the atmosphere and increases the lifetime.

Although methane is relatively short-lived, its warming impact is far greater than CO_2 in the first few centuries and has an even greater indirect impact on a prolonged timescale. The methane pulse results in a peak GMSAT anomaly nearly 10x greater than the anomaly resulting from the same sized CO_2 pulse. In addition, the thermal inertia of the climate system leads to a decline in GMSAT much more slowly than the decline in atmospheric concentrations. A modeled GMSAT anomaly of 0.4 °C and 0.2 °C, for pulses of CH_4 and CO_2, respectively, remain for the scope of the study.

We note that the 100 GtC emissions pulse of CO_2 is approximately 10x annual anthropogenic emissions, but is also 350x annual anthropogenic methane emissions. It does suggest that we should scale down the methane pulse size to 2.8 GtC for an approximately equal comparison in magnitudes. While this is one type of analysis, we wanted to use the same pulse size in GtC to have a fair comparison of equal amounts of carbon in the atmosphere and to see where carbon is exchanged with the reservoirs.

One unique finding is the transient response of the terrestrial and ocean carbon sinks, as carbon uptake decreases initially for a methane pulse. For five years following the 100 GtC methane perturbation, a net 4.9 GtC is emitted from the land as methane-induced warming leads to increased vegetative and soil respiration, and high levels of O_3 reduce CO_2 fixation. In comparison, for the same time-horizon and pulse size, a CO_2 perturbation results in a additional uptake of 20.8 GtC compared to the baseline scenario, where 61% is absorbed into the upper ocean and the other 39% is absorbed by the terrestrial biosphere. These differences in biogeochemical cycling of carbon reveal that future methane emissions and related temperature induced increases could create an adverse effect on the carbon cycle, which may lead to a supplementary weakening of carbon sinks. Therefore, any metric that compares methane impacts to CO_2 climate impacts should incorporate a full representation of the feedbacks that

affect fundamental atmospheric chemical and biogeochemical processes.

While the primary purpose of the idealized pulse emission experiments was to understand the feedbacks to the system, these experiments, especially the smaller pulse sizes (0.1–0.5 GtC), can also reveal insight on the climate response of a more realistic emission pathway in methane. Annually, human activity emits an estimated 0.28 GtC yr^{-1}. Naturally, this annual estimate is broken down into several tiny pulses spread out across the globe each day of the year. They are all additive and the cumulative climate impact will be the combined effect, much like the pulses in our experiments. Using the intermediate complexity model framework, we are able to capture the daily changes in methane's budget as small daily emissions alter the strength of methane's sink. The model experiments can also capture the change in zonal mean atmospheric concentration as emissions and important atmospheric species like OH are not uniformly geographically spread out. And finally, the pulse experiments show that if our emission trajectory continues its upward trend, leading to higher annual "pulses" that build upon the previous pulses, methane feedbacks could become more prevalent and expedite unfavorable climate responses.

Chapter 4

Introducing a methane lifetime concentration dependency and natural emissions model into the FaIR climate model

4.1 Abstract

Methane feedback mechanisms resulting from interactive chemistry and biospheric emissions have the potential to intensify climate change impacts and bring us closer to climate tipping points. Few low-complexity climate models are able to represent feedbacks to the methane cycle. We demonstrate how to modify the FaIR reduced-complexity model to incorporate methane feedbacks. Our update to FaIR includes a natural methane emission component dependent on global mean temperature and an interactive methane lifetime with a positive self-abundance feedback. We calibrate the newly introduced parameters so that our modified version of FaIR matches the output of the MESM, which is capable of modeling climate-induced changes to the methane cycle. The combined methane feedbacks increase total atmospheric methane concentration and methane lifetime, thus increasing the projected global mean temperature. Evaluating the modified FaIR model in the context of representative concentration pathways, we estimate that methane emissions and the addition of methane feedbacks cause global mean

temperature to increase another 0.43 °C above the projected 4.33 °C temperature anomaly relative to preindustrial levels for a high emission RCP8.5 scenario in 2100. The projected end of century temperature anomaly, 1.47 °C, for a low emission RCP2.6 scenario decreases 0.095 °C when reduced methane feedbacks in a cooler low-emission world limit additional natural emissions and decrease methane lifetime.

4.2 Introduction

Reduced-complexity climate models represent their model physics through parameterizations and mathematical approximations (Smith et al., 2014). As new insights are made from more complex models, reduced-complexity models are improved to emulate the new behaviors of the more complex models. In one such case, modelers have begun introducing climate feedback mechanisms that have the potential of intensifying natural systems and worsening their climate impacts (Wolff et al., 2015). Despite ongoing efforts, feedbacks related to the methane cycle are omitted in many climate models within integrated assessment frameworks (Gasser et al., 2017; Marten et al., 2015). Two important methane cycle feedbacks include the effect methane has on its own lifetime and the temperature-induced feedback to natural emissions. We explore these two feedbacks and their impacts on model projections.

Complex Earth System Models with detailed atmospheric chemistry simulate the methane lifetime feedback effect. This feature results when variations in the methane sink directly impact how long methane stays in the atmosphere (Prather, 1994). Methane's primary atmospheric sink is the oxidation reaction with tropospheric hydroxyl radical (OH). As methane and other reactant species accumulate in the atmosphere, OH radicals are suppressed. As a result, the rate at which methane oxidizes slows down and methane's residence time increases. Since the doubling of preindustrial methane concentration, it is estimated that the increasing feedback has extended methane's lifetime by 55%, from 5.9 to 9.2 years (Dlugokencky, 2019; Holmes, 2018).

While the lifetime feedback is primarily determined by the methane burden, modelers are exploring other meteorological variables and trace pollutants that drive changes in methane's lifetime. For example, tropospheric ozone and carbon monoxide emissions from biomass burning weakly interact with methane's primary sink catalyst, hydroxyl radical, creating a slight increase methane's lifetime. (Fry et al., 2012; Dalsøren et al., 2010; Hoor et al., 2009). Other

meteorological variables that drive atmospheric chemistry such as temperature and humidity are thought to reduce methane's lifetime through increased reaction rates with OH (Holmes, 2018; Ehhalt et al., 2001; Krol and Van Weele, 1997). But when all variables are considered, this century is projected to see an increase in methane lifetime by about 13%, where the sensitivity is dominated by methane's feedback on it's own OH sink (Holmes et al., 2013). Since the longevity in lifetime would raise methane's radiative impact, reduced-form methane cycle models should include the most significant mechanisms that impact methane's primary sink.

The second important methane feedback is related to the several natural wetland systems that are susceptible to the changing climate. Wetlands are the largest source of natural methane emissions, releasing 150 to 225 Tg-CH$_4$ each year or approximately a third of total global methane emissions (Saunois et al., 2016). Shifts in temperature, precipitation, and vegetation processes have the potential to increase methane emissions from wetlands and freshwater systems (Dean et al., 2018). If natural methane emissions were to increase with the changing climate, the amplified emissions from these systems would further induce an increase in atmospheric concentration and lead to a positive climate feedback.

The production of methane in these environments is predominately due to the degradation of organic matter by methanogen microbes in anaerobic (low-oxygen) conditions (Ferry, 1999). It is well known that temperature controls the rate of microbiological processes, and the production and oxidation of methane in wetland environments (Kip et al., 2010; Frenzel and Karofeld, 2000). With projected warming, rising surface air temperatures will pervade the top soil layers where the majority of methanotrophs reside, thus increasing the methane emitted from the wet soils.

We introduce these two important methane feedbacks, the chemical feedback on its lifetime and the wetland emission feedback, into a reduced-complexity climate model, FaIR v1.3 (Finite Amplitude Impulse Response) (Smith et al., 2018), a modified version of the Intergovernmental Panel on Climate Change impulse-response model (Rogelj et al., 2018) that accounts for climate-carbon cycle feedbacks. FaIR does not include climate feedbacks to other important forcing agents - particularly methane. Using the MIT Earth System Model (MESM) (Sokolov et al., 2018), we develop a parameterization for methane feedbacks and include this in the FaIR model. We then test the new FaIR methane module by simulating past concentrations and future projections of the MESM, a higher complexity model.

Within this paper, we first describe the current model structure of the methane component

within the FaIR (v1.3). We then provide a brief description of the target data sets, prescribed emission scenarios, and framework to be parameterized through a calibration process. Our results assess the parameter optimization and model fit to the target data sets. We briefly comment on the changes to the FaIR projections in context of climate policy decision-making.

4.3 Current Setup of the FaIR Methane Module

In its current setup, FaIR v1.3 assumes a one-box model for each of the non-CO_2 agents (Smith et al., 2018). The box model converts prescribed annual global emissions into an equivalent change in the atmospheric molar mixing ratio, δC_t. The concentration burden, C_{t-1}, is reduced by an exponential decay with a constant decay timescale, τ. We will refer to Eq. 4.1 for the current setup of the FaIR box-model of the methane cycle. Run on an annual time-step, the box model calculates the annual methane concentration (in parts per billion; ppb) as a balance between the sources and sinks.

$$C_t = C_{t-1} + \frac{1}{2}(\delta C_{t-1} + \delta C_t) - C_{t-1}\left(1 - \exp\left(\frac{-1}{\tau}\right)\right) \tag{4.1}$$

Blue = source term. Red = sink term.

The source term takes an average atmospheric molar mixing ratio from the previous and current time-step emissions. Exogenous emissions are prescribed for both anthropogenic and natural methane sources. Historic emissions of anthropogenic sources are reconstructed to match observed atmospheric concentrations starting in 1765. And, future emission scenarios are set up to follow the extended Representative Concentration Pathway (RCPs) scenarios out to 2500 (Meinshausen et al., 2011b). If desired, the flexibility of FaIR allows the user to provide their own emission scenario.
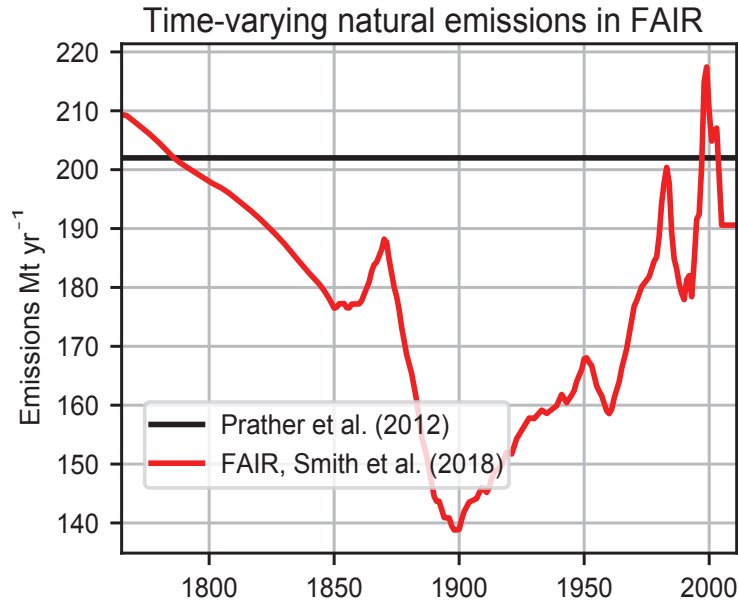
Figure 4.1. Natural emissions of methane used in the FaIR model (red) and present-day emission estimate from Prather et al. (2012) (black). Figure taken from Smith et al. (2018).

In addition to anthropogenic emissions, FaIR also includes time-varying natural methane emissions (Figure 4.1). Historic natural emissions are calculated to match observed concentrations by balancing the atmospheric budget to changes in anthropogenic emissions. This approach explains the variation of up to 30% seen in Figure 4.1. Hence, they are not based on observations of natural emissions. Beyond 2005, natural methane emissions are fixed at a constant yearly rate of 191 Mt-CH_4 yr^{-1}, which is slightly below the present-day best estimate, 202 Mt-CH_4 yr^{-1} (Prather et al., 2012). Granted, natural emissions are still highly uncertain and vary between methods of estimation. For example, uncertainty ranges for top-down methods span 142–208 Mt-CH_4 yr^{-1}; and bottom-up methods average even higher, 177–284 Mt-CH_4 yr^{-1} (Kirschke et al., 2013).

In FaIR v1.3, the total sink of methane is modeled as an exponential decay of the airborne concentration anomaly (Smith et al., 2018). The atmospheric decay relies on a constant lifetime of the species, τ. Instead of the 12.4 years referenced in the AR5 (Myhre et al., 2013), FaIR uses a constant methane lifetime of 9.3 years in order to better agree with calculated changes in historic natural emissions and to fit RCP projections made by MAGICC6 (Meinshausen et al.,

2011b). The model developers found that the larger, 12.4 yr lifetime found in the AR5 results in concentrations too high to match projected RCP concentrations in MAGGIC6.

Based on the current setup of the methane module in FaIR v1.3, we find two areas in need of improvement:

- Assuming fixed natural methane emissions into the future overlooks the natural changes in wetland soil respiration to changes in temperature and precipitation.

- Implementing a constant atmospheric lifetime omits any chemical feedbacks methane has on its own lifetime.

Addressing these two areas, our work improves upon the current FaIR model by first adding a natural emissions component responding to changes in global temperature, and also adding a dynamic methane lifetime. Providing additional skill to the FaIR model, we integrate these two methane feedbacks.

4.4 Methods

4.4.1 Using the MESM Output as Target Calibration Data Sets

We propose altering the methane module of FaIR that calculates the change in methane concentration anomaly with a change in emission. The new FaIR methane module will emulate projected climate variables of the MIT Earth System Model (MESM), including global temperature, methane concentration and natural wetland emissions. We use a set of model simulations from MESM to calibrate the methane module.

We follow the standard approach to running the MESM as described in Sokolov et al. (2018) and develop a set of simulations that provide a set of target data for FaIR to emulate. The MESM is run in a two-step sequence starting with a historical simulation, which forces the model with observed greenhouse gas concentrations, tropospheric and stratospheric ozone, aerosols, and the solar constant from 1861 to 2005. At this stage, the climate system properties including climate sensitivity, rates of oceanic heat and carbon uptakes, and aerosol forcing are set to be consistent with available observations of surface air and ocean temperatures. We systematically
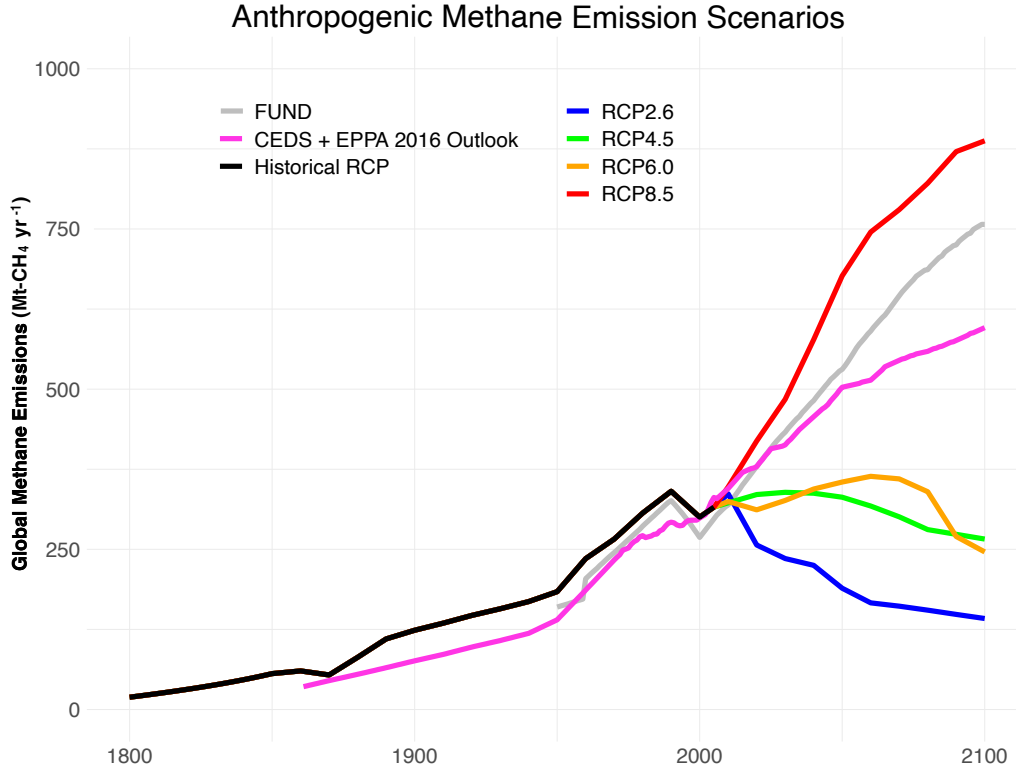
Figure 4.2. A comparison of anthropogenic methane emission scenarios. We calibrate the FaIR model using the CEDS historical emissions (1861–2005) and the EPPA Outlook scenario (2006–2100).

vary the three parameters (climate sensitivity, rates of oceanic heat and carbon uptakes, and aerosol forcing) by drawing from the joint probability distribution of Libardoni et al. (2019). We produce 49 drawings of parameter sets to run a 49 member ensemble of the MESM. Additional details on the ensemble selection can be found in Chapter 3 and Appendix A.

The second stage uses the full dynamic chemistry version of the MESM, forced with projected emissions of greenhouse gases and aerosols for an economic growth scenario of the Emissions Prediction and Policy Analysis Model (EPPA) (Chen et al., 2016; Paltsev et al., 2005). Methane emissions for the EPPA Outlook scenario fall in between the RCP 8.5, a highly intensive emission scenario, and the RCP 6.0, a more moderate emission scenario (van Vuuren et al., 2011b)(Figure 4.2). To keep the emission scenarios between the MESM and FaIR consistent during the calibration process, we use the EPPA Outlook scenario as input into the FaIR model for the 2006 – 2100 period. In its default settings, FaIR uses the four RCP projections and their historical extensions (van Vuuren et al., 2011b; Meinshausen et al., 2011b). This historical

emissions data set comes from the global, gridded estimates used within the Coupled Model Intercomparison Project phase 5 (CMIP5) (Lamarque et al., 2010). We update FaIR to run with the new historical anthropogenic methane emissions used within the CMIP6. Developed with the Community Emissions Data System (CEDS) (Hoesly et al., 2018), the new historical emissions data set estimates methane emissions lower and smoother than that of the RCP extension (Figure 4.2), likely attributed to the drop in agricultural emission estimates.

A integral component of the MESM for this study is its ability to estimate changes in terrestrial methane emissions. The Natural Ecosystem Model (NEM) of the MESM interacts with the atmospheric dynamics model to simulate biogeochemical processes that release methane and nitrous oxide emissions from the terrain (Liu, 1996). More specifically, the methane emission model simulates methanogenesis dependent on changes to the water table level and soil temperature for five soil layers on hourly time steps. With a spatial resolution of 1° x 1°
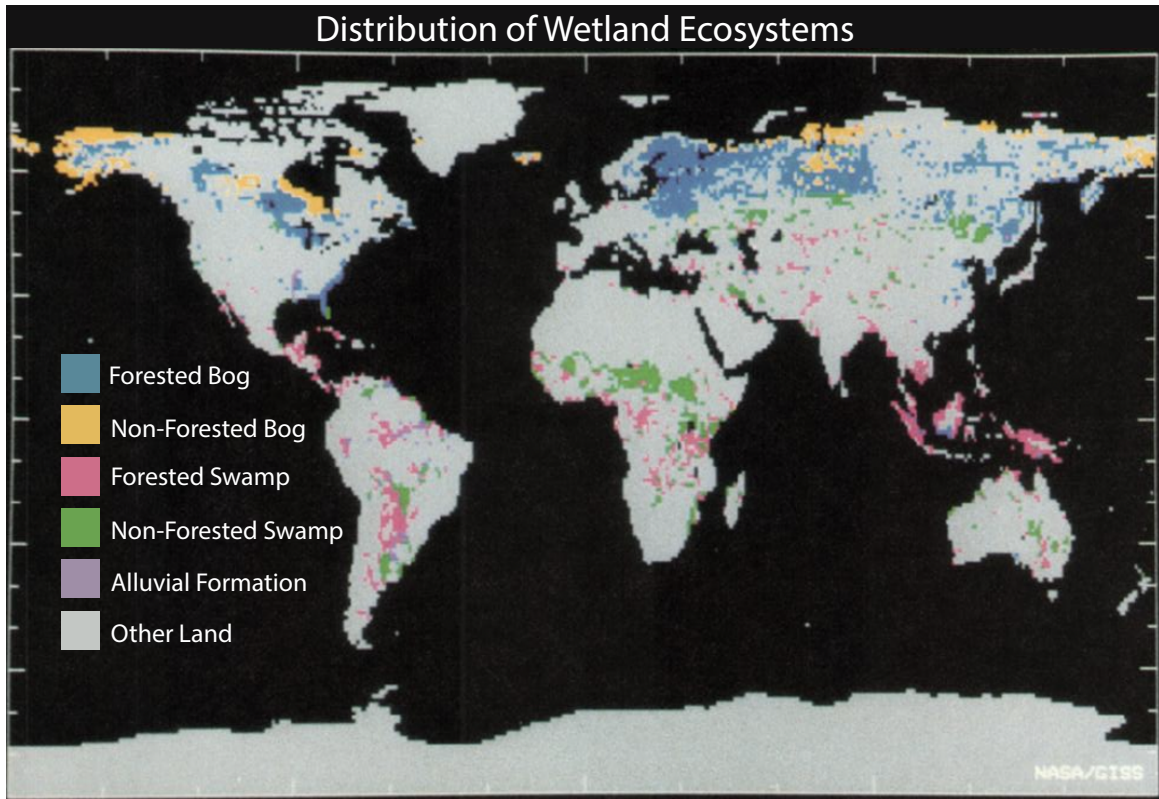
Figure 4.3. Global distribution of wetland ecosystems on a 1° x 1° grid within the Natural Ecosystems Model of the MESM. Figure taken from Matthews and Fung (1987).

(Shown in Figure 4.3), a data set of global wetland distribution and inundated areal fraction are provided to calculate the methane flux distribution over 5,263,000 km² of wetlands (Matthews and Fung, 1987). To model local ecological climate changes, wetlands are further divided by land type based on tropical, temperate, and boreal; forested or non-forested bogs, swamps, and alluvial floodplains. Schlosser et al. (2007) show that MESM estimates of global annual methane flux fall near the middle range of current global uncertainty estimates, making the MESM a reliable tool for our modelling study.

Using the MESM, we estimate changes in future methane emissions from wetland environments. Because soil properties are coupled with the atmospheric variables of temperature and precipitation, the MESM captures the growing uncertainty in future projections of wetland emissions. Figure 4.4 shows simulated MESM global wetland methane emissions for each decade starting in 2010 through 2100. The distributions encompass the 49 MESM ensemble members. The 2010 emissions distribution shows a bell-curve with a peak emission just under 210 Mt-CH$_4$ per year. By 2100, the curve shows elongated tails spanning 246 to 288 Mt-CH$_4$ per year.
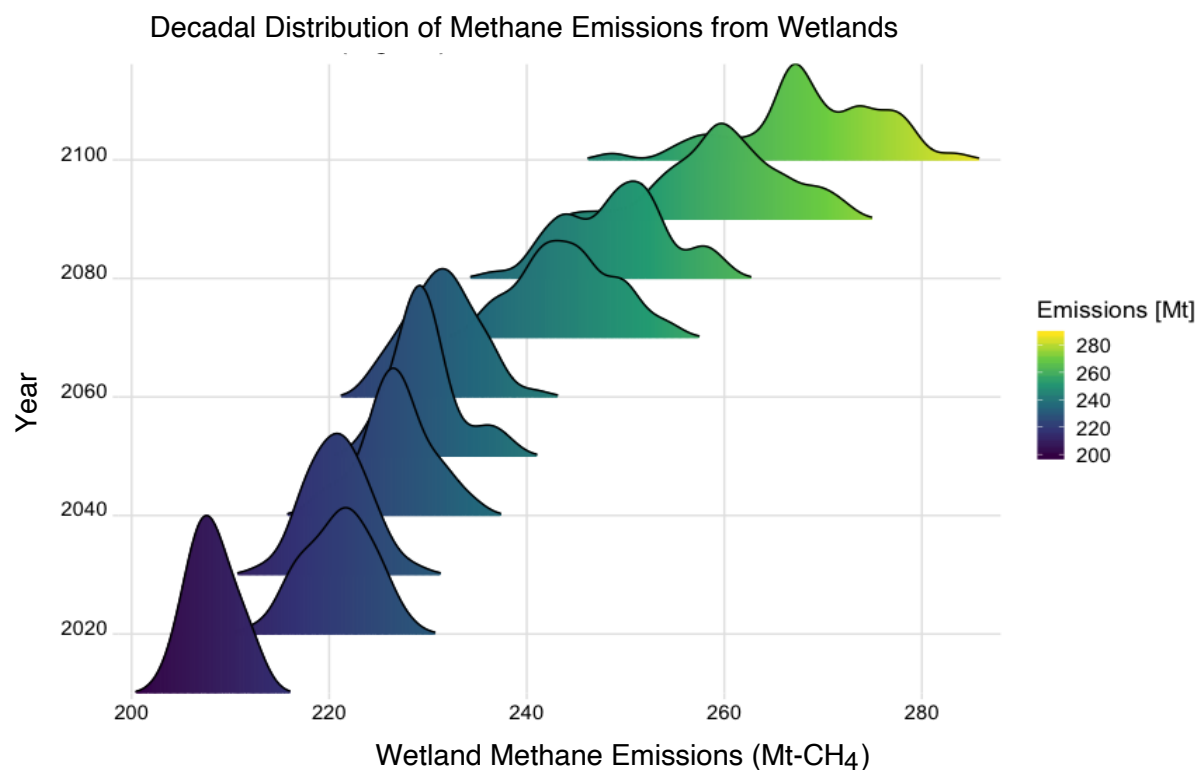
Figure 4.4. Distribution of wetland methane emissions (Mt-CH$_4$) simulated in the 49 member MESM ensemble, shown every decade through 2100.

4.4.2 Alterations to FaIR Methane Module

As discussed earlier, we are improving the FaIR methane module by introducing a natural wetland emissions component and a new lifetime calculation to emulate the results of the MESM. Figure 4.5 shows a schematic of the proposed modifications to FaIR model. In the following sections, we discuss the addition of a natural emissions model that is sensitive to the global mean temperature projection. We also introduce a dynamic methane lifetime, sensitive to the atmospheric abundance of methane.

4.4.2.1 Natural Wetlands Methane Emission Model

As the first alteration to the FaIR model, we modify the natural emissions component. In the current setup, historic natural emissions are calculated to match observed concentrations by balancing the atmospheric budget to changes in anthropogenic emissions. Currently, the model assumes future natural emissions are held at a constant 191 Mt-CH_4 per year. Since scientific
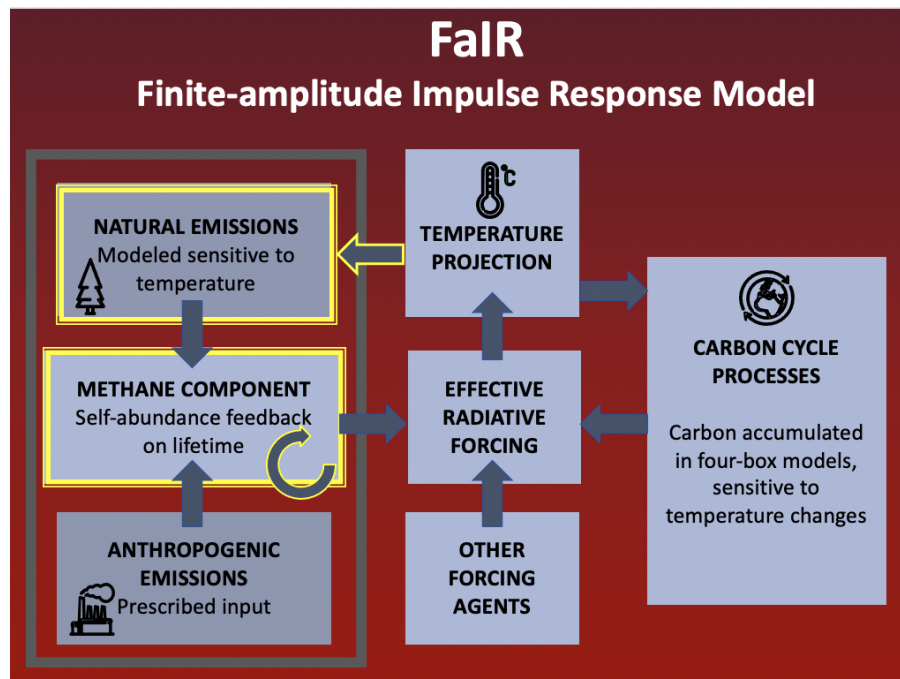
Figure 4.5. A schematic of the Finite-amplitude Impulse Response (FaIR) model. Shown in yellow are the methane components modified to add methane feedbacks. Figure adapted from Smith et al. (2018).

literature is in agreement that natural wetland emissions are expected to increase with climate change, assuming constant natural emissions is a great weakness of the current FaIR methane module.

Our improved approach to modeling natural methane emissions uses an intuitive representation of the relationship between temperature and rate of microbiological activity. The basis of this model came from preliminary analysis of MESM output for a 49 member ensemble (See Figure 4.6). The MESM results indicate a strong linear relationship (R^2=99%) between increasing global mean surface temperature and increasing global wetland methane emissions. The relationship holds true for the historical period, as well as, projections for a "business as
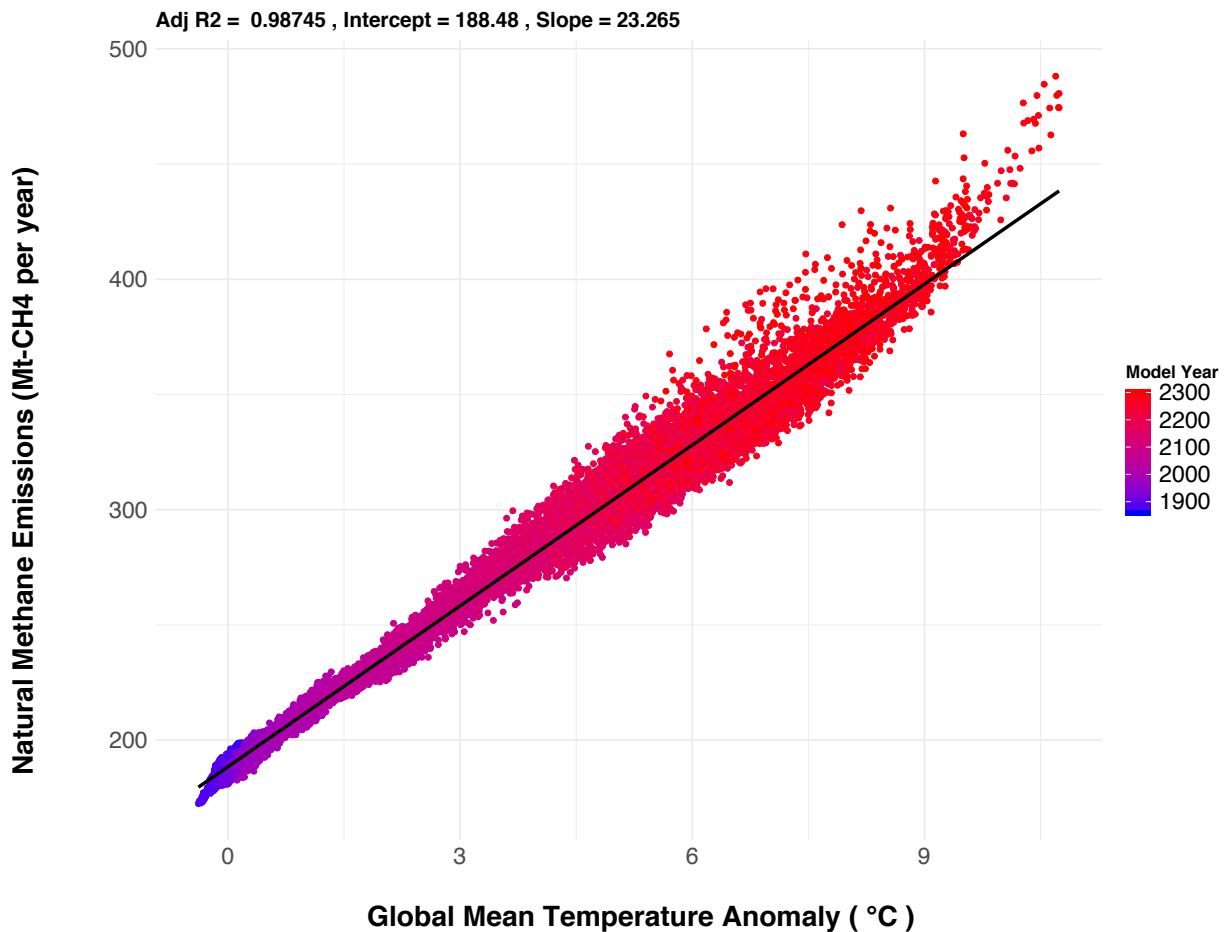
Figure 4.6. Mean annual CH_4 emissions from wetlands within the MESM model as a linear function of global mean surface temperature anomaly. The colored scale refers to the modeled year.

usual" future emission scenario. Methane emissions in the preindustrial period of the MESM span 172 to 198 Mt-CH$_4$ yr^{-1}, falling within the uncertainty range of previous studies (Paudel et al., 2016; Houweling et al., 2000).

But, as the global temperature anomaly exceeds 4 °C in the late 21st century, uncertainty in natural emissions grows and the linear relationship weakens. MESM projections for end of the century global wetland emissions are 248–283 Mt-CH$_4$ yr^{-1}, a substantial 43% increase from preindustrial levels. Lacking the rise in future wetland emissions, the former FaIR v1.3 model underestimates a cumulative 3,973 Mt-CH$_4$ of wetland emissions, on average, over the 21st century. Omitting such a large sum of wetland emissions is equivalent to omitting nearly 10 years of anthropogenic methane emissions (assuming 362–378 Mt-CH$_4$ yr^{-1} from Saunois et al. (2016)).

The simple linear relationship in Figure 4.6 between natural emissions and global mean surface temperature is the basis of our FaIR methane module. The new linear term for the annual global natural methane emissions in the FaIR model is:

$$N_t = m_N * (T_{t-1}) + b_N \qquad (4.2)$$

where N_t is the global wetland emissions in Mt-CH$_4$ per year and T_{t-1} is the previous time-step's global mean temperature calculated within FaIR. m_N is the slope and b_N is the intercept of the linear function. In the following section, we calibrate the FaIR model by adjusting the newly added parameters, m_N and b_N, to simulate a time-series which can reproduce the MESM trend.

Looking back at Eq. 4.1 of the FaIR methane box model, we update the methane source term to include a natural emissions component that depends on annual global mean temperature. The increase in atmospheric molar mixing ratio, δC_t, in year t considers both anthropogenic and wetland methane emissions (in units Mt-CH$_4$):

$$\delta C_t = \frac{A_t + N_t}{M_a} \frac{w_a}{w_{\text{CH}_4}} \qquad (4.3)$$

where A_t is the anthropogenic emissions of methane each year. N_t is the wetland natural

71

emissions of methane per year. M_a is the mass of the atmosphere. w_a is the molecular mass of the atmosphere. And, w_{CH_4} is the molecular mass of methane.

We acknowledge that the rate of natural emissions depends on several ecological and climate variables beyond just global mean temperature. For one, the amount of precipitation determines the water-saturation of the wetland soils, which is necessary to create anaerobic conditions for methanogenesis. With this in mind, we also examine the relationship between global precipitation and wetland methane emissions in Appendix D. As expected, the MESM results show global mean precipitation is strongly correlated with wetland methane emissions. While this shows precipitation may be a good predictor of natural methane emissions and could be used to build a simple model representation, precipitation is not a variable currently built into the FaIR model. To maintain the reduced-complexity structure of the FaIR model and to only focus on modifying the methane module, we do not model FaIR natural emissions as a function of precipitation. Our modification only models natural emissions to a change in simulated global mean temperature in FaIR.

4.4.2.2 Methane Lifetime Calculation

After updating the source term of the methane module with a natural emissions calculation, we next alter the FaIR model sink term by modifying the methane lifetime. In the current FaIR model, a constant 9.3 years is assigned for the methane lifetime, τ. However, this is not well representative of atmospheric chemistry that influences the methane sink. Rather, methane lifetime is a dynamic property that varies due to changes in atmospheric chemistry. The primary reaction methane has with OH is the dominant loss mechanism in the troposphere. The net effect suppresses OH concentrations and prolongs the methane lifetime, leading to a strengthened lifetime feedback that amplifies the methane concentration.

In the MESM, methane lifetime is not a prescribed parameter, but instead, is a property that emerges from the model chemistry. The MESM contains a gas-phase atmospheric chemistry component, which includes interactions between tropospheric gases (O$_3$-HOx-NOx-CO-CH$_4$-CO$_2$) (Crutzen and Zimmermann, 1991). This allows the MESM to simulate the complex chemical reaction sequence following methane oxidation, as well as, changes in the methane lifetime feedback to OH concentrations. For our purposes, the MESM only considers the tropospheric OH sink (it does not model the methane sink to chlorine, soils, and stratosphere).

Because it would be too complicated to insert the full set of MESM chemical reactions into the FaIR model, we must find a simpler, intuitive way of adjusting the FaIR methane lifetime. Further, our modification aims to maintain the box model representation (Eq. 4.1) to preserve the reduce-complexity structure.

Our approach solves for the methane lifetime in the FaIR budget equation (Eq. 4.1) by providing all of the other known quantities of the equation with MESM data. That is to say, we use the MESM concentrations data (C_t), and emissions data (converted to molar mixing ratios; δC_t) to solve for the methane lifetime, τ, at each time-step. In essence, this recalculates the methane lifetime required to achieve the observed change in methane concentration over the historical period and future projections produced by the MESM. We do this for each of the 49 MESM ensemble members.

Figure 4.7 shows the resulting time-series for the methane lifetime. The jagged shape reflects major changes in the historic methane budget, as the lifetime responds to changes in emissions. Our preindustrial estimates for methane's lifetime range higher than the original FaIR model assumption, averaging 9.8 $\pm$ 0.2 years before the late 1970s (Figure 4.7). The 1980s and early 1990s are marked by large fluctuations and peaks in methane's lifetime following volcanic events such as the eruptions of Mt. St. Helens (1980), El Chichón (1982), and Pinatubo (1991). During this period, methane's OH sink weakened due to feedbacks from strong stratospheric aerosol-induced cooling and reduced humidity, driving OH concentrations down (John et al., 2012).

The 1980s to 2000s show a decreasing trend in methane lifetime in the MESM (Figure 4.7), agreeing with the findings of Arora et al. (2018). Interestingly, this trend occurs simultaneously with the "plateau" period where methane concentrations flattened out before continuing an upward climb in the mid-2000s. While still under speculation, reconstructions link the concentration plateau to a changing methane sink, in combination with stagnating emissions from oil, natural gas, and coal (Schaefer et al., 2016). Our analysis indicates that a change in the hydroxyl radical sink and chemical feedbacks of the MESM may have contributed to the "plateau" period. As a final check, our present-day (for the year 2000) methane lifetime estimate is 9.5 $\pm$ 0.1 years, well within the range of ACCMIP models of 9.7 $\pm$ 1.5 years (Naik et al., 2013) and recent observation-based calculations for 2010, 9.1 $\pm$ 0.9 years (Prather et al., 2012).

Using the MESM future emissions projections, we can also predict how methane lifetime may
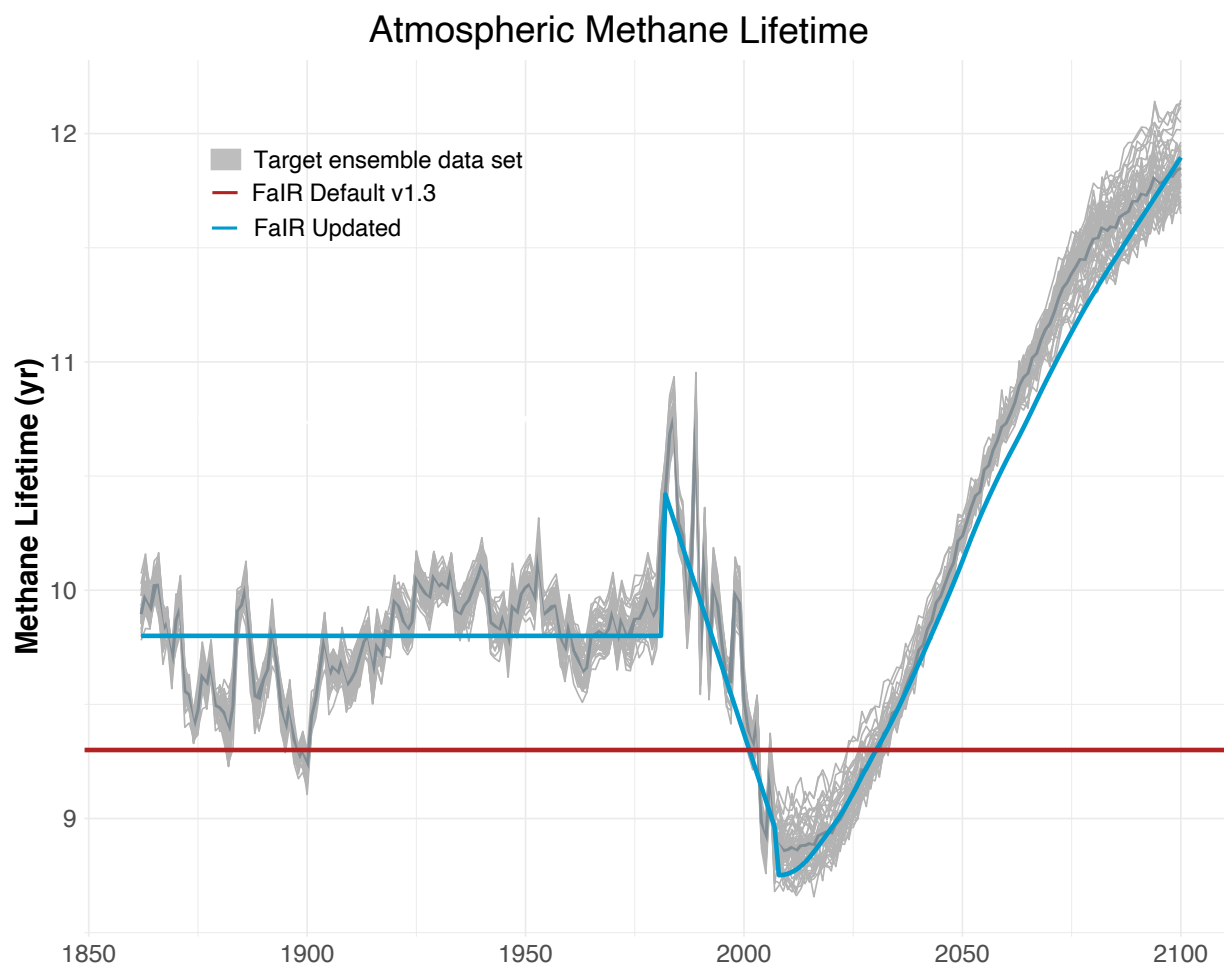
Figure 4.7. A time series of the calculated methane lifetime for the default FaIR model (red), the 49 member ensemble of the MESM (gray), and an example of a fitted model for our modified FaIR lifetime (blue).

evolve over time. The future projections indicate a steep incline in methane lifetime, increasing from just below 9.0 years to nearly 12.8 years by the end of the century. This demonstrates the deficiencies in a constant lifetime assumption and highlights the utility of a fully complex chemistry model for calibration of a reduced-complexity model.

To reiterate, we want an uncomplicated way to predict methane lifetime into the future within the FaIR reduced-complexity model structure. Our approach is to model methane lifetime as a function of atmospheric methane abundance. Shown on a log-log plot (Figure 4.8), methane's calculated lifetime is strongly correlated with the MESM predicted methane concentration for
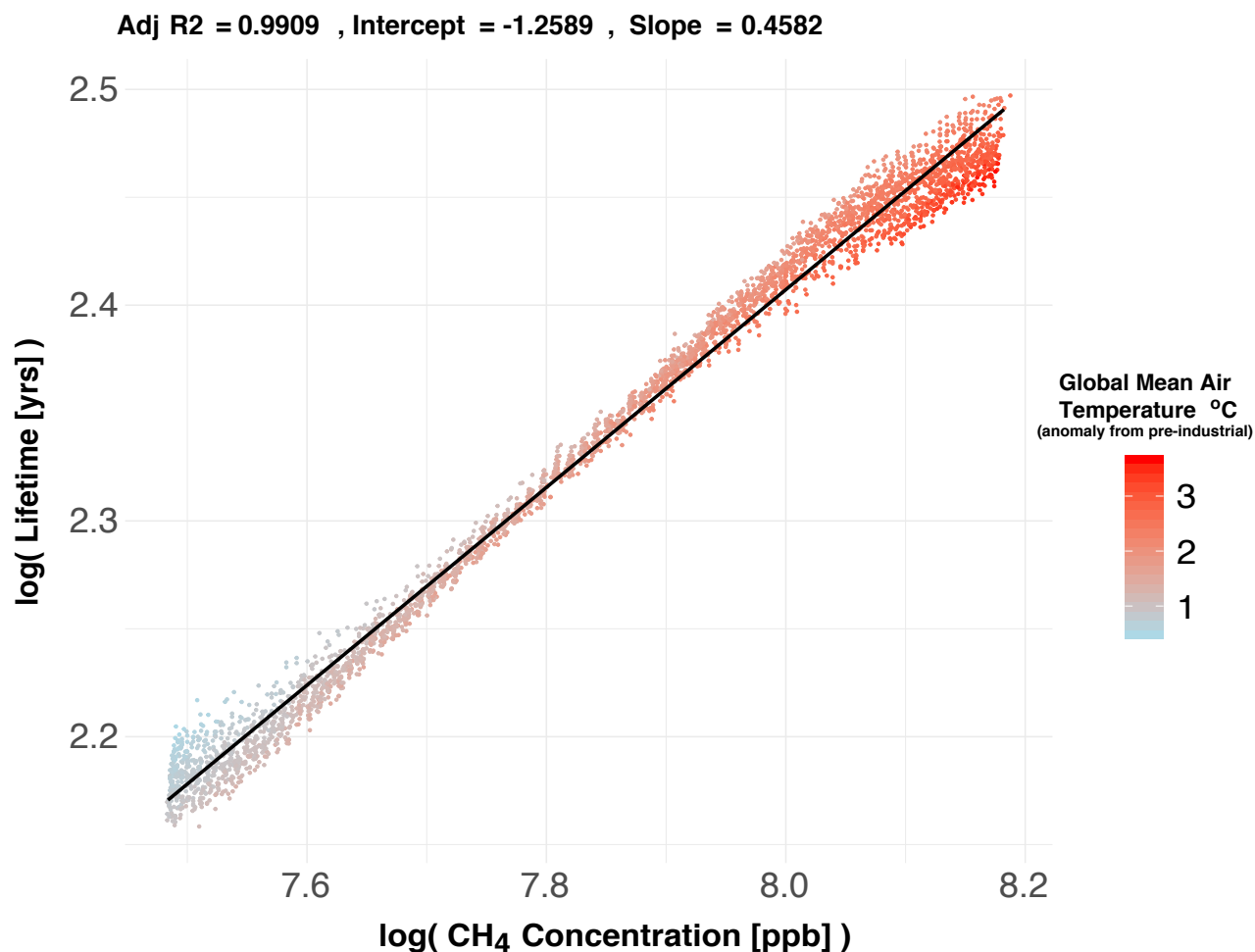
Figure 4.8. Methane lifetime as a function of atmospheric methane concentration within the MESM. Logarithmic scales are shown on both the horizontal and vertical axes. Global mean surface air temperature anomaly from the preindustrial is used for the color scale.

the 2008–2100 period. At higher concentrations, and thus, at higher temperature anomalies, the lifetime of methane increases - an indication of the weakening OH sink. It also appears that for a given concentration in Figure 4.8, the corresponding lifetime is shorter for higher temperatures and vice-versa for lower temperatures, reflecting the reaction rate temperature effect on methane's oxidation.

We aspire to find a simple and intuitive model to reflect the variations in the methane lifetime of Figure 4.7. However, the complex nature of methane's calculated lifetime calls for a

piecewise-defined function, dependent on the model year:

$$\tau(t) = \begin{cases} 9.8 & t \leq 1981 \\ \beta_0 + \beta_1 * t & 1981 \leq t \leq 2008 \\ exp[k_0 + k_1 * log(C_{t-1})] & 2008 \leq t \end{cases} \tag{4.4}$$

The first and largest subdomain, spanning $1861 - 1981$, assumes a constant average value for methane's lifetime of 9.8 years. The second subdomain, which corresponds to the "plateau" in methane concentrations, uses a linear time series regression of the predicted year, t. The third subdomain through 2100, predicts the lifetime as a function of methane's atmospheric burden, C_{t-1}. Introducing the piecewise-defined function (Eq. 4.4) into the FaIR box model (Eq. 4.1), changes the constant lifetime term, τ, into a time-dependent lifetime term, τ_t. It also improves the model by incorporating lifetime feedback effect on the methane sink.

4.4.3 Model-Fitting and Calibration Procedure

Our edits to the methane module in the FaIR v1.3 model adds six new uncertain parameters, $\theta = (m_N, b_N, \beta_0, \beta_1, k_0, k_1)$. The natural emission model linearly dependent on temperature introduces m_N and b_N. And, the methane lifetime calculation introduces β_0 and β_1 for the stabilization period of the early 2000s, as well as, k_0 and k_1 for a self-abundance methane feedback. We use a robust adaptive Metropolis Markov Chain Monte Carlo (MCMC) algorithm within a Bayesian framework to extract parameter estimates that are consistent with projections from the MESM. The intent of the calibration procedure is to produce a simulated time-series for methane concentration in FaIR that best follows the trend in the MESM data. The Bayesian calibration procedure is described in detail in the Appendix C. Here, we provide a brief overview of the model-fitting and calibration of uncertain parameters.

4.4.3.1 Fitting FaIR to the MESM Ensemble Data Sets

The purpose of the calibration is to find a set of parameter values, θ, that optimizes the fit of the FaIR simulated data to an "observation" data set, or target data set, from the MESM.

The MESM time-series output used to constrain FaIR includes annual global means of (1) atmospheric methane concentration, (2) methane lifetime, and (3) natural methane emissions from wetlands over the 1861-2100 period. To account for internal variability not captured by MESM, we assume a small error term in each data set, by several orders of magnitude smaller.

For the calibration purpose, the methane module is isolated from the remainder of the FaIR components, that is to say, we are only simulating methane concentration from Eq. 4.1. Since the natural wetland emissions model requires an exogeneous temperature as an input, we provide the MESM global mean temperature values.

To span the uncertainty caused by several different climate states, we calibrate the FaIR methane parameters to each of the 49 ensemble members from the MESM. Effectively, we are calibrating the uncertain parameters to 49 separate target data sets. This allows us to span the uncertainty in the parameters and understand their sensitivity to the modeled climate state. After the 49 separate calibrations are complete, they are then combined to form a single marginal posterior distribution for each uncertain parameter.

4.4.3.2   Markov Chain Monte Carlo

A powerful sampling procedure in a Bayesian inference is the Markov Chain Monte Carlo (MCMC) method (Metropolis et al., 1953; Hastings, 1970) MCMC simulates random variables by drawing samples from a given prior probability distribution. An initial parameter vector starts a sequence of successive draws dependent on the previous draw (Markov chain), so that the parameter space is fully explored in small step sizes (Gasparini et al., 1997). If a desired acceptance criterion is met, the proposed point represents a sample of the posterior distribution. The chain will conclude by converging around an optimal value.

While there are several variants of the MCMC, we use the Robust Adaptive Metroplis (RAM) algorithm (Vihola, 2012). The RAM allows for a more efficient way to estimate the target distribution by updating the proposal distribution with each sampling. We also account for potential residual autocorrelation in the model error and time-varying heteroskedastic observation errors, by estimating the residuals with a stationary first-order autoregressive process AR(1) model (Ruckert et al., 2017). For additional details, see Appendix C.

The initial guess for the the six new uncertain parameters is based on some previous knowledge, in this case, the preliminary regression fits for natural wetland emissions (Figure 4.6) and methane lifetime (Figure 4.8). We assume a uniform probability density for the prior distributions (see Table 4.1). We use 100,000 iterations and remove 10% of the initial "burn-in" from the starting values of the Markov chain. The burn-in is to ensure that the results are not dependent on the initial conditions. In addition, we "thin" the sample chains to a 1,000 iteration segment to produce more independent values for the analysis. A visual inspection of the thinned chain checks for convergence (See Appendix C, Figure C.1). We also use a statistical check for convergence of each parameter chain using the Heidelberger and Welch diagnostic (Heidelberger and Welch, 1981). The diagnostic calculates a test statistic to accept or reject a null hypothesis that the parameter chain is stabilized. Additional details on checking for convergence are found in Appendix A.

Once the samples are generated, the "best" estimates for the uncertain parameters can be determined through attributes like posterior means and maximum likelihood values (Table 4.1). The posterior distributions can also provide intervals of parameter uncertainty. A strength of the MCMC is the ability to sample the joint probability distribution of all the uncertain parameters, reflecting the correlations and relationships between the uncertain parameters.

Table 4.1. Uncertain methane model parameters and statistical process parameters with their prior distribution assumptions. Maximum likelihood estimates, means, and 95% confidence intervals are shown for the posterior distributions.

Parameter	Symbol	Prior Distribution	Maximum Likelihood	Mean	95% CI
Intercept of Natural Emissions	b_N	Uniform(182, 190)	188.01	188.08	[187.38, 188.77]
Slope of Natural Emissions	m_N	Uniform(20, 29)	23.97	23.94	[23.03, 25.00]
Intercept of Time Series Regression	β_0	Uniform(15, 20)	17.52	17.61	[16.92, 18.31]
Slope of Time Series Regression	β_1	Uniform(-0.1, 0.0)	-0.058	-0.058	[-0.064, -0.053]
Intercept of CH$_4$ Lifetime	k_0	Uniform(-3, 2)	-1.17	-1.20	[-1.35, -1.04]
Slope of CH$_4$ Lifetime	k_1	Uniform(0, 2)	0.44	0.45	[0.43, 0.47]
Standard Deviation Natural Emissions	σ_N	Uniform(0, 5)	3.42	3.45	[3.12, 3.77]
Standard Deviation CH$_4$ Concentration	$\sigma_{[CH_4]}$	Uniform(0, 5)	1.97	1.98	[1.82, 2.15]
Standard Deviation CH$_4$ Lifetime	σ_τ	Uniform(0, 1)	0.145	0.145	[0.133, 0.158]
Autocorrelation Natural Emissions	ρ_N	Uniform(-1, 1)	0.122	0.120	[-0.014, 0.254]
Autocorrelation CH$_4$ Concentration	$\rho_{[CH_4]}$	Uniform(0, 1)	0.990	0.990	[0.973, 0.997]
Autocorrelation CH$_4$ Lifetime	ρ_τ	Uniform(0, 1)	0.625	0.625	[0.530, 0.870]

4.5 Results

Reduced-complexity climate models such as the FaIR model include several parameterized processes and are typically tuned to replicate the results of higher complexity ESMs. When the optimal parameter values are found, the model best matches historical records and emulates future climate projections of more complex model simulations. It is assumed that the optimal parameter estimate would then improve the reduced-complexity model so it can better represent the climate system behavior for a specific set of climate variables and predictions. Here, we analyze the calibrated parameter estimates of the newly developed methane component of the FaIR model, and evaluate the model performance.

4.5.1 Posterior Parameter Distributions

Our alterations to the methane component of the FaIR v1.3 model results in six new uncertain parameters, $\theta = (m_N, b_N, \beta_0, \beta_1, k_0, k_1)$. We take a probabilistic approach using a robust adaptive Markov Chain Monte Carlo to estimate the uncertain parameters jointly, by running a complete sampling of the parameter space while spending a majority of the time in high probability regions. The resulting likelihood function from the calibration incorporates all of the information obtained from the MESM output for methane concentration, lifetime, and natural methane emissions. The measure of the likelihood of a given parameter set, when used in the FaIR model, will yield model output that closely matches the MESM patterns for the same initial inputs.

As discussed in the Methods, we calibrate the uncertain parameters to 49 separate realizations of the MESM, to span a range in climate states. In effect, each calibration set and corresponding parameter estimates then match one instance of the climate state. We combine all of the calibration sets to fully integrate the uncertainty in the parameter estimates that result from the uncertainty in the climate system. Combining the thinned Markov chain results for each of the 49 calibrations, we arrive at a total of 49,000 independent parameter set combinations.

We present histogram and density plots of the parameter distributions in Figure 4.9. The constraints on the parameter distributions are sensitive to the choice in emission scenario and target calibration data sets. Interestingly, most of the parameters exhibit nearly Gaussian shapes, with a symmetric unimodal peak. Each has a clear maximum likelihood estimate that is
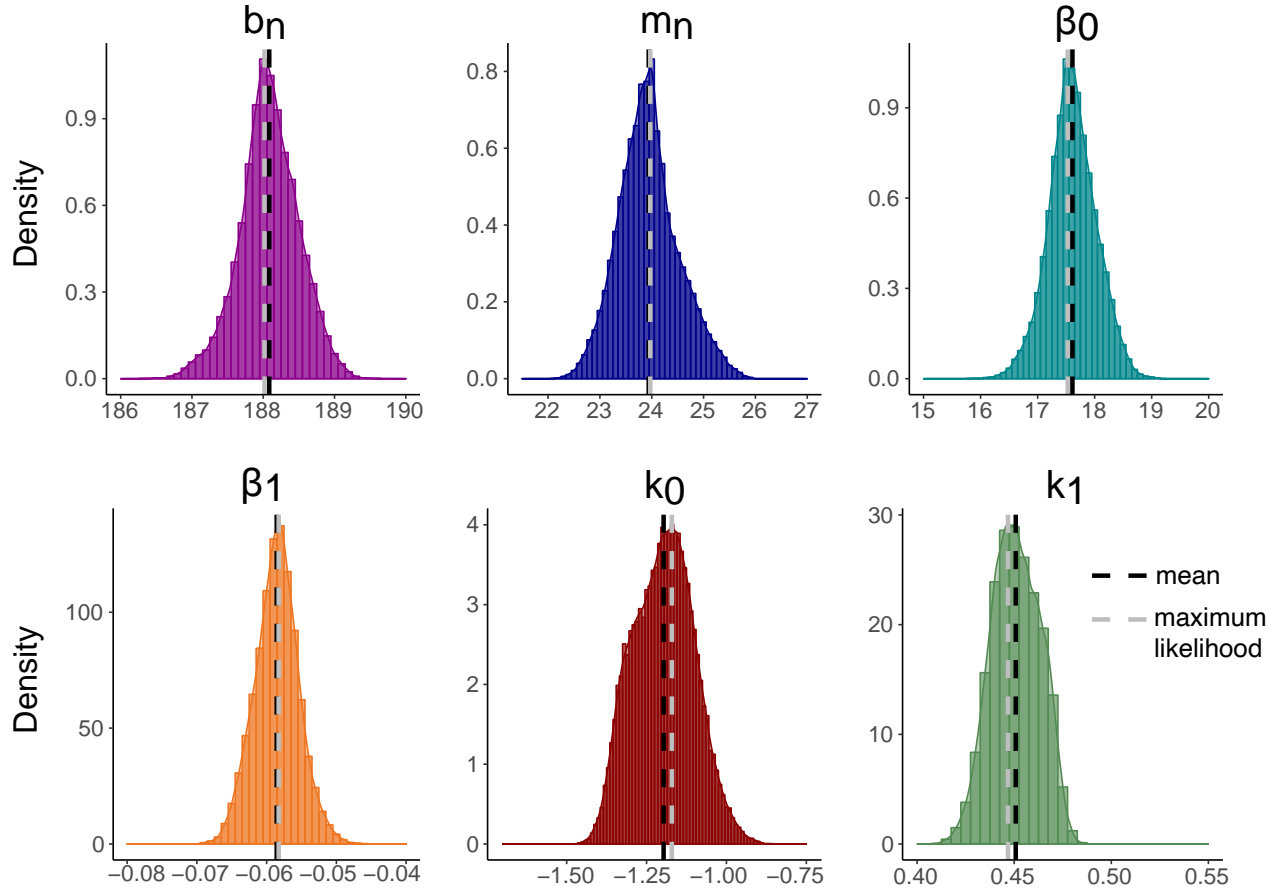
Figure 4.9. Histograms and kernel density functions for the six new parameters in the FaIR methane module. Distribution means and maximum likelihood estimates are represented by black and gray dashed lines.

approximately equal to their mean value. A list of statistical attributes for the final parameter distribution are found in Table 4.1. Of the six parameters, the shapes of the methane lifetime parameters, k_0 and k_1, appear to have a larger skew toward their tails. This suggests that the lifetime parameters are most sensitive to the state of the climate.

4.5.2 Evaluating the New Methane Model Fit

When calibrating and fitting any sort of predictive model to data, it is essential to verify that the newly calibrated model can represent the target data before deploying it for real-world applications. A visual examination of the fitted curve is the first first step to evaluate and assess a model fit. Beyond that, a statistical toolbox of metrics checking for prediction accuracy and spread of the residuals will also provide an assessment of the fit. Common practice is to calculate the Pearson correlation coefficient (r^2) as a standardized measure of the predictive accuracy of a model. The Pearson correlation coefficient establishes how well a predicted set of data from a statistical model matches or correlates to a target data set. We also calculate the root mean squared error (RMSE) to check the average distance between the predicted values and actual target values. Additional figures for assessing the model fit are found in Appendix D.

In this study, the FaIR methane model is calibrated to 49 different realizations of the MESM. It is essential to asses how well the model behaves for each case. From each of the 49 calibration cases and their Markov chains, the maximum likelihood value is estimated for each of the new parameters, θ. We then run a 49 member ensemble of the new methane model, plugging in the maximum likelihood estimates for each parameter specific to the calibration case.

4.5.2.1 Assessment of the Natural Methane Emissions

The first check is to see if the new the natural wetland emissions model in FaIR resembles that of the MESM. In Figure 4.10, the MESM ensemble range and mean value are plotted with the natural emissions model in the updated FaIR. It appears that the predictive model is capturing the pattern of the MESM output. The uncertainty range is small in the historical period and grows into the future projections, just as the MESM uncertainty tends to grow over time. The mean ensemble estimate from FaIR follows the mean ensemble estimate of the MESM. However, the year to year variability is is much greater in the MESM and tends to be smoothed out in the FaIR model. The smoother year to year variability is constrained by the choice in linear relationship to the temperature fluctuations.
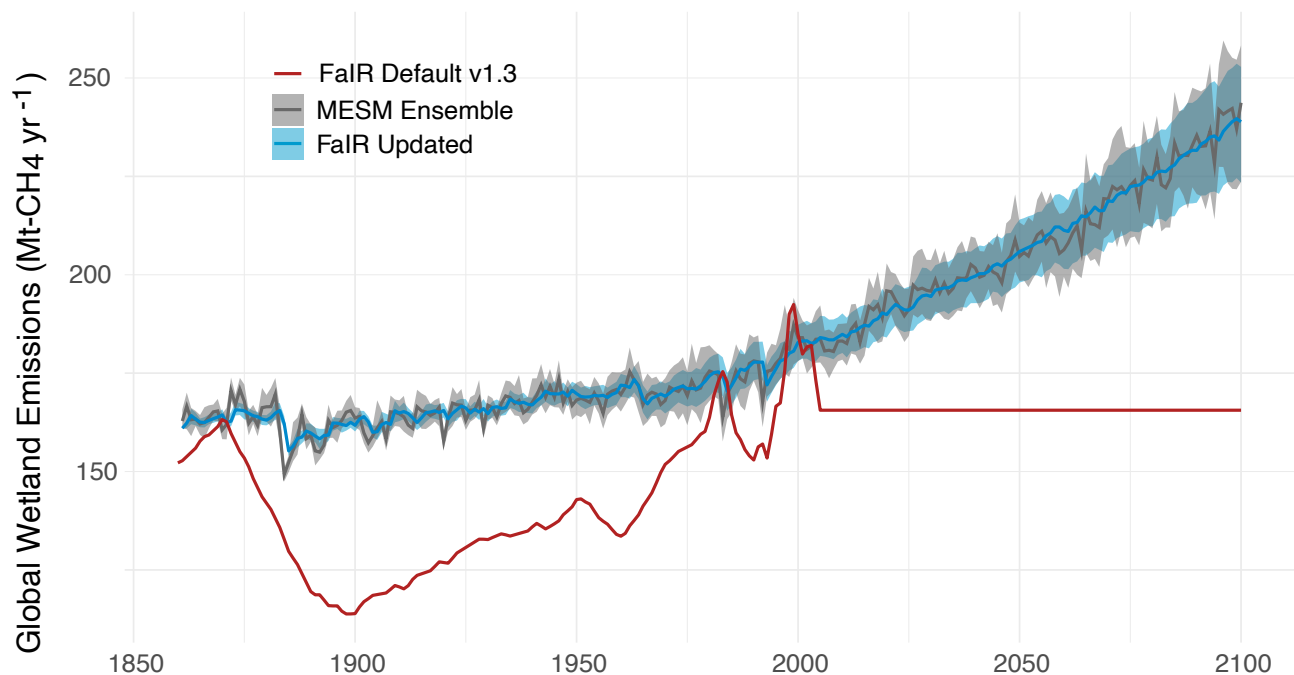
Figure 4.10. Comparisons of global wetland methane emissions. Shown are the default FaIR model (red), the MESM ensemble target data set (gray) and the updated FaIR model using a temperature-driven natural emissions model (blue). Displayed are the full ranges for the ensembles and their mean ensemble estimates.

4.5.2.2   Assessment of the Simulated Methane Concentration

The next check is to see how accurately the updated methane module does at simulating methane concentration. The atmospheric global mean methane concentration extracted from the MESM ensemble data set is the target data set. In Figure 4.11, the updates for each component of methane model are compared against the MESM ensemble and observations. Derived observational data sets of global atmospheric methane concentrations from Mauna Loa and Law Dome ice cores are plotted as a reference for the historical period.

We run the default FaIR v1.3 model, as well as, the updated methane module with a new natural emissions model (with the defaulted constant lifetime), the updated module with a new lifetime calculation (but no new natural emissions), and the fully updated model, containing the natural emissions model and lifetime calculation. Each of the FaIR model versions is run using the same initial conditions, emissions inputs and maximum likelihood estimates for the uncertain
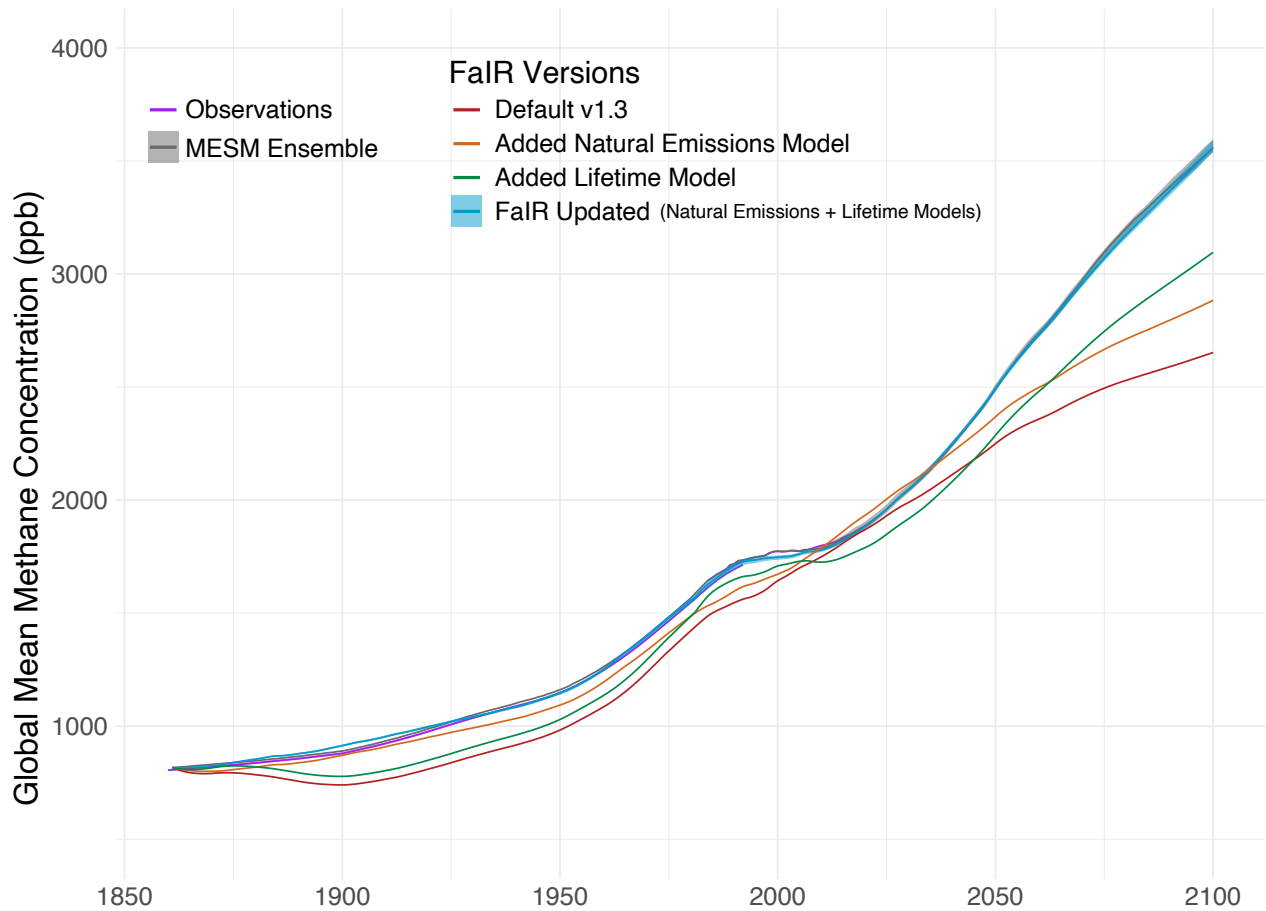
Figure 4.11. Global mean methane concentration simulated by the FaIR default v1.3 model (red) and the methane model updates. Model updates include the natural emissions model alone (orange), concentration-driven lifetime model alone (green), and the two combined to give the fully updated model (light blue). The MESM 49 member ensemble is shown with its mean response (gray). And observations from Mauna Loa and Law Dome are shown (purple).

parameters (parameter estimates found in Table 4.1). The "FaIR Updated" ensemble is the same as that as Figure 4.10, where 49 ensemble members are run with uncertain parameters using maximum likelihood values determined through each of the 49 calibration processes. The only change to the default FaIR v1.3 model is the methane emissions input. All of the FaIR model versions use the Outlook emissions provided by the EPPA model (i.e. the emission scenario used within the calibration process).

Exploring one update at a time allows for the isolation of the independent impacts and combined impacts of including a new natural emissions model and concentration-driven lifetime. First looking at the default FaIR v1.3 (shown in red in Figure 4.11), the default model poorly matches the historical observations. This underestimated concentration from the default model is due to the fact that its concentrations were originally calibrated to match a higher assumed historic anthropogenic methane emissions (i.e. historic RCP scenario) than that used by the CEDS historical emissions scenario. But what is notable is the default model greatly underestimates the projected future methane concentration, falling 903 ppb below the mean projection of the MESM ensemble in 2100. Clearly, the default model for the methane cycle requires an update to better match projections of a higher complexity Earth System Model.

The first update explored was replacing the prescribed external natural methane emissions data set in the default model with a natural wetland emissions model dependent on the global temperature. Replacing only the natural emissions component of the default model improves the concentration projections significantly for the historical period (Figure 4.11). The higher natural methane emissions calculated in the new model raises the total source term of the box model calculation (Eq. 4.1), allowing for higher methane concentrations. This change alone does not sufficiently match future methane projections, a change to the lifetime calculation is the next logical step. However, replacing the constant lifetime assumption in the default model with a dynamic methane lifetime dependent on atmospheric burden, alone, also does not fully capture the methane projections. The profile and shape of the curve (green curve in Figure 4.11) resemble that of the MESM, but the magnitude of the concentration still falls below the target data set for the entirety of the simulation.

Combining both the new natural emissions model and lifetime calculation into the FaIR methane module provides the best representation of the MESM target data set. Visual inspection indicates that the updated FaIR model accurately captures the historical observations and future projection of methane from the MESM. The ensemble of FaIR closely matches the ensemble uncertainty of the MESM. There are only two periods in which the updated model shows a deviation from the target data set; in the early 1900s and 2000s where the deviation reaches up to 25 ppb. This deviation is primarily due to the FaIR lifetime not matching the simulated MESM lifetime. Checking the Pearson correlation coefficient ($r^2 = 0.999$) as a statistical standard, we concluded that the updated FaIR model can accurately predict the methane concentration from the prescribed anthropogenic emissions scenario.

4.5.2.3 Assessment of a Pulse Emission Scenario

The Finite Amplitude Impulse Response Model (FaIR) is designed to compute and represent the temporal evolution of the warming response to a pulse emission. In its development the FaIR v1.3 model was calibrated to reproduce the pulse-response behavior following a CO_2 pulse emission of 100 GtC in present-day climate conditions of several ESMs and EMICs (Joos et al., 2013). Its strength is in its ability to correctly account for the speed and shape in the CO_2 concentration, dependent on the background climate state and pulse size. The model has yet to be explicitly tested in terms of its pulse behavior to other greenhouse gas emissions like methane.

Here, we evaluate the pulse-response behavior of the newly updated methane module to a methane emission pulse of 1 GtC (1336 Mt-CH_4) in modeled year 2006. From Chapter 3, we learn that a 1 GtC pulse provides a good signal-to-noise ratio. We choose 2006 to be the pulse year because the MESM switches to a active atmospheric chemistry model and the FaIR soon switches to a concentration-driven lifetime calculation in 2008. The pulse response is the difference between the perturbation run and the control run, shown in Figure 4.11. Again, we test each additional update to the methane model separately and as a joint update. The results are shown in Figure 4.10. All of the model versions tend to rise to a peak concentration of about 445 ppb following the impulse emission, nearly 30 ppb below that of the target data set from the MESM. While they use the same emissions, the difference in the peak concentration could result from the time-step difference, where the FaIR uses a 1 year time-step and the MESM uses a daily time-step.

The rate at which the peak concentration decays is related to the different representations of the methane lifetime. The default model and the updated FaIR model with only new natural emissions use a constant lifetime of 9.3 years. This relatively short lifetime would mean the sink term of the box model quickly removes the atmospheric burden, this is why the shape of the decay function shows such a large and rapid decay in Figure 4.12. Updating the model to include a lifetime dependent on atmospheric burden significantly improves the profile of the pulse response. The rate of decay mirrors that of the MESM response, but slightly underestimates the concentration by about 11 ppb on average. The underestimate is directly related to the lifetime, we see that the calibrated model also underestimates the methane lifetime through the later half of the century (see Appendix D.2).
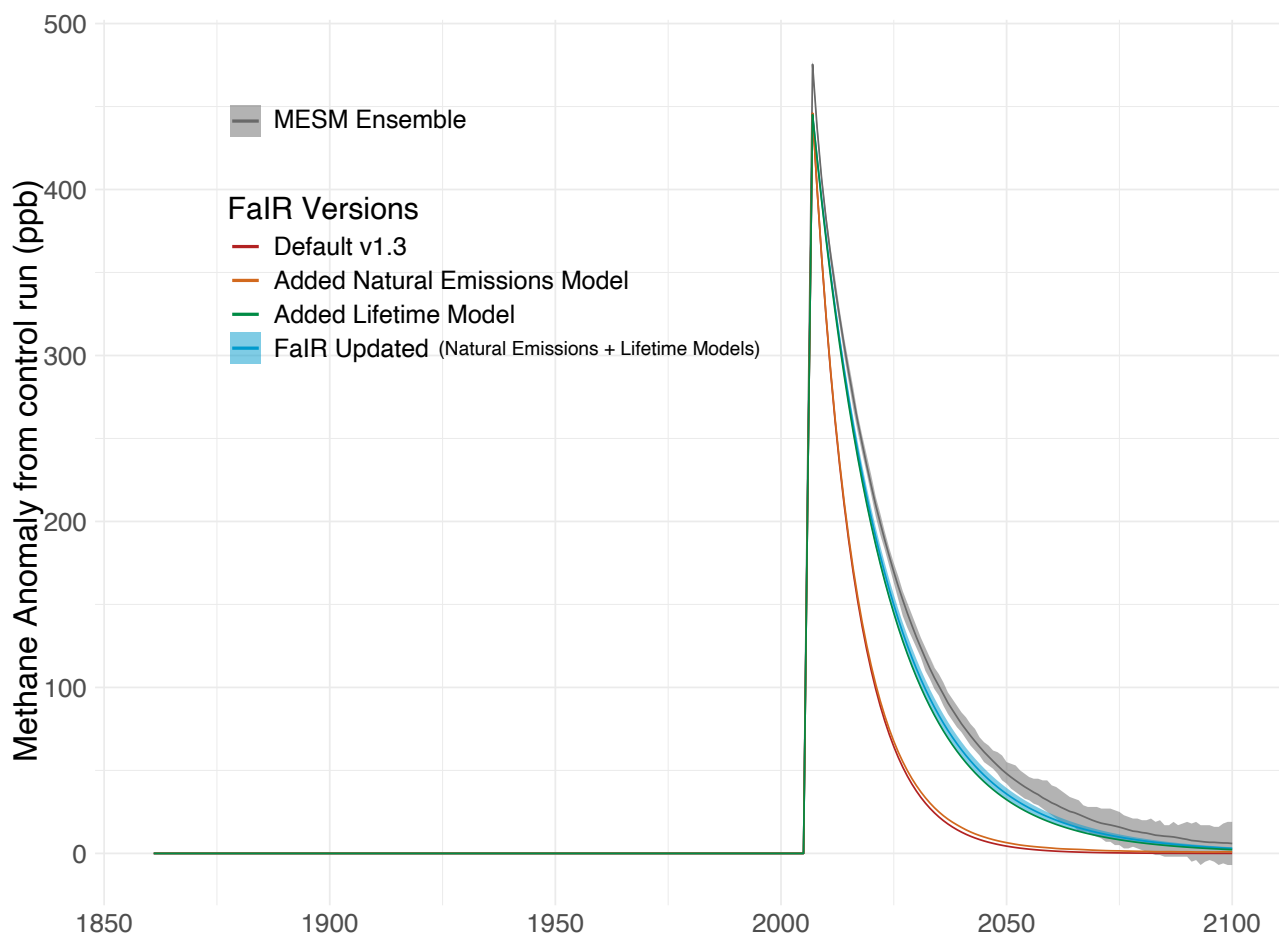
Figure 4.12. Methane concentration anomaly from a control run for a pulse perturbation experiment using the FaIR model. Each FaIR model update is shown. The fully updated model with a new natural emissions and lifetime component is run for a 49 member ensemble (light blue) best calibrated to the 49 member ensemble of the MESM (gray).

4.5.3 Testing the New Fully Coupled FaIR Model

Thus far, we have shown results of the updated methane module isolated from the full FaIR model. Turning on all the components of the FaIR model shows the effect and significance of the methane component changes on the other components. The model updates to the atmospheric methane burden will then change the radiative budget of the model and the global temperature response. Here, we run the FaIR model fully coupled with the maximum likelihood parameter estimates from Table 4.1 for two Representative Concentration Pathways (RCPs).
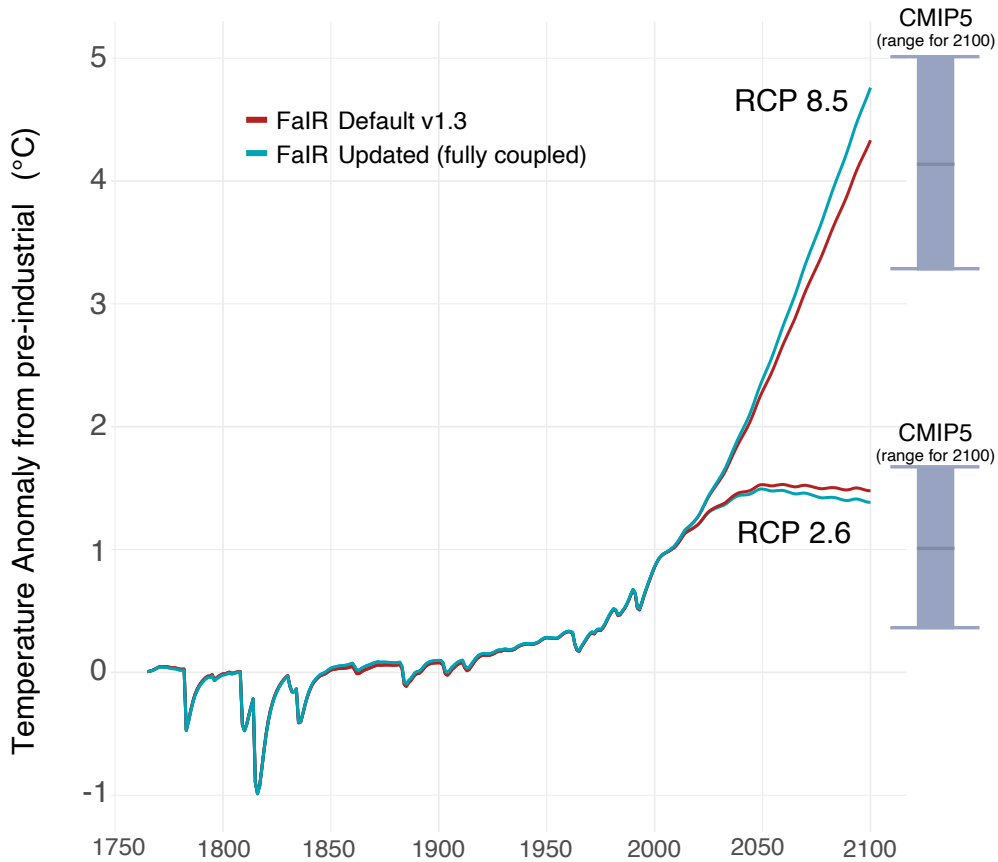
Figure 4.13. The global mean temperature anomaly as a difference from the preindustrial for emission scenarios RCP8.5 and RCP2.6 using the default FaIR v1.3 (red) and the updated FaIR (light blue) with a new natural emissions model and lifetime calculation, and with all model components turned on. Shown on the right side are the CMIP5 ranges for the temperature projection in 2100. CMIP5 data taken from Knutti and Sedláček (2013a).

Running the updated FaIR model to the defaulted future emission scenarios, RCP2.6 and RCP8.5, shows that the change in the methane cycle structure influences the projected temperature anomaly (Figure 4.13). For RCP2.6, the lower emissions of other greenhouse gases reduces the expected temperature anomaly through the end of the century by 0.095 °C. That reduction in temperature then reduces the amount of wetland emissions released from the temperature-driven natural emissions model, so that natural emissions remain relatively steady at 222 Mt-CH_4 per year. Also, such a rapid reduction in emissions and a 47% drop in concentrations reduces the methane lifetime by nearly 24% from 2008 to 2100 (see Appendix D.5). Neither that short of methane lifetime nor that rapid of a decline in concentration has been seen in modern history. Modeling studies suggest that during the Last Glacial Maximum, global methane concentrations dropped about 40% (Valdes et al., 2005) and the lifetime fell to 7.28 years (Kaplan et al., 2006). A change in natural emissions were the primary drivers of prehistoric methane fluctuations.

We next run the FaIR model with RCP 8.5, the emission scenario most realistic to the current anthropogenic emission rate. Running the updated methane module in the FaIR model with all components to the RCP8.5 scenario results in an even higher temperature anomaly by the end of the century (Figure 4.13). The global mean temperature anomaly for 2100 increases by 0.43 °C when switching from the default model to the updated FaIR model. The modeled natural emissions reach nearly 300 Mt-CH_4 per year, a 57% increase from the default model assumption of present-day emissions (see Appendix D.6). Moreover, methane lifetime increase exponentially from today's (2020) 9.0 years to 14.8 years in 2100. This is an indication that the concentration-driven feedback methane's oxidation rate will weaken the OH sink and lead to an extension of lifetime.

4.6 Discussion and Conclusion

We demonstrate that adding methane feedbacks arising from natural wetlands and atmospheric chemical interactions into the FaIR model will greatly improve its projections of methane concentration, reproducing the projections of a EMIC. Our modified version of FaIR introduces a natural wetland methane emissions model with a temperature dependency, reflecting the thermal feedback on methanogenesis within wetland soils. The modified version also now includes a dynamic methane lifetime, which will increase the residence time with increasing atmospheric

abundance of methane. This captures the weakening methane sink as the main oxidant of many trace-gases, OH, is depleted from the high methane abundance.

Adding the feedbacks of the natural ecosystem and the chemical feedbacks of the OH sink can greatly alter the interpretations of the RCP scenarios for policy-relevant temperature targets. Our results from the reduced emission scenario RCP2.6 suggests that a rapid reduction in methane emissions will lead to a climatic response that lowers the emission rate from wetlands and will lead to a concurrent increase in the OH sink of methane. Such an effect through the methane cycle would be beneficial for climate policy targets aiming at a achieving a rapid decline in the global temperature. Whereas the results from the RCP8.5 suggest that a delay in reductions or even an expedited increase methane emissions could lead to an even greater positive feedback response. In this scenario concentrations grow rapidly as a result of an increase in natural emissions and increasing methane lifetime, taking a longer time to remove methane's atmospheric burden. These results indicate that policy makers should be aware of the possible feedbacks and their potential to disrupt or potentially hinder any mitigation they may suggest.

Chapter 5

Including feedbacks in an updated calculation of the social cost of methane

5.1 Abstract

Integrated assessment models (IAMs) are valuable tools that consider the interactions between socioeconomic systems and the climate system. Decision-makers and policy analysts employ IAMs to calculate the marginalized monetary cost of climate damages resulting from an incremental emission of a greenhouse gas. Used within the context of regulating anthropogenic methane emissions, this metric is called the social cost of methane (SC-CH$_4$). Because several IAMs used for social cost estimation contain a simplified model structure that prevents the exogeneous modeling of non-CO$_2$ greenhouse gases, very few estimates of the SC-CH$_4$ exist. For this reason, IAMs should be updated to better represent changes in atmospheric methane to future emissions as seen by more comprehensive Earth System Models. We estimate the first SC-CH$_4$ estimates to include potential feedbacks on the methane cycle. To weigh the value of future benefits and costs, we vary the discount rate by using 2.5%, 3.0%, and 5.0%. Our expected value for the SC-CH$_4$ is \$1,163/t-CH$_4$ using a constant 3.0% discount rate. This represents a 44% increase relative to a mean estimate without feedbacks on the methane cycle.

5.2 Introduction

Developing economically feasible climate policies has become an urgent task because increasing anthropogenic greenhouse gas emissions could lead to climate-driven consequences that threaten humanity and the environment (Xu and Ramanathan, 2017; Pearce, 2003; Tol, 2001). To evaluate climate policies, researchers have developed integrated assessment models (IAMs), to estimate the interactions between the socioeconomic systems and the Earth system (Weyant, 2017). IAMs are important tools for comparing the trade-offs of proposed policies, as well as, optimizing a balance between emission reductions and adaptive approaches to cope with climate impacts (Ferraro et al., 2015; Stern, 2008). IAMs are typically used to answer the question: How much should we be willing to pay to reduce emissions and avert future climate damages (Ranson et al., 2016; Greenstone et al., 2013)? The U.S. Government uses a metric called the "social cost" estimation to value emissions within regulations affecting government agencies and industries (Metcalf and Stock, 2017; Burtraw et al., 2014; Tol, 2005). Social cost estimates are also increasingly cited in state mandated regulations (Danner, 2009).

As CO_2 remains the most prominent greenhouse gas, research has greatly focused on the estimation of the Social Cost of Carbon (SCC), a monetary evaluation of climate change damage associated with an additional unit tonne of CO_2 emissions per year ($\$/tCO_2$). To be computed in a transparent manner and reflect the uncertainty in the existing science, SCC has typically been estimated using an IAM (Tol, 2005). Starting with a socioeconomic scenario for GDP growth and population, greenhouse gas emissions are projected for a baseline scenario (National Academies, 2017). That baseline scenario is then compared to a pulsed emission trajectory, where an additional unit of CO_2 is then added to the baseline emission in a single year. Taking in the two emission pathways, a reduced-complexity climate model within the IAM will estimate the changes in the climate (atmospheric concentration, temperature, precipitation, sea-level, etc.) for each time-step and pass along that information to an economic damage function (Thompson, 2018; Nordhaus, 2017). Damages encompass losses to human health, natural ecosystems, productivity, and property. Future damages for each incremental year are converted to present value terms by discounting (Anthoff et al., 2009). The difference in monetary damages from the baseline and pulsed trajectories is the marginal damage per additional unit of CO_2 emission (i.e. the SCC estimate).

With multiple modeling components, estimating the SCC possesses many uncertainties; including the emission scenarios, climate system dynamics, damage estimation and the weight we put on the time preference or discount rate (Dietz, 2012). As such, producing sound SCC estimates requires spanning the full range of the IAM parameter space. A formal probabilistic analysis of the relevant uncertainties (through Monte Carlo simulations) will derive probability distributions, including upper and lower bounds to a central tendency for the SCC. The standard approach to decision making under uncertainty utilizes the expected value, assigning subjective weights to probabilities associated with each state of the world (National Academies, 2017; Fankhauser, 1994).

Uncertainties will also arise from model choice, as different models treat economic and climate systems differently. IAMs vary in their computational algorithms, resolution, and design for specific applications (Rose et al., 2017). Although many IAMs exist and appear to be suitable for the computation of the SCC, three prominent ones (FUND, DICE, and PAGE) form the basis of the U.S. Government SCC estimates. They specialize in modeling global aggregate climate damages through simplified representations of the climate system and economy. The key differences in structural representations and parameter calibration efforts have led to a wide range of published SCC estimates, from \$0 to over \$200 per metric ton of CO_2 (in 2007 dollars) (National Academies, 2017).

While the U.S. Government Interagency Working Group (IWG) released updated values of the social cost of CO_2 in 2017 (National Academies, 2017), it did not provide estimates for the social cost of other greenhouse gases that would reflect the best available science and treatment of uncertainty. Although a few estimates of the social cost of methane (SC-CH_4) exist in the literature, we consider four deficiencies in their model structures and assumptions that make them inadequate for policy design and inconsistent with the methodology used for the social cost of CO_2 (Shindell et al., 2017; Marten et al., 2015; Waldhoff et al., 2014; Marten and Newbold, 2012; Hope, 2006). For one, studies have converted methane into CO_2-equivalent values using the global warming potential (GWP), and then multiplied by the SCC to derive the SC-CH_4 (Kumari et al., 2019). This method fails to capture the temporal nature of short-lived greenhouse gases, like methane, on the temperature response. Second, weighting the GWP over time also fails to reflect how damages from climate change are likely to increase faster than the rise of the global mean temperature (Brühl, 1993). Third, several studies of the SC-CH_4 omit important parametric uncertainty analysis, lacking transparency to their central estimates. Finally, others have not been calibrated to observations of the climate record and have not demonstrated that

they can replicate key behavior of comprehensive Earth System Models (National Academies, 2017; Harmsen et al., 2015).

Only a select few studies are consistent with the estimation method of the SCC. The work of Marten et al. (2015) is recognized by the U.S. Government for estimating the SC-CH$_4$ following the standard setup as the SCC estimate; with the three standard IAMs, socioeconomic scenarios, time-horizon, and discount rates (National Academies, 2017). One shortcoming of their study is it uses a one-box atmospheric gas cycle model for methane concentrations. The lifetime of methane is assumed to be constant and no feedbacks are considered for natural emissions or the lifetime. When compared to an analogous projection from the climate model MAGICC (Meinshausen et al., 2011a), the methane concentration from the box model differs by 15% in the first year following a pulse emission and the difference in radiative forcing escalates in the subsequent two decades. The growing difference is largely attributed to the lifetime assumption, whereas MAGICC takes into account the concentrations of other gases and atmospheric temperature on methane lifetime.

Here, we provide an improved SC-CH$_4$ estimate that includes feedbacks to the methane cycle. With a reduced-form model we represent the feedbacks to natural wetland emissions as the global temperature rises and atmospheric chemistry feedbacks that affect methane's lifetime. Our model has been carefully calibrated to reproduce methane concentrations from observations and a more comprehensive Earth System Model of Intermediate Complexity (see Chapter 4).

We insert our improved methane module into the framework of one of the U.S. Government IAMs, FUND (Climate Framework for Uncertainty, Negotiation, and Distribution model) (Anthoff and Tol, 2014). We choose FUND because it is the only U.S. Government IAM that explicitly models non-CO$_2$ gases. PAGE and DICE account for the impact of all other gases through an exogenous radiative forcing projection. Computing the social cost of non-CO$_2$ gases in PAGE and DICE requires a substantial change to the underlying climate models of the IAMs, making the task inconsistent with SCC estimates used by the U.S. Government (National Academies, 2017). By sampling the parameter space of the modified FUND methane module, climate components, and socioeconomic components, we incorporate structural uncertainty into our probability distributions. Including methane feedbacks in our new SC-CH$_4$ estimate improves the work of previous estimation studies and begins to fill the gap in the social cost estimates consistent with the methodology of the SCC.

5.3 Methods

We calculate the SC-CH$_4$ using an integrated assessment model that can model the marginal monetized climate damages to a incremental increase in methane emissions. Spanning the parameter space of the uncertain variables, we present a new probability distribution for the SC-CH$_4$ that incorporates feedbacks to the methane cycle. In this section, we describe the integrated assessment model structure of the FUND (Climate Framework for Uncertainty, Negotiation, and Distribution) (Anthoff and Tol, 2014) and the model modifications to include feedback mechanisms in the computation of atmospheric methane. We follow this with an explanation of the social cost of methane calculation and the related uncertainty analysis.

5.3.1 Description of FUND

To calculate the social cost of methane, our study uses version 3.9 of the Climate Framework for Uncertainty, Negotiation, and Distribution (FUND) (Anthoff and Tol, 2014). As an integrated assessment model, FUND adopts simplified representations of socioeconomic components, climate dynamics, and impact analysis. Compared to other IAMs used by the U.S. Government for decision making, it differs in its more detailed depiction of sectoral and regional economic impacts, as well as, its endogenous greenhouse gas calculations. Here, we discuss the major components of the FUND model.

The FUND model runs on yearly time-steps, from 1950 to 3000. It initiates with assumptions of population, energy use, and emission intensity for 16 major regions of the world. Climate-induced environmental and societal impacts perturb models of population and economic growth. Climate change impacts relating heat stress, disease, and storm damage increases the modelled population mortality rate. And, sea level rise induces a change in regional population through migration. Other impact categories apply to ecosystems, biodiversity and the benefits of the landscape to society, where increasing global temperature principally plays a role in loss rate. Through simplified equations, losses extend further to forestry and agricultural production, water resources, and loss of dryland and wetland area to rising seas. All impacts are eventually monetized and aggregated per region. Monetary impacts are larger if the climate conditions move further away from a defined optimum climate.

Besides simulating climate damages, FUND allows for the opportunities of adaptation and mitigation. For example, the agricultural sector can speed up its adaption to counteract the estimated damage resulting from regional temperature change. Socioeconomic regions can also reduce their energy use and CO_2 emissions through a policy intervention. The emission reductions could then equate to a monetary cost or savings over time. However, emission reductions are limited to changes in energy use and technologies, since emissions from land use change and deforestation are exogenous and cannot be mitigated.

Meant to illustrate the various carbon sinks and corresponding timescales of carbon removal from the atmosphere, the FaIR carbon cycle is modeled as a five-box model. To model the carbon sinks, a fraction of annual emissions is allocated to each of the five boxes which contains a unique decay timescale (Hammitt et al., 1992; Maier-Reimer and Hasselmann, 1987). Furthermore, anthropogenic emissions of CO_2 are determined from a Kaya identity (Kaya, 1989), where total emissions are expressed by a product of population, gross domestic product (GDP), and emission and energy intensity of production. Terrestrial biosphere CO_2 emissions are modeled as a function of global mean temperature and remaining stock of potential emissions.

FUND also models changes in atmospheric methane, nitrous oxide, and sulfur hexaflouride (SF_6). CH_4 and N_2O emissions are exogenous, using a single scenario built into FUND based on the IS92a scenario of Leggett et al. (1992), and SF_6 emissions rise linearly with GDP. Natural emissions are not considered. Concentrations are modeled using a linear depletion function (Forster et al., 2007). In this work, we change the concentration calculation for methane, as discussed in the next section.

The climate dynamics model calculates the radiative forcing from the Third IPCC Assessment Report (Ramaswamy et al., 2001)) and accounts for the indirect effect of methane on tropospheric ozone. Further, the radiative forcing causes a change in temperature. Global mean temperature is calibrated to a 3.0 °C rise in equilibrium temperature for a doubling of CO_2, such that the e-folding time for a climate sensitivity of 3.0 °C is 66 years. For impact analysis, regional temperatures are derived by a fixed factor that corresponds to the averaged spatial pattern of 14 GCMs (Mendelsohn et al., 2000), and global mean sea level change is estimated by a sensitivity to global temperature.

5.3.2 New Atmospheric Methane Component

We improve the FUND methane module by introducing a natural wetland emissions component and new methane lifetime calculation. As demonstrated in Chapter 4, the new methane module successfully emulates the results of a higher complexity Earth system model, the MIT Earth System Model (MESM) (Sokolov et al., 2018), for a given emission scenario and reproduces observed methane concentrations.

Run on an annual time-step, the new model calculates the annual methane concentration (in parts per billion; ppb) as a balance between the sources and sinks. Annual global emissions from anthropogenic (A_t) and natural sources (N_t) are converted into an equivalent increase in the atmospheric molar mixing ratio, δC_t (1 ppb = 2.8403 Mt-CH$_4$). The concentration burden, C_{t-1}, is reduced by an exponential decay with a dynamic timescale dependent on the atmospheric concentration, τ_t.

$$C_t = C_{t-1} + \frac{1}{2}(\delta C_{t-1} + \delta C_t) - C_{t-1}\left(1 - \exp\left(\frac{-1}{\tau_t}\right)\right) \tag{5.1}$$

Our approach is improved by modeling natural emissions linearly with global mean surface temperature, and by including a relationship between temperature and rate of wetland soil microbiological activity. The model calibration used the MESM output of global mean temperature output and global mean wetland methane emissions. The linear term for the global wetland methane emissions, N_t, is:

$$N_t = m_N * (T_{t-1}) + b_N \tag{5.2}$$

where N_t is in Mt-CH$_4$ yr^{-1} and T_{t-1} is the previous time-step's global mean temperature. m_N is the slope and b_N is the intercept of the linear function.

The second alteration to the methane module is changing the decay function, so that the methane lifetime parameter takes into account changes in methane abundance to capture the atmospheric chemistry that leads to fluctuations in OH concentration. As the primary loss

mechanism, the tropospheric OH term tends to dominate the uncertainty in methane's lifetime (Prather et al., 2012). We calibrate the methane lifetime parameters to reproduce the observed changes in methane concentration over the historical period and future projections produced by the MESM. The complex nature of methane's calculated lifetime calls for a piecewise-defined function approach. From the model initiation until 1981, a constant lifetime is assumed to be 9.8 yr. The second subdomain, which corresponds to the "plateau" in methane concentrations up until 2008, uses a linear time series regression of the predicted year, t. These two assumptions accurately reproduce historic observed global mean methane concentrations. For present-day and future projections of methane emissions, the lifetime is a function of atmospheric methane concentration. Thus, the new lifetime term (Equation 5.3) improves the model by incorporating feedback effects on the methane sink with increasing concentrations.

$$\tau(t) = \begin{cases} 9.8 & t \leq 1981 \\ \beta_0 + \beta_1 * t & 1981 \leq t \leq 2008 \\ exp[k_0 + k_1 * log(C_{t-1})] & 2008 \leq t \end{cases} \tag{5.3}$$

For additional details on the calibration process and skill of the methane model, see Chapter 4 of this dissertation.

5.3.3 Social Cost of Methane Calculation

The social cost estimate is the monetary measure of the aggregated damage done by a unit-ton greenhouse gas emission in a given year (National Academies, 2017). Conversely, the estimate can also represent the value of damages avoided for a unit reduction in emissions. The social cost is not a stagnant estimate. In principal, it increases over time because future emissions are expected to grow and produce larger incremental damages, through even greater levels of climate change. For our analysis, we estimate the net present value of climate change damages between 2020 and 3000 from an additional unit emission of CH_4 between 2020 and 2029. Our estimate of the social cost of methane (SC-CH_4) improves upon previous work by using a modified version of the FUND model, with a new calculation for atmospheric methane concentration that includes feedback mechanisms.

Two climate trajectories are used for the estimation of the SC-CH$_4$; a baseline trajectory that follows a set emission scenario, and a pulse emission trajectory that demonstrates the perturbation response to one ton of global methane emissions, spread out over 10 years in FUND (Waldhoff et al., 2014). The response in global temperature and sea level result in monetary damages. The difference between the two damage trajectories is the annual marginal climate damages, $D_{t,x}$ (in 2007 U.S. dollars per year), calculated at each of the 16 geographic regions, x, per year, t:

$$D_{t,x} = D_{pulse_{t,x}} - D_{baseline_{t,x}} \tag{5.4}$$

The marginal damages are discounted back to present-day values using a chosen discount rate. The discount rate weights how much future costs or benefits are considered to be less significant than present costs and benefits. This is analogous to the idea that if you become richer over time, extra costs or benefits have less impact on you than when you were poorer.

The discount rate, r, is inherently related to economic growth, g, as demonstrated by the Ramsey formula (Ramsey, 1928),

$$r = \delta + \eta * g \tag{5.5}$$

where δ is the pure time preference rate, η is the elasticity of marginal utility of consumption, and g is the economic growth per capita. As discussed in National Academies (2017), δ reduces future values 0–3% per year, η measures aversion to differences in consumption between individuals today or generations across time, and g reflects the monetary value of all market goods and services over the past few decades.

To compare SC-CH$_4$ estimates cited by the U.S. Government (National Academies, 2017), all of our results assume a constant consumption discount rate, by holding η at zero. Because the discount rate compounds impacts over time, small differences in the selected discount rate can have large impacts on the social cost estimate. For this reason, we explore the SC-CH$_4$ estimated using three suggested discount rates used in the estimation of the SCC, 2.5%, 3.0%, and 5.0% (Marten et al., 2015).

In FUND, the social cost is first estimated per region, SC_x by solving for the discounted sum of the annual marginal damages, $D_{t,x}$, normalized by the pulse emission, ϵ, for all time following the pulse emission:

$$SC_x = \frac{1}{\epsilon} \sum_{t=2020}^{3000} \frac{D_{t,x}}{(1+r)^t} \tag{5.6}$$

The 16 regions in FUND are of the United States, Canada, Western Europe, Japan and South Korea, Australia and New Zealand, Central and Eastern Europe, the Former Soviet Union, the Middle East, Central America, South America, South Asia, Southeast Asia, China and related East Asian countries, North Africa, Sub-Saharan Africa, and the small island nations.

The final social cost estimate, SC, is the aggregate of the 16 regional social cost estimates, SC_x.

$$SC = \sum_{x=1}^{16} SC_x \tag{5.7}$$

To review, we estimate the social cost of methane for a 1 t-CH$_4$ emission pulse spread out over 10 years starting in 2020. The baseline emission trajectory follows the built-in emission scenario, IS92a. Methane concentrations change using our modified concentrations model which includes natural wetland emissions and feedbacks on the methane lifetime. Global and regional temperature, as well as, sea level changes lead to monetized impacts. Climate damages per region are summed through year 3000 using three different constant discount rate assumptions, 2.5%, 3.0%, and 5.0%. The final SC-CH$_4$ estimate sums all regional social cost estimates. We further align our SC-CH$_4$ estimates with U.S. Government social cost of CO$_2$ estimates by expressing the values in 2007 U.S. dollars per ton of methane.

5.3.4 Uncertainty Estimation

Producing sound estimates of SC-CH$_4$ requires spanning the full range of the FUND parameter space. We conduct a formal probabilistic analysis through random-sampling Monte Carlo simulations (Metropolis et al., 1953; Hastings, 1970). The Monte Carlo sampling technique is a classic procedure of repeating random draws from a defined probability distribution of a variable. A sufficient number of draws will result in a posterior distribution that reflects the shape of the prior defined distribution of the random variable.

We perform a Monte Carlo sampling of 10,000 samples on each of the 852 uncertain parameters of the modified FUND model. A selection of the parameters and their distributions are displayed in Appendix E. To include the uncertainty in the selection of the discount rate, we repeat the Monte Carlo sampling for simulations using a constant discounting assumption of 2.5%, 3.0%, and 5.0%. With 10,000 posterior parameter samples per discount rate yields 30,000 unique SC-CH$_4$ estimates.

5.4 Results

5.4.1 New Estimates for the Social Cost of Methane

We calculate the new estimates for the social cost of methane with feedbacks under different discount rate assumptions using version 3.9 of the FUND model. Exploring the parameter space through a Monte Carlo sampling produced 10,000 unique SC-CH$_4$ estimates for each of the constant consumption discount rates (2.5%, 3.0%, and 5.0%). We present our SC-CH$_4$ probability distributions with estimates of the expected value, mean estimate, as well as, the 5% , 50%, and 95% predictive confidence bounds (Table 5.1).

Posterior distributions for our SC-CH$_4$ estimates are shown in Figure 5.1. At a high discount rate of 5.0%, future costs are worth significantly less than present-day costs. This results in a low-range for the SC-CH$_4$, between \$150 and \$1,076 (2007 U.S. dollars per t-CH$_4$), with an expected value of \$408. In comparison, a low discount rate of 2.5% produces a higher expected value of \$1,492 and a distribution with a very long tail that extends to a 95% predictive

Table 5.1. The SC-CH$_4$ estimate for the default model of FUND and the modified version of FUND that includes methane feedbacks. The rows indicate the SC-CH$_4$ estimate under constant consumption discounting (2.5%, 3.0%, and 5.0%). Columns indicate the posterior distribution expected value, percent change of expected value from the updated model to the default model, median, and selected confidence intervals. All units are in 2007 U.S. dollars per ton of methane ($/t-CH$_4$).

| Model | Discount Rate | Expected Value [±% change] | Median | Confidence Interval | | |
				5%	50%	95%
Default FUND	**2.5%**	1074	999	181	998	2288
	3.0%	806	804	182	803	1813
	5.0%	360	370	125	370	793
Updated FUND	**2.5%**	1492 [+39%]	1520	262	1520	3331
	3.0%	1163 [+44%]	1193	253	1193	2624
	5.0%	480 [+33%]	497	150	497	1076
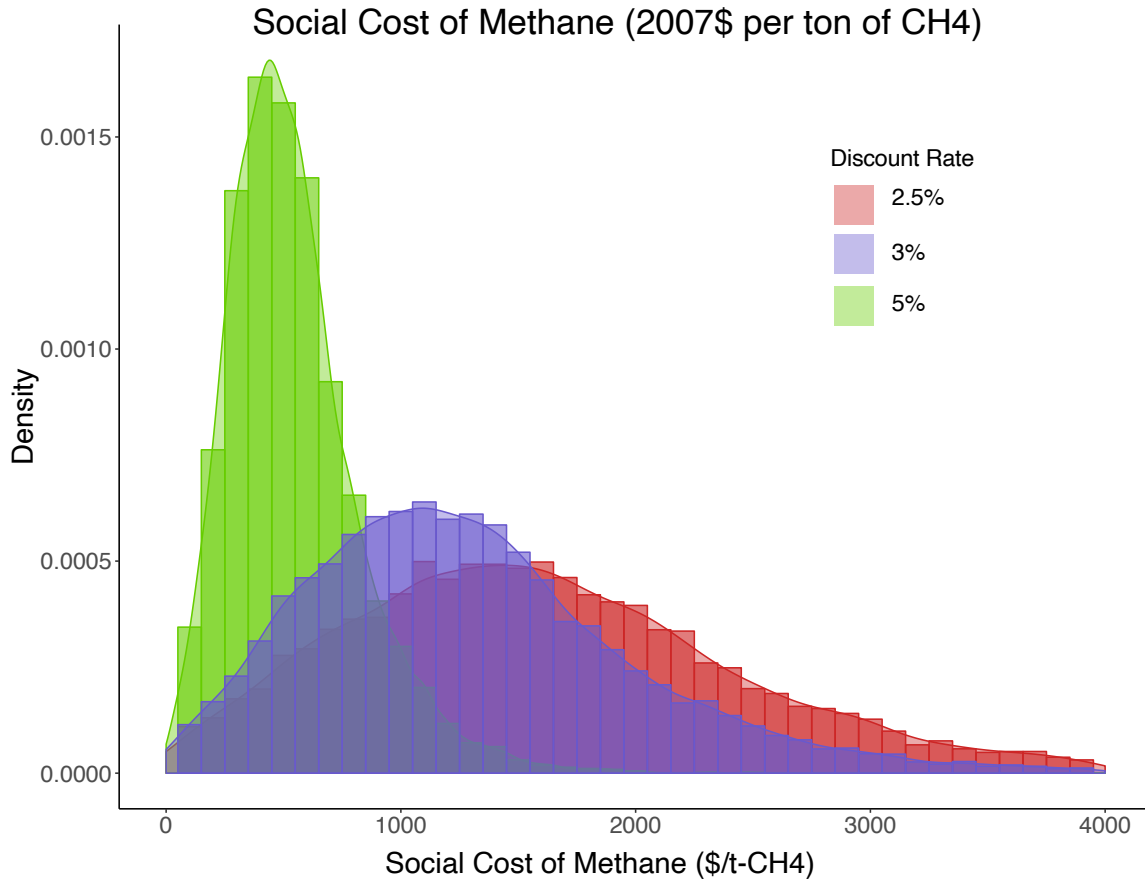
Figure 5.1. Kernel density distributions of the social cost of methane in units of 2007$ per ton of methane emitted, for constant discount rates of 2.5% (red), 3.0% (purple), and 5.0% (green) using the updated FUND model containing methane feedbacks.

confidence interval of \$3,331 per ton of methane. Looking more closely at the 3.0% constant discount rate, the expected value is \$1,163. The distribution for the SC-CH$_4$ also contains a long tail, where 95% of the SC-CH$_4$ estimates fall below \$2,624. However, when methane feedbacks are turned off, the SC-CH$_4$ distribution is shifted to lower values, with a shorter tail and expected value of \$806 (Figure 5.2). Our results indicate that adding methane feedbacks to the FUND climate model increases the expected value of the social cost of methane by 44%. Further, the 95th percentile, chosen to represent potential higher-than-expected impacts of methane, is shifted 45% higher when feedbacks are included in the calculation of SC-CH$_4$. In effect, these results demonstrate that methane feedbacks can lead to extreme levels of climate change and generate even larger future damages.
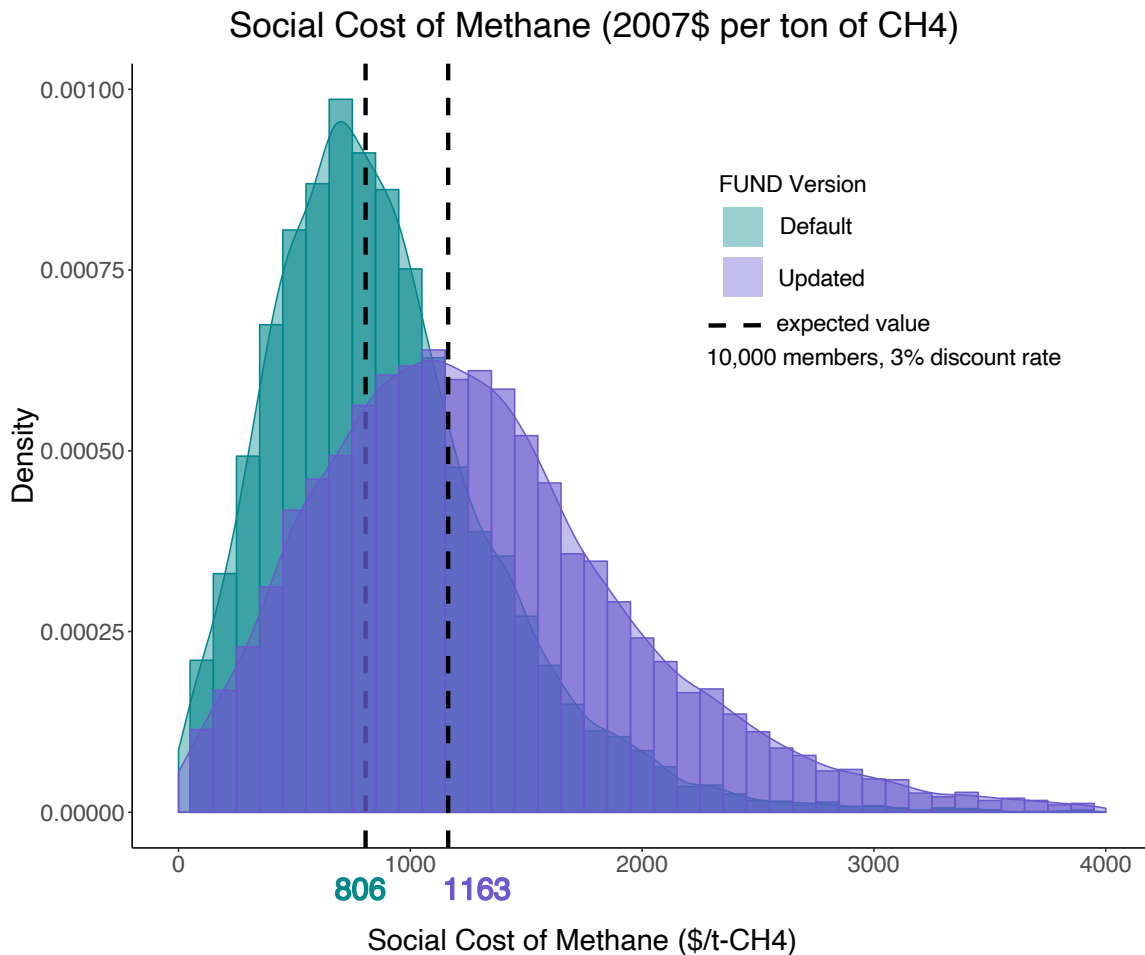
Figure 5.2. A comparison of the SC-CH$_4$ distribution for the default version 3.9 of FUND (teal) and the modified version containing methane feedbacks (purple) under a 3.0% constant discount rate assumption. Dashed lines indicate the mean SC-CH$_4$ estimate for each distribution.

The marginal atmospheric methane concentration and discounted monetary damages (3.0% discount rate) following a unit ton emission pulse of methane are displayed in Figure 5.3. There are a few distinct changes in the methane concentration response after updating the methane cycle in FUND. The peak in atmospheric methane concentration is 14% higher for the updated model because natural emissions from wetlands increase the overall total emissions. A second notable difference is the decay rate of the perturbed concentration anomaly. In the default model without any methane feedbacks, the peak concentration drops 50% over 8 years. Switching the FUND model to include a dynamic methane lifetime dependent on concentration extends the lifetime following a unit increase in emission (See Appendix F, Figure F.2). The overall increased lifetime slows the decay so that half of the perturbed concentration anomaly takes nearly 13 years to be removed from the atmosphere.

The differences between the default model and modified model with feedbacks are apparent when examining the response of the monetized marginal damage profile to a one-ton methane emission pulse (Figure 5.3b). In the default model, annual marginal damages peak around $11, on average, following nearly a decade after the initial pulse emission. In contrast, the model with the updated methane component reaches a $15 maximum damage approximately 50 years following the pulse emission. This is because the damages peak when the temperature response peaks, indicating the increased methane residence time is prolonging the time it takes for the atmosphere to reach a maximum temperature following a pulse.

The damage profile shows a stark amount of uncertainty compared to the atmospheric methane response. For one reason, there are hundreds of uncertain parameters within the damage component of FUND and only six uncertain parameters in the methane module. Many of the randomly selected damage parameters could be combined to form unrealistic responses that may be able to reach a certain numerical threshold, explaining why there are spikes seen in a few of the damage projections. These large spikes could sum up to sizeable cumulative damages, producing the long tails seen in the probability distributions (Figure 5.2).

Another interesting feature of the damage profile is that some of the projections fall into negative damage estimates, where society benefits from increased agricultural production in a higher temperature world (Diaz and Moore, 2017). While this may be the case for a select few projections, the majority indicates current methane emissions will lead to losses from future climate damages that we could pay the price for over 200 years.
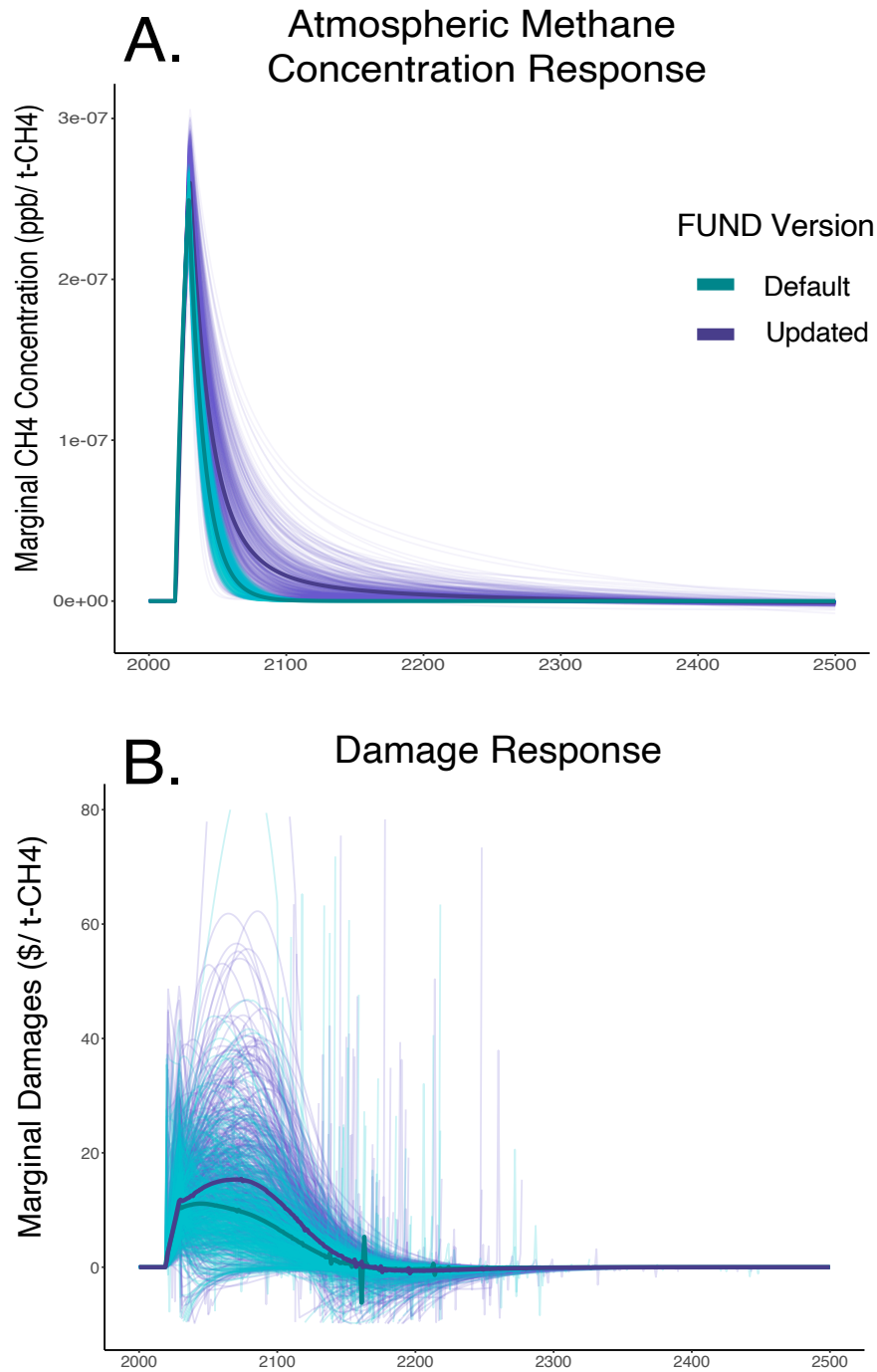
Figure 5.3. Impulse response behavior and uncertainties following a one-ton methane pulse in 2020 using the FUND integrated assessment model. The solid lines indicate the mean response for 500 randomly selected members of the 10,000 model runs. a) Atmospheric methane concentration response for the default FUND version 3.9 (teal) and modified FUND with methane feedbacks (purple). b) Predicted discounted climate damage using a 3.0% constant consumption discount rate.
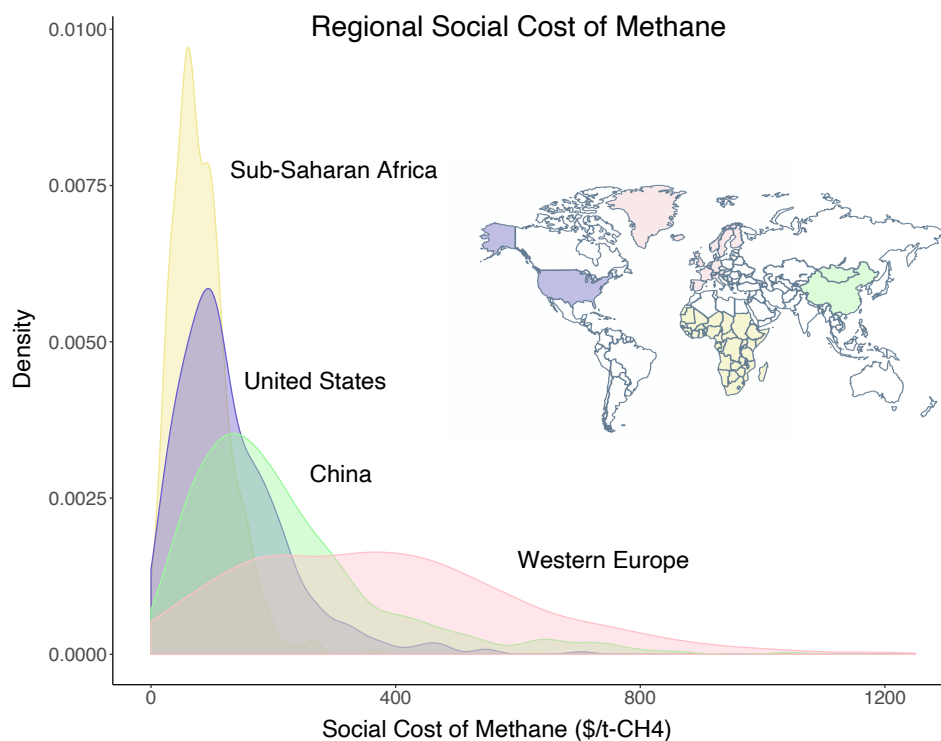
Figure 5.4. Probability distributions of the social cost of methane for four regions in FUND (2007 U.S. dollars per ton of methane emitted). The damages are calculated using a 3.0% constant discount rate.

5.4.2 Regional Damages

Compared to other IAMs used for calculating the social cost of methane, FUND contains a more detailed regional and sectoral impact assessment. FUND predicts climate damages on a regional scale for 16 different regions of the world. Disaggregating the world into regions gives insight into the distribution of impacts and where mitigation options might benefit the most.

Damages resulting from anthropogenic methane emissions will be felt globally, but will vary in intensity from location-to-location. To represent various levels in welfare and disproportionate costs of future climate impacts, we select four regions of interest; Western Europe, China, the United States, and Sub-Saharan Africa (Figure 5.4). All regions are expected to experience some degree of climate damages resulting from methane emissions. Previous analysis suggests the most important parameters that distinguish regional damages are related to cooling energy, migration, and agriculture (Anthoff and Tol, 2013). In poorer regions, health parameters linked to disease become more prevalent.

Of the four regions, Sub-Saharan Africa displays the lowest amount of predicted damages, $81 per ton of methane emitted on average. Annual Sub-Saharan damages remain relatively stable around $0.75 per year, following an emission pulse (See Appendix F, Figure F.3). In contrast, China experiences an initial surge in damages immediately after the methane release, as agricultural impacts are parameterized to escalate more rapidly in large and developing regions (Tol et al., 2012). The greater population and infrastructure face more risk in damages in China than in Sub-Saharan Africa.

We determine that some of the highest-emitting countries of all heat-trapping gases, like the United States and China (Le Quéré et al., 2018), may face the costliest economic impacts. The United States averages $128 per ton of methane emitted, where cooling energy becomes the dominate source of future costs (Anthoff and Tol, 2013).

Finally, Western Europe shows the greatest spread in climate damages, where damages of $175 to $430 are about equally likely to occur. In the FUND model, Western Europe is able to quickly adapt to climate changes in the early half of the century, where changes in climate actually end up resulting in benefits to Western Europe (negative marginal damages in Appendix F, Figure F.3). If Western Europe cannot keep up with adaption, even higher damages can be felt into the future.

5.4.3 Comparison to Other Social Cost of Methane Estimates

Direct comparison with previous estimates is difficult, given the differences in IAM model choice and socioeconomic emission scenarios. To make a fair comparison with other studies, the emission scenario, time horizon, IAM, and choice in discount rate must be the same. The work referenced by the U.S. Government Interagency Working Group (IWG) on Social Cost of Greenhouse Gases, Marten et al. (2015), contains the closest comparison. Their results indicated a mean SC-CH_4 between $980 and $1,400 (2007 dollars per ton CH_4) using FUND at a 3.0% constant discount rate. Albeit, their study used four different emission scenarios that spanned emissions lower and greater than that used within our analysis. Our expected value of $1,163 falls within their estimate, yet, improves upon their work by adding natural methane emissions and a dynamic lifetime to the atmospheric concentration calculation. This in effect, as we have shown, increases the overall social cost of methane.

Because our estimates use the default emission scenario from FUND, it is difficult to directly compare to estimates using alternative emission scenarios. The choice in emission scenario would ultimately affect the total radiative forcing and temperature response of the model. The FUND emission scenario, designed in 1992, is significantly outdated. Further, the five scenarios used for the SCC are also becoming increasingly outdated and replaced in scientific literature (National Academies, 2017). To best conform with current literature and climate analyses, further analysis would benefit from updating the methane emission scenarios to the latest RCP emission scenarios used within the IPCC Fifth Assessment Report (AR5) (IPCC, 2013). The only drawback to this suggested methodology would be it removes the integrated nature of the SC-CH$_4$ estimation, as emissions are prescribed for CO$_2$ rather than being adjusted to changes in socioeconomic variables built into FUND.

5.5 Conclusion

We utilize the FUND model, a prominent IAM, for the calculation of the social cost of methane. Our SC-CH$_4$ is the first to include feedbacks to the natural wetland emission rate and to the methane lifetime. As a potent greenhouse gas, methane will produce a stronger temperature response with feedbacks included. That temperature response would then equate to greater climate damages related to agricultural productivity, human health, changes in energy system costs, and ecosystem destruction. Our expected value for the SC-CH$_4$ is \$1,211/t-CH$_4$ under a constant three percent discount rate. Relative to the expected value without methane feedbacks, our approach to feedbacks leads to a 44% increase in the SC-CH$_4$. In a high impact scenario (95% predictive interval), the SC-CH$_4$ reaches \$2,624/t-CH$_4$. Our estimates for the SC-CH$_4$ are 21 to 28 times greater than their corresponding social cost of carbon dioxide (SCC) estimates. This may suggest that mitigating the risks of global warming from methane emissions could provide additional societal benefits than previously considered.

Chapter 6

Conclusions

Consisting of intricate and interconnected components, the Earth system responds to changes in physical, chemical, and biological processes. Any small perturbation in one component can initiate a counter-response or amplification in another component, each of which may have its own response timescale. While it may be difficult to measure and isolate the changes with observations alone, climate models have been developed to simulate the best available science. Their complexities can vary from the most comprehensive and high-resolution to fundamental formulations and parameterizations. How they simulate changes in the Earth system depends on their structural complexity and their capability to simulate interactions among subsystems.

For this research, we assess the Earth system response to differences in the structural complexity of the methane cycle. The methane cycle is a dynamic system sensitive to changes in emissions coming from human activities and natural ecosystems, as well as, changes to its primary chemical sink. Perturbations of atmospheric methane can initiate a sequential reaction of other heat-trapping atmospheric constituents. As a result, methane can create indirect impacts on the Earth's radiative budget, which can have consequences for temperature-sensitive carbon cycle and biogeochemical processes. All of the subsystem responses are additive, so a modest perturbation in methane can lead to significant changes in several Earth system components. Conversely, a modest methane emission reduction could subsequently weaken the strength of positive feedbacks and substantially reduce global temperatures. Understanding the Earth system response to growing methane perturbations will be useful for emission reduction strategies, especially in the agricultural sector.

Using Earth system models of reduced- and intermediate-complexity, we demonstrate how simplifications of methane dynamics in reduced-complexity models often miss key feedbacks that amplify changes in the climate to future methane concentrations. Because the reduced-complexity models do not include dynamical processes, they can only resemble one state of the climate system. This prohibits their ability to model nonlinearities and feedbacks under different scenarios. In contrast, intermediate-complexity models contain all implicit processes of the state-of-the-art models, albeit, at a lower resolution and through parameterization of climate properties. Their model structure permits the simulation of key modeled feedbacks to the methane cycle. And, their computational-efficiency allows for simulations to detect the sensitivity of feedbacks under several different climate states and scenarios. Through impulse response tests, a intermediate-complexity model can simulate nonlinear responses in the atmospheric chemistry, methane lifetime, and natural ecosystems that result from changing background conditions and emission perturbation sizes. By modifying the structure of the reduced-complexity models to emulate the evolution of methane concentrations and lifetime, reduced-complexity models can better project future changes to methane emissions.

As reduced-complexity models are often used in the context of integrated assessment models, their methane model description and complexity can greatly influence modeled economic impacts. Missing key methane feedbacks will provide poor projections of climate change and likely underestimate future economic damages that result from the changing climate. This explains why updating reduced-complexity models to include methane feedback mechanisms improves their ability to address climate issues.

In summary, this research has contributed to the field of climate modeling by investigating the impact of the methane cycle on the Earth system response within reduced- and intermediate-complexity models. The work described in this dissertation made the following contributions and conclusions:

- Plausible agricultural and dairy emission reductions, especially methane, will help reach established temperature targets.

- Future methane and carbon dioxide emissions are able to influence the Earth system response by leading to potential feedbacks in the carbon cycle, atmospheric chemistry, and biogeochemistry that may further increase atmospheric methane concentrations.

- Incorporating methane feedbacks into an integrated assessment framework increases the costs of future climate damages to projected methane emissions.

6.1 Chapter Insights and Conclusions

The investigation in Chapter 2 exemplifies how non-CO_2 emission mitigation in the agricultural sector can assist in reaching temperature targets set by international policy in a warming world. As the principal contributor to global non-CO_2 emissions, the agricultural sector has the option to move toward low-emission practices that can sustain the increasing demand for food as the global population grows exponentially. Extensive onsite research and life cycle assessments of large industrial-sized and small-scale dairy farms have shown that implementation of appropriate farm management practices can reduce whole-farm greenhouse gas emissions while simultaneously increasing productivity (Veltman et al., 2018; Hristov et al., 2013; Montes et al., 2013).

Our publication (Rolph et al., 2019) is the first to assess how effective recommended dairy farm management practices are at mitigating future warming under plausible future emission reduction pathways. Dairy and agricultural emissions from the FAO database (FAO, 2018) are partitioned into 16 world regions to account for localized differences in production and practices. Our emission scenarios are further informed by life cycle assessments of 150-cow and 1500-cow farms (Veltman et al., 2018; Alan Rotz et al., 2015). Manipulating a business as usual emission scenario developed by the MIT Economic Projection Policy Analysis (EPPA) (Paltsev et al., 2005), we apply emission reductions of CH_4, CO_2, and N_2O across the global agricultural sector and global dairy subsector. Modeling the plausible scenarios in an Earth system model of intermediate complexity, the MIT Earth System Model (MESM) (Sokolov et al., 2018), our results indicate that immediate mitigation from the agricultural sector could, on average, reduce future warming 0.21 °C, with better dairy farm practices contributing to 14% of the total temperature reduction by the end of the century.

Chapter 2 demonstrates the critical role methane plays in projected global warming, Of the total temperature reductions associated with decreasing global agricultural emissions, 88% of the temperature change by the end of the century is due to methane reductions and 12% is from N_2O and CO_2 reductions. While methane emission reductions from the agricultural sector alone cannot stabilize global temperatures to 2 °C above preindustrial levels, it does complement efforts within other sectors to reduce anthropogenic greenhouse emissions. Possible implications of our results could incentivize dairy farmers to switch to low-emission practices and technologies through voluntary action, stringent regulations, or cap-and-trade offset payments (Horowitz and

Gottlieb, 2010). As our results assume a global effort to methane and greenhouse gas reductions, it could further revitalize international climate commitments to agricultural emission reductions (UNFCCC, 2015).

After developing plausible emission reductions from farm-based estimates, we characterize the distinct impact atmospheric methane has on climate model results in Chapter 3. Here, we continue to run and evaluate the MESM intermediate complexity climate model. As with any model, it is necessary to diagnose the MESM model response and evaluate its performance for appropriate applications, including integrated assessments of climate policy implications and emission abatement measures (like that of Chapter 2) (Rolph et al., 2019; Reilly et al., 2012; Gurgel et al., 2011). With well-documented representations of biogeochemistry and atmospheric chemistry (Sokolov et al., 2018; Schlosser et al., 2007; Wang et al., 1998), the MESM reveals time-dependent and temperature-dependent characteristics of the methane and carbon cycles under changing background conditions. In this chapter, we investigate how impulse simulations are able to uncover chemical and physical feedbacks associated with the carbon cycle that would otherwise be obscured in standard emission scenarios. As the system responses are additive, the feedbacks are specific to the climate state and perturbation size. Unable to capture the changes in the climate state to different perturbation sizes, impulse response function (IRF) models are too simplistic and miss key feedbacks. A process-based model like the MESM is necessary to simulate the nonlinearities of the climate system.

Methane pulse emissions of various magnitudes show how increasing abundance of atmospheric methane greatly influences atmospheric chemical interactions and the concentrations of other greenhouse gases and related aerosols. As the primary reactant for methane oxidation, OH is depleted with the overabundance of tropospheric methane and affects the perturbation residence time of methane and ozone. As a result, even the smallest pulse size (equivalent to half the annual anthropogenic methane emissions) takes more than 60 years to be completely oxidized to CO_2. Further, the cumulative increased radiative forcing from all of the perturbed atmospheric species increases the global mean surface air temperature enough to weaken the uptake of the terrestrial and ocean carbon sinks. We also see the effect increased global ozone concentrations have on decreasing CO_2 fixation of vegetation. Lastly, simulated temperature-induced biogeochemical feedbacks lead to increased wetland soil methanogenesis and an additional flux of methane into the atmosphere. As a whole, Chapter 3 demonstrates that the MESM impulse response is nonlinear due to the selection of the methane perturbation size, changing background atmospheric composition, and temperature-dependence of the atmospheric, land, and ocean chemistry.

Linear mathematical formulations that describe the a subsystem response to a infinitesimally small perturbation (i.e. impulse response functions, IRFs) that stem from pulse tests like those explored in Chapter 3, can sometimes be used to substitute a component of a fully complex climate model. One example of a model that incorporates an IRF to portray changes in atmospheric concentrations is the Finite Amplitude Impulse Response (FaIR) model (Smith et al., 2018). As a climate model with a reduced-form structure, FaIR can be tuned to emulate more comprehensive Earth system models (Millar et al., 2017), giving FaIR the upper hand in computational efficiency and transparency to policy-makers. In one example, FaIR has been utilized by the Intergovernmental Panel on Climate Change (IPCC) to warn policy-makers of the mitigation and adaptation needs to limit warming to 1.5 °C above preindustrial temperatures (Rogelj et al., 2018).

While the FaIR model includes the thermal feedback on CO_2 uptake, it omits indirect effects of non-CO_2 gases which lead to climate-carbon feedbacks (as demonstrated in Chapter 3). Within Chapter 4, we modify the FaIR methane IRF to include methane feedbacks arising from natural wetlands and atmospheric chemical interactions. By emulating the MESM, the modified version creates a temperature dependency on natural wetland methane emissions, reflecting the thermal feedback on methanogenesis within wetland soils. It also captures the weakening methane sink as the main oxidant of many trace-gases, OH, is depleted through an interactive methane lifetime with a positive self-abundance feedback.

The new methane IRF of the FaIR model greatly alters the interpretations of the Representative Concentration Pathway (RCP) scenarios for policy-relevant temperature targets. For instance, a rapid reduction in methane emissions seen in RCP2.6 boosts methane oxidation rates and lowers temperature-dependent wetland emissions, thus rapidly declining projected global warming. However, the benefits of reduced methane feedbacks reverses in a high emission world. Increased atmospheric methane drives a positive feedback response leading to a 0.43 °C rise in global temperatures that could potentially disrupt or hinder mitigation efforts suggested by policy makers.

In Chapter 5, we study the affect of including feedbacks in the new methane IRF on the calculation of the social cost of methane (SC-CH_4). As a climate metric cited in emission regulations, the SC-CH_4 presents an cumulative monetary estimate of damages to human life, property, economic productivity, and natural ecosystems from an additional unit CH_4 emission (National Academies, 2017). Very few SC-CH_4 methods exist that are consistent with the

methods directed by the U.S. government for the social cost of CO_2. And to our knowledge, our SC-CH_4 estimates are the first to include feedbacks on the methane lifetime and natural emissions.

We follow the standard approach to estimating the SC-CH_4 in an integrated assessment model, FUND (Anthoff and Tol, 2014). The approach takes two emission pathways, a baseline scenario and a pulsed emission trajectory, and compares the monetized climate change damages between the two to estimate the SC-CH_4. Uncertainties of the integrated climate-socioeconomic framework are addressed by performing an extensive Monte Carlo sampling on uncertain model parameters and interchanging the choice in constant consumption discount rate. By including methane feedbacks in the FUND concentration calculations, we estimate the expected value of the probabilistic SC-CH_4 to be \$1,163 per ton of methane emitted, a 44% increase relative to an expected value estimate without methane feedbacks. In addition, our updated SC-CH_4 is 28 times greater than the corresponding social cost of CO_2. Therefore, it may be more economically beneficial to consider increasing regulations and prices on methane emissions to avoid or mitigate projected future climate damages.

To conclude this dissertation, we link the first and final research chapters for a full circle analysis. Initially, we projected that better farm management practices from the dairy sub-sector and aggregate agricultural sector could potentially reduce 0.9 to 9.6 billion tons of global methane emissions by the end of the century. Using the newly updated SC-CH_4, those agricultural methane reductions could offset 1.1 to 11.6 trillion dollars in future global damages, where 27% of the avoided damages would have resulted from methane feedbacks alone. The conclusions made here testify to the societal benefits of feasible low-emission climate solutions and further illuminate the need to avoid detrimental feedbacks of catastrophic climate change.

Appendix A

MESM Ensemble Parameter Sets

The computational speed of the MIT Earth System Model (MESM) allows for multiple simulations by parameterizing three climate variables; the equilibrium climate sensitivity, effective diffusivity for ocean heat anomalies, and net aerosol forcing strength. We run a Latin Hypercube Sampling on the joint probability distribution from Libardoni et al. (2018b) to produce 50 sets of correlated parameters.
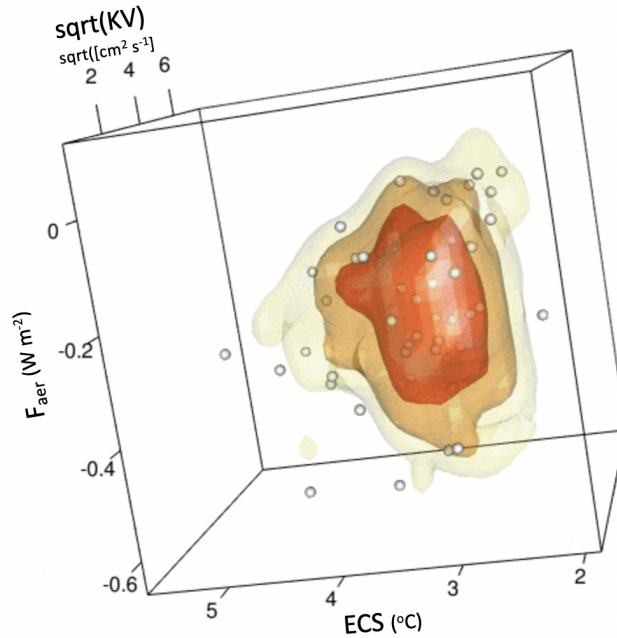
Figure A.1. A 3D image of the joint probability distribution and the 50 parameter sets drawn from a LHS (white spheres).

Table A.1. MESM parameter sets for 50 ensemble members. ECS = Equilibrium Climate Sensitivity (°C), sqrt(KV) = Effective Diffusivity for Ocean Heat Anomalies (sqrt[$cm^2\,s^{-1}$]), and F_{aer} = Net Aerosol Forcing Strength ($W\,m^{-2}$).

Ensemble	sqrt(KV)	ECS	F_{aer}	Ensemble	sqrt(KV)	ECS	F_{aer}
1	0.68	2.94	-0.47	26	1.81	4.94	-0.29
2	0.86	2.93	-0.15	27	1.84	2.67	-0.16
3	0.95	2.76	-0.18	28	1.88	3.02	-0.40
4	1.01	3.12	-0.22	29	1.92	3.19	-0.03
5	1.06	3.36	-0.25	30	1.96	3.62	-0.56
6	1.11	2.42	-0.11	31	2.00	3.08	-0.27
7	1.15	3.01	-0.30	32	2.04	2.93	-0.05
8	1.19	3.24	-0.20	33	2.09	4.52	-0.33
9	1.23	2.48	-0.03	34	2.14	2.92	-0.33
10	1.26	3.53	-0.14	35	2.18	4.11	-0.37
11	1.30	3.08	-0.49	36	2.24	3.40	-0.38
12	1.33	3.78	-0.40	37	2.29	3.17	-0.19
13	1.36	3.69	-0.09	38	2.35	2.65	-0.06
14	1.40	2.73	-0.26	39	2.42	2.87	-0.08
15	1.43	2.65	-0.25	40	2.49	3.52	-0.15
16	1.46	3.33	-0.32	41	2.57	2.21	-0.30
17	1.49	3.21	-0.29	42	2.66	4.08	-0.23
18	1.53	2.90	-0.27	43	2.77	3.11	-0.36
19	1.56	3.02	-0.21	44	2.89	2.52	-0.08
20	1.59	3.31	-0.31	45	3.03	3.41	-0.11
21	1.63	3.64	-0.15	46	3.20	2.80	-0.17
22	1.66	4.38	-0.55	47	3.42	4.26	-0.18
23	1.70	2.81	-0.14	48	3.75	2.46	-0.05
24	1.73	3.10	-0.32	49	4.29	3.08	-0.24
25	1.77	4.03	-0.35	50	5.54	4.75	-0.37
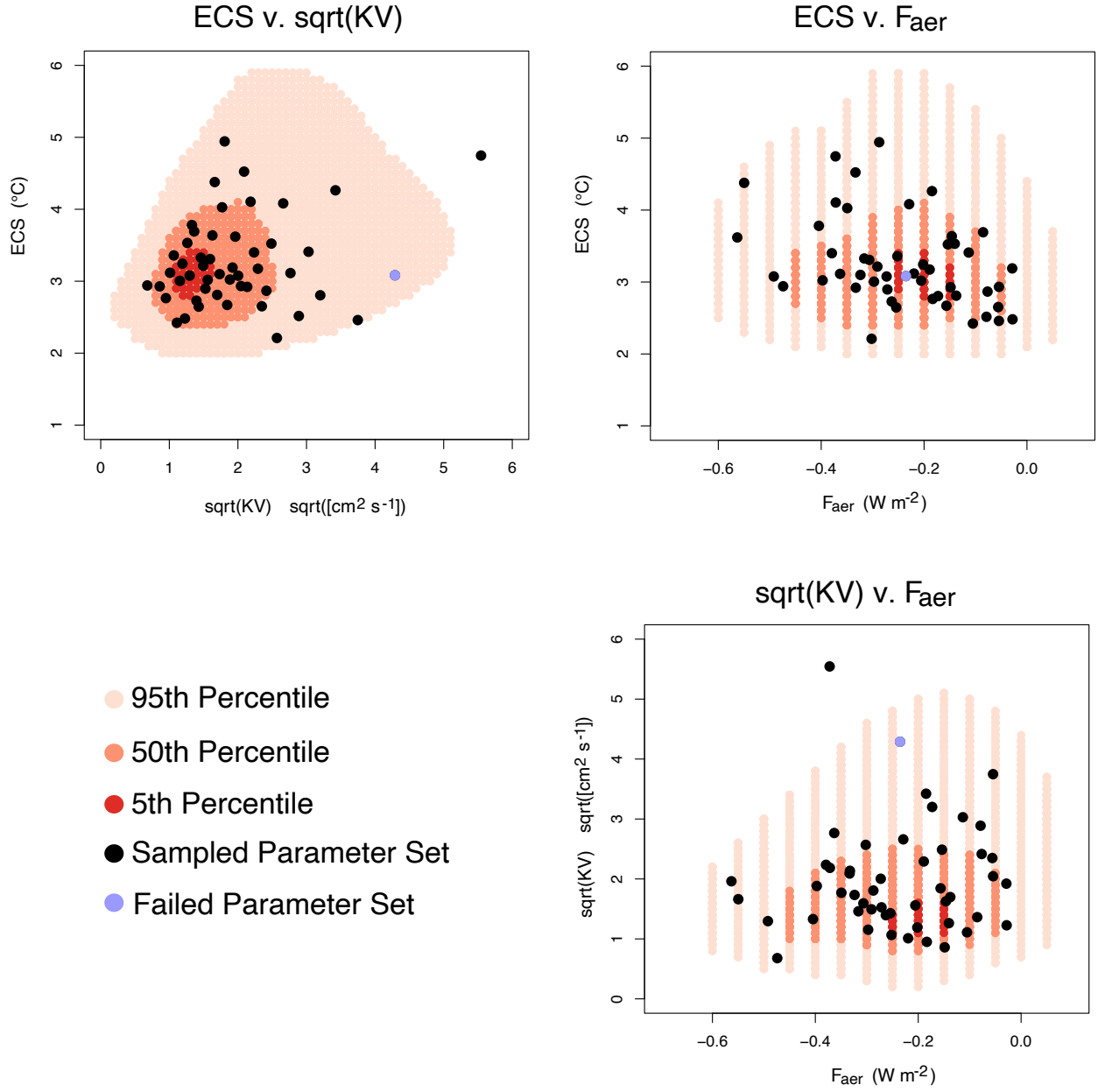
Figure A.2. Two-dimensional joint distributions of the MESM parameters. Red shading indicates the 95th, 50th, and 5th percentiles. Black and blue dots show the values of the 50 member Latin Hypercube Sample.

117
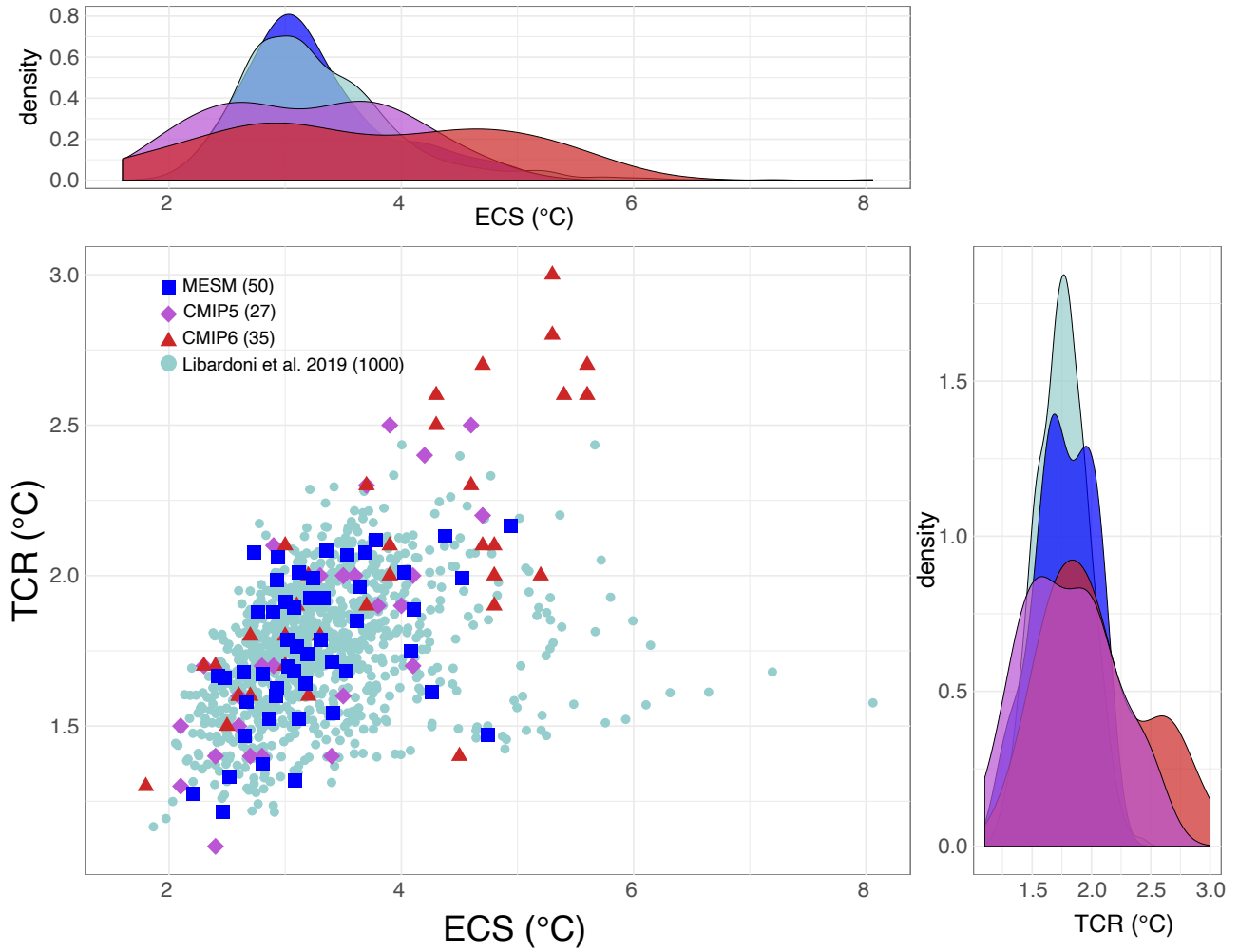
Figure A.3. Scatterplot of the Transient Climate Response (TCR) against the Equilibrium Climate Sensitivity (ECS) for the MESM 50 member ensemble (blue), CMIP5 models (purple), CMIP6 models (red), and 1000 member ensemble of Libardoni et al. (2019) (turquoise). A linear regression is fit to each data set. The legend indicates the number of individual models for each CMIP and number of MESM ensemble members. Also shown are density plots for TCR and ECS. CMIP model information obtained from Meehl et al. (2020).

Appendix B

Impulse Response: Additional Figures

Species Contribution to Total Radiative Forcing
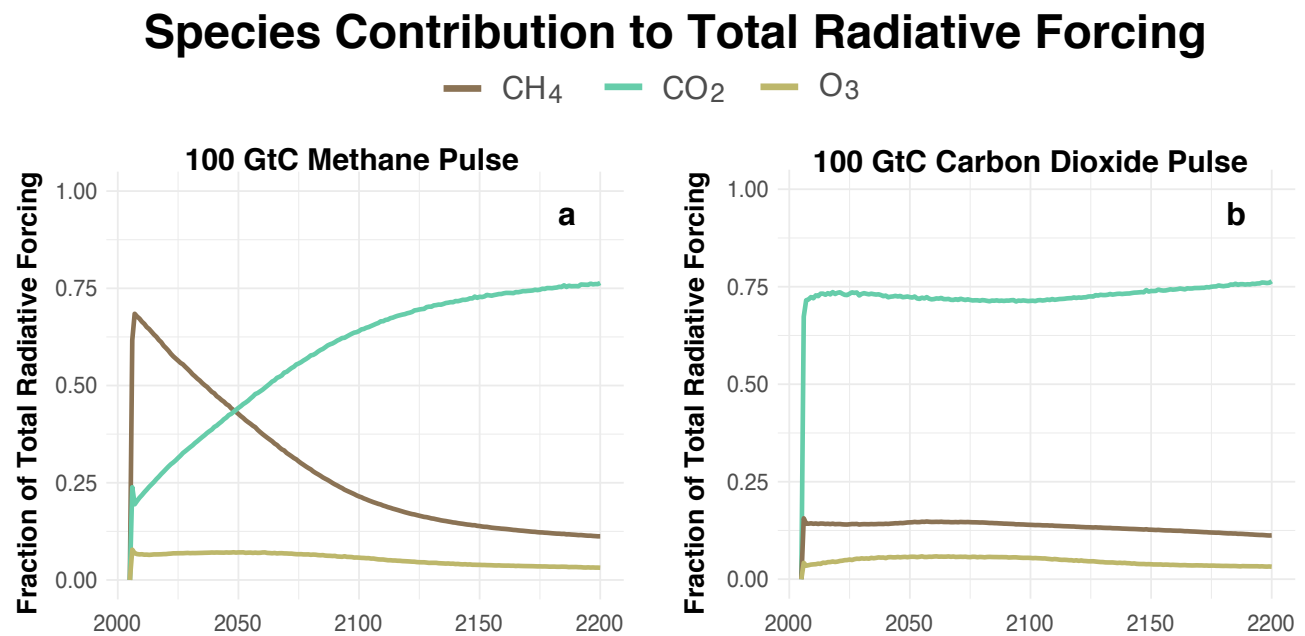
Figure B.1. Greenhouse gas species contribution to the total radiative forcing for CH_4, CO_2, and O_3. Shown are the fractional contributions for the 100 GtC pulse scenarios of a) methane and b) carbon dioxide.

Atmospheric Species Response to Pulse
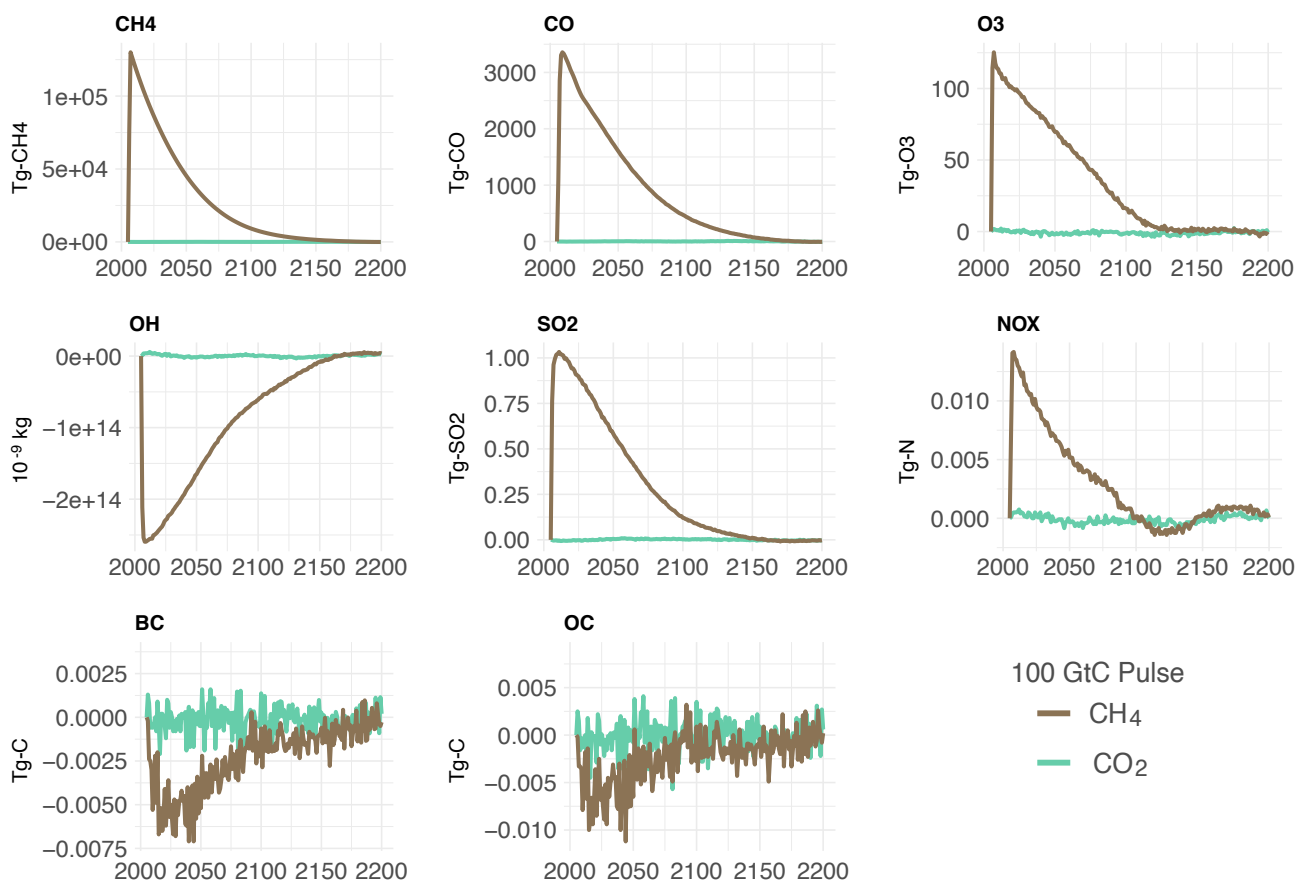
Figure B.2. Atmospheric species response to 100 GtC pulse perturbations of methane and CO_2.
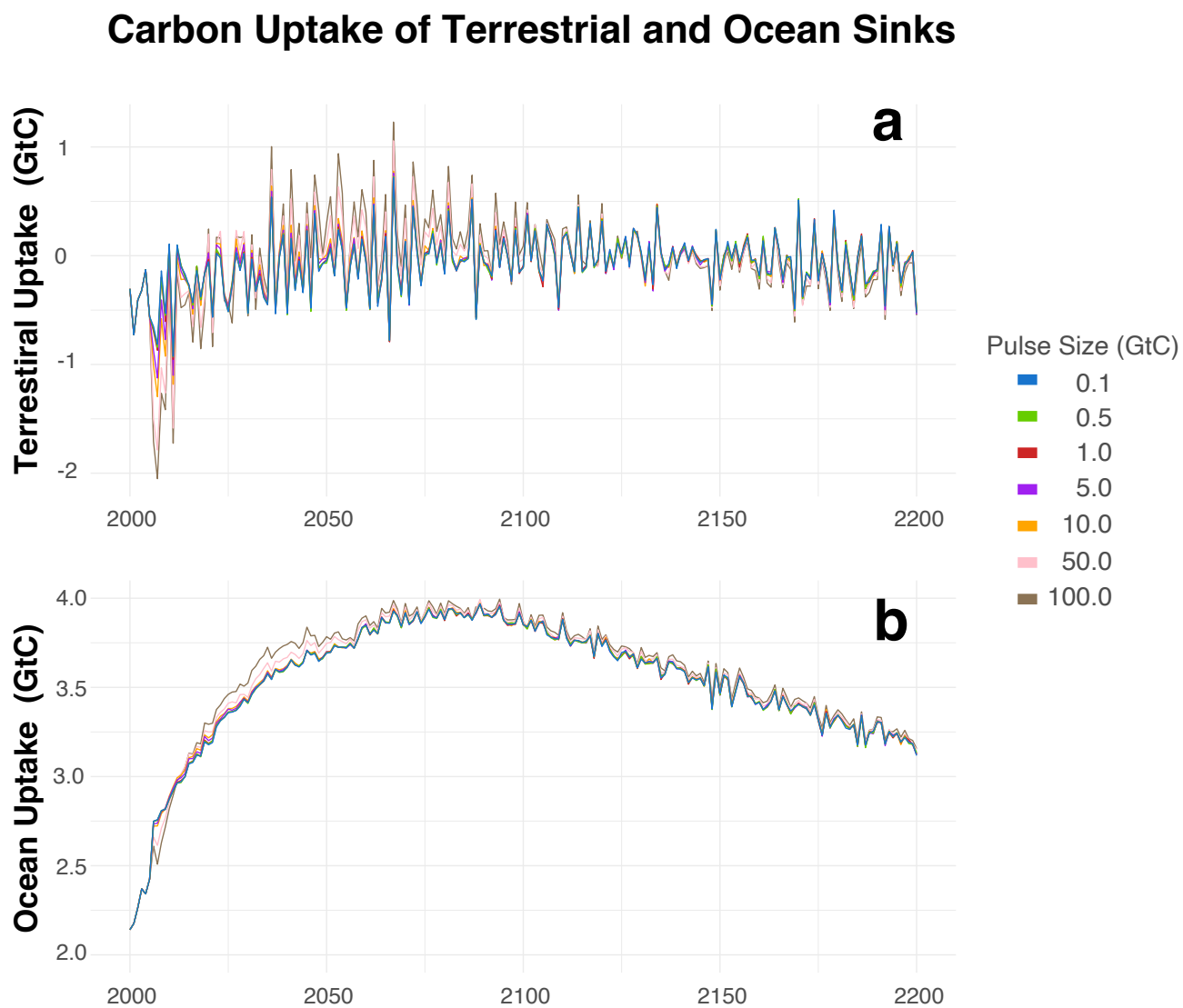
Figure B.3. Net carbon fluxes from the atmosphere to the a) land and b) ocean sinks for the different methane pulse sizes. Take note that this is not a difference from the baseline scenario.

Appendix C

A Bayesian Calibration of the FaIR Model

C.1 Accounting for Error Structures

We employ the robust adaptive Metropolis Markov Chain Monte Carlo (MCMC) algorithm within a Bayesian framework to extract parameter estimates that are consistent with projections from the MIT Earth System Model (MESM). This procedure assumes that the observational data set from the MESM, y, consists of the FaIR model prediction of each observation given the set of parameters, $f(\theta, t)$, plus a residual term between the two time-series, R_t.

$$y_t = f(\theta, t) + R_t \tag{C.1}$$

The data-model residual, R_t, stands as a place to describe the unexplained variations in the observations that are not always well represented in a physical model. We approximate the data-model residual as a combination of the observational error, ϵ_t, and model error, ω_t.

$$R_t = \epsilon_t + \omega_t \tag{C.2}$$

To avoid the possibility of biased parameter estimates and overconfident model projections that can result from too simplistic error structures within the statistical model fitting framework (Ricciuto et al., 2008), we estimate the residuals with a stationary first-order autoregressive process AR(1) model (Zellner and Tiao, 1964). The AR(1) process accounts for potential residual autocorrelation in the model error and time-varying heteroskedastic observation errors, thus better accounting for the uncertainty in the parameter estimates (Ruckert et al., 2017).

In an AR(1) process, the model error will depend on the previous residual term, the autocorrelation coefficient, ρ and a sequence of continuously independent and identically distributed stochastic error terms, or white noise δ_t:

$$\omega_t = \rho * \omega_{t-1} + \delta_t \tag{C.3}$$

where the remaining structural model errors and natural climate variability are captured within δ_t. The initial model error, $\omega_0 \sim N(0, [\sigma_{AR1}^2/1 - \rho^2])$, comes from a multivariate normal distribution, described with a variance σ_{AR1}^2 and correlation structure given by a AR(1) parameter, ρ. We treat ρ and σ_{AR1}^2 as uncertain statistical process parameters estimated during the calibration.

The observation error, ϵ_t, are from the MESM data sets for global mean methane concentration, natural wetland emissions, and methane lifetime. Following that of Ruckert et al. (2017), the observation errors are treated as uncorrelated with a normal distribution of a mean-zero and variance, $\sigma_{\epsilon,t}^2$.

C.2 The Robust Adaptive MCMC Algorithm

To assimilate the MESM data into the FaIR model and estimate the joint posterior distribution of the newly added parameters, we implement a Bayesian inversion technique using a Markov chain Monte Carlo (MCMC) algorithm (Metropolis et al., 1953; Hastings, 1970). The MCMC algorithm generates a representative sample of the joint posterior distribution conditional on the observed data. The most applicable MCMC method is the random walk Metropolis algorithm that uses an acceptance/rejection rule on a sequence (or Markov chain) of candidate points in order to converge on a target distribution (Gasparini et al., 1997).

First, an initial guess is made on the value of the uncertain parameter within a prior distribution based on some previous knowledge. In our procedure, we apply a uniform probability density function for each prior of the uncertain parameters, meaning any value between the cut-off values of the distribution are of equal likelihood. A sample candidate point centered on within its own proposal distribution is drawn from the prior. A list of prior distributions for the uncertain parameters, θ, and statistical process parameters, σ and ρ, are found in Table 4.1. The foundation for our priors are based on the preliminary regression fits for natural wetland emissions (Figure 4.6) and methane lifetime (Figure 4.8).

The candidate point drawn from the prior is either accepted or rejected through the use of Bayes theorem (Bayes and Price, 1763). The theorem states that the probability of observing the parameters given the data, $\pi(\theta|\vec{y})$, is proportional to the likelihood of the data given the parameters, $L(\vec{y}|\theta)$, times the prior probability distribution of the parameters, $\pi(\theta)$.

$$\pi(\theta|\vec{y})) \propto L(\vec{y}|\theta) \cdot \pi(\theta) \tag{C.4}$$

If the probability density π of the candidate point is higher than that of the previous chain element, the candidate point is accepted with the proposed probability density. Otherwise, the proposed candidate is rejected and a new sample is drawn from the previous chain element. The chain will move onto the next sample at a predetermined step size. Samples are then continued to be drawn in sequence where the distribution of the next realization is dependent on the previous distribution. After several iterations, the chain will converge on the "true" value of the uncertain parameter. For every segment of the chain, the likelihood of the data given

proposed parameters must be computed assuming the residuals follow an AR(1). The task can be computationally consuming for long iterations.

Still, the speed of the convergence can be improved by learning about the properties of the target distribution amid the sampling. Replacing the constant proposal distribution matrix with one that learns and adapts to the past allows the algorithm to more efficiently estimate the shape of the target distribution. We use the Robust Adaptive Metropolis (RAM) algorithm to update the proposal distribution such that it captures the shape of the target distribution while attaining a set acceptance rate (Vihola, 2012). If the acceptance probability of the proposal, α_t, is smaller than the desired mean acceptance rate, typically $\alpha^* = 23.4\%$, then the proposal distribution is shrunk. Otherwise the proposal distribution enlarged if the acceptance probability of the proposal distribution is higher than the targeted acceptance rate, α^*. For the RAM sampler, we use the Klara package within the programming environment of Julia (Papamarkou, 2018).

The adaption technique of the RAM algorithm provides several advantages. It is not dependent on the model being calibrated, so the likelihood function and chain algorithm is the same for any number of parameters. Also, the RAM algorithm can handle the realization of posterior multimodal and heavy-tailed target distributions.

C.3 Testing for Convergence of an MCMC Chain

C.3.1 Visual Check for Convergence

To know when a physical model is sufficiently calibrated we must diagnose when the MCMC operation has "converged" onto a posterior distribution; that is to say, the sampling has reached a well-mixed state and the output can be trusted for analysis. Before testing for convergence, we subtract the burn-in period to remove the effects of the chosen starting values. For our application, we remove the first 10% of the 100,000 iteration sampling. We then "thin" the samples from the posterior, saving every 10th sample. This effectively reduces the autocorrelation in the sample while reducing the number of samples to 1,000 saved for the analysis.

One quick way to check for convergence is by plotting a time series of the sampler iterations, i.e. a trace plot. A trace plot is shown for each of our uncertain parameters in the FaIR methane module in Figure C.1. A converged trace plot will show the chain jumping around an averaged value. If the MCMC chain becomes stuck or does not fully explore the full parameter space, the chain has not yet converged and will need to be run for longer iterations.

C.3.2 Heidelberger and Welch Diagnostic

A statistical check for convergence of each parameter chain is the Heidelberger and Welch diagnostic (Heidelberger and Welch, 1981). The diagnostic calculates a test statistic to accept or reject a null hypothesis that the parameter chain is stabilized. The test is split into two parts;

1. Checks if the whole chain comes from a stationary distribution, where the starting state does not matter and will come to a stable state over time. If the test fails, it will remove the first 10% of the chain and test again. If it fails again, the test will repeat until half of the chain is removed.

2. If the first part is passed, then a test is done for the mean of the chain. Half of the width of the 95% confidence interval around the mean must be lower than some tolerance value, $\epsilon = 0.1$, to pass.

Thinned MCMC Chains of Uncertain Parameters
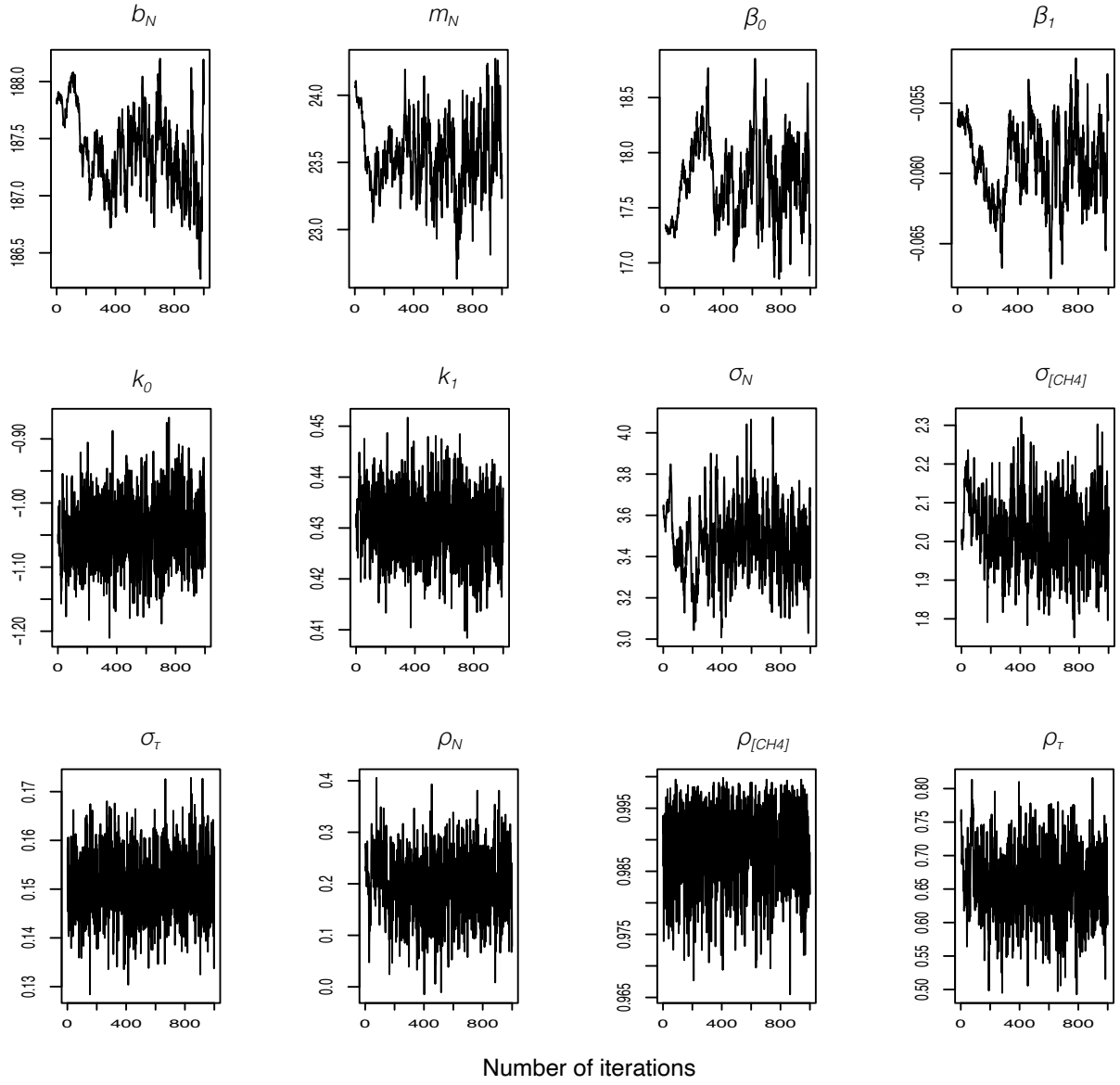
Figure C.1. An initial-burned and thinned chain (1,000 iterations) of the uncertain parameters within the new methane module of FaIR for just one of the 49 member ensemble calibrations. This exemplifies a visual check for a well mixed sampling and convergence of the Markov chain.

C.4 Correlations of Uncertain Parameters

We determine whether the multivariate data contains any statistical correlations through a correlation matrix (Figure C.2). Shown on the matrix is the Pearson correlation coefficient, which measures the linear correlation between two random variables. We find a strong correlation between β_0 and β_1, as well as, k_0 and k_1. This makes sense because these variables are parameters within linear relationships and are expected to be strongly correlated. All other bivariate combinations do not show a correlation.

Another way to visualize the relationships between multivariate data is through parallel coordinate plots. In these plots, each variable contains its own vertical axis. The "web" that connects the several axes is for one realization of the Markov chain. One can tune an interactive graphic to "brush" or highlight a variable set for a range of values. Shown on Figure C.3, we highlight $-1.1 \leq k_0 \leq -1.0$ to visualize a subset of the variable space. Since k_0 and k_1 are strongly negatively correlated ($\rho = -1.00$), we can see how higher values of k_0 link to lower values of k_1.

Correlation Matrix
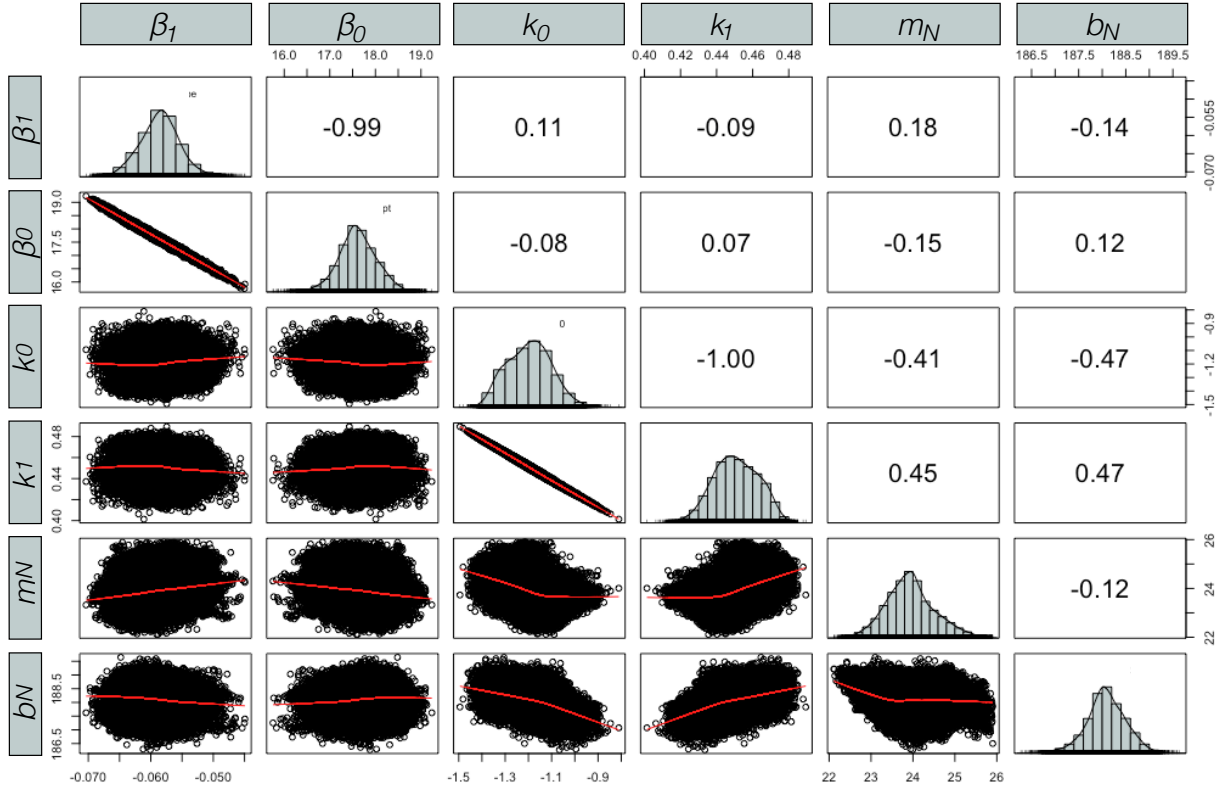
Figure C.2. A table of correlation coefficients for the uncertain parameters in the new methane module of FaIR. Also shown are the bivariate scatter plots with a fitted red line. Distributions of each variable are along the diagonal.
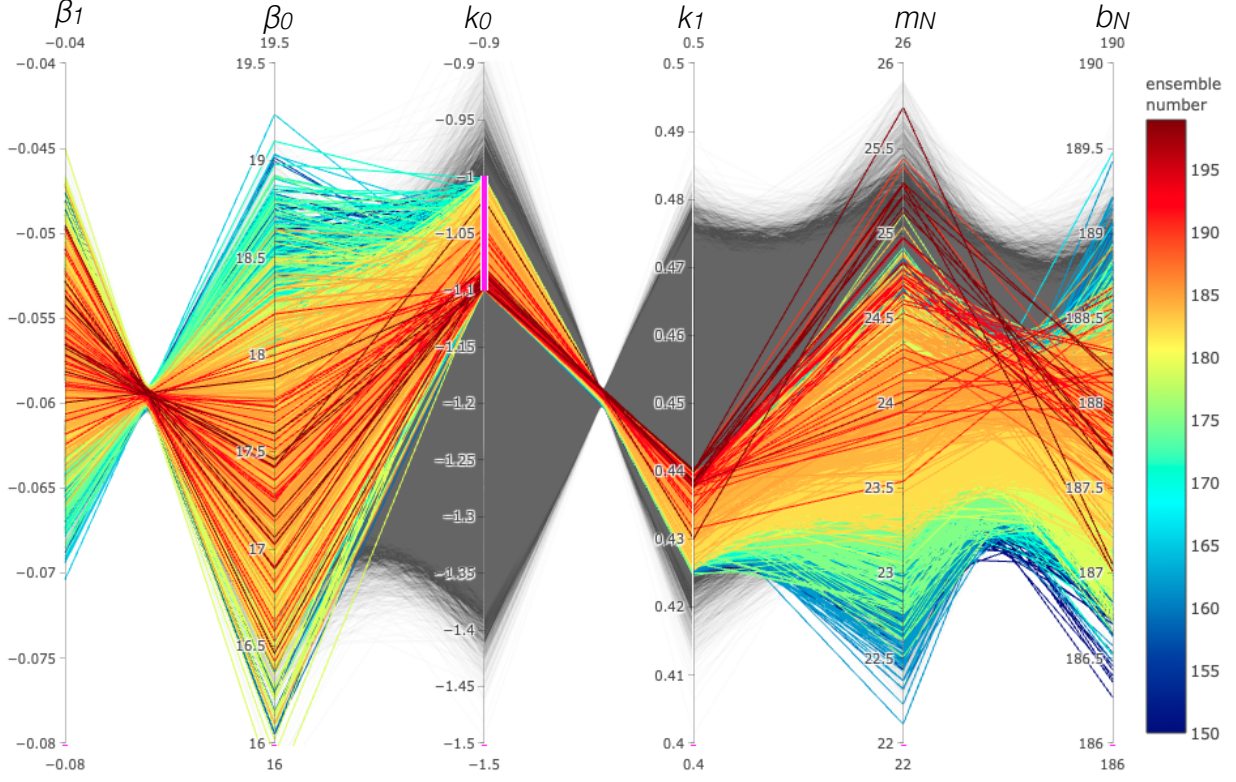
Figure C.3. A parallel coordinates plot for the uncertain parameters within the new methane module of FaIR. Each variable is given its own axis. We "brush" or highlight a selection of k_0 values to bring attention to and isolate a section of the plot. The color gradient indicates the MESM ensemble number that FaIR is calibrated against.

Appendix D

Evaluating the FaIR Model Update: Additional Figures

We use the MIT Earth System Model to model changes in natural methane emissions coming from wetlands. To find a good predictor variable for methane emissions, we evaluate the relationship between natural emissions and precipitation. Figure D.1 shows the mean annual methane emissions from the MESM as a linear function of global mean precipitation.

Figures D.2 and D.3 show the elements of the box model referred to in Eq. 4.1. The FaIR model update is a single run using the maximum likelihood values for the six uncertain parameters added to the methane module (see Table 4.1). The MESM model run is a single run that closely resembles the ensemble mean. Both models are run with the 2016 EPPA Outlook emission scenario for model years 2006 to 2100 (Chen et al., 2017). Prior to 2006, the MESM is run using prescribed concentrations based on derived observations from NASA GISS (Sokolov et al., 2018). The FaIR model (Smith et al., 2018) assumes exogenous anthropogenic emissions from the CEDS emission database (Hoesly et al., 2018) for the historic period.

Additional figures within this Appendix evaluate the FaIR model fit for the RCP2.6 and RCP8.5 scenarios.
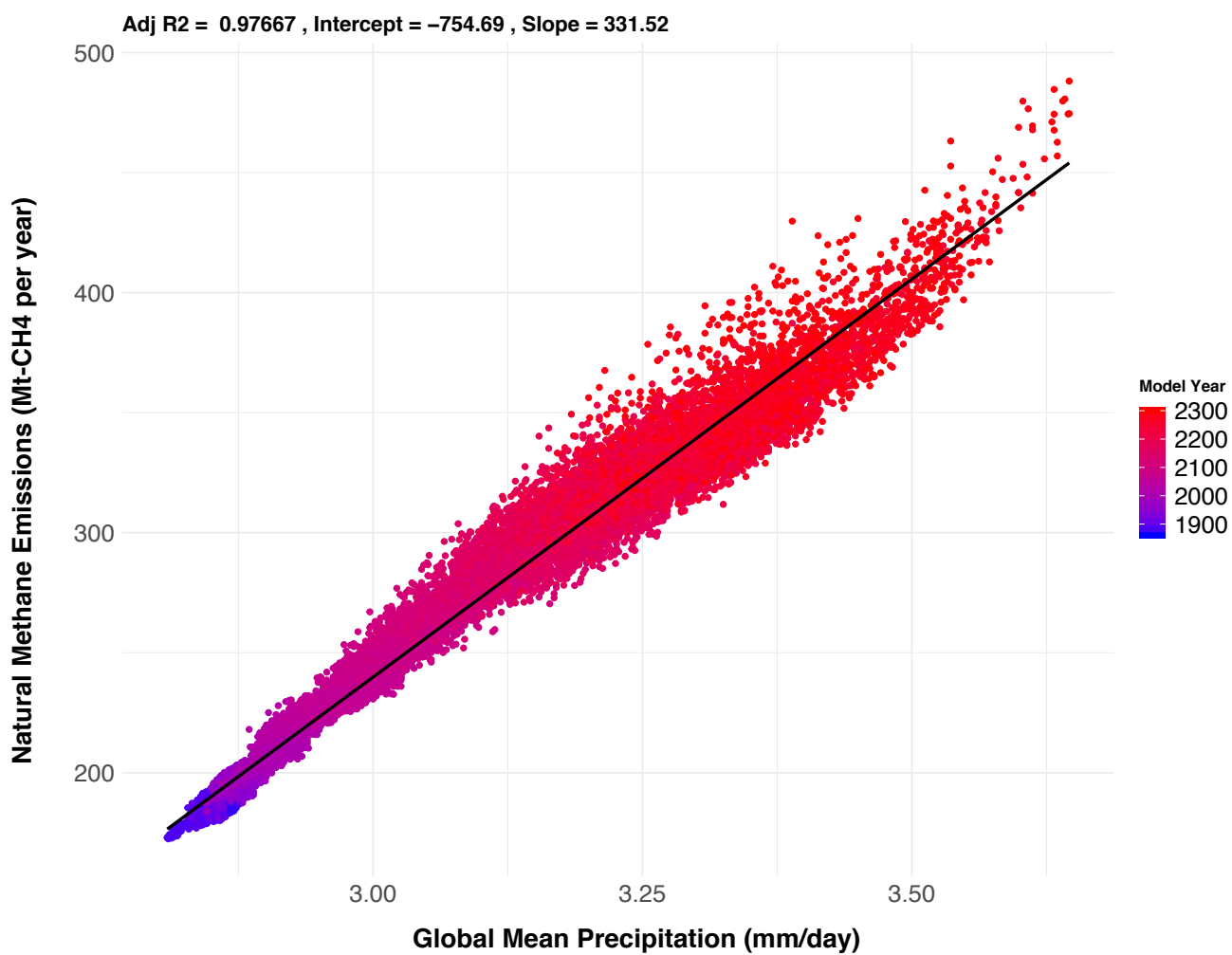
Figure D.1. Mean annual CH$_4$ emissions from wetlands within the MESM model as a linear function of global mean precipitation. The color scale indicates the modeled year.
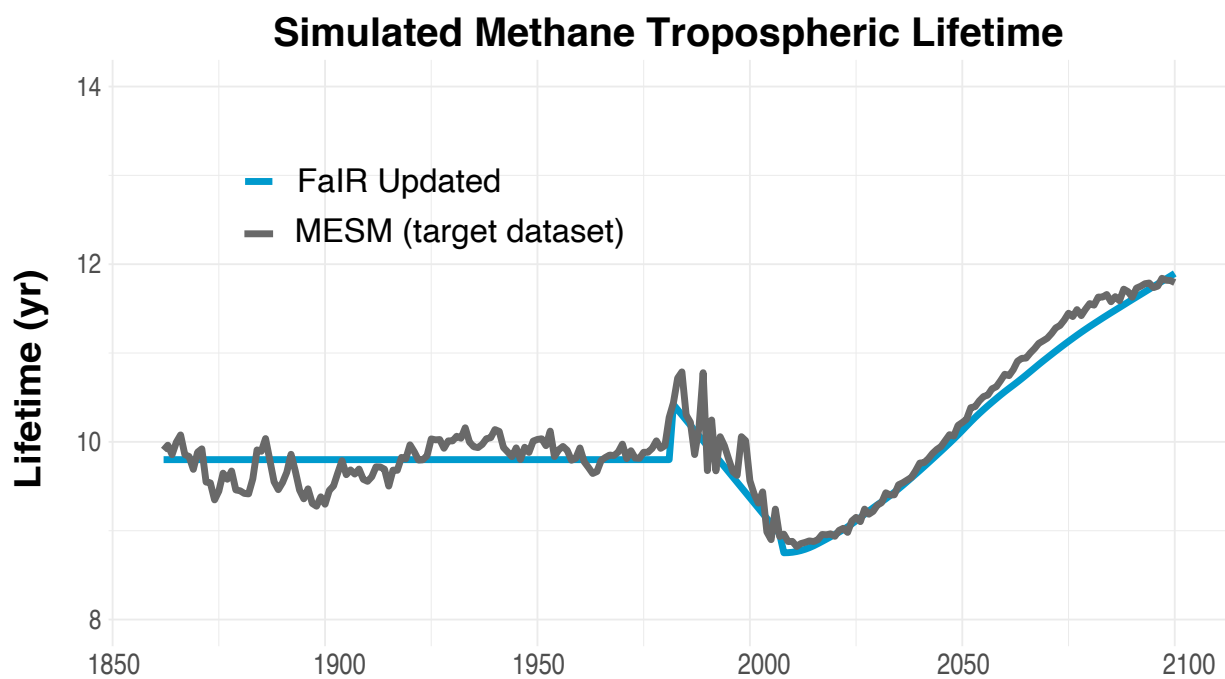
Figure D.2. Methane lifetime calculated from the FaIR box model for the updated FaIR methane module and the MESM output.
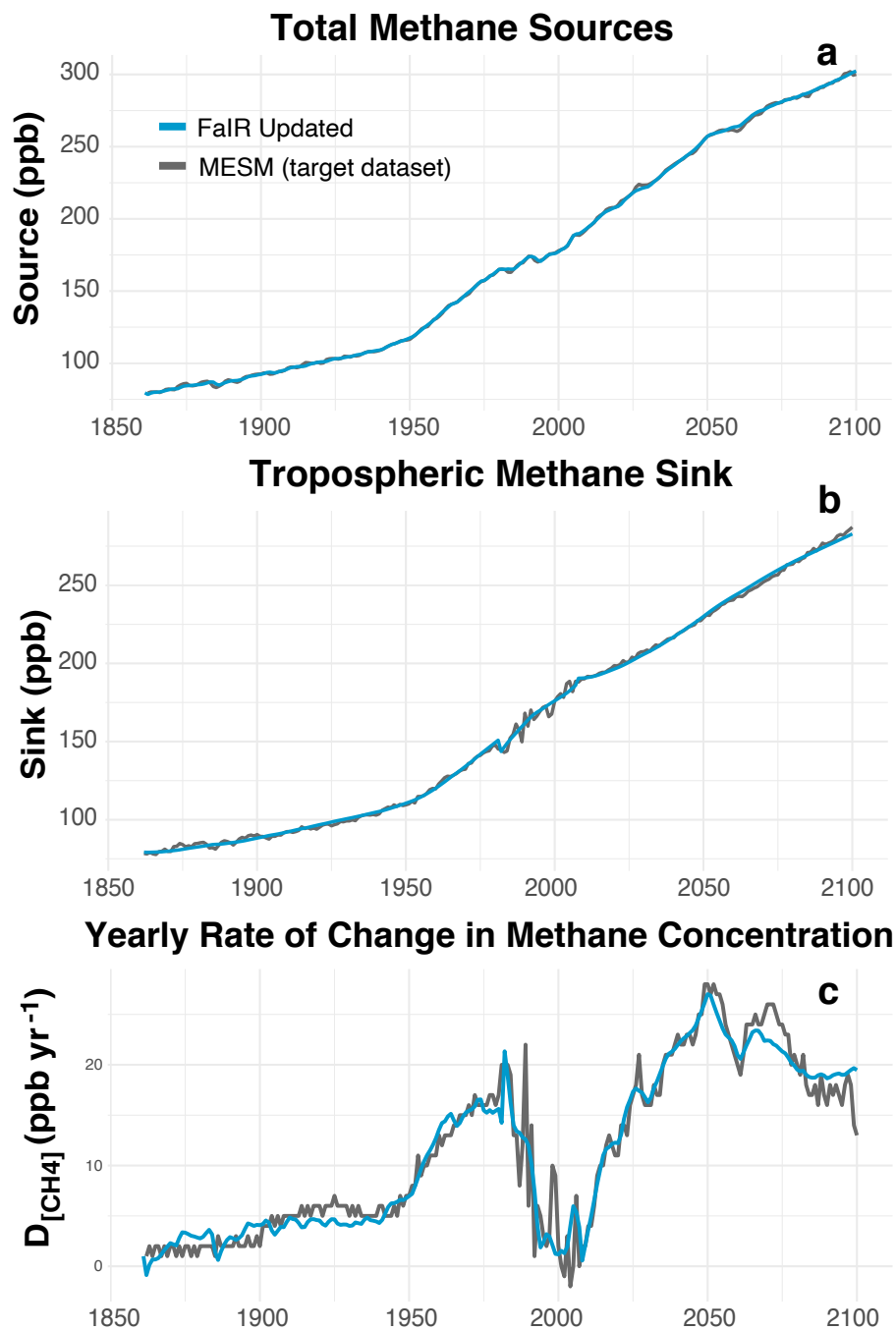
Figure D.3. The components of the FaIR methane box model. a) Total methane sources calculated from the anthropogenic and natural emissions. b) Tropospheric methane sink calculated with a concentration-dependent lifetime. c) The yearly rate of change in methane concentration, i.e. the difference between the sources and sinks.
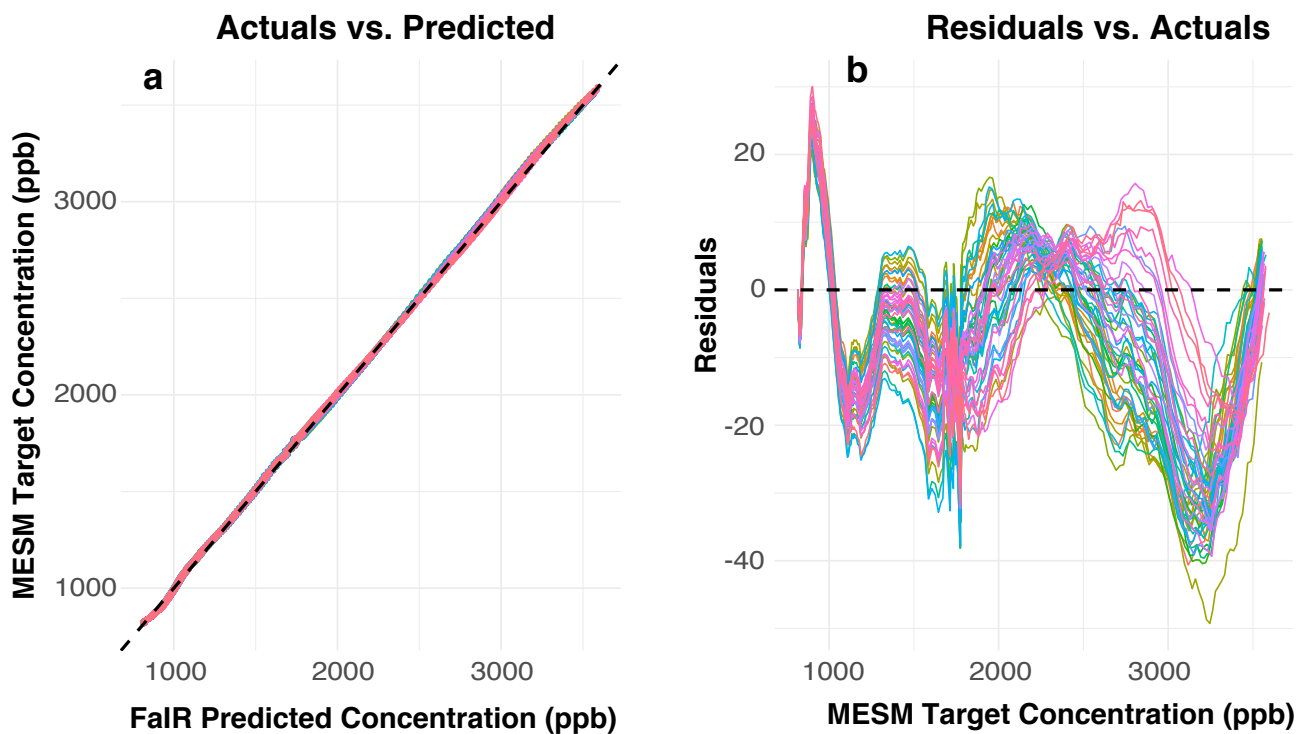
Figure D.4. An analysis of the goodness of fit for the FaIR methane concentration projections. Shown in colors are the 49 member calibrations. a) The target MESM concentration data set plotted against the FaIR predicted concentration. Also shown for reference is a dashed 1:1 line. b) The residuals (Predicted - Target) plotted against the target MESM methane concentration data set.
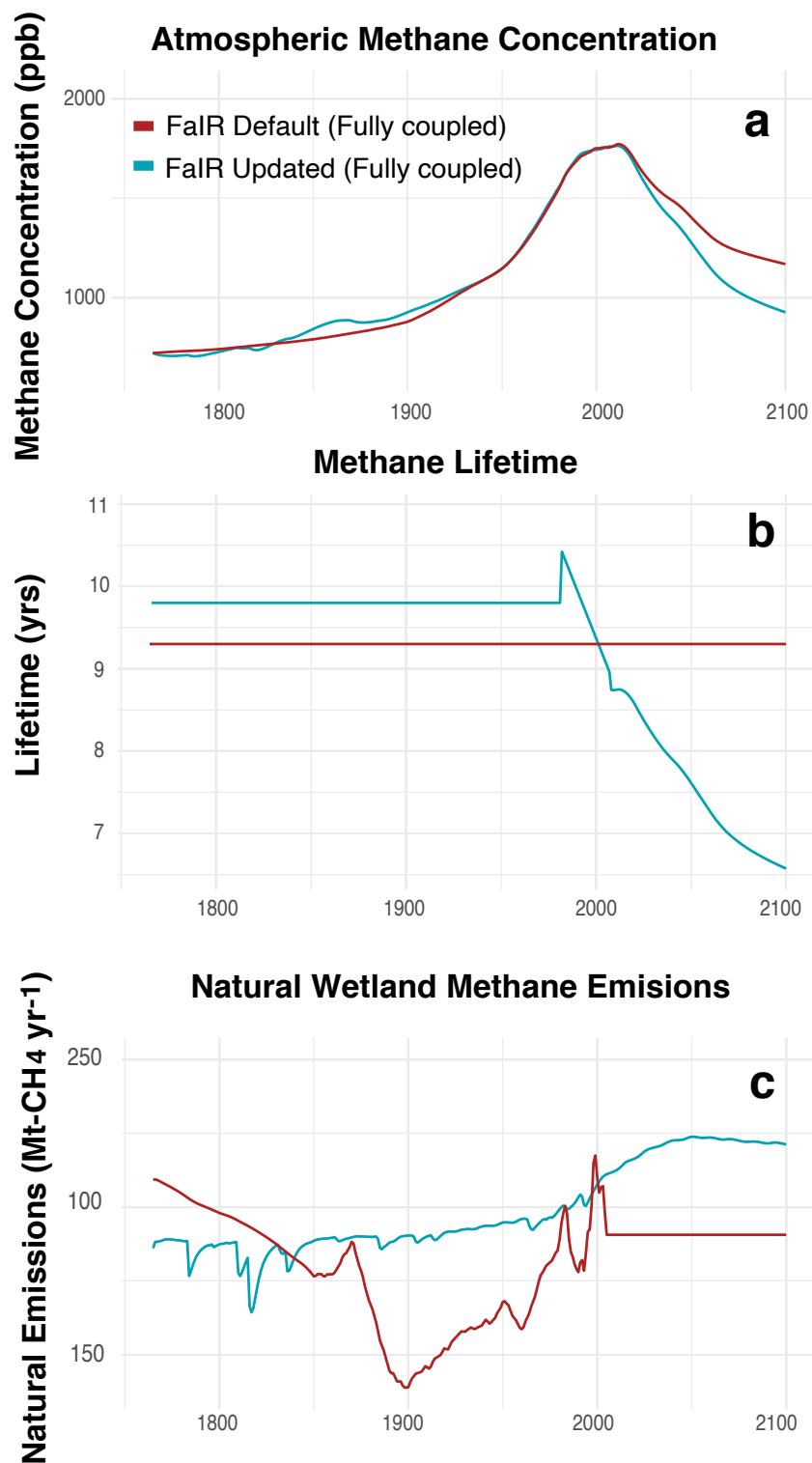
Figure D.5. Components of the FaIR methane box model for the default FaIR v1.3 model version and the updated model developed here, driven by RCP2.6 emission scenario. a) Modeled atmospheric methane concentration, b) calculated methane lifetime, and c) modeled natural wetland methane emissions.
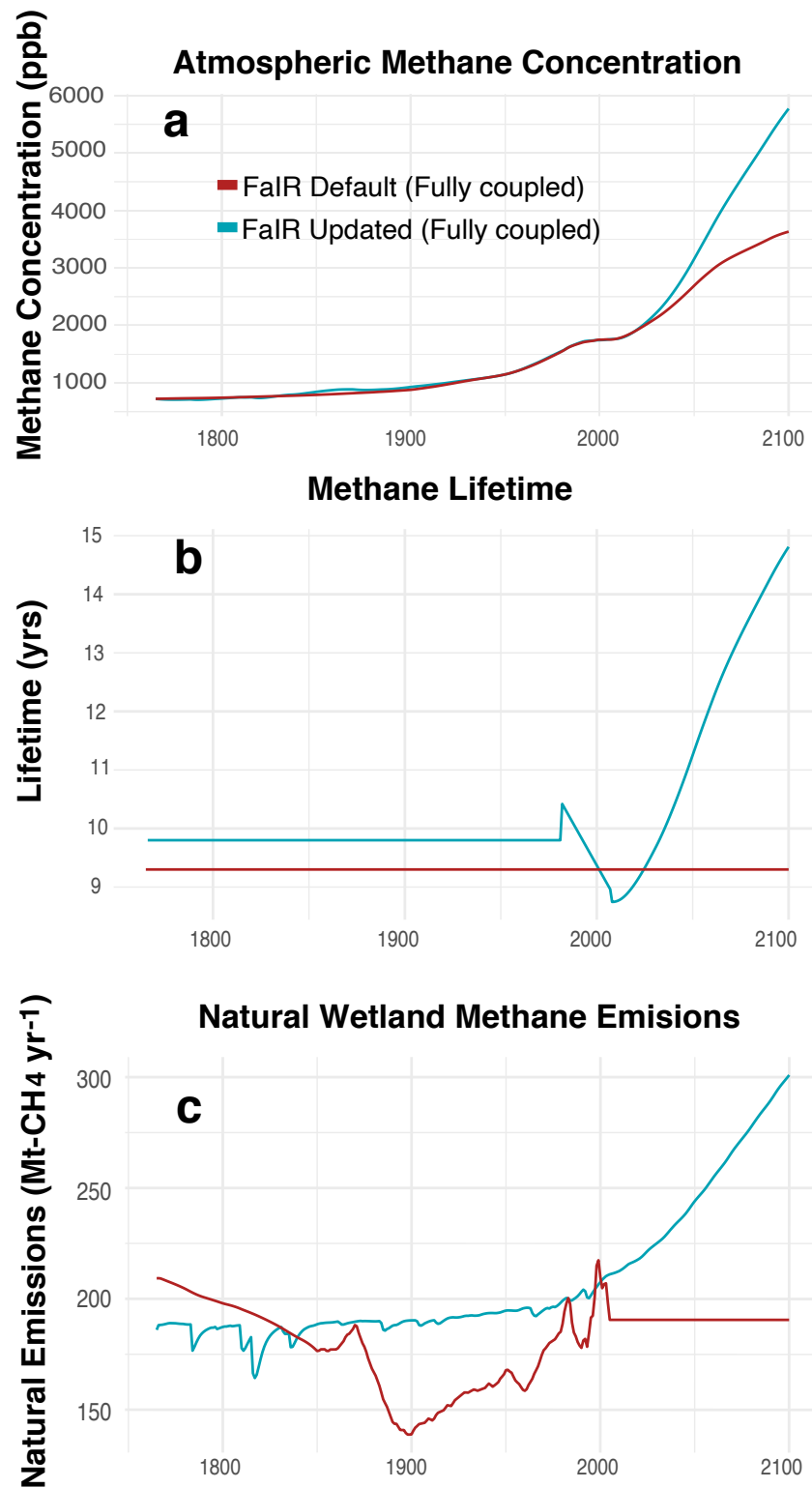
Figure D.6. Same as Figure D.5, but for RCP8.5 emission scenario.

Appendix E

Selection of FUND Parameters

Table E.1. A selection of uncertain parameters in FUND. Given are the types of prior distributions and the shape description from which a Monte Carlo sampling draws. The sections are divided as follows: climate model parameters, added methane cycle parameters, and socioeconomic impact parameters.

Parameter	Distribution	Bounds or Shape Description
Climate Sensitivity	Gamma	$\alpha = 6.47$, $\theta = 0.54$
Sea Level Sensitivity	Gamma	$\alpha = 6.0$, $\theta = 0.4$
Perturbed Methane Emissions	Normal	$\mu = 0.0$, $\sigma = 6.83$
Perturbed Nitrous Oxide Emissions	Normal	$\mu = 0.0$, $\sigma = 0.0059$
Constant Methane Lifetime	Triangular	low = 8.0, mid = 12.0, high = 16.0
Constant Nitrous Oxide Lifetime	Triangular	low = 100, mid = 114, high = 170
Box 2 Carbon Dioxide Lifetime	Truncated Normal	$\mu = 363.00$, $\sigma = 90.75$, low = 0.00
Box 3 Carbon Dioxide Lifetime	Truncated Normal	$\mu = 74.0$, $\sigma = 18.5$, low = 0.00
Box 4 Carbon Dioxide Lifetime	Truncated Normal	$\mu = 17.0$, $\sigma = 4.25$, low = 0.00
Box 5 Carbon Dioxide Lifetime	Truncated Normal	$\mu = 2.0$, $\sigma = 0.5$, low = 0.00
Intercept of Natural Emissions	Truncated Normal	$\mu = 188.0$, $\sigma = 0.4$, [186.2, 189.6]
Slope of Natural Emissions	Truncated Normal	$\mu = 23.9$, $\sigma = 0.6$, [22.1, 25.9]
Intercept of Time Series Regression	Truncated Normal	$\mu = 17.6$, $\sigma = 0.4$, [15.7, 19.2]
Slope of Time Series Regression	Truncated Normal	$\mu = -0.058$, $\sigma = 0.003$, [-0.070, -0.044]
Intercept of Methane Lifetime	Truncated Normal	$\mu = -1.19$, $\sigma = 0.09$, [-1.49, -0.81]
Slope of Methane Lifetime	Truncated Normal	$\mu = 0.45$, $\sigma = 0.01$, [0.40, 0.48]
Population Growth	Normal	$\mu = 0.0$, $\sigma = 0.006$
Biodiversity Loss	Truncated Normal	$\mu = 0.003$ $\sigma = 0.002$), low = 0.0
Agricultural Adaptation Time	Truncated Normal	$\mu = 10.0$ $\sigma = 5.0$), low = 1.0
Perturbed Cardiovascular Disease	Truncated Normal	$\mu = 0.0259$ $\sigma = 0.0096$), low = 0.0
Statistical Life Value	Truncated Normal	$\mu = 1.0$ $\sigma = 0.2$, low = 0.0

Appendix F

The Social Cost of Methane: Additional Figures
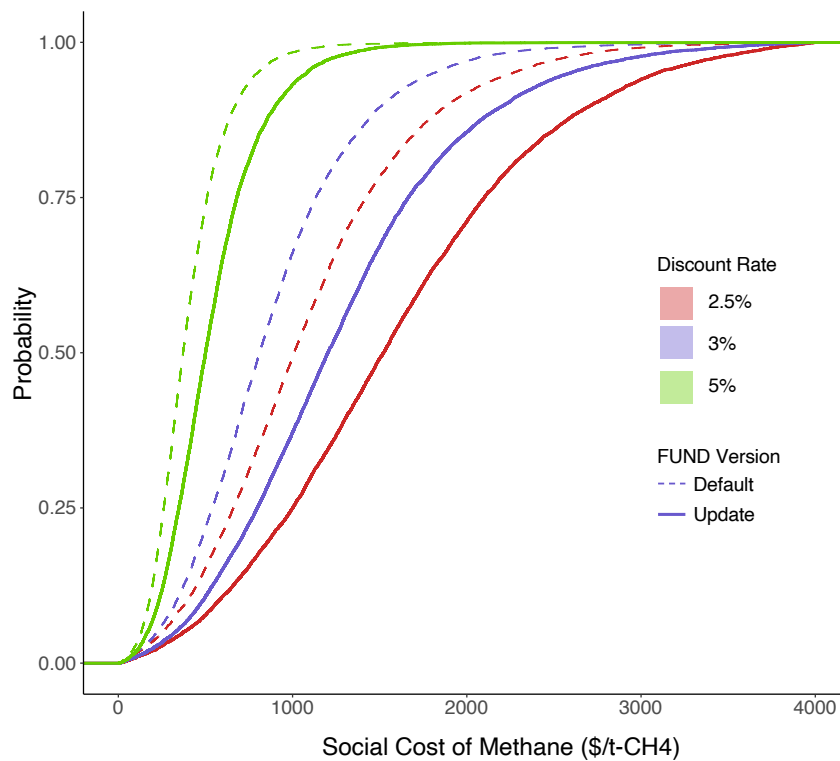
Figure F.1. Cumulative distribution function (CDF) showing the probability of the social cost of methane for three constant discount rates. Dashed lines refer to the default version 3.9 FUND and straight lines refer to the modified version with methane feedbacks.
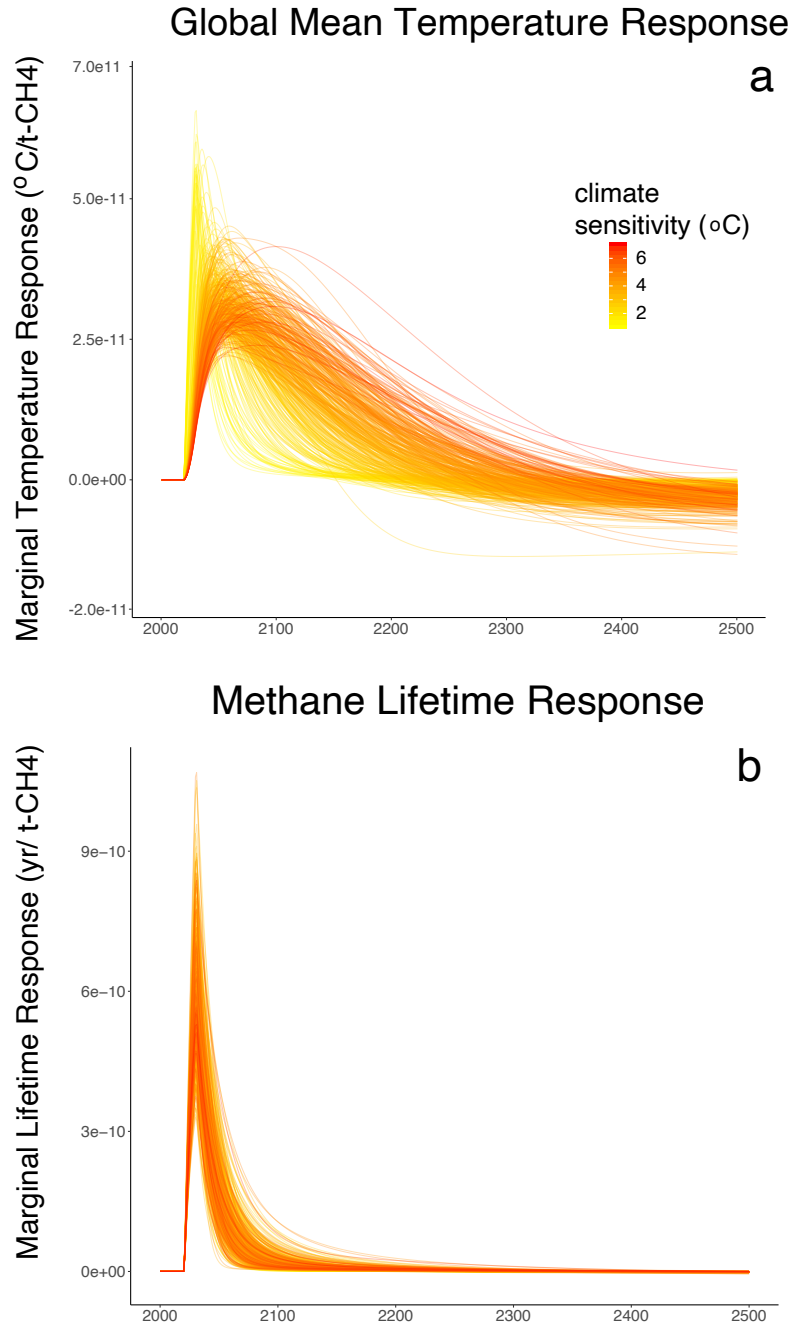
Figure F.2. Marginalized impulse response behavior following a one-ton methane pulse in 2020 using the modified FUND model with methane feedbacks. The vertical scales are small because of the 1 ton methane pulse emission. For comparison, annual CH4 emissions are 4.167e+8 tons. The color gradient shows the equilibrium climate sensitivity (°C). Shown are 500 randomly selected projections from the 10,000 model runs. a) Global mean temperature response, and b) methane lifetime response following the ten-year pulse perturbation between 2020-2030.
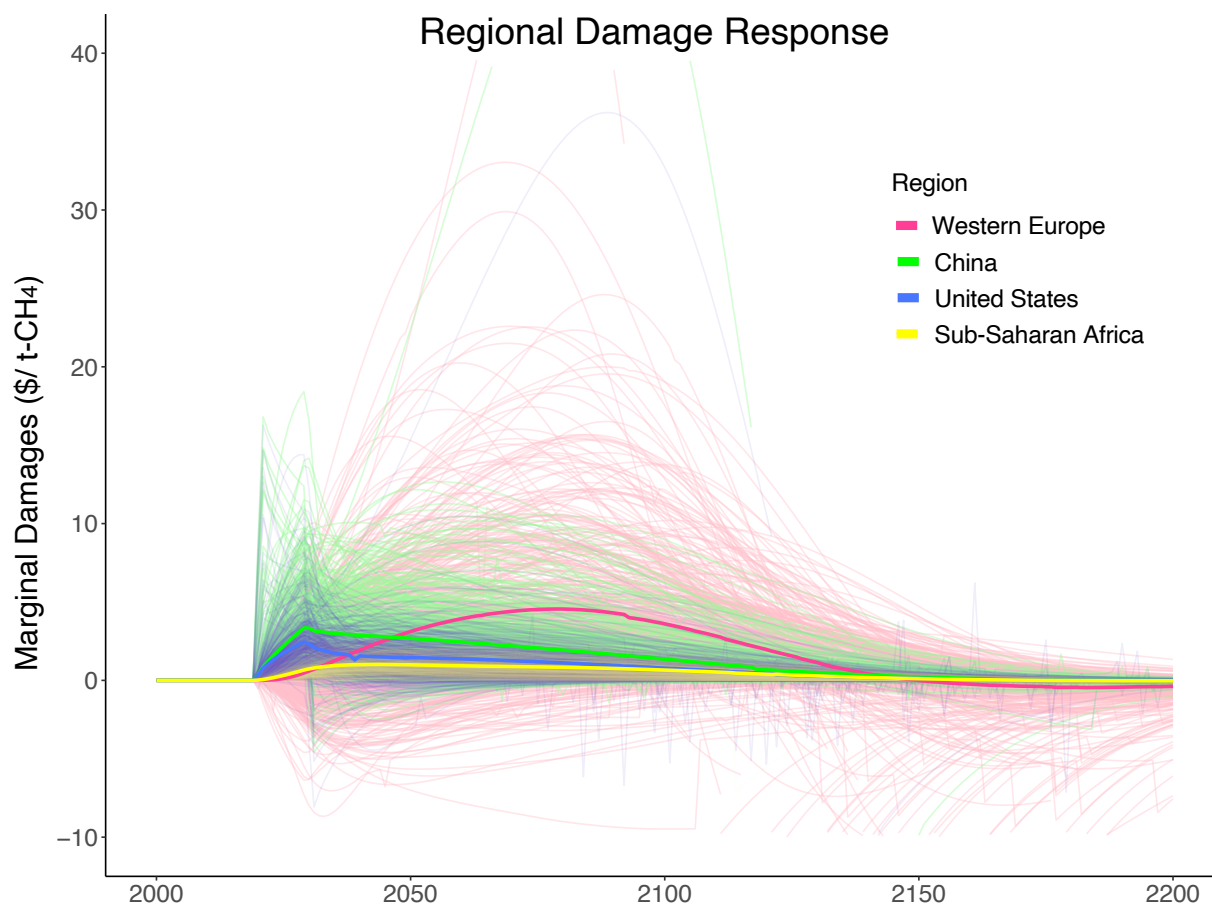
Figure F.3. Marginal monetary damages following a unit ton methane pulse for a select four of the 16 regions in the FUND model. Damages are calculated using a constant 3% consumption discount rate. Shown are 500 randomly selected projections from the 10,000 model runs. The bold lines indicates the ensemble mean response for each of the regions.

Bibliography

Aamaas, B., G. P. Peters, and J. S. Fuglestvedt, 2013: Simple emission metrics for climate impacts. *Earth Syst. Dyn.*, **4 (1)**, 145–170, doi:10.5194/esd-4-145-2013.

Adams, R. M., R. A. Fleming, C.-C. Chang, B. A. McCarl, and C. Rosenzweig, 1995: A reassessment of the economic effects of global climate change on U.S. agriculture. *Clim. Change*, **30 (2)**, 147–167, doi:10.1007/BF01091839.

Alan Rotz, C., R. Howard Skinner, A. M.K. Stoner, and K. Hayhoe, 2015: Farm simulation: a tool for evaluating the mitigation of greenhouse gas emissions and the adaptation of dairy production to climate change. *ASABE 1st Clim. Chang. Symp. Adapt. Mitig.*, American Society of Agricultural and Biological Engineers, St. Joseph, MI, 1–3, doi:10.13031/cc.20152121235.

Allan, W., H. Struthers, and D. C. Lowe, 2007: Methane carbon isotope effects caused by atomic chlorine in the marine boundary layer: Global model results compared with Southern Hemisphere measurements. *J. Geophys. Res.*, **112 (D4)**, D04 306, doi:10.1029/2006JD007369.

Anthoff, D., and R. S. J. Tol, 2013: The uncertainty about the social cost of carbon: A decomposition analysis using FUND. *Clim. Chang.*, **117 (3)**, 515–530, doi:10.1007/s10584-013-0706-7.

Anthoff, D., and R. S. J. Tol, 2014: The climate framework for uncertainty, negotiation and distribution (FUND), technical description, version 3.9. Tech. rep., University of California, Berkeley.

Anthoff, D., R. S. J. Tol, and G. W. Yohe, 2009: Discounting for Climate Change. *Economics: The Open-Access*, **3 (2009-24)**, 1, doi:10.5018/economics-ejournal.ja.2009-24.

Archer, D., and Coauthors, 2009: Atmospheric Lifetime of Fossil Fuel Carbon Dioxide. *Annu. Rev. Earth Planet. Sci.*, **37 (1)**, 117–134, doi:10.1146/annurev.earth.031208.100206.

Arora, V. K., J. R. Melton, and D. Plummer, 2018: An assessment of natural methane fluxes simulated by the CLASS-CTEM model. *Biogeosciences*, **15 (15)**, 4683–4709, doi:10.5194/bg-15-4683-2018.

Arora, V. K., and Coauthors, 2013: Carbon–Concentration and Carbon–Climate Feedbacks in CMIP5 Earth System Models. *J. Clim.*, **26 (15)**, 5289–5314, doi:10.1175/JCLI-D-12-00494.1.

Bastviken, D., L. J. Tranvik, J. A. Downing, P. M. Crill, and A. Enrich-Prast, 2011: Freshwater methane emissions offset the continental carbon sink. *Science*, **331 (6013)**, 50, doi:10.1126/science.1196808.

Bayes, T., and R. Price, 1763: An Essay towards Solving a Problem in the Doctrine of Chances By the Late Rev. Mr. Bayes. *Philos. Trans.*, **53**, 370–418.

Beach, R. H., J. Creason, S. B. Ohrel, S. Ragnauth, S. Ogle, C. Li, P. Ingraham, and W. Salas, 2015: Global mitigation potential and costs of reducing agricultural non-CO_2 greenhouse gas emissions through 2030. *J. Integr. Environ. Sci.*, **12**, 87–105, doi:10.1080/1943815X.2015.1110183.

Blake, D. R., E. W. Mayer, S. C. Tyler, Y. Makide, D. C. Montague, and F. S. Rowland, 1982: Global increase in atmospheric methane concentrations between 1978 and 1980. *Geophys. Res. Lett.*, **9 (4)**, 477–480, doi:10.1029/GL009i004p00477.

Börjesson, G., and B. H. Svensson, 1997: Seasonal and Diurnal Methane Emissions From a Landfill and Their Regulation By Methane Oxidation. *Waste Manag. Res.*, **15 (1)**, 33–54, doi:10.1177/0734242X9701500104.

Bouwman, A., T. Kram, and K. Klein Goldewijk, 2006: *Integrated modelling of global environmental change. An overview of IMAGE 2.4.* The Netherlands Environmental Assessment Agency, Bilthoven, The Netherlands.

Bowen, G. J., D. J. Beerling, P. L. Koch, J. C. Zachos, and T. Quattlebaum, 2004: A humid climate state during the Palaeocene/Eocene thermal maximum. *Nature*, **432 (7016)**, 495–499, doi:10.1038/nature03115.

Brasseur, G. P., M. Schultz, C. Granier, M. Saunois, T. Diehl, M. Botzet, E. Roeckner, and S. Walters, 2006: Impact of Climate Change on the Future Chemical Composition of the Global Troposphere. *J. Clim.*, **19 (16)**, 3932–3951, doi:10.1175/JCLI3832.1.

Brasseur, G. P., and Coauthors, 2016: Impact of aviation on climate: FAA's Aviation Climate Change Research Initiative (ACCRI) phase II. *Bull. Am. Meteorol. Soc.*, **97 (4)**, 561–583, doi:10.1175/BAMS-D-13-00089.1.

Brühl, C., 1993: The impact of the future scenarios for methane and other chemically active gases on the GWP of methane. *Chemosphere*, **26 (1)**, 731–738, doi:10.1016/0045-6535(93)90457-G.

Burtraw, D., J. Linn, K. Palmer, and A. Paul, 2014: The Costs and Consequences of Clean Air Act Regulation of CO_2 from Power Plants. *Am. Econ. Rev.*, **104 (5)**, 557–562, doi:10.1257/aer.104.5.557.

Calvin, K., and Coauthors, 2017: The SSP4: A world of deepening inequality. *Global Environmental Change*, **42**, 284–296, doi:10.1016/j.gloenvcha.2016.06.010.

Carlson, K. M., and Coauthors, 2017: Greenhouse gas emissions intensity of global croplands. *Nat. Clim. Chang.*, **7 (1)**, 63–68, doi:10.1038/nclimate3158.

Chen, Y.-H. H., S. Paltsev, J. Reilly, J. Morris, and H. Babiker, Mustafa, 2015: The MIT EPPA6 Model: Economic growth, energy use, emissions, and food consumption. Tech. Rep. 278, MIT Joint Program on the Science and Policy of Global Change, Cambridge, MA.

Chen, Y.-H. H., and Coauthors, 2016: Food, Water, Energy, Climate Outlook: Perspectives from 2016. Tech. rep., MIT Joint Program on the Science and Policy of Global Change, Cambridge, MA.

Chen, Y.-H. H., and Coauthors, 2017: The MIT Economic Projection and Policy Analysis (EPPA) Model: Version 5. Tech. Rep. 16, MIT Joint Program on the Science and Policy of Global Change, Cambridge, MA.

Claussen, M., and Coauthors, 2002: Earth system models of intermediate complexity: closing the gap in the spectrum of climate system models. *Clim. Dyn.*, **18 (7)**, 579–586, doi:10.1007/s00382-001-0200-1.

Collins, W. J., M. M. Fry, H. Yu, J. S. Fuglestvedt, D. T. Shindell, and J. J. West, 2013: Global and regional temperature-change potentials for near-term climate forcers. *Atmos. Chem. Phys.*, **13 (5)**, 2471–2485, doi:10.5194/acp-13-2471-2013.

Crutzen, P. J., and P. H. Zimmermann, 1991: The changing photochemistry of the troposphere. *Tellus B*, **43 (4)**, 136–151, doi:10.1034/j.1600-0889.1991.t01-1-00012.x.

Curry, C. L., 2007: Modeling the soil consumption of atmospheric methane at the global scale. *Global Biogeochem. Cycles*, **21 (4)**, doi:10.1029/2006GB002818.

Dalsøren, S. B., M. S. Eide, G. Myhre, Ø. Endresen, I. S. Isaksen, and J. S. Fuglestvedt, 2010: Impacts of the large increase in international ship traffic 2000-2007 on tropospheric ozone and methane. *Environ. Sci. Technol.*, **44 (7)**, 2482–2489, doi:10.1021/es902628e.

Danner, C., 2009: Greenhouse gas policy and California electricity prices. *J. Regul. Econ.*, **37 (1)**, 98, doi:10.1007/s11149-009-9105-4.

de Bruin, K., R. Dellink, and S. Agrawala, 2009: Economic Aspects of Adaptation to Climate Change: Integrated Assessment Modelling of Adaptation Costs and Benefits. *OECD Environ. Work. Pap.*, **6**, 1–7,11–48, doi:10.1787/225282538105.

Dean, J. F., and Coauthors, 2018: Methane Feedbacks to the Global Climate System in a Warmer World. *Rev. Geophys.*, **56 (1)**, 207–250, doi:10.1002/2017RG000559.

DeConto, R. M., S. Galeotti, M. Pagani, D. Tracy, K. Schaefer, T. Zhang, D. Pollard, and D. J. Beerling, 2012: Past extreme warming events linked to massive carbon release from thawing permafrost. *Nature*, **484 (7392)**, 87–91, doi:10.1038/nature10929.

Deemer, B. R., and Coauthors, 2016: Greenhouse Gas Emissions from Reservoir Water Surfaces: A New Global Synthesis. *Bioscience*, **66 (11)**, 949–964, doi:10.1093/biosci/biw117.

Delmas, R. J., J.-M. Ascencio, and M. Legrand, 1980: Polar ice evidence that atmospheric CO2 20,000 yr BP was 50% of present. *Nature*, **284 (5752)**, 155–157, doi:10.1038/284155a0.

DeMore, W. B., 1996: Experimental and Estimated Rate Constants for the Reactions of Hydroxyl Radicals with Several Halocarbons. *J. Phys. Chem.*, **100 (14)**, 5813–5820, doi:10.1021/jp953216+.

Diaz, D., and F. Moore, 2017: Quantifying the economic risks of climate change. *Nat. Clim. Chang.*, **7 (11)**, 774–782, doi:10.1038/nclimate3411.

Dietz, S., 2012: The Treatment of Risk and Uncertainty in the Us Social Cost of Carbon for Regulatory Impact Analysis. *SSRN Electron. J.*, **6**, 0–13, doi:10.2139/ssrn.1973473.

Dijkstra, J., O. Oenema, and A. Bannink, 2011: Dietary strategies to reducing N excretion from cattle: Implications for methane emissions. *Curr. Opin. Environ. Sustain.*, **3 (5)**, 414–422, doi:10.1016/j.cosust.2011.07.008.

Dlugokencky, E., 2019: Trends in Atmospheric Methane. ESRL Global Monitoring Division - Global Greenhouse Gas Reference Network, NOAA/ESRL, www.esrl.noaa.gov/gmd/ccgg/trends_ch4/.

Dlugokencky, E. J., K. A. Masarie, P. M. Lang, and P. P. Tans, 1998: Continuing decline in the growth rate of the atmospheric methane burden. *Nature*, **393 (6684)**, 447–450, doi:10.1038/30934.

Dolfing, A. G., 2017: Scenarios for reducing the greenhouse gas emissions of the Dutch dairy sector. Ph.D. thesis, Utrecht University.

Dontala, S. P., T. B. Reddy, and R. Vadde, 2015: Environmental Aspects and Impacts its Mitigation Measures of Corporate Coal Mining. *Procedia Earth Planet. Sci.*, **11**, 2–7, doi:10.1016/j.proeps.2015.06.002.

Eby, M., K. Zickfeld, A. Montenegro, D. Archer, K. J. Meissner, and A. J. Weaver, 2009: Lifetime of anthropogenic climate change: Millennial time scales of potential CO_2 and surface temperature perturbations. *J. Clim.*, **22 (10)**, 2501–2511, doi:10.1175/2008JCLI2554.1.

Ehhalt, D., and Coauthors, 2001: Chapter 4: Atmospheric and Greenhouse Gases. *IPCC Third Assessment Report Climate Change 2001: The Scientific Basis.*, Cambridge University Press, United Kingdom.

Ehhalt, D. H., 1974: The atmospheric cycle of methane. *Tellus*, **26 (1-2)**, 58–70, doi:10.1111/j.2153-3490.1974.tb01952.x.

Ehhalt, D. H., and U. Schmidt, 1978: Sources and sinks of atmospheric methane. *Pure Appl. Geophys.*, **116 (2)**, 452–464, doi:10.1007/BF01636899.

EPA, 2012: Summary Report: Global Anthropogenic Non-CO_2 Greenhouse Gas Emissions: 1990 - 2030. techreport 430-S-12-002, EPA, 1–23 pp.

EPA, 2016: Inventory of U.S. Greenhouse Gas Emissions and Sinks: 1990–2014. techreport 430-R-16-002, EPA, 1–27 pp.

EPA, 2019: Global Non-CO_2 Greenhouse Gas Emission Projections and Mitigation: 2015–2050. techreport 430-R-19-010, EPA, 1–80 pp.

Etiope, G., G. Ciotoli, S. Schwietzke, and M. Schoell, 2019: Gridded maps of geological methane emissions and their isotopic signature. *Earth Syst. Sci. Data*, **11 (1)**, 1–22, doi: 10.5194/essd-11-1-2019.

Etminan, M., G. Myhre, E. J. Highwood, and K. P. Shine, 2016: Radiative forcing of carbon dioxide, methane, and nitrous oxide: A significant revision of the methane radiative forcing. *Geophys. Res. Lett.*, **43 (24)**, 12,614–12,623, doi:10.1002/2016GL071930.

Fankhauser, S., 1994: The Social Costs of Greenhouse Gas Emissions: An Expected Value Approach. *Energy J.*, **15 (2)**, doi:10.5547/ISSN0195-6574-EJ-Vol15-No2-9.

FAO, 2018: FAOSTAT Statistical Database. FAO, Rome, Italy. Accessed: 2019-04-25, www.fao.org/faostat/.

Felzer, B., J. Reilly, J. Melillo, D. Kicklighter, M. Sarofim, C. Wang, R. Prinn, and Q. Zhuang, 2005: Future Effects of Ozone on Carbon Sequestration and Climate Change Policy Using a Global Biogeochemical Model. *Clim. Change*, **73 (3)**, 345–373, doi:10.1007/s10584-005-6776-4.

Ferraro, P. J., M. M. Hanauer, D. A. Miteva, J. L. Nelson, S. K. Pattanayak, C. Nolte, and K. R. E. Sims, 2015: Estimating the impacts of conservation on ecosystem services and poverty by integrating modeling and evaluation. *Proc. Natl. Acad. Sci.*, **112 (24)**, 7420 LP – 7425, doi:10.1073/pnas.1406487112.

Ferry, J. G., 1999: Enzymology of one-carbon metabolism in methanogenic pathways. *FEMS Microbiol. Rev.*, **23 (1)**, 13–38, doi:10.1016/S0168-6445(98)00029-1.

Fiedler, S., and M. Sommer, 2000: Methane emissions, groundwater levels and redox potentials of common wetland soils in a temperate-humid climate. *Global Biogeochem. Cycles*, **14 (4)**, 1081–1093, doi:10.1029/1999GB001255.

Forest, C. E., 2002: Quantifying Uncertainties in Climate System Properties with the Use of Recent Climate Observations. *Science*, **295 (5552)**, 113–117, doi:10.1126/science.1064419.

Forest, C. E., P. H. Stone, and A. P. Sokolov, 2006: Estimated PDFs of climate system properties including natural and anthropogenic forcings. *Geophys. Res. Lett.*, **33 (1)**, L01 705, doi:10.1029/2005GL023977.

Forest, C. E., P. H. Stone, and A. P. Sokolov, 2008: Constraining climate model parameters from observed 20th century changes. *Tellus A Dyn. Meteorol. Oceanogr.*, **60 (5)**, 911–920, doi:10.1111/j.1600-0870.2008.00346.x.

Forster, P., and Coauthors, 2007: Changes in Atmospheric Constituents and in Radiative Forcing. Chapter 2. *Climate Change 2007. The Physical Science Basis. Contribution of Working Group I to the Fourth Assessment Report of the Intergovernmental Panel on Climate Change.*, Cambridge University Press, United Kingdom.

Frenzel, P., and E. Karofeld, 2000: CH_4 emission from a hollow-ridge complex in a raised bog: The role of CH_4 production and oxidation. *Biogeochemistry*, **51 (1)**, 91–112, doi:10.1023/A:1006351118347.

Fricko, O., and Coauthors, 2017: The marker quantification of the Shared Socioeconomic Pathway 2: A middle-of-the-road scenario for the 21st century. *Glob. Environ. Change*, **42**, 251–267, doi:10.1016/j.gloenvcha.2016.06.004.

Friedlingstein, P., and Coauthors, 2006: Climate–Carbon Cycle Feedback Analysis: Results from the CMIP4 Model Intercomparison. *J. Clim.*, **19 (14)**, 3337–3353, doi:10.1175/JCLI3800.1.

Friedlingstein, P., and Coauthors, 2019: Global Carbon Budget 2019. *Earth Syst. Sci. Data*, **11 (4)**, 1783–1838, doi:10.5194/essd-11-1783-2019.

Frieling, J., H. H. Svensen, S. Planke, M. J. Cramwinckel, H. Selnes, and A. Sluijs, 2016: Thermogenic methane release as a cause for the long duration of the PETM. *Proc. Natl. Acad. Sci.*, **113 (43)**, 12 059–12 064, doi:10.1073/pnas.1603348113.

Fry, M. M., and Coauthors, 2012: The influence of ozone precursor emissions from four world regions on tropospheric composition and radiative climate forcing. *J. Geophys. Res. Atmos.*, **117 (7)**, doi:10.1029/2011JD017134.

Fujimori, S., T. Hasegawa, T. Masui, K. Takahashi, D. S. Herran, H. Dai, Y. Hijioka, and M. Kainuma, 2017: SSP3: AIM implementation of Shared Socioeconomic Pathways. *Glob. Environ. Change*, **42**, 268–283, doi:10.1016/j.gloenvcha.2016.06.009.

Fung, I. Y., S. C. Doney, K. Lindsay, and J. John, 2005: Evolution of carbon sinks in a changing climate. *Proc. Natl. Acad. Sci.*, **102 (32)**, 11 201–11 206, doi:10.1073/pnas.0504949102.

Füssel, H. M., 2007: Methodological and empirical flaws in the design and application of simple climate-economy models. *Clim. Chang.*, **81**, 161–185, doi:10.1007/s10584-006-9154-y.

Gambhir, A., and Coauthors, 2017: The Contribution of Non-CO_2 Greenhouse Gas Mitigation to Achieving Long-Term Temperature Goals. *Energies*, **10 (5)**, 602, doi:10.3390/en10050602.

Gasparini, M., W. R. Gilks, S. Richardson, and D. J. Spiegelhalter, 1997: Markov Chain Monte Carlo in Practice. *Technometrics*, **39 (3)**, 338, doi:10.2307/1271145.

Gasser, T., P. Ciais, O. Boucher, Y. Quilcaille, M. Tortora, L. Bopp, and D. Hauglustaine, 2017: The compact Earth system model OSCAR v2.2: Description and first results. *Geosci. Model Dev.*, **10 (1)**, 271–319, doi:10.5194/gmd-10-271-2017.

Gerber, P., T. Vellinga, K. Dietze, A. Falcucci, and G. Gianni, 2010: Greenhouse Gas Emissions from the Dairy Sector. techreport K7930E, FAO.

Gerber, P. J., H. Steinfeld, B. Henderson, a. Mottet, C. Opio, J. Dijkman, a. Falculli, and G. Tempio, 2013: *Tackling Climate Change Through Livestock: A Global Assessment of Emissions and Mitigation Opportunities*. FAO, 1–139 pp., doi:10.1016/j.anifeedsci.2011.04.074.

Gillett, N. P., and H. D. Matthews, 2010: Accounting for carbon cycle feedbacks in a comparison of the global warming effects of greenhouse gases. *Environ. Res. Lett.*, **5 (3)**, 34 011, doi: 10.1088/1748-9326/5/3/034011.

Goodess, C., C. Hanson, M. Hulme, and T. Osborn, 2003: Representing Climate and Extreme Weather Events in Integrated Assessment Models: A Review of Existing Methods and Options for Development. *Integr. Assess.*, **4**, 145–171, doi:10.1076/iaij.4.3.145.23772.

Greenstone, M., E. Kopits, and A. Wolverton, 2013: Developing a Social Cost of Carbon for US Regulatory Analysis: A Methodology and Interpretation. *Rev. Environ. Econ. Policy*, **7 (1)**, 23–46, doi:10.1093/reep/res015.

Gregory, J. M., C. D. Jones, P. Cadule, and P. Friedlingstein, 2009: Quantifying Carbon Cycle Feedbacks. *J. Clim.*, **22 (19)**, 5232–5250, doi:10.1175/2009JCLI2949.1.

Gregory, P., J. Ingram, and M. Brklacich, 2005: Climate change and food security. *Philos. Trans. R. Soc. B Biol. Sci.*, **360 (1463)**, 2139–2148, doi:10.1098/rstb.2005.1745.

Gurgel, A., T. Cronin, J. Reilly, S. Paltsev, D. Kicklighter, and J. Melillo, 2011: Food, fuel, forests, and the pricing of ecosystem services. *Am. J. Agric. Econ.*, **93 (2)**, 342–348, doi: 10.1093/ajae/aaq087.

Hagemann, M., A. Ndambi, T. Hemme, and U. Latacz-Lohmann, 2012: Contribution of milk production to global greenhouse gas emissions. *Environ. Sci. Pollut. Res.*, **19 (2)**, 390–402, doi:10.1007/s11356-011-0571-8.

Hammitt, J. K., R. J. Lempert, and M. E. Schlesinger, 1992: A sequential-decision strategy for abating climate change. *Nature*, **357 (6376)**, 315–318, doi:10.1038/357315a0.

Hansen, J., M. Sato, R. Ruedy, A. Lacis, and V. Oinas, 2000: Global warming in the twenty-first century: An alternative scenario. *Proc. Natl. Acad. Sci.*, **97 (18)**, 9875–9880, doi: 10.1073/pnas.170278997.

Harmsen, M. J. H. M., and Coauthors, 2015: How well do integrated assessment models represent non-CO_2 radiative forcing? *Clim. Change*, **133 (4)**, 565–582, doi:10.1007/s10584-015-1485-0.

Harvey, D., and Coauthors, 1997: *An introduction to simple climate models used in the IPCC Second Assessment Report*. Intergovernmental Panel on Climate Change.

Hastings, W. K., 1970: Monte carlo sampling methods using Markov chains and their applications. *Biometrika*, **57 (1)**, 97–109, doi:10.1093/biomet/57.1.97.

Hausmann, P., R. Sussmann, and D. Smale, 2016: Contribution of oil and natural gas production to renewed increase in atmospheric methane (2007–2014): top–down estimate from ethane and methane column observations. *Atmos. Chem. Phys.*, **16 (5)**, 3227–3244, doi:10.5194/acp-16-3227-2016.

Hayashida, S., A. Ono, S. Yoshizaki, C. Frankenberg, W. Takeuchi, and X. Yan, 2013: Methane concentrations over Monsoon Asia as observed by SCIAMACHY: Signals of methane emission from rice cultivation. *Remote Sens. Environ.*, **139**, 246–256, doi:10.1016/j.rse.2013.08.008.

Heidelberger, P., and P. D. Welch, 1981: A spectral method for confidence interval generation and run length control in simulations. *Commun. ACM*, **24 (4)**, 233–245, doi:10.1145/358598.358630.

Hoesly, R., and Coauthors, 2018: Historical (1750–2014) anthropogenic emissions of reactive gases and aerosols from the Community Emissions Data System (CEDS). *Geosci. Model Dev.*, **11**, 369–408, doi:10.5194/gmd-11-369-2018.

Hof, A. F., C. W. Hope, J. Lowe, M. D. Mastrandrea, M. Meinshausen, and D. P. van Vuuren, 2012: The benefits of climate change mitigation in integrated assessment models: the role of the carbon cycle and climate component. *Clim. Chang.*, **113 (3)**, 897–917, doi:10.1007/s10584-011-0363-7.

Holm, S., J. Walz, F. Horn, S. Yang, M. N. Grigoriev, D. Wagner, C. Knoblauch, and S. Liebner, 2020: Methanogenic response to long-term permafrost thaw is determined by paleoenvironment. *FEMS Microbiol. Ecol.*, **96 (3)**, doi:10.1093/femsec/fiaa021.

Holmes, C. D., 2018: Methane Feedback on Atmospheric Chemistry: Methods, Models, and Mechanisms. *J. Adv. Model. Earth Syst.*, **10 (4)**, 1087–1099, doi:10.1002/2017MS001196.

Holmes, C. D., M. J. Prather, O. A. Søvde, and G. Myhre, 2013: Future methane, hydroxyl, and their uncertainties: Key climate and emission parameters for future predictions. *Atmos. Chem. Phys.*, **13 (1)**, 285–302, doi:10.5194/acp-13-285-2013.

Hoor, P., and Coauthors, 2009: The impact of traffic emissions on atmospheric ozone and OH: Results from QUANTIFY. *Atmos. Chem. Phys.*, **9 (9)**, 3113–3136, doi:10.5194/acp-9-3113-2009.

Hooss, G., R. Voss, K. Hasselmann, E. Maier-Reimer, and F. Joos, 2001: A nonlinear impulse response model of the coupled carbon cycle-climate system (NICCS). *Clim. Dyn.*, **18 (3-4)**, 189–202, doi:10.1007/s003820100170.

Hope, C. W., 2006: The marginal impacts of CO_2, CH_4 and SF_6 emissions. *Clim. Policy*, **6 (5)**, 537–544, doi:10.1080/14693062.2006.9685619.

Horowitz, J. K., and J. Gottlieb, 2010: The Role of Agriculture in Reducing Greenhouse Gas Emissions. Tech. Rep. EB-15, United States Department of Agriculture Economic Research Service. doi:10.22004/ag.econ.138910.

Houweling, S., F. Dentener, and J. Lelieveld, 2000: Simulation of preindustrial atmospheric methane to constrain the global source strength of natural wetlands. *J. Geophys. Res. Atmos.*, **105 (D13)**, 17 243–17 255, doi:10.1029/2000JD900193.

Hristov, A. N., and Coauthors, 2013: Special Topics - Mitigation of methane and nitrous oxide emissions from animal operations: I. A review of enteric methane mitigation options. *J. Anim. Sci.*, **91 (11)**, 5045–5069, doi:10.2527/jas2013-6583.

Hugelius, G., and Coauthors, 2014: Estimated stocks of circumpolar permafrost carbon with quantified uncertainty ranges and identified data gaps. *Biogeosciences*, **11 (23)**, 6573–6593, doi:10.5194/bg-11-6573-2014.

IPCC, 2013: Summary for Policymakers. *Climate Change 2013: The Physical Science Basis. Contribution of Working Group I to the Fifth Assessment Report of the Intergovernmental Panel on Climate Change*, T. Stocker, D. Qin, G.-K. Plattner, M. Tignor, S. Allen, J. Boschung, A. Nauels, Y. Xia, V. Bex, and P. Midgley, Eds., Cambridge University Press, Cambridge, United Kingdom and New York, NY, USA., doi:10.1017/CBO9781107415324.

John, J. G., A. M. Fiore, V. Naik, L. W. Horowitz, and J. P. Dunne, 2012: Climate versus emission drivers of methane lifetime against loss by tropospheric OH from 1860-2100. *Atmos. Chem. Phys.*, **12 (24)**, 12 021–12 036, doi:10.5194/acp-12-12021-2012.

Johnson, K. A., and D. E. Johnson, 1995: Methane emissions from cattle. *J. Anim. Sci.*, **73 (8)**, 2483–2492, doi:10.2527/1995.7382483x.

Joos, F., and M. Bruno, 1996: Pulse response functions are cost-efficient tools to model the link between carbon emissions, atmospheric CO_2 and global warming. *Phys. Chem. Earth*, **21 (5-6)**, 471–476, doi:10.1016/S0079-1946(97)81144-5.

Joos, F., G. K. Plattner, and T. F. Stocker, 1999: Global warming and marine carbon cycle feedbacks on future atmospheric CO_2. *Science*, doi:10.1126/science.284.5413.464.

Joos, F., and Coauthors, 2013: Carbon dioxide and climate impulse response functions for the computation of greenhouse gas metrics: A multi-model analysis. *Atmos. Chem. Phys.*, **13 (5)**, 2793–2825, doi:10.5194/acp-13-2793-2013.

Kaplan, J., G. Folberth, and D. Hauglustaine, 2006: The role of methane and biogenic volatile organic compound sources in late glacial and Holocene fluctuations of atmospheric methane concentrations. *Global Biogeochem. Cycles*, **20**, doi:10.1029/2005GB002590.

Karacan, C. Ö., F. A. Ruiz, M. Cotè, and S. Phipps, 2011: Coal mine methane: A review of capture and utilization practices with benefits to mining safety and to greenhouse gas reduction. *Int. J. Coal Geol.*, **86 (2-3)**, 121–156, doi:10.1016/j.coal.2011.02.009.

Karakurt, I., G. Aydin, and K. Aydiner, 2012: Sources and mitigation of methane emissions by sectors: A critical review. *Renew. Energy*, **39 (1)**, 40–48, doi:https://doi.org/10.1016/j.renene.2011.09.006.

Kaya, Y., 1989: Impact of carbon dioxide emission control on GNP growth: interpretation of proposed scenarios. *IPCC Response Strategies Working Group Memorandum 1989*, IPCC Energy and Industry Subgroup, Response Strategies Working Group.

Keeling, C. D., R. B. Bacastow, A. E. Bainbridge, C. A. Ekdahl Jr., P. R. Guenther, L. S. Waterman, and J. F. S. Chin, 1976: Atmospheric carbon dioxide variations at Mauna Loa Observatory, Hawaii. *Tellus*, **28**, 538–551, doi:10.3402/tellusa.v28i6.11322.

Kip, N., and Coauthors, 2010: Global prevalence of methane oxidation by symbiotic bacteria in peat-moss ecosystems. *Nat. Geosci.*, **3 (9)**, 617–621, doi:10.1038/ngeo939.

Kirschke, S., and Coauthors, 2013: Three decades of global methane sources and sinks. *Nat. Geosci.*, **6 (10)**, 813–823, doi:10.1038/ngeo1955.

Knapp, J., G. Laur, P. Vadas, W. Weiss, and J. Tricarico, 2014: Invited review: Enteric methane in dairy cattle production: Quantifying the opportunities and impact of reducing emissions. *J. Dairy Sci.*, **97 (6)**, 3231–3261, doi:10.3168/jds.2013-7234.

Knutti, R., and J. Sedláček, 2013a: Robustness and uncertainties in the new CMIP5 climate model projections. *Nat. Clim. Chang.*, **3 (4)**, 369–373, doi:10.1038/nclimate1716.

Knutti, R., and J. Sedláček, 2013b: Robustness and uncertainties in the new CMIP5 climate model projections. *Nat. Clim. Chang.*, **3 (4)**, 369–373, doi:10.1038/nclimate1716.

Koven, C. D., and Coauthors, 2015: A simplified, data-constrained approach to estimate the permafrost carbon–climate feedback. *Philos. Trans. R. Soc. A Math. Phys. Eng. Sci.*, **373 (2054)**, 20140 423, doi:10.1098/rsta.2014.0423.

Kriegler, E., and Coauthors, 2017: Fossil-fueled development SSP5: An energy and resource intensive scenario for the 21st century. *Glob. Environ. Change*, **42**, 297–315, doi:10.1016/j.gloenvcha.2016.05.015.

Krol, M. C., and M. Van Weele, 1997: Implications of variations in photodissociation rates for global tropospheric chemistry. *Atmos. Environ.*, **31 (9)**, 1257–1273, doi:10.1016/S1352-2310(96)00323-8.

Kumari, S., M. Hiloidhari, S. Naik, and R. Dahiya, 2019: Social cost of methane: Method and estimates for Indian livestock. *Environ. Dev.*, **32**, 100 462, doi:10.1016/j.envdev.2019.100462.

Lamarque, J.-F., and Coauthors, 2010: Historical (1850–2000) gridded anthropogenic and biomass burning emissions of reactive gases and aerosols: methodology and application. *Atmos. Chem. Phys.*, **10 (15)**, 7017–7039, doi:10.5194/acp-10-7017-2010.

Lamb, B. K., and Coauthors, 2015: Direct Measurements Show Decreasing Methane Emissions from Natural Gas Local Distribution Systems in the United States. *Environ. Sci. Technol.*, **49 (8)**, 5161–5169, doi:10.1021/es505116p.

Le Quéré, C., and Coauthors, 2018: Global Carbon Budget 2018. *Earth Syst. Sci. Data*, **10 (4)**, 2141–2194, doi:10.5194/essd-10-2141-2018.

Leach, N. J., and Coauthors, 2020: GIR v1.0.0: a generalised impulse-response model for climate uncertainty and future scenario exploration. *Geosci. Model Dev. Discuss.*, **in review**, 1–29, doi:10.5194/gmd-2019-379.

Leggett, J., W. J. Pepper, R. J. Swart, J. Edmonds, L. Meira Filho, I. Mintzer, and M. Wang, 1992: Emissions scenarios for IPCC: An update. *Climate Change 1992 - The Supplementary Report to the IPCC Scientific Assessment.*, Cambridge University Press, United Kingdom.

Lelieveld, J., F. J. Dentener, W. Peters, and M. C. Krol, 2004: On the role of hydroxyl radicals in the self-cleansing capacity of the troposphere. *Atmos. Chem. Phys.*, **4 (9/10)**, 2337–2344, doi:10.5194/acp-4-2337-2004.

Libardoni, A. G., and C. E. Forest, 2011: Sensitivity of distributions of climate system properties to the surface temperature dataset. *Geophys. Res. Lett.*, **38 (22)**, doi:10.1029/2011GL049431.

Libardoni, A. G., C. E. Forest, A. P. Sokolov, and E. Monier, 2018a: Baseline evaluation of the impact of updates to the MIT Earth System Model on its model parameter estimates. *Geosci. Model Dev.*, **11 (8)**, 3313–3325, doi:10.5194/gmd-11-3313-2018.

Libardoni, A. G., C. E. Forest, A. P. Sokolov, and E. Monier, 2018b: Estimates of climate system properties incorporating recent climate change. *Geosci. Model Dev.*, **11**, 3313–3325, doi:0.5194/gmd-11-3313-2018.

Libardoni, A. G., C. E. Forest, A. P. Sokolov, and E. Monier, 2019: Underestimating Internal Variability Leads to Narrow Estimates of Climate System Properties. *Geophys. Res. Lett.*, **46 (16)**, 10 000–10 007, doi:10.1029/2019GL082442.

Lipper, L., and Coauthors, 2014: Climate-Smart Agriculture for food security. *Nat. Clim. Chang.*, **4 (12)**, 1068–1072, doi:10.1038/nclimate2437.

Liu, Y., 1996: Modeling the Emissions of Nitrous Oxide (N_2O) and Methane (CH_4) from the Terrestrial Biosphere to the Atmosphere. Ph.D. thesis, Massachusetts Institute of Technology, Cambridge, MA.

Loulergue, L., and Coauthors, 2008: Orbital and millennial-scale features of atmospheric CH_4 over the past 800,000 years. *Nature*, **453 (7193)**, 383–386, doi:10.1038/nature06950.

Luderer, G., R. C. Pietzcker, C. Bertram, E. Kriegler, M. Meinshausen, and O. Edenhofer, 2013: Economic mitigation challenges: how further delay closes the door for achieving climate targets. *Environ. Res. Lett.*, **8 (3)**, 034 033, doi:10.1088/1748-9326/8/3/034033.

Maier-Reimer, E., and K. Hasselmann, 1987: Transport and storage of CO_2 in the ocean - an inorganic ocean-circulation carbon cycle model. *Clim. Dyn.*, **2 (2)**, 63–90, doi:10.1007/BF01054491.

Manne, A. S., and R. G. Richels, 2005: Merge: An Integrated Assessment Model for Global Climate Change. *Energy Environ.*, Springer-Verlag, New York, 175–189, doi: 10.1007/0-387-25352-1_7.

Marten, A. L., E. a. Kopits, C. W. Griffiths, S. C. Newbold, and A. Wolverton, 2015: Incremental CH_4 and N_2O mitigation benefits consistent with the US Government's $SC-CO_2$ estimates. *Clim. Policy*, **15 (2)**, 272–298, doi:10.1080/14693062.2014.912981.

Marten, A. L., and S. C. Newbold, 2012: Estimating the social cost of non-CO_2 GHG emissions: Methane and nitrous oxide. *Energy Policy*, **51**, 957–972, doi:10.1016/j.enpol.2012.09.073.

Matthews, E., and I. Fung, 1987: Methane emission from natural wetlands: Global distribution, area, and environmental characteristics of sources. *Global Biogeochem. Cycles*, **1 (1)**, 61–86, doi:10.1029/GB001i001p00061.

Matthews, H. D., and K. Caldeira, 2008: Stabilizing climate requires near-zero emissions. *Geophys. Res. Lett.*, **35 (4)**, 1–5, doi:10.1029/2007GL032388.

Mc Geough, E., S. Little, H. Janzen, T. McAllister, S. McGinn, and K. Beauchemin, 2012: Life-cycle assessment of greenhouse gas emissions from dairy production in Eastern Canada: A case study. *J. Dairy Sci.*, **95 (9)**, 5164–5175, doi:10.3168/jds.2011-5229.

McGuffie, K., and A. Henderson-Sellers, 2005: *A Climate Modeling Primer*. 3rd ed., John Wiley & Sons, Ltd, Chichester, UK, doi:10.1002/0470857617.

McGuffie, K., and A. Henderson-Sellers, 2014: *A Climate Modeling Primer*. 4th ed., Wiley & Sons, Ltd, Chichester, UK.

Meehl, G. A., C. A. Senior, V. Eyring, G. Flato, J.-F. Lamarque, R. J. Stouffer, K. E. Taylor, and M. Schlund, 2020: Context for interpreting equilibrium climate sensitivity and transient climate response from the CMIP6 Earth system models. *Sci. Adv.*, **6 (26)**, eaba1981, doi: 10.1126/sciadv.aba1981.

Meinshausen, M., N. Meinshausen, W. Hare, S. C. Raper, K. Frieler, R. Knutti, D. J. Frame, and M. R. Allen, 2009: Greenhouse-gas emission targets for limiting global warming to 2 °C. *Nature*, **458 (7242)**, 1158–1162, doi:10.1038/nature08017.

Meinshausen, M., S. C. Raper, and T. M. Wigley, 2011a: Emulating coupled atmosphere-ocean and carbon cycle models with a simpler model, MAGICC6 - Part 1: Model description and calibration. *Atmos. Chem. Phys.*, **11 (4)**, 1417–1456, doi:10.5194/acp-11-1417-2011.

Meinshausen, M., and Coauthors, 2011b: The RCP greenhouse gas concentrations and their extensions from 1765 to 2300. *Clim. Change*, **109 (1)**, 213–241, doi:10.1007/s10584-011-0156-z.

Mendelsohn, R., M. Schlesinger, and L. Williams, 2000: Comparing impacts across climate models. *Integr. Assess.*, **1 (1)**, 37–48, doi:10.1023/A:1019111327619.

Metcalf, G. E., and J. H. Stock, 2017: Integrated Assessment Models and the Social Cost of Carbon: A Review and Assessment of U.S. Experience. *Review of Environmental Economics and Policy*, **11 (1)**, 80–99, doi:10.1093/reep/rew014.

Metropolis, N., A. W. Rosenbluth, M. N. Rosenbluth, A. H. Teller, and E. Teller, 1953: Equation of state calculations by fast computing machines. *J. Chem. Phys.*, **21 (6)**, 1087–1092, doi:10.1063/1.1699114.

Milkov, A. V., 2005: Molecular and stable isotope compositions of natural gas hydrates: A revised global dataset and basic interpretations in the context of geological settings. *Org. Geochem.*, **36 (5)**, 681–702, doi:10.1016/j.orggeochem.2005.01.010.

Millar, J. R., Z. R. Nicholls, P. Friedlingstein, and M. R. Allen, 2017: A modified impulse-response representation of the global near-surface air temperature and atmospheric concentration response to carbon dioxide emissions. *Atmos. Chem. Phys.*, **17 (11)**, 7213–7228, doi:10.5194/acp-17-7213-2017.

Montes, F., and Coauthors, 2013: Special Topics - Mitigation of methane and nitrous oxide emissions from animal operations: II. A review of manure management mitigation options. *J. Anim. Sci.*, **91 (11)**, 5070–94, doi:10.2527/jas2013-6584.

Montzka, S. A., E. J. Dlugokencky, and J. H. Butler, 2011: Non-CO_2 greenhouse gases and climate change. *Nature*, **476 (7358)**, 43–50, doi:10.1038/nature10322.

Morgenstern, O., and Coauthors, 2018: Ozone sensitivity to varying greenhouse gases and ozone-depleting substances in CCMI-1 simulations. *Atmos. Chem. Phys.*, **18 (2)**, 1091–1114, doi:10.5194/acp-18-1091-2018.

Moss, R. H., and Coauthors, 2010: The next generation of scenarios for climate change research and assessment. *Nature*, **463 (7282)**, 747–756, doi:10.1038/nature08823.

Murray, C., and J. Riley, 1971: The solubility of gases in distilled water and sea water—IV. Carbon dioxide. *Deep Sea Res. Oceanogr. Abstr.*, **18 (5)**, 533–541, doi:10.1016/0011-7471(71)90077-5.

Myhre, G., and Coauthors, 2013: Chapter 8: Anthropogenic and Natural Radiative Forcing. *Climate Change 2013: The Physical Science Basis. Contribution of Working Group I to the Fifth Assessment Rep. of the Intergovernmental Panel on Climate Change*, Cambridge University Press, Cambridge, United Kingdom and New York, NY, USA.

Naik, V., and Coauthors, 2013: Preindustrial to present-day changes in tropospheric hydroxyl radical and methane lifetime from the Atmospheric Chemistry and Climate Model Intercomparison Project (ACCMIP). *Atmos. Chem. Phys.*, **13 (10)**, 5277–5298, doi:10.5194/acp-13-5277-2013.

National Academies, 2017: *Valuing Climate Damages: Updating Estimation of the Social Cost of Carbon Dioxide*. The National Academies Press, Washington, DC, doi:10.17226/24651.

Nisbet, E. G., and Coauthors, 2016: Rising atmospheric methane: 2007-2014 growth and isotopic shift. *Global Biogeochem. Cycles*, **30 (9)**, 1356–1370, doi:10.1002/2016GB005406.

Nisbet, E. G., and Coauthors, 2020: Methane Mitigation: Methods to Reduce Emissions, on the Path to the Paris Agreement. *Rev. Geophys.*, **58 (1)**, e2019RG000 675, doi:10.1029/2019RG000675.

Norby, R. J., and Coauthors, 2005: Forest response to elevated CO_2 is conserved across a broad range of productivity. *Proc. Natl. Acad. Sci.*, **102 (50)**, 18 052–18 056, doi:10.1073/pnas.0509478102.

Nordhaus, W. D., 2017: Revisiting the social cost of carbon. *Proc. Natl. Acad. Sci.*, **114 (7)**, 1518–1523, doi:10.1073/pnas.1609244114.

North, G. R., R. F. Cahalan, and J. A. Coakley Jr., 1981: Energy balance climate models. *Rev. Geophys.*, **19 (1)**, 91–121, doi:10.1029/RG019i001p00091.

Olivié, D. J., and G. P. Peters, 2013: Variation in emission metrics due to variation in CO_2 and temperature impulse response functions. *Earth Syst. Dyn.*, **4**, 267–286, doi:10.5194/esd-4-267-2013.

Paltsev, S., and Coauthors, 2005: The MIT Emissions Prediction and Policy Analysis (EPPA) model version 4. Tech. Rep. 125, MIT Joint Program on the Science and Policy of Global Change, Cambridge, MA.

Papamarkou, T., 2018: The Julia Klara package provides a generic engine for Markov Chain Monte Carlo (MCMC) inference. GitHub, github.com/JuliaStats/Klara.jl.

Paudel, R., N. M. Mahowald, P. G. M. Hess, L. Meng, and W. J. Riley, 2016: Attribution of changes in global wetland methane emissions from pre-industrial to present using CLM4.5-BGC. *Environ. Res. Lett.*, **11 (3)**, 34 020, doi:10.1088/1748-9326/11/3/034020.

Pearce, D., 2003: The Social Cost of Carbon and its Policy Implications. *Oxford Rev. Econ. Policy*, **19 (3)**, 362–384, doi:10.1093/oxrep/19.3.362.

Persson, U. M., D. J. Johansson, C. Cederberg, F. Hedenus, and D. Bryngelsson, 2015: Climate metrics and the carbon footprint of livestock products: Where's the beef? *Environ. Res. Lett.*, **10 (3)**, 034 005, doi:10.1088/1748-9326/10/3/034005.

Poulter, B., and Coauthors, 2017: Global wetland contribution to 2000–2012 atmospheric methane growth rate dynamics. *Environ. Res. Lett.*, **12 (9)**, 094 013, doi:10.1088/1748-9326/aa8391.

Prather, M. J., 1994: Lifetimes and eigenstates in atmospheric chemistry. *Geophys. Res. Lett.*, **21 (9)**, 801–804, doi:10.1029/94GL00840.

Prather, M. J., 1996: Time scales in atmospheric chemistry: Theory, GWPs for CH_4 and CO, and runaway growth. *Geophys. Res. Lett.*, **23 (19)**, 2597–2600, doi:10.1029/96GL02371.

Prather, M. J., C. D. Holmes, and J. Hsu, 2012: Reactive greenhouse gas scenarios: Systematic exploration of uncertainties and the role of atmospheric chemistry. *Geophys. Res. Lett.*, **39 (9)**, doi:10.1029/2012GL051440.

Pratt, C., and K. Tate, 2018: Mitigating Methane: Emerging Technologies To Combat Climate Change's Second Leading Contributor. *Environ. Sci. Technol.*, **52 (11)**, 6084–6097, doi:10.1021/acs.est.7b04711.

Ramaswamy, V., and Coauthors, 2001: Radiative Forcing of Climate Change in Climate Change. Chapter 6. *Climate Change 2001: The Scientific Basis – Contribution of Working Group I to the Third Assessment Report of the Intergovernmental Panel on Climate Change*, Cambridge University Press, United Kingdom.

Ramsey, F. P., 1928: A Mathematical Theory of Saving. *Econ. J.*, **38 (152)**, 543, doi:10.2307/2224098.

Ranson, M., L. Tarquinio, and A. Lew, 2016: Modeling the Impact of Climate Change on Extreme Weather Losses. NCEE Working Paper Series 201602, National Center for Environmental Economics, EPA.

Reay, D., E. Davidson, K. Smith, P. Smith, J. Melillo, F. Dentener, and P. Crutzen, 2012: Global agriculture and nitrous oxide emissions. *Nat. Clim. Chang.*, **2 (6)**, 410–416, doi: DOI:10.1038/NCLIMATE1458.

Reay, D. S., P. Smith, T. R. Christensen, R. H. James, and H. Clark, 2018: Methane and Global Environmental Change. *Annu. Rev. Environ. Resour.*, **43 (1)**, 165–192, doi:10.1146/annurev-environ-102017-030154.

Reilly, J., and Coauthors, 2012: Using land to mitigate climate change: Hitting the target, recognizing the trade-offs. *Environ. Sci. Technol.*, **46 (11)**, 5672–5679, doi:10.1021/es2034729.

Reisinger, A., and H. Clark, 2018: How much do direct livestock emissions actually contribute to global warming? *Glob. Chang. Biol.*, **24 (4)**, 1749–1761, doi:10.1111/gcb.13975.

Revelle, R., and H. E. Suess, 1957: Carbon Dioxide Exchange Between Atmosphere and Ocean and the Question of an Increase of Atmospheric CO_2 during the Past Decades. *Tellus*, **9 (1)**, 18–27, doi:10.1111/j.2153-3490.1957.tb01849.x.

Ricciuto, D. M., K. J. Davis, and K. Keller, 2008: A Bayesian calibration of a simple carbon cycle model: The role of observations in estimating and reducing uncertainty. *Global Biogeochem. Cycles*, **22 (2)**, doi:10.1029/2006GB002908.

Rigby, M., and Coauthors, 2008: Renewed growth of atmospheric methane. *Geophys. Res. Lett.*, **35 (22)**, L22 805, doi:10.1029/2008GL036037.

Rigby, M., and Coauthors, 2017: Role of atmospheric oxidation in recent methane growth. *Proc. Natl. Acad. Sci.*, **114 (21)**, 5373–5377, doi:10.1073/pnas.1616426114.

Rogelj, J., M. Meinshausen, M. Schaeffer, R. Knutti, and K. Riahi, 2015: Impact of short-lived non-CO_2 mitigation on carbon budgets for stabilizing global warming. *Environ. Res. Lett.*, **10 (7)**, 075 001, doi:10.1088/1748-9326/10/7/075001.

Rogelj, J., and Coauthors, 2018: Chapter 2: Mitigation pathways compatible with 1.5°C in the context of sustainable development. *Global Warming of 1.5 °C an IPCC special report on the impacts of global warming of 1.5 °C above pre-industrial levels and related global greenhouse gas emission pathways, in the context of strengthening the global response to the threat of climate change*, Cambridge University Press, United Kingdom.

Rolph, K. A., C. E. Forest, and M. D. Ruark, 2019: The role of non-CO_2 mitigation options within the dairy industry for pursuing climate change targets . *Environ. Res. Lett.*, **14 (8)**, 084 039, doi:10.1088/1748-9326/ab28a3.

Rose, S. K., D. B. Diaz, and G. J. Blanford, 2017: Understanding the social cost of carbon: a model diagnostic and inter-comparison study. *Clim. Chang. Econ.*, **08 (02)**, 1750 009, doi:10.1142/S2010007817500099.

Rowlinson, M. J., and Coauthors, 2019: Impact of El Niño–Southern Oscillation on the interannual variability of methane and tropospheric ozone. *Atmos. Chem. Phys.*, **19 (13)**, 8669–8686, doi:10.5194/acp-19-8669-2019.

Ruckert, K. L., Y. Guan, A. M. Bakker, C. E. Forest, and K. Keller, 2017: The effects of time-varying observation errors on semi-empirical sea-level projections. *Clim. Change*, **140 (3-4)**, 349–360, doi:10.1007/s10584-016-1858-z.

Sanderson, B. M., B. C. O'Neill, and C. Tebaldi, 2016: What would it take to achieve the Paris temperature targets? *Geophys. Res. Lett.*, **43 (13)**, 7133–7142, doi:10.1002/2016GL069563.

Sarmiento, J. L., T. M. C. Hughes, R. J. Stouffer, and S. Manabe, 1998: Simulated response of the ocean carbon cycle to anthropogenic climate warming. *Nature*, **393 (6682)**, 245–249, doi:10.1038/30455.

Sarmiento, J. L., J. C. Orr, and U. Siegenthaler, 1992: A perturbation simulation of CO_2 uptake in an ocean general circulation model. *Journal of Geophysical Research*, **97 (C3)**, 3621, doi:10.1029/91JC02849.

Saunois, M., and Coauthors, 2016: The global methane budget 2000-2012. *Earth Syst. Sci. Data*, **8 (2)**, 697–751, doi:10.5194/essd-8-697-2016.

Saunois, M., and Coauthors, 2020: The Global Methane Budget 2000–2017. *Earth Syst. Sci. Data*, **12 (3)**, 1561–1623, doi:10.5194/essd-12-1561-2020.

Schaefer, H., and Coauthors, 2016: A 21st-century shift from fossil-fuel to biogenic methane emissions indicated by 13CH4. *Science (80-.).*, **352 (6281)**, 80–84, doi:10.1126/science.aad2705.

Schlosser, C. A., D. Kicklighter, and A. Sokolov, 2007: A Global Land System Framework for Integrated Climate-Change Assessments. Tech. Rep. 147, MIT Joint Program on the Science and Policy of Global Change, Cambridge, MA.

Schneider, S. H., 1997: Integrated assessment modeling of global climate change: Transparent rational tool for policy making or opaque screen hiding value-laden assumptions? *Environ. Model. Assess.*, **2 (4)**, 229–249, doi:10.1023/A:1019090117643.

Schuur, E. A. G., and Coauthors, 2015: Climate change and the permafrost carbon feedback. *Nature*, **520 (7546)**, 171–179, doi:10.1038/nature14338.

Schwalm, C. R., S. Glendon, and P. B. Duffy, 2020: RCP8.5 tracks cumulative CO_2 emissions. *Proc. Natl. Acad. Sci.*, **117 (33)**, 19 656–19 657, doi:10.1073/pnas.2007117117.

Schwarber, A. K., S. J. Smith, C. A. Hartin, B. A. Vega-Westhoff, and R. Sriver, 2019: Evaluating climate emulation: fundamental impulse testing of simple climate models. *Earth Syst. Dyn.*, **10 (4)**, 729–739, doi:10.5194/esd-10-729-2019.

Shindell, D., J. S. Fuglestvedt, and W. J. Collins, 2017: The Social Cost of Methane: Theory and Applications. *Faraday Discuss.*, **200**, 429–451, doi:10.1039/C7FD00009J.

Smith, C. J., P. M. Forster, M. Allen, N. Leach, R. J. Millar, G. A. Passerello, and L. A. Regayre, 2018: FAIR v1.3: A simple emissions-based impulse response and carbon cycle model. *Geosci. Model Dev.*, **11 (6)**, 2273–2297, doi:10.5194/gmd-11-2273-2018.

Smith, M. J., and Coauthors, 2014: Changing how earth system modeling is done to provide more useful information for decision making, science, and society. *Bull. Am. Meteorol. Soc.*, **95 (9)**, 1453–1464, doi:10.1175/BAMS-D-13-00080.1.

Smith, P., and Coauthors, 2008: Greenhouse gas mitigation in agriculture. *Philos. Trans. R. Soc. B Biol. Sci.*, **363 (1492)**, 789–813, doi:10.1098/rstb.2007.2184.

Smith, S. J., and J. A. Edmonds, 2006: The economic implications of carbon cycle uncertainty. *Tellus B*, **58 (5)**, 586–590, doi:10.1111/j.1600-0889.2006.00217.x.

Sokolov, A., and Coauthors, 2018: Description and Evaluation of the MIT Earth System Model (MESM). *J. Adv. Model. Earth Syst.*, **10 (8)**, 1759–1789, doi:10.1029/2018MS001277.

Sokolov, A. P., D. W. Kicklighter, J. M. Melillo, B. S. Felzer, C. A. Schlosser, and T. W. Cronin, 2008: Consequences of considering carbon-nitrogen interactions on the feedbacks between climate and the terrestrial carbon cycle. *J. Clim.*, **21 (15)**, 3776–3796, doi:10.1175/2008JCLI2038.1.

Sokolov, A. P., and P. H. Stone, 1998: A flexible climate model for use in integrated assessments. *Clim. Dyn.*, **14 (4)**, 291–303, doi:10.1007/s003820050224.

Sokolov, A. P., and Coauthors, 2005: The MIT Integrated Global System Model (IGSM) Version 2: Model Description and Baseline Evaluation. Tech. Rep. 124, MIT Joint Program on the Science and Policy of Global Change, Cambridge, MA.

Stanley, E. H., N. J. Casson, S. T. Christel, J. T. Crawford, L. C. Loken, and S. K. Oliver, 2016: The ecology of methane in streams and rivers: patterns, controls, and global significance. *Ecol. Monogr.*, **86 (2)**, 146–171, doi:10.1890/15-1027.

Stern, N., 2008: The Economics of Climate Change. *Am. Econ. Rev.*, **98 (2)**, 1–37, doi: 10.1257/aer.98.2.1.

Strassmann, K. M., and F. Joos, 2018: The Bern Simple Climate Model (BernSCM) v1.0: an extensible and fully documented open-source re-implementation of the Bern reduced-form model for global carbon cycle–climate simulations. *Geosci. Model Dev.*, **11 (5)**, 1887–1908, doi:10.5194/gmd-11-1887-2018.

Thompson, T. M., 2018: Modeling the climate and carbon systems to estimate the social cost of carbon. *Wiley Interdiscip. Rev. Clim. Chang.*, **9 (5)**, 1–12, doi:10.1002/wcc.532.

Tol, R. S., 2006: Multi-Gas Emission Reduction for Climate Change Policy: An Application of Fund. *Energy J.*, **SI2006 (01)**, doi:10.5547/ISSN0195-6574-EJ-VolSI2006-NoSI3-11.

Tol, R. S., and S. Fankhauser, 1998: On the representation of impact in integrated assessment models of climate change. *Environ. Model. Assess.*, **3 (1)**, 63–74, doi:10.1023/A: 1019050503531.

Tol, R. S. J., 2001: Equitable cost-benefit analysis of climate change policies. *Ecol. Econ.*, **36 (1)**, 71–85, doi:10.1016/S0921-8009(00)00204-4.

Tol, R. S. J., 2005: The marginal damage costs of carbon dioxide emissions: an assessment of the uncertainties. *Energy Policy*, **33 (16)**, 2064–2074, doi:10.1016/j.enpol.2004.04.002.

Tol, R. S. J., T. K. Berntsen, B. C. O'Neill, J. S. Fuglestvedt, and K. P. Shine, 2012: A unifying framework for metrics for aggregating the climate effect of different emissions. *Environ. Res. Lett.*, **7 (4)**, 044 006, doi:10.1088/1748-9326/7/4/044006.

Tubiello, F., and Coauthors, 2014: Agriculture , Forestry and Other Land Use Emissions by Sources and Removals by Sinks. techreport ESS Work. Pap. No.2, FAO, 4–89 pp.

Tubiello, F. N., M. Salvatore, S. Rossi, A. Ferrara, N. Fitton, and P. Smith, 2013: The FAOSTAT database of greenhouse gas emissions from agriculture. *Environ. Res. Lett.*, **8 (1)**, 015 009, doi:10.1088/1748-9326/8/1/015009.

Turner, A. J., C. Frankenberg, and E. A. Kort, 2019: Interpreting contemporary trends in atmospheric methane. *Proc. Natl. Acad. Sci. U. S. A.*, **116 (8)**, 2805–2813, doi:10.1073/pnas. 1814297116.

UNFCCC, 2015: Paris Agreement. *Report of the Conference of the Parties to the United Nations Framework Convention on Climate Change.*

Valdes, P. J., D. J. Beerling, and C. E. Johnson, 2005: The ice age methane budget. *Geophys. Res. Lett.*, **32 (2)**, doi:10.1029/2004GL021004.

van der Werf, G. R., and Coauthors, 2017: Global fire emissions estimates during 1997–2016. *Earth Syst. Sci. Data*, **9 (2)**, 697–720, doi:10.5194/essd-9-697-2017.

van Vuuren, D. P., J. Weyant, and F. de la Chesnaye, 2006: Multi-gas scenarios to stabilize radiative forcing. *Energy Econ.*, **28 (1)**, 102–120, doi:10.1016/j.eneco.2005.10.003.

van Vuuren, D. P., and Coauthors, 2011a: How well do integrated assessment models simulate climate change? *Clim. Change*, **104 (2)**, 255–285, doi:10.1007/s10584-009-9764-2.

van Vuuren, D. P., and Coauthors, 2011b: The representative concentration pathways: An overview. *Clim. Change*, **109 (1)**, 5–31, doi:10.1007/s10584-011-0148-z, 9605103.

van Vuuren, D. P., and Coauthors, 2017: Energy, land-use and greenhouse gas emissions trajectories under a green growth paradigm. *Glob. Environ. Change*, **42**, 237–250, doi:10.1016/j.gloenvcha.2016.05.008.

VanderZaag, A. C., H. Baldé, A. Crolla, R. J. Gordon, N. M. Ngwabie, C. Wagner-Riddle, R. Desjardins, and J. D. MacDonald, 2018: Potential methane emission reductions for two manure treatment technologies. *Environ. Technol.*, **39 (7)**, 851–858, doi:10.1080/09593330.2017.1313317.

Veltman, K., and Coauthors, 2018: A quantitative assessment of Beneficial Management Practices to reduce carbon and reactive nitrogen footprints and phosphorus losses on dairy farms in the US Great Lakes region. *Agric. Syst.*, **166**, 10 – 25, doi:10.1016/j.agsy.2018.07.005.

Vihola, M., 2012: Robust adaptive Metropolis algorithm with coerced acceptance rate. *Stat. Comput.*, **22 (5)**, 997–1008, doi:10.1007/s11222-011-9269-5, 1011.4381.

Voulgarakis, A., and Coauthors, 2013: Analysis of present day and future OH and methane lifetime in the ACCMIP simulations. *Atmos. Chem. Phys.*, **13**, doi:10.5194/acp-13-2563-2013.

Waldhoff, S., D. Anthoff, S. Rose, and R. S. J. Tol, 2014: The Marginal Damage Costs of Different Greenhouse Gases: An Application of FUND. *Economics: The Open-Access*, **8 (2014-31)**, 1, doi:10.5018/economics-ejournal.ja.2014-31.

Wallmann, K., E. Pinero, E. Burwicz, M. Haeckel, C. Hensen, A. Dale, and L. Ruepke, 2012: The Global Inventory of Methane Hydrate in Marine Sediments: A Theoretical Approach. *Energies*, **5 (7)**, 2449–2498, doi:10.3390/en5072449.

Wang, C., R. G. Prinn, and A. Sokolov, 1998: A global interactive chemistry and climate model: formulation and testing. *J. Geophys. Res. Atmos.*, **103 (D3)**, 3399–3417, doi:10.1029/97JD03465.

Wania, R., and Coauthors, 2013: Present state of global wetland extent and wetland methane modelling: methodology of a model inter-comparison project (WETCHIMP). *Geosci. Model Dev.*, **6 (3)**, 617–641, doi:10.5194/gmd-6-617-2013.

Weber, S. L., 2010: The utility of Earth system Models of Intermediate Complexity (EMICs). *Wiley Interdiscip. Rev. Clim. Chang.*, **1 (2)**, 243–252, doi:10.1002/wcc.24.

Weiler, V., H. M. Udo, T. Viets, T. A. Crane, and I. De Boer, 2014: Handling multi-functionality of livestock in a life cycle assessment: the case of smallholder dairying in Kenya. *Curr. Opin. Environ. Sustain.*, **8**, 29–38, doi:10.1016/j.cosust.2014.07.009.

Weyant, J., 2017: Some contributions of integrated assessment models of global climate change. *Rev. Environ. Econ. Policy*, **11 (1)**, 115–137, doi:10.1093/reep/rew018.

Wolff, E. W., J. G. Shepherd, E. Shuckburgh, and A. J. Watson, 2015: Feedbacks on climate in the Earth system: introduction. *Phil. Trans. R. Soc. S-A*, **373 (20140428)**, doi:10.1098/rsta.2014.0428.

Wollenberg, E., and Coauthors, 2016: Reducing emissions from agriculture to meet the 2 °C. *Glob. Chang. Biol.*, **22 (12)**, 3859–3864, doi:10.1111/gcb.13340.

Xu, J., R. E. Grumbine, A. Shrestha, M. Eriksson, X. Yang, Y. WAng, and A. Wilkes, 2009: The Melting Himalayas: Cascading Effects of Climate Change on Water, Biodiversity, and Livelihoods. *Conserv. Biol.*, **23 (3)**, 520–530, doi:10.1111/j.1523-1739.2009.01237.x.

Xu, Y., and V. Ramanathan, 2017: Well below 2 °C: Mitigation strategies for avoiding dangerous to catastrophic climate changes. *Proc. Natl. Acad. Sci.*, **114 (39)**, 10 315–10 323, doi:10.1073/pnas.1618481114.

Yan, M.-J., J. Humphreys, and N. M. Holden, 2013: Evaluation of process and input-output-based life-cycle assessment of Irish milk production. *J. Agric. Sci.*, **151 (5)**, 701–713, doi:10.1017/S0021859613000257.

Yan, Y., and Coauthors, 2019: Two-million-year-old snapshots of atmospheric gases from Antarctic ice. *Nature*, **574 (7780)**, 663–666, doi:10.1038/s41586-019-1692-3.

Yvon-Durocher, G., A. P. Allen, D. Bastviken, R. Conrad, C. Gudasz, A. St-Pierre, N. Thanh-Duc, and P. A. Del Giorgio, 2014: Methane fluxes show consistent temperature dependence across microbial to ecosystem scales. *Nature*, **507 (7493)**, 488–491, doi:10.1038/nature13164.

Zeebe, R. E., 2013: What caused the long duration of the Paleocene-Eocene Thermal Maximum? *Paleoceanography*, **28 (3)**, 440–452, doi:10.1002/palo.20039.

Zellner, A., and G. C. Tiao, 1964: Bayesian Analysis of the Regression Model with Autocorrelated Errors. *J. Am. Stat. Assoc.*, **59 (307)**, 763–778, doi:10.1080/01621459.1964.10480726.

Zhang, Y., B. McCarl, and J. Jones, 2017: An Overview of Mitigation and Adaptation Needs and Strategies for the Livestock Sector. *Climate*, **5 (4)**, 95, doi:10.3390/cli5040095.

Zhao, Y., and Coauthors, 2019: Inter-model comparison of global hydroxyl radical (OH) distributions and their impact on atmospheric methane over the 2000–2016 period. *Atmos. Chem. Phys.*, **19 (21)**, 13 701–13 723, doi:10.5194/acp-19-13701-2019.

Zhuang, Q., J. M. Melillo, D. W. Kicklighter, R. G. Prinn, A. D. McGuire, P. A. Steudler, B. S. Felzer, and S. Hu, 2004: Methane fluxes between terrestrial ecosystems and the atmosphere at northern high latitudes during the past century: A retrospective analysis with a process-based biogeochemistry model. *Global Biogeochem. Cycles*, **18 (3)**, doi:10.1029/2004GB002239.

Zickfeld, K., M. Eby, H. D. Matthews, A. Schmittner, and A. J. Weaver, 2011: Nonlinearity of Carbon Cycle Feedbacks. *J. Clim.*, **24 (16)**, 4255–4275, doi:10.1175/2011JCLI3898.1.

Zickfeld, K., and T. Herrington, 2015: The time lag between a carbon dioxide emission and maximum warming increases with the size of the emission. *Environ. Res. Lett.*, **10 (3)**, 31 001, doi:10.1088/1748-9326/10/3/031001.

Zickfeld, K., and Coauthors, 2013: Long-Term Climate Change Commitment and Reversibility: An EMIC Intercomparison. *J. Clim.*, **26 (16)**, 5782–5809, doi:10.1175/JCLI-D-12-00584.1.

<div align="center">

Vita
Kristina Alixis Rolph

</div>

kar5469@psu.edu

(301) 821-7554

Education

Ph.D. in Meteorology and Atmospheric Science   **2020**

  The Pennsylvania State University, University Park, PA

  Dissertation title: Assessing the impact of model structural complexity of the methane cycle on the Earth system response

  Advisor: Chris E. Forest

B.A. in Astrophysics   **2015**

  Franklin and Marshall College, Lancaster, PA

  Minor: Applied Mathematics

Employment

Research Assistant   **2015 - 2020**

  Use of advanced data modeling technologies to derive insights on global climate change.

Teaching Assistant   **2018 - 2020**

  In-classroom teaching of undergraduate courses; Introductory Meteorology (METEO 003), Climate Dynamics (METEO 470), Weather Risk and Financial Markets (METEO 460). Held regular group review sessions.

Consultant for Prescient Weather   **Summer 2018**

  Wrote weekly commentaries and analyses for clients on quantitative potential yield estimates for U.S. crops given evolving weather and satellite information.

Noteworthy Publications and Presentations

Rolph, K. A., C. E. Forest, and M. D. Ruark, 2019: The role of non-CO_2 mitigation options within the dairy industry for pursuing climate change targets. *Environ. Res. Lett.*, **14 (8)**, 084039, doi:0.1088/1748-9326/ab28a3.

Rolph, K. A. and C. E. Forest, 2018: Climate-carbon cycle feedbacks during the response to pulse perturbations of methane. Abstract A43P-3354 presented at 2018 Fall Meeting, AGU, Washington, D.C.

Crawford, F., A. Rane, L. Tran, **K. Rolph**, D. R. Lorimer, and J. P. Ridley, 2016: A search for highly dispersed fast radio bursts in three Parkes multibeam surveys. *Mon. Not. R. Astron. Soc.*, **460 (3)**, 3370–3375, doi:10.1093/mnras/stw1233, arXiv:1605.06074v1.

Shkolnik, E. L., **K. A. Rolph**, S. Peacock, and T. S. Barman, 2014: Predicting Lyα and Mg II fluxes from K and M dwarfs using galaxy evolution explorer ultraviolet photometry. *Astrophys. J. Lett.*, **796 (1)**, 1–6, doi:10.1088/2041-8205/796/1/L20.

Service

Co-Chair of the EMS Graduate Student Council   **2018 - 2020**

  Advocated for the graduate student body in the College of Earth and Mineral Sciences. Fostered scientific communication between the departments and awarded student achievements.

Science Education Outreach Volunteer   **Summer 2017**

  Organized and facilitated hands-on learning activities about weather and climate for elementary schoolers.

Volunteer at PAWS Animal Shelter   **2016 - 2020**

  Extended care for abandoned or ailing animals by providing food, shelter, cleaning services, and companionship. Assisted in public adoptions and front desk clerical support.